



University
of Glasgow

Galloway, Kyle W. (2009) *New routes to single molecule magnets*.
PhD thesis.

<http://theses.gla.ac.uk/867/>

Copyright and moral rights for this thesis are retained by the author

A copy can be downloaded for personal non-commercial research or
study, without prior permission or charge

This thesis cannot be reproduced or quoted extensively from without first
obtaining permission in writing from the Author

The content must not be changed in any way or sold commercially in any
format or medium without the formal permission of the Author

When referring to this work, full bibliographic details including the
author, title, awarding institution and date of the thesis must be given

New Routes to
Single Molecule Magnets

Kyle William Galloway

M.Sci.

Submitted in fulfilment of the requirements for the Degree of
Doctor of Philosophy

Department of Chemistry
Faculty of Physical Sciences
University of Glasgow

May 2009



University
of Glasgow



Abstract

Structural and magnetic studies of citrate coordination clusters are presented for reaction systems involving cobalt(II), copper(II) and nickel(II). The cobalt(II) compounds incorporate cubane structural motifs that are of particular interest for the generation of single molecule magnet (SMM) behaviour. The product family includes a Co₄ SMM cluster, a Co₆ SMM cluster and a 3D network of linked SMM units. A new route to the erinaceous Co₆ cluster crystals is reported, which allows further investigation of the hydration dependent magnetic behaviour of the samples. The structures of a range of copper(II) cluster sizes are described, including a monomer, dimers, trimers and a tetramer. Correlations between structure and magnetic properties are discussed, including the important structural role of the citrate ligand. Two types of citrate-based copper(II) dimers are shown to undergo unusual structural transformations at high pressure. Initial results of the development of *3d-4f* systems based on cobalt(II) and copper(II) are described, including a discussion of reaction methodology. Finally, a brief examination of the nickel(II) citrate system includes an overview of the complicated synthetic conditions, then considers the magnetic properties of the nickel(II) analogue of the Co₄ cluster.

Index

1.0 – Introduction	7
1.1 – Magnetism	7
1.2 – Magnetostructural Correlation	11
1.3 – Single Molecule Magnets	12
1.4 – Summary of Relevant Literature	15
1.5 – Analysis Techniques	19
1.5.1 – Infrared Spectroscopy	19
1.5.2 – Electronic Spectroscopy	20
1.5.3 – X-ray Diffraction	21
1.5.4 – SQUID Magnetometer	22
2.0 – The Cobalt Citrate System	27
2.1 – The Co₄ Cluster [C(NH₂)₃]₈{Co₄(cit)₄}.4H₂O	27
2.1.1 – Synthesis of [C(NH ₂) ₃] ₈ {Co ₄ (cit) ₄ }.4H ₂ O	27
2.1.2 – Structure of [C(NH ₂) ₃] ₈ {Co ₄ (cit) ₄ }.4H ₂ O	28
2.1.3 – Electronic Spectroscopy of [C(NH ₂) ₃] ₈ {Co ₄ (cit) ₄ }.4H ₂ O	30
2.1.4 – Magnetic Properties of [C(NH ₂) ₃] ₈ {Co ₄ (cit) ₄ }.4H ₂ O	31
2.1.5 – Co ₄ High Pressure Structural Study	36
2.1.6 – Heterometallic Cubane Systems	41
2.1.6.1 – Heterometallic Cubane Syntheses	41
2.1.6.2 – Discussion of Heterometallic Cubane Syntheses	42
2.1.6.3 – Magnetic Properties of [C(NH ₂) ₃] ₈ Co ₂ Zn ₂ (cit) ₄ .7H ₂ O	44
2.2 – The Co₆ Cluster {Co₄(cit)₄[Co(H₂O)₅]₂}⁴⁻	47
2.2.1 – Synthesis of [NMe ₄] ₃ Na{Co ₄ (cit) ₄ [Co(H ₂ O) ₅] ₂ }.11H ₂ O	47
2.2.2 – Structure of [NMe ₄] ₃ Na{Co ₄ (cit) ₄ [Co(H ₂ O) ₅] ₂ }.11H ₂ O	48
2.2.3 – Co ₆ Reaction Solution Spectroscopic Study	50
2.2.4 – Magnetic Properties of Na{Co ₆ }	52
2.2.5 – Hydration Dependent Magnetic Properties of Na{Co ₆ }	57

2.3 – Alkali Metal Analogues of Na{Co₆}	65
2.3.1 – Lithium Analogue	66
2.3.1.1 – Synthesis of [NMe ₄] ₃ Li{Co ₄ (cit) ₄ [Co(H ₂ O) ₅] ₂ }.16H ₂ O	66
2.3.1.2 – Structure of [NMe ₄] ₃ Li{Co ₄ (cit) ₄ [Co(H ₂ O) ₅] ₂ }.16H ₂ O	67
2.3.1.3 – Magnetic Properties of Li{Co ₆ }	68
2.3.2 – Potassium Analogue	70
2.3.2.1 – Synthesis of [NMe ₄] ₃ K{Co ₄ (cit) ₄ [Co(H ₂ O) ₅] ₂ }.14H ₂ O	70
2.3.3 – Caesium Analogue	71
2.3.3.1 – Synthesis of [NMe ₄] ₃ Cs{Co ₄ (cit) ₄ [Co(H ₂ O) ₅] ₂ }.16H ₂ O	71
2.3.3.2 – Structure of [NMe ₄] ₃ Cs{Co ₄ (cit) ₄ [Co(H ₂ O) ₅] ₂ }.16H ₂ O	71
2.3.3.3 – Hydration Dependent Magnetic Properties of Cs{Co ₆ }	72
2.3.4 – Attempted Rubidium Analogue	75
2.3.4.1 – Synthesis of [NMe ₄] ₄ {Co ₄ (cit) ₄ [Co(H ₂ O) ₅] ₂ }.18H ₂ O	75
2.3.4.2 – Structure of [NMe ₄] ₄ {Co ₄ (cit) ₄ [Co(H ₂ O) ₅] ₂ }.18H ₂ O	76
2.3.4.3 – Hydration Dependent Magnetic Properties of NMe ₄ {Co ₆ }	79
2.4 – The 3D Network {Na₄Co₄(cit)₄[Co(H₂O)₃]₂(H₂O)₁₅}.3H₂O	83
2.4.1 – Synthesis of {Na ₄ Co ₄ (cit) ₄ [Co(H ₂ O) ₃] ₂ (H ₂ O) ₁₅ }.3H ₂ O	83
2.4.2 – Structure of {Na ₄ Co ₄ (cit) ₄ [Co(H ₂ O) ₃] ₂ (H ₂ O) ₁₅ }.3H ₂ O	84
2.4.3 – Magnetic Properties of the 3D Network	85
3.0 – The Copper Guanidinium System	92
3.1 – Copper Citrate Dimer [C(NH₂)₃]₄{Cu₂(cit)₂}.H₂O	93
3.1.1 – Synthesis of [C(NH ₂) ₃] ₄ {Cu ₂ (cit) ₂ }.H ₂ O	93
3.1.2 – Structure of [C(NH ₂) ₃] ₄ {Cu ₂ (cit) ₂ }.H ₂ O	93
3.1.3 – Magnetic Properties of [C(NH ₂) ₃] ₄ {Cu ₂ (cit) ₂ }.H ₂ O	95
3.1.4 – Copper Citrate Dimer High Pressure Structural Study	99
3.1.5 – Copper Citrate Dimer High Pressure Electronic Spectroscopy	100

3.2 – Hydroxy Bridged Dimer [C(NH₂)₃]{Cu₂cit[C(NH₂)₂NH]₂(OH)}	102
3.2.1 – Synthesis of [C(NH ₂) ₃]{Cu ₂ cit[C(NH ₂) ₂ NH] ₂ (OH)}	102
3.2.2 – Structure of [C(NH ₂) ₃]{Cu ₂ cit[C(NH ₂) ₂ NH] ₂ (OH)}	103
3.2.3 – Comparison of Citrate Based Dimer Electronic Spectra	106
3.2.4 – Magnetic Properties of [C(NH ₂) ₃]{Cu ₂ cit[C(NH ₂) ₂ NH] ₂ (OH)}	106
3.2.5 – Hydroxy Bridged Dimer High Pressure Structural Study	108
3.3 – Copper Citrate Trimer {Cu₃(cit)₃Na(OH)}⁶⁻	111
3.3.1 – Synthesis of Copper Citrate Trimer	111
3.3.2 – Structure of {Cu ₃ (cit) ₃ Na(OH)} ⁶⁻	113
3.3.2 – Magnetic Properties of Na ⁺ Copper Citrate Trimer	116
3.4 – Related Ligand Systems	118
3.4.1 – Copper Carbonate Network [C(NH ₂) ₃] ₂ Cu(CO ₃) ₂	120
3.4.1.1 – Synthesis of [C(NH ₂) ₃] ₂ Cu(CO ₃) ₂	120
3.4.1.2 – Structure of [C(NH ₂) ₃] ₂ Cu(CO ₃) ₂	121
3.4.1.3 – Magnetic Properties of [C(NH ₂) ₃] ₂ Cu(CO ₃) ₂	122
3.4.2 – Copper Triol Dimer {Cu ₂ (H ₂ L1) ₂ }(NO ₃) ₂	123
3.4.2.1 – Synthesis of {Cu ₂ (H ₂ L1) ₂ }(NO ₃) ₂	123
3.4.2.2 – Structure of {Cu ₂ (H ₂ L1) ₂ }(NO ₃) ₂	123
3.4.2.3 – Magnetic Properties of {Cu ₂ (H ₂ L1) ₂ }(NO ₃) ₂	126
3.4.3 – Copper Tetramer {Cu ₄ (L2) ₂ [C(NH ₂) ₂ NH] ₄ (OMe) ₂ }.2MeOH.3H ₂ O	127
3.4.3.1 – Synthesis of	
{Cu ₄ (L2) ₂ [C(NH ₂) ₂ NH] ₄ (OMe) ₂ }.2MeOH.3H ₂ O	127
3.4.3.2 – Structure of	
{Cu ₄ (L2) ₂ [C(NH ₂) ₂ NH] ₄ (OMe) ₂ }.2MeOH.3H ₂ O	128
3.4.3.3 – Magnetic Properties of	
{Cu ₄ (L2) ₂ [C(NH ₂) ₂ NH] ₄ (OMe) ₂ }.2MeOH.3H ₂ O	130
4.0 – 3d-4f Reaction Systems	132
4.1 – Addition of Lanthanide Ions to the Cobalt Citrate System	132
4.1.1 – Discussion of Reaction Methodology	132

4.2 – Addition of Lanthanide Ions to the Copper Citrate System	137
4.2.1 – Copper(II) Monomer $[\text{C}(\text{NH}_2)_3]_2\{\text{Cu}(\text{H}_2\text{cit})_2\}$	137
4.2.1.1 – Synthesis of $[\text{C}(\text{NH}_2)_3]_2\{\text{Cu}(\text{H}_2\text{cit})_2\}$	137
4.2.1.2 – Structure of $[\text{C}(\text{NH}_2)_3]_2\{\text{Cu}(\text{H}_2\text{cit})_2\}$	138
4.2.2 – The Copper(II) Erbium(III) Network	
$\{[\text{C}(\text{NH}_2)_3]_{5.33}\text{Na}_2\text{Cu}_{1.33}\text{Er}_2(\text{CO}_3)_8(\text{H}_2\text{O})_2\} \cdot 6\text{H}_2\text{O}$	142
4.2.2.1 – Synthesis of	
$\{[\text{C}(\text{NH}_2)_3]_{5.33}\text{Na}_2\text{Cu}_{1.33}\text{Er}_2(\text{CO}_3)_8(\text{H}_2\text{O})_2\} \cdot 6\text{H}_2\text{O}$	142
4.2.2.2 – Structure of	
$\{[\text{C}(\text{NH}_2)_3]_{5.33}\text{Na}_2\text{Cu}_{1.33}\text{Er}_2(\text{CO}_3)_8(\text{H}_2\text{O})_2\} \cdot 6\text{H}_2\text{O}$	142
4.2.2.3 – Magnetic Properties of	
$\{[\text{C}(\text{NH}_2)_3]_{5.33}\text{Na}_2\text{Cu}_{1.33}\text{Er}_2(\text{CO}_3)_8(\text{H}_2\text{O})_2\} \cdot 6\text{H}_2\text{O}$	147
5.0 – The Nickel Citrate System	149
5.1 – Discussion of Reaction Methodology	151
5.2 – Investigation of the Ni₂₁ Synthesis	151
5.2.1 – Addition of Guanidinium Ions to the Ni ₂₁ Synthesis	151
5.2.2 – Nickel(II) Monomer $[\text{NMe}_4]_4\{\text{Ni}(\text{Hcit})_2\} \cdot 11\text{H}_2\text{O}$	154
5.2.2.1 – Synthesis of $[\text{NMe}_4]_4\{\text{Ni}(\text{Hcit})_2\} \cdot 11\text{H}_2\text{O}$	154
5.2.2.2 – Structure of $[\text{NMe}_4]_4\{\text{Ni}(\text{Hcit})_2\} \cdot 11\text{H}_2\text{O}$	155
5.3 – The Ni₄ Cluster $[\text{C}(\text{NH}_2)_3]_8\{\text{Ni}_4(\text{cit})_4\} \cdot 6\text{H}_2\text{O}$	156
5.3.1 – Synthesis of $[\text{C}(\text{NH}_2)_3]_8\{\text{Ni}_4(\text{cit})_4\} \cdot 6\text{H}_2\text{O}$	156
5.3.2 – Structure of $[\text{C}(\text{NH}_2)_3]_8\{\text{Ni}_4(\text{cit})_4\} \cdot 6\text{H}_2\text{O}$	156
5.3.3 – Magnetic Properties of $[\text{C}(\text{NH}_2)_3]_8\{\text{Ni}_4(\text{cit})_4\} \cdot 6\text{H}_2\text{O}$	157
Conclusions	161
Appendix – Crystallography	164
Acknowledgements	167

1.0 – Introduction

1.1 – Magnetism

Any moving charged particle creates a magnetic field [1]. In the context of atoms the magnetism is created by the spin of the electrons, by electron movement around the nucleus within the orbitals, and in some cases by nuclear spin, in which case the nucleus itself has an overall net spin (such as hydrogen).

There are five main magnetic states of matter [2]. In a *diamagnetic* material all of the electron spins are paired and so the overall net spin is zero. This results in a weak repulsion to an applied magnetic field. All atomic and molecular compounds exhibit diamagnetic behaviour to some extent. A *paramagnetic* material has an attraction to an applied magnetic field due to interaction of the external field with one or more unpaired electrons within the material. The interaction between paramagnetic atoms or molecules with their surrounding neighbours gives rise to the bulk magnetic properties of the material (Figure 1-1). In the case of *paramagnetism* each unpaired electron has no effect on any other electrons in its neighbours and so the spins are in random directions. The spins can be easily changed to a uniform direction by application of an external magnetic field. *Ferromagnetism* occurs when adjacent spins are aligned parallel and in the same direction, which results in a large net magnetic moment, even with no applied field. *Antiferromagnetism* occurs when the spins are parallel but face in opposite directions, which leads to a cancelling of the spins and hence a zero magnetic moment. A special case of antiferromagnetic behaviour results in the last main class, *ferrimagnetism*. Here the spins are still aligned in an antiparallel arrangement, but the spins in each direction are of different magnitudes and so the substance has an overall magnetic moment.



Figure 1-1 – The arrangement of spins for a paramagnet, antiferromagnet, ferrimagnet and ferromagnet.

(The following section is summarised from [3], [4])

The magnetic susceptibility (χ) is the quantitative response of a magnetic material to an applied magnetic field (H) and is related to the magnetisation (M) via the equation

$$\chi = \frac{dM}{dH} \quad \text{Equation 1}$$

If the applied field is weak then the magnetic susceptibility is essentially independent of the magnetic field such that

$$\chi = \frac{M}{H} \quad \text{Equation 2}$$

The magnetic susceptibility consists of two components, the diamagnetic susceptibility (χ^D , negative) and the paramagnetic susceptibility (χ^P , positive).

$$\chi = \chi^D + \chi^P \quad \text{Equation 3}$$

Diamagnetism is a property of matter and is always present, even in paramagnetic compounds. χ^D is essentially independent of temperature and field strength and so can be estimated based on the compound formula weight [3] or by using Pascal's Constants (since χ^D is additive).

The classical model considers the spins to be freely rotating vectors (Figure 1-1) that can adopt a minimum energy orientation on the application of a magnetic field. However angular momentum is quantised in nature and so the quantum model is modified such that a state with total spin angular momentum S has $2S+1$ sublevels with spin quantum numbers m_s . These sublevels are all degenerate in the absence of an applied field unless there is coupling with other excited states (as in the case of Zero Field Splitting (ZFS), see later). The application of a field leads to a Zeeman splitting of the sublevels, with the energy of each level given by the equation

$$E_n = m_s g \beta H \quad \text{Equation 4}$$

where β is the Bohr magneton and H is the magnetic field. This is the first order Zeeman effect where the splitting is proportional to H . However the application of the magnetic field may also lead to the mixing of ground and excited states in the second order Zeeman effect that is proportional to H^2 . The energy of the level n can be expressed as the power series

$$E_n = E_n^{(0)} + E_n^{(1)} H + E_n^{(2)} H^2 + \dots \quad \text{Equation 5}$$

where the first term is the energy in zero field, the second term gives the energy in an applied field and the third term refers to the interactions with excited states.

Under the classical approach, the magnetisation of a sample in a field (H) is related to its energy (E) by the equation

$$M = -\frac{dE}{dH} \quad \text{Equation 6}$$

but since the quantum mechanical model has an energy spectrum for the molecule (E_n with $n = 1, 2, 3, \dots$) there is a microscopic magnetisation (μ_n) for each energy level with

$$\mu_n = -\frac{dE_n}{dH} \quad \text{Equation 7}$$

The sum of the microscopic magnetisations weighted to the Boltzmann distribution for the occupation of the energy levels gives the macroscopic magnetisation (M) and the fundamental equation of molecular magnetism

$$M = \frac{N \sum_n -\frac{dE_n}{dH} \exp(E_n / kT)}{\sum_n -\exp(E_n / kT)} \quad \text{Equation 8}$$

where N is Avogadro's number, T is the absolute temperature and k is the Boltzmann constant. This equation is difficult to apply, so by expanding the energies as a power series and assuming that $H/kT \ll 1$, Van Vleck proposed the simplified equation

$$M = \frac{N \sum_n [(E_n^{(1)})^2 / kT - 2E_n^{(2)}] \exp(E_n^{(0)} / kT)}{\sum_n -\exp(E_n^{(0)} / kT)} \quad \text{Equation 9}$$

where $E_n^{(0)}$ is the energy of level n in zero applied field, $E_n^{(1)}$ and $E_n^{(2)}$ are the first and second order Zeeman coefficients. The Van Vleck equation can be simplified further (including an assumption that E_n are linear with H) to give the Curie Law

$$\chi = \frac{Ng^2 \beta^2}{3kT} S(S+1) \quad \text{Equation 10}$$

where S is the spin ground state and g is a constant known as the g factor (~ 2). Under the cgsemu system of units the Curie Law conveniently approximates to

$$\chi T = \frac{g^2}{8} S(S+1) \quad \text{Equation 11}$$

The Curie Law is only valid when the approximation used in the simplification ($H/kT \ll 1$) is applicable, which is under conditions where the applied field (H) is not too

large and the temperature is not too small. If the value H/kT is large, such as when large fields are applied, the magnetisation tends towards a saturated value (M_{sat}) that occurs when the magnetic dipoles of the sample are completely aligned.

$$M_{sat} = Ng\beta S \quad \text{Equation 12}$$

It can also be useful to consider paramagnetism using the magnetic moment (μ) given by the equation

$$\mu_{LS} = \sqrt{[g^2 S(S+1) + L(L+1)]} \quad \text{Equation 13}$$

where S is the total spin quantum number and L is the total orbital angular momentum quantum number (note that this formula applies to a free ion). The orbital contribution becomes significant if an electron can have orbital angular momentum. This occurs if the orbital that the electron occupies can be transformed into an exactly equivalent and degenerate orbital by rotation. In the case of an octahedral ligand field an electron in a t_{2g} orbital can contribute to orbital angular momentum whereas an electron in an e_g orbital can not. Under the Russell-Saunders coupling scheme, in the A and E states the orbital angular momentum is quenched by the crystal field, whereas in the T state some residual orbital momentum remains. There is therefore no first order orbital contribution expected for octahedral Ni^{2+} (d^8) or Cu^{2+} (d^9). However for Co^{2+} (d^7) there is a significant orbital contribution since the T ground term results in first order spin-orbit coupling. This gives a large splitting of the energy levels, and so the population of the levels and the magnetic moment become temperature dependent (the Curie Law is not obeyed).

When considering a magnetic molecule, a cluster of C spins of S_i has a total number of magnetic states given by the equation

$$\text{Number of cluster spin states} = (2S_i + 1)^C \quad \text{Equation 14}$$

For a copper dimer $S_i = 1/2$, $C = 2$ and so there are 4 states in total, which are $S = 0$ (1 level) and $S = 1$ (3 degenerate levels with $m_s = +1, 0, -1$). The $S = 0$ and $S = 1$ states are separated with a difference in energy of $2J$ (the interaction energy). For ferromagnetic coupling J is positive and the $S = 1$ state is lower in energy, conversely for antiferromagnetic coupling J is negative and the $S = 0$ state is lower in energy. The magnetic properties of the molecules are modelled using effective exchange parameters (J) between spin centres.

It is clear from the cluster spin state equation that since the number of spin states varies to the power of C , for clusters with large numbers of spin centres there will be a very large number of spin levels. On increasing the value of C , eventually there will be so many spin levels that they will merge into a continuum. Consequently in the study of molecular magnetism there is interest in synthesising ever larger clusters (or joining smaller clusters together) in order to investigate the changeover from molecular behaviour (with discrete levels) to bulk magnetic behaviour (with a continuum of levels).

1.2 – Magnetostructural Correlation

Control of cluster topology is a major objective in the synthesis of spin clusters due to correlation between structure and magnetism. Coupling between the spins of the metal centres in a cluster usually occurs via superexchange pathways provided by the coordinating atoms of the ligand species (often oxygen). The orbital overlap between the two metal centres and the intermediate ligand atom is therefore very important in determining the nature of the coupling interactions. Figure 1-2 shows that when the bridging angle between two metal centres is 180° the spin coupling is antiferromagnetic, while at 90° it is ferromagnetic. It is therefore desirable to have ‘orthogonal steps’ in the cluster structure to maximise the total spin, since a sizable cluster with numerous metal ions is not particularly useful for generating a large spin ground state if antiferromagnetic exchange dominates and the spins simply cancel each other out.

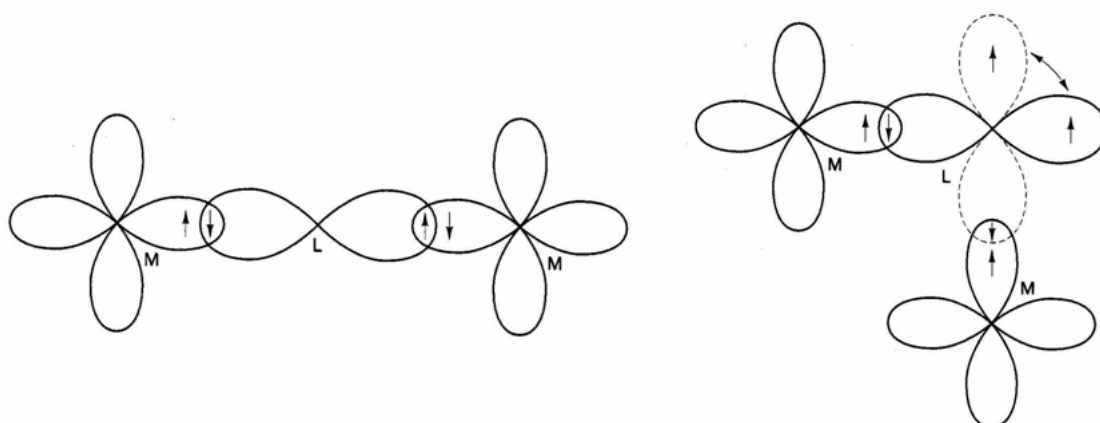


Figure 1-2 – Orbital diagram illustrating the effect of bridging angle on the spin coupling between metal centres (M) via superexchange using ligand atoms (L), with antiferromagnetic coupling at 180° and ferromagnetic coupling at 90° [2].

At some point between 180° and 90° there must be a changeover in the coupling behaviour. It is possible to study a family of related structures in order to determine magnetostructural correlations, such as Table 1-1 which shows the relationship between the bridging angle and coupling constant for planar hydroxo-bridged copper dimers. The relationship is linear in this case with a changeover angle of 97.6° [5,6], while a similar linear relationship has been observed with alkoxo-bridged copper dimers with a changeover in coupling at 95.8° [6,7]. It can also be useful to employ computational chemistry to model magnetic interactions over a much wider variety of structural conditions than are accessible experimentally [8,9,10]. Magnetostructural correlations are therefore very useful for the analysis of magnetic clusters.

Complex	$\phi_{\text{Cu-O-Cu}}$, deg	$2J$, cm^{-1}
[Cu(bpy)OH] ₂ (NO ₃) ₂	95.6 (1)	+172
[Cu(bpy)OH] ₂ (ClO ₄) ₂	96.6 (2)	+93
[Cu(bpy)OH] ₂ SO ₄ ·5H ₂ O	97.0 (2)	+49
[Cu(eaep)OH] ₂ (ClO ₄) ₂	98.8-99.5 (3)	-130
β -[Cu(dmaep)OH] ₂ (ClO ₄) ₂	100.4 (1)	-200
[Cu(tmen)OH] ₂ (ClO ₄) ₂	102.3 (4)	-360
[Cu(teen)OH] ₂ (ClO ₄) ₂	103.0 (3)	-410
[Cu(tmen)OH] ₂ Br ₂	104.1 (2)	-509

Table 1-1 – A study of planar hydroxo-bridged dimers illustrates the changeover from ferromagnetic (positive J) to antiferromagnetic coupling (negative J) at a bridging angle of ~97° [5].

1.3 – Single Molecule Magnets

A Single Molecule Magnet (SMM) consists of a central large spin metal-oxo core, which is surrounded by organic ligands to form a discrete molecular species. It has the characteristic property that the molecule retains its spin orientation even in the absence of an external magnetic field. If the molecule possesses a large spin ground state (S) as well as an Ising type magnetic anisotropy ($D < 0$) then this gives rise to an energy barrier that lies between the ‘spin-up’ and ‘spin down’ configurations as shown in Figure 1-3 [11]. This is the result of Zero Field Splitting (ZFS) of the ground state caused by spin-orbit coupling of the ground and excited states, which splits the M_s levels in the absence of an applied field [3,4].

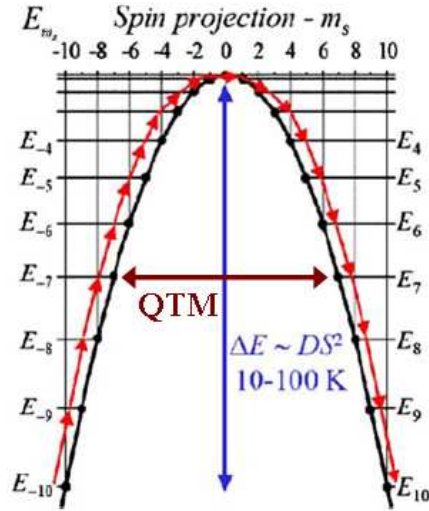


Figure 1-3 – The ZFS of the M_S levels for an $S = 10$ system with energy barrier ΔE between the $m_s = -10$ and $m_s = +10$ states. The dark red arrow shows a shortcut through the barrier via Quantum Tunneling of the Magnetisation [11].

The size of the energy barrier (ΔE) varies with the spin (S) and axial zero-field splitting parameter (D) via the equations

$$\Delta E = S^2/D \text{ \{for integer spin\}} \quad \text{Equation 15}$$

$$\Delta E = (S^2 - 1/4)/D \text{ \{for half-integer spin\}} \quad \text{Equation 16}$$

This energy barrier will therefore oppose the re-orientation of the magnetisation, and so if the height of the barrier is large in comparison to the available thermal energy, the resulting relaxation of the magnetisation will be slow [11,12].

The relaxation rate can be investigated by ac magnetic susceptibility measurements. Ac measurements are used to examine the dynamic susceptibility (Equation 1) of a sample by applying an oscillating magnetic field. The dynamic susceptibility is a complex quantity with real (dispersion) and imaginary (absorption) components that are dependent on the angular frequency ($\omega = 2\pi\nu$) of the ac field.

$$\chi(\omega) = \chi'(\omega) - i\chi''(\omega) \quad \text{Equation 17}$$

The relaxation process follows an Arrhenius law for a thermal activation process to overcome the energy barrier with

$$\tau = \tau_0 \exp(\Delta E / kT) \quad \text{Equation 18}$$

where $\tau = (\omega)^{-1}$. So from an Arrhenius plot of $\ln(\tau)$ versus $(1/T)$ the energy barrier (ΔE) can be determined from the gradient of the line. [4, 13]

As the ac magnetic field frequency becomes close to the relaxation rate of the molecules the observed in-phase susceptibility (χ') reduces. Therefore the out-of-phase component (χ'') will increase. For measurements where there is only one relaxation process operating, a graph of χ'' against temperature will show a peak at the temperature where $\omega = (\tau)^{-1}$. If the switching frequency of the applied field is increased, the peak should be shifted to a higher temperature [14]. This effect is demonstrated in the data obtained for the first SMM $[\text{Mn}_{12}\text{O}_{12}(\text{MeCO}_2)_{16}(\text{H}_2\text{O})_4] \cdot 2\text{MeCO}_2\text{H} \cdot 4\text{H}_2\text{O}$ [15], which is shown in Figure 1-4.

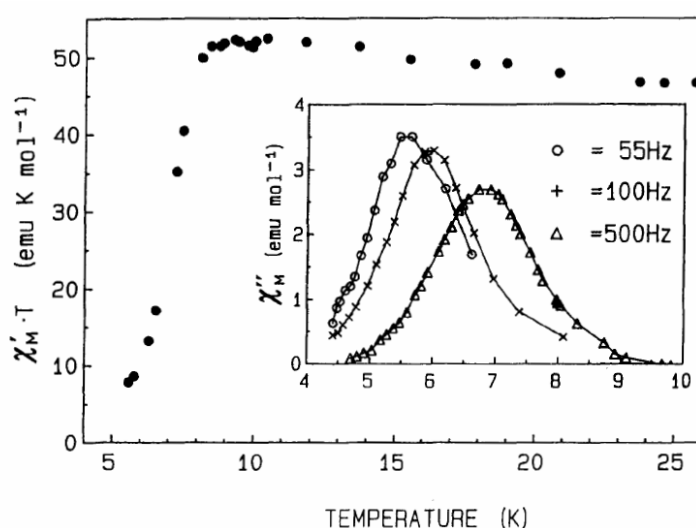


Figure 1-4 – The frequency dependent χ'' peaks seen in the ac susceptibility measurements for the SMM $[\text{Mn}_{12}\text{O}_{12}(\text{MeCO}_2)_{16}(\text{H}_2\text{O})_4] \cdot 2\text{MeCO}_2\text{H} \cdot 4\text{H}_2\text{O}$ [16].

A single molecule magnet will also display magnetisation versus field hysteresis loops as shown in Figure 1-5. These often have characteristic steps in the loop due to Quantum Tunnelling of the Magnetisation (QTM) through the energy barrier (see Figure 1-3) [17]. QTM is the result of transverse anisotropy which gives a superposition of states of both sides of the barrier with a tunnel splitting. The axial anisotropy (described by the D term of the spin Hamiltonian) splits the m_s levels, while the transverse anisotropy (E term) mixes the m_s states (as do the higher terms of the spin Hamiltonian). The application of a magnetic field will alter the relative energies of the m_s states. QTM is only possible when the energy levels on both sides of the barrier are aligned and can therefore only occur at certain points as the field is swept, thus creating steps in the hysteresis loop. SMM hysteresis is temperature and

sweep rate dependent, and the loops broaden on decreasing the temperature or on increasing the sweep rate of the magnetic field.

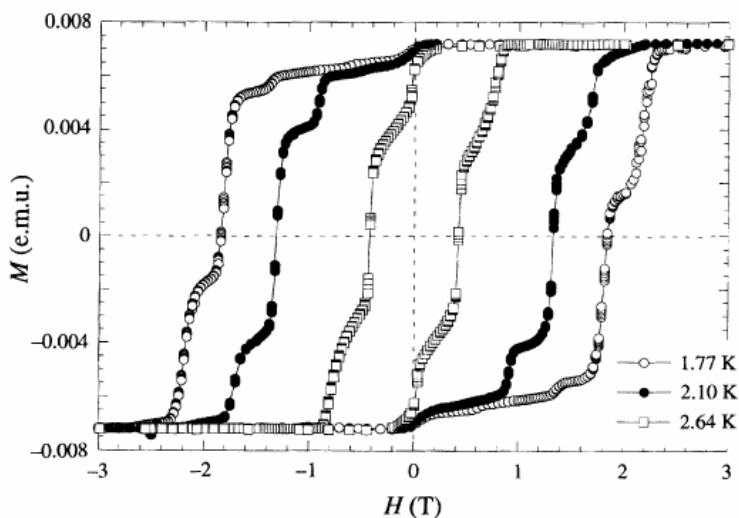


Figure 1-5 – Magnetisation versus field hysteresis loops observed for the SMM $[\text{Mn}_{12}\text{O}_{12}(\text{MeCO}_2)_{16}(\text{H}_2\text{O})_4] \cdot 2\text{MeCO}_2\text{H} \cdot 4\text{H}_2\text{O}$. The steps in the loops are due to quantum tunnelling of the magnetisation [17].

The initial proposal for the application of SMMs was for high density data storage with each molecule representing one bit, however this now appears less likely due to the technological limitations for addressing individual molecules and in obtaining functionality at non-cryogenic temperatures. More promising future applications of SMMs include quantum computing, MRI contrast agents and magnetic refrigeration [12,14].

1.4 – Summary of Relevant Literature

The definitive experimental evidence for SMM behaviour is the observation of a frequency dependent signal in the out-of-phase component of the ac magnetic susceptibility, together with temperature and sweep rate dependent hysteresis loops. It should be noted that the majority of literature SMMs are identified only by ac measurements since in many cases the hysteresis loops occur at temperatures below the limit of commercial SQUID magnetometers [11].

In the field of single molecule magnets an objective of considerable importance is the synthesis of new clusters possessing greater barriers to the re-orientation of the magnetisation [18]. Efforts to increase the barrier height have targeted the synthesis of clusters containing larger numbers of metal centres in order to increase S , the use of metals with a large anisotropy to increase D , or by using a directed synthesis approach towards specific cluster geometries [19]. A large number of metal centres do not guarantee a large molecular S : one approach is to have a cluster topology that provides ferromagnetic interactions such as a metal-oxo cubane structure that can promote ferromagnetic interactions via superexchange.

Metal-oxo cubane structures often appear as structural elements in clusters produced by self-assembly from complex inorganic reaction systems. This is illustrated by the work of Aromi *et al.* [20] on the cobalt-pivalate system that offers a wide variety of products including Co_2 , Co_4 , Co_5 , Co_6 , Co_7 and Co_{14} clusters. The authors propose a reaction scheme based on the assembly of small binuclear units and stepwise addition of cobalt(II) ions to form cubane units. These can then be further enlarged, eventually allowing the formation of stacked, face sharing di- and tri- cubane units. The use of pivalate in conjunction with 8-hydroxyquinaldine gives a discrete cubane with isostructural products using nickel(II) or cobalt(II) [21]. In this case both cubanes show overall antiferromagnetic coupling. The specific geometry of the cubane has a marked effect on the nature of the interactions as illustrated by magnetostructural correlations such as those of nickel(II) cubanes by Halcrow *et al.* [22]. Ni_4 cubanes can function as SMMs, such as the cluster family reported by Yang *et al.* [23] which have $S = 4$ ground states and exhibit interesting exchange bias features. Exchange bias has also been studied in detail for dimers of Mn_4 cubane SMMs [24]. The effect of cubane structural geometry on cluster magnetism is elegantly illustrated by the ferrous cubes synthesized by Oshio *et al.* [25]. Here the D parameter can be tuned by adjusting the bite of the coordinating ligand and hence the local geometry at the Fe(II) centres.

SMM research has extensively investigated manganese chemistry in order to utilize the large single ion anisotropy of Mn(III) to obtain a large barrier to the reorientation of the magnetisation (ΔE). Another promising candidate with a large single ion

anisotropy is Co(II), although in comparison to Mn-based SMMs, the field of Co(II) SMMs is at early stage of development. Slow relaxation of the magnetisation has been observed in a mononuclear Co(II) SMM [26], trinuclear Co-Ln-Co clusters (where Ln = Gd, Tb, Dy, Ho) [27], a metal-oxo cubane [28], heptanuclear disks [29, 30], a cubane-based octanuclear cluster [31], an octanuclear phosphonate cage [32], spherical Co-W/Mo clusters [33] and a large Co₁₂ cluster consisting of three metal-oxo cubanes in a triangular arrangement [34]. Recently, further work on the synthesis of cobalt-sodium phosphonate cages was reported including a variety of cage sizes with early indications of slow relaxation in some examples [35].

The Murrie Research Group has a long-standing interest in the chemistry of cobalt(II) and nickel(II) with the citrate ligand $[C(O^-)(CO_2^-)(CH_2CO_2^-)_2 = cit^{4-}]$ that can promote cubane formation [36]. The family of nickel(II) citrate products and their syntheses will be discussed later in Chapter 5. In 2003, Murrie *et al.* reported a hexanuclear cobalt(II) citrate SMM $[NMe_4]_3Na\{Co_4(cit)_4[Co(H_2O)_5]_2\} \cdot 11H_2O$ which consists of a central $\{Co_4(cit)_4\}^{8-}$ cubane with two peripheral cobalt(II) centres (see Section 2.2) [37]. The cobalt(II) citrate cubane $[C(NH_2)_3]_8\{Co_4(cit)_4\} \cdot 4H_2O$ was recently reported to have a non-magnetic ground state [38]. Since this cubane has the same structure as the core of the Co₆ SMM and due to the close correlation of structure and magnetic properties, we would have expected the discrete $\{Co_4(cit)_4\}^{8-}$ cubane to function as an SMM. Hence, we synthesised our own samples to further investigate the magnetic properties, and observed SMM behaviour, both by ac susceptibility and hysteresis measurements as we had anticipated (see Section 2.1) [39]. The cobalt(II) citrate cubane has also been reported as a structural subunit in network compounds [40, 41] which will be discussed later (Sections 2.2 and 2.3).

Since the discovery of the first SMM, Mn₁₂ [15], a topic of interest has been the synthesis of increasingly large SMM clusters in order to investigate the proposed transition between the quantum behaviour of small, discrete SMM clusters to classical behaviour at greater sizes, the largest SMM reported to date being the Mn₈₄ wheel reported by Tassiopoulos *et al.* [19(a)]. Another approach is to use small SMM clusters as building blocks and link these together to form extended arrays. These are particularly attractive since the overall architecture is similar to a classical magnet, but the structural subunits already possess interesting magnetic properties such as Ising

type anisotropy and exchange coupling patterns that may favour a large spin. Wernsdorfer *et al.* have shown that intermolecular interactions in a dimer of manganese SMMs gives quantum behaviour that is different to the individual SMM cluster [24(a)]. Related work by Tiron *et al.* on a three dimensional exchange coupled network of manganese SMMs linked by weak intermolecular interactions has demonstrated that quantum tunneling of the magnetisation can be controlled using exchange interactions [42]. Therefore, it can be seen that linking SMM units into a coordination network can be used to create novel magnetic behaviour that may not otherwise be accessible.

The first examples of linked SMMs were based on the Mn_4 SMM $[Mn_4(hmp)_6Br_2(H_2O)_2]Br_2 \cdot 4H_2O$ (Hhmp = 2-hydroxymethylpyridine), which has a double cuboidal metal-oxo core [43]. The labile Mn(II) sites of this mixed valence SMM offer terminal ligands that are easily exchanged for bridging ligands, making it an ideal candidate for the synthesis of networks. Yoo *et al.* reported a 1D chain of Mn_4 clusters bridged by chloride ions that displays slow magnetic relaxation of the magnetisation and metamagnetic behaviour [44]. Miyasaka *et al.* reported a family of three 2D networks of Mn_4 with dicyanamide (dcn) linkers [45] that demonstrate the changeover from single-molecule magnet behaviour to classical long range canted antiferromagnetic order, due to the differences in the Mn_4 orientation within the lattices. One of the 2D networks also showed complex magnetic behaviour, as the results suggested a canted antiferromagnetic order with simultaneous slow relaxation of the magnetisation, and therefore had properties between the limits of the SMM and classical regimes. Miyasaka *et al.* have also reported the Mn_4 SMM linked into a 3D network [46] using a Mn(II) linker $[Mn\{N(CN)_2\}_6]^{4+}$ which displays long range ferrimagnetic ordering. The Mn_4 SMM has therefore been studied as the discrete cluster and as the complete dimensional set of 1D, 2D and 3D networks. In Section 2.3 a set of linked SMMs based on the cobalt(II) citrate cubane subunit will be described, which is only the second example of a single molecule magnet to be studied in this manner.

The synthesis of *3d-4f* SMM clusters is desirable due to the large spin and anisotropy contributed by the lanthanide ion. Chapter 4 considers the addition of lanthanide ions to the cobalt(II) and copper(II) reaction systems with citrate. The linear Co-Ln-Co

cluster $[L_2Co_2Ln][NO_3]$ (where $Ln = Gd, Tb, Dy, Ho$ and $LH_3 = (S)P[N(Me)N=CH-C_6H_3-2-OH-3-OMe]_3$) is currently the only reported type of cobalt(II)/lanthanide(III) SMM [27]. The syntheses use a specially designed ligand to fulfill the coordination requirements for both types of metal centre within the cluster. The gadolinium(III) centre provides a large spin contribution while the ferromagnetically coupled cobalt(II) centres provide significant anisotropy. This generates an energy barrier $\Delta E/k_B = 27.2$ K with $\tau_0 = 1.7 \times 10^{-7}$ s, which is a respectable size for such a relatively small cluster. The first example of a $3d-4f$ SMM was a Cu_2Dy_2 cluster reported by Osa *et al.* in 2004 and had an energy barrier of $\Delta E/k_B = 21$ K with $\tau_0 = 2.7 \times 10^{-8}$ s [47]. This was followed by a $CuDy_2$ cluster reported by Mori *et al.* in 2006, with an energy barrier $\Delta E/k_B = 47$ K with $\tau_0 = 1.1 \times 10^{-7}$ s, which is a remarkably large value for such a small number of metal centres [48]. Other examples include a Cu_6Dy_3 SMM with a structure consisting of three corner sharing cubanes [49], and a $CuDy_4$ cluster with antiferromagnetic coupling between the copper and lanthanide centres leading to a high spin ferrimagnetic cluster with SMM behaviour [50].

1.5 – Analysis Techniques

1.5.1 – Infrared Spectroscopy

Infrared (IR) spectra were recorded on a Jasco FT/IR-4100 equipped with a Pike Technologies MIRacle ATR. The Attenuated Total Reflectance (ATR) attachment allows the measurement of an IR spectrum by crushing the compound into close contact with the sample plate using an anvil on a screw thread. The spectrometer beam is diverted through the attachment such that it has a zigzag path along the sample plate and reflects off of the compound in contact with the plate (Figure 1-6). The compound therefore absorbs and reflects the appropriate wavelength as the beam passes, thus allowing collection of the spectrum.



Figure 1-6 – The IR spectrometer beam path through the ATR attachment [51].

The use of an ATR attachment for the measurement of IR spectra has several advantages over the traditional technique of dispersing the sample in a pressed KBr disc. Much less sample is required since only a small ATR plate must be covered, and this is very useful due to the low yields often encountered from crystallisation trials. In some cases the spectrum of a single crystal lifted from vial using a needle could be obtained by careful positioning on the ATR plate combined with increasing the number of scans to reduce the background noise. Indeed, it is possible to compare the spectra of individual crystals with a powdered sample of the bulk material. The sample can also be recovered after the measurement, which is obviously very difficult after pressing a KBr disc. The reflectance spectrum is also obtained from the pure sample that has not been altered in any way, which is important for sensitive samples such as those that are dependent on the level of hydration.

1.5.2 – Electronic Spectroscopy

Electronic spectra were recorded a Shimadzu UV-3101PC spectrometer. Solution samples were measured in a 0.1 cm cell unless otherwise stated. For measuring the solid state spectra of the compounds, the samples were dispersed in KBr discs. The disc was mounted in the sample beam of the spectrometer, with a manually adjusted attenuator in the reference beam. For samples measured at low temperature using a Displex cooler, the KBr disc was mounted in the sample holder using cryogrease. The spectrometer sample compartment was removed and the Displex sample windows carefully positioned in the spectrometer beam. A manual attenuator was again used in

the reference beam, and the equipment covered in a light exclusion fabric material. The samples were measured at the minimum temperature limit of the equipment at ~20 K.

1.5.3 – X-ray Diffraction

The principal crystallographic details for the novel compounds reported can be found in the Appendix. The X-ray diffraction studies for the majority of the product crystals were collected at 100 K on a Bruker APEX II diffractometer using Mo K α radiation. Weakly diffracting samples were collected at 100 K on a Rigaku R-Axis Rapid diffractometer with an image plate area detector using Mo K α radiation. The structures were solved using SIR92 or SUPERFLIP and refined using full-matrix least-squares refinement on F² using CRYSTALS. The atoms were refined anisotropically with the exception of hydrogen atoms which were placed geometrically and refined as riding groups. If required, the identities of bulk samples were confirmed by powder diffraction on a Bruker d8 diffractometer using Cu K α radiation.

Single crystal X-ray diffraction studies at high pressure were carried out in collaboration with the University of Edinburgh. A summary of the procedures are given below, however for full details refer to [52].

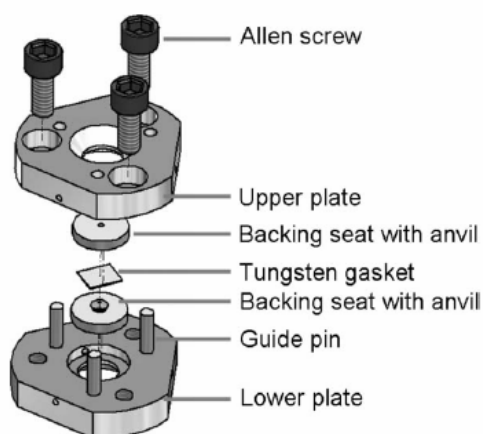


Figure 1-7 – Exploded view of the Merrill–Bassett diamond anvil cell [53].

High-pressure experiments were carried out with a modified Merrill-Bassett diamond anvil cell equipped with 600 μm culet diamonds and a tungsten gasket (Figure 1-7) [53]. The sample and a chip of ruby (as a pressure calibrant) were loaded into the DAC with a liquid hydrostatic medium. The ruby fluorescence method was utilized to measure the pressure [54]. Diffraction data were collected at ambient pressure on a Bruker SMART APEX diffractometer with Mo $K\alpha$ radiation. High pressure diffraction data were collected with synchrotron radiation on a Bruker APEX II diffractometer at the STFC Daresbury Laboratory on Station 9.8 ($\lambda = 0.4767 \text{ \AA}$).

1.5.4 – SQUID Magnetometer

Magnetic measurements were made on samples of mass 20-30 mg consisting of crystals which were lightly ground to give a randomly oriented polycrystalline sample and loaded into a gelatin capsule. The samples were restrained by compression of the inverted top half of the capsule. Samples of products with a large spin which showed slow magnetic relaxation, such as those containing cobalt(II), were restrained using eicosane wax to prevent torquing of the crystallites. The data were measured using a Quantum Design MPMS XL SQUID magnetometer and (for high frequency ac susceptibility) a Quantum Design PPMS magnetometer. Single crystal magnetic measurements were carried out using a microSQUID [55]. Diamagnetic corrections have been applied to the data presented.

- [1] Young, H. D.; Freedman, R. A. *University Physics*, 9th Edition, Addison Wesley, 1996, 903.
- [2] Kettle, S. F. A. *Physical Inorganic Chemistry – A Coordination Chemistry Approach*, Spektrum Academic Publishers, Oxford, 1996.
- [3] Kahn, O. *Molecular Magnetism*, VCH Publishers, 1993.
- [4] Murrie, M. *Molecular Magnetism*, lecture series, University of Glasgow.
- [5] Crawford, V. H.; Richardson, H. W.; Wasson, J. R.; Hodgson D. J.; Hatfield, W. E. *Inorg. Chem.* 1976, 15, 2107.
- [6] Astheimer, H.; Haase, W. *J. Chem. Phys.* 1986, 85, 1427.
- [7] Merz, L.; Haase, W. *J. Chem. Soc. Dalton Trans.* 1980, 875.
- [8] Hu, H.; Liu, Y.; Zhang, D.; Liu, C. *Journal of Molecular Structure (Theochem)* 2001, 546, 73.
- [9] Ruiz, E.; Alemany, P.; Alvarez, S.; Cano, J. *J. Am. Chem. Soc.* 1997, 119, 1297.
- [10] Ruiz, E.; Alemany, P.; Alvarez, S.; Cano, J. *Inorg. Chem.* 1997, 36, 3683.
- [11] Aromi, G.; Brechin, E. K., Synthesis of 3d Metallic Single-Molecule Magnets, *Structure and Bonding*, Springer, Berlin, 2006, 122, 1.
- [12] Murrie, M.; Price, D. J. *Annu. Rep. Prog. Chem., Sect A*, 2007, 103, 20.
- [13] Novak, M. A.; Folly, W. S. D.; Sinnecker, J. P.; Soriano, S.; *J. Mag. Mag. Mat.* 2005, 294, 133.
- [14] Long, J. R., Molecular Cluster Magnets, *Chemistry of Nano-structured Materials*, P. Yang Ed., World Scientific, Hong Kong, 2003.
- [15] Sessoli, R.; Gatteschi, D.; Caneschi, A.; Novak, M. A. *Nature*, 1993, 365, 141.
- [16] Sessoli, R.; Tsai, H.; Schake, A. R.; Wang, S.; Vincent, J. B.; Folting, K.; Gatteschi, D.; Christou, G.; Hendrickson, D. N. *J. Am. Chem. Soc.* 1993, 115, 1804.
- [17] Thomas, L.; Lioni, F.; Ballou, R.; Gatteschi, D.; Sessoli, R.; Barbara B. *Nature*, 1996, 383, 145.
- [18] Milios, C. J.; Vinslava, A.; Wernsdorfer, W.; Moggach, S.; Parsons, S.; Perlepes, S. P.; Christou, G.; Brechin, E. K. *J. Am. Chem. Soc.* 2007, 129, 2754.
- [19] (a) Tassiopoulos, A. J.; Vinslave, A.; Wernsdorfer, W.; Abboud, K. A.; Christou, G. *Angew. Chem. Int. Ed.*, 2004, 43, 2117. (b) Ako, A. M.; Hewitt, I. J.; Mereacre, V.; Clerac, R.; Wernsdorfer, W.; Anson, C. E.; Powell, A. K. *Angew. Chem. Int. Ed.* 2006, 45, 4926. (c) Brechin, E. K.; Boskovic, C.; Wernsdorfer, W.; Yoo, J.; Yamaguchi, A; Sanudo, E. C.; Concolino, T. R.; Rheingold, A. L.; Ishimoto, H; Hendrickson, D. N.; Christou, G. *J. Am. Chem. Soc.* 2002, 124, 9710. (d) Wang, W.;

Zhou, A.; Zhang, W.; Tong, M.; Chen, X.; Nakano, M.; Beedle, C. C.; Hendrickson, D. N. *J. Am. Chem. Soc.* 2007, 129, 1014. (e) Mereacre, V. M.; Ako, A. M.; Clerac, R.; Wernsdorfer, W.; Filoti, G.; Bartolome, J.; Anson, C. E.; Powell, A. K. *J. Am. Chem. Soc.* 2007, 129, 9248. (f) Schelter, E. J.; Prosvirin, A. V.; Dunbar, K. R. *J. Am. Chem. Soc.* 2004, 126, 15004. (g) Ako, A. M.; Mereacre, V.; Clerac, R.; Hewitt, I. J.; Lan, Y.; Anson, C. E.; Powell, A. K. *Dalton Trans.* 2007, 5245. (h) Osa, S.; Kido, T.; Matsumoto, N.; Re, N.; Pochaba, A.; Mrozinski, J. *J. Am. Chem. Soc.* 2004, 126, 420. (i) Beltran, L. M. C.; Long, J. R. *Acc. Chem. Res.* 2005, 38, 325. (j) Schelter, E. J.; Karadas, F.; Avendano, C.; Prosvirin, A. V.; Wernsdorfer, W.; Dunbar, K. R. *J. Am. Chem. Soc.* 2007, 129, 8139. (k) Milios, C. J.; Inglis, R.; Vinslava, A.; Bagai, R.; Wernsdorfer, W.; Parsons, S.; Perlepes, S. P.; Christou, G.; Brechin, E. K. *J. Am. Chem. Soc.* 2007, 129, 12505.

[20] Aromi, G.; Batsanov, A. S.; Christian, P.; Helliwell, M.; Parkin, A.; Parsons, S.; Smith, A. A.; Timco, G. A.; Winpenny, R. E. P. *Chem. Eur. J.* 2003, 9, 5142.

[21] Aromi, G.; Batsanov, A. S.; Christian, P.; Helliwell, M.; Roubeau, O.; Timco, G. A.; Winpenny, R. E. P. *Dalton Trans.* 2003, 4466.

[22] Halcrow, M. A.; Sun, J.; Huffman, J. C.; Christou, G. *Inorg. Chem.* 1995, 34, 4167.

[23] Yang, E.; Wernsdorfer, W.; Hill, S.; Edwards, R.S.; Nakano, M.; Maccagnano, S.; Zakharov, L. N.; Rheingold, A. L.; Christou, G.; Hendrickson, D.N. *Polyhedron.* 2003, 22, 1727.

[24](a) Wernsdorfer, W.; Aliaga-Alcalde, N.; Hendrickson, D. N.; Christou, G. *Nature.* 2002, 416, 406. (b) Hill, S.; Edwards, R. S.; Aliaga-Alcalde, N.; Christou, G. *Science.* 2003, 302, 1015.

[25] Oshio, H.; Hoshino, N.; Ito T.; Nakano, M. *J. Am. Chem. Soc.* 2004, 126, 8805.

[26] Karasawa, S.; Yoshihara, D.; Watanabe, N.; Nakano, M.; Koga, N. *Dalton Trans.* 2008, 1418.

[27](a) Chandrasekhar, V.; Pandian, B. M.; Azhakar, R.; Vittal, J. J.; Clerac, R. *Inorg. Chem.* 2007, 46, 5140. (b) Chandrasekhar, V.; Pandian, B. M.; Vittal, J. J.; Clerac, R. *Inorg. Chem.* 2009, 48, 1148.

[28] Yang, E. C.; Hendrickson, D. N.; Wernsdorfer, W.; Nakano, M.; Zakharov, L. N.; Sommer, R. D.; Rheingold, A. L.; Ledezma-Gairaud, M.; Christou, G. *J. Appl. Phys.* 2002, 91, 7382.

- [29] Zhang, Y.; Wernsdorfer, W.; Pan, F.; Wanga Z.; Gao, S. *Chem. Commun.* 2006, 3302.
- [30] Ferguson, A.; Parkin, A.; Sanchez-Benitez, J.; Kamenev, K.; Wernsdorfer W.; Murrie, M. *Chem. Commun.* 2007, 3473.
- [31] Moubaraki, B.; Murray, K. S.; Hudson, T. A.; Robson, R. *Eur. J. Inorg. Chem.* 2008, 4525.
- [32] Langley, S. J.; Helliwell, M.; Sessoli, R.; Rosa, P.; Wernsdorfer, W.; Winpenny, R.E.P. *Chem. Commun.* 2005, 5029.
- [33] Song, Y.; Zhang, P.; Ren, X.; Shen, X.; Li, Y.; You, X. *J. Am. Chem. Soc.* 2005, 127, 3708.
- [34] Zeng, M.; Yao, M.; Liang, H.; Zhang W.; Chen, X. *Angew. Chem. Int. Ed.* 2007, 46, 1832.
- [35] Langley, S.; Helliwell, M.; Sessoli, R.; Teat, S. J.; Winpenny, R. E. P. *Dalton Trans.*, 2009, DOI: 10.1039/b819976k
- [36] Murrie, M.; Biner, D; Stöckli-Evans, H.; Gudel, H. U. *Chem. Commun.* 2003, 230.
- [37] Murrie, M.; Teat, S. J.; Stöckli-Evans, H.; Gudel, H. U. *Angew. Chem. Int. Ed.* 2003, 42, 4653.
- [38] Hudson, T. A.; Berry, K. J.; Moubaraki, B.; Murray, K. S.; Robson, R. *Inorg. Chem.* 2006, 45, 3549.
- [39] Galloway, K. W.; Whyte, A. M.; Wernsdorfer, W.; Sanchez-Benitez, J.; Kamenev, K. V.; Parkin, A.; Peacock, R. D.; Murrie, M. *Inorg. Chem.* 2008, 47, 7438.
- [40] Campo, J.; Falvello, L. R.; Mayoral, I.; Palacio, F.; Soler, T.; Tomás, M. *J. Am. Chem. Soc.* 2008, 130, 2932.
- [41] Xiang, S.; Wu, X.; Zhang, J.; Fu, R.; Hu, S.; Zhang, X. *J. Am. Chem. Soc.* 2005, 127, 16352.
- [42] Tiron, R.; Wernsdorfer, W.; Aliaga-Alcalde, N.; Christou, G. *Phys. Rev.B* 2003, 68, 140407.
- [43](a) Yoo, J.; Yamaguchi, A.; Nakano, M.; Krystek, J.; Streib, W. E.; Brunel, L. C.; Ishimoto, H.; Christou, G.; Hendrickson, D. N. *Inorg. Chem.* 2001, 40, 4604. (b) Hendrickson, D. N.; Christou, G.; Ishimoto, H.; Yoo, J.; Brechin, E. K.; Yamaguchi, A.; Rumberger, E. M.; Aubin, S. M. J.; Sun, Z.; Aromi, G. *Polyhedron* 2001, 20, 1479.

- [44] Yoo, J.; Wernsdorfer, W.; Yang, E.-C.; Nakano, M.; Rheingold, A. L.; Hendrickson, D. N. *Inorg. Chem.* 2005, 44, 3377.
- [45] Miyasaka, H.; Nakata, K.; Lecren, L.; Coulon, c.; Nakazawa, Y.; Fujisaki, T.; Sugiura, K.; Yamashita, M.; Clérac, R. *J. Am. Chem. Soc.* 2006, 128, 3770.
- [46] Miyasaka, H.; Nakata, K.; Sugiura, K.; Yamashita, M.; Clérac, R. *Angew. Chem. Int. Ed.* 2004, 43, 707.
- [47] Osa, S.; Kido, T.; Matsumoto, M.; Re, N.; Pochaba, A.; Mrozinski, J. *J. Am. Chem. Soc.* 2004, 126, 420.
- [48] Mori, F.; Nyui, T.; Ishida, T.; Nogami, T.; Choi, K.; Nojiri, H. *J. Am. Chem. Soc.* 2006, 128, 1440.
- [49] Aronica, C.; Pilet, G.; Chastanet, G.; Wernsdorfer, W.; Jacquot, F.; Luneau, D. *Angew. Chem. Int. Ed.* 2006, 45, 4659.
- [50] Ueki, S.; Ishida, T.; Nogami, T.; Choi, K.; Nojiri, H. *Chem. Phys. Letters.* 2007, 440, 263.
- [51] Pike Technologies OEM MIRacle ATR Product Data Sheet.
- [52] Parois, P. *The Effect of Pressure on Single Molecule Magnets*, University of Glasgow, 2009.
- [53] Moggach, S. A.; Allan, D. R.; Parsons, S.; Warren, J. E. *J. Appl. Cryst.* 2008, 41, 249.
- [54] Piermarini, G. J.; Block, S.; Barnett, J. D.; Forman, R. A. *J. Appl. Phys.* 1975, 46, 2774.
- [55] Hasselbach, K.; Veauvy, C.; Mailly, D. *Physica C* 2000, 332, 140.
- SIR92 – Altomare, A.; Cascarano, G.; Giacovazzo, G.; Guagliardi, A.; Burla, M. C.; Poldori, G.; Camalli, M. *J. Appl. Cryst.* 1994, 27, 435.
- SUPERFLIP – Oszlanyi, G.; Suto, A. *Acta Crystallogr. A* 2004, 60, 134.
- CRYSTALS – Betteridge, P. W.; Carruthers, J. R., Cooper, R. I.; Prout, K.; Watkin, D. J. *J. Appl. Cryst.* 2003, 36, 1487.

2.0 – The Cobalt Citrate System

2.1 – The Co₄ Cluster [C(NH₂)₃]₈{Co₄(cit)₄}.4H₂O

2.1.1 – Synthesis of [C(NH₂)₃]₈{Co₄(cit)₄}.4H₂O

To a solution of citric acid monohydrate (0.55 g, 2.6 mmol) in water (50 mL) was added a solution of Co(NO₃)₂.6H₂O (0.76 g, 2.6 mmol) in water (50 mL) followed by a solution of guanidinium carbonate (1.87 g, 10.4 mmol) in water (50 mL). The solution was then left to stand overnight, producing a very large yield of purple crystals, which were air-dried. Powdered samples were found to be slightly hygroscopic and analyse as the pentahydrate. Analysis, calculated (found) for C₃₂H₇₄Co₄N₂₄O₃₃: C, 24.65 (24.53); H, 4.78 (4.57); N, 21.56 (21.57). Selected IR data (cm⁻¹): 3330 (m), 3136 (m), 1656 (s), 1605 (m), 1579 (m), 1536 (s), 1426 (m), 1378 (s), 1233 (m), 1082 (w), 958 (m), 923 (m), 849 (m).

The product formed rapidly from the reaction conditions reported by Hudson *et al.* [1], however working at half concentration produced samples with a greater number of large, well-formed single crystals. The rapid formation of the product is presumably a consequence of the extensive hydrogen-bonding network present in the crystal lattice. Further investigation of the cobalt(II)/citrate/guanidinium reaction system suggests that the stability of the Co₄ cubane gives little synthetic flexibility, and the cubane forms regardless of reactant ratios.

It is interesting to note that this discrete cubane can be obtained by simply changing the tetramethylammonium counterions present in our Co₆ cluster ([NMe₄]₃Na{Co₄(cit)₄[Co(H₂O)₅]₂}.11H₂O) reaction system for guanidinium [2]. This highlights the important role of the counterions in such self-assembly reactions and their ability to vary the product obtained, as we have previously reported for the Co₆ citrate reaction system at lower pH [3].

The identity of the bulk sample was confirmed by powder diffraction at 130 K on a Bruker d8 diffractometer using Cu K α radiation. Figure 2-1 shows the measured and calculated (CSD structure CEHVAN) powder patterns and these are seen to match

closely. The unit cell dimensions of several single crystals were also confirmed on a Bruker APEXII diffractometer using Mo K α radiation at 100 K [expected (130 K data from CSD structure CEHVAN) $a = 16.1224(8) \text{ \AA}$, $c = 11.5088(11) \text{ \AA}$, $V = 2991.5(4) \text{ \AA}^3$; found (100 K data) $a = 16.09 \text{ \AA}$, $c = 11.55 \text{ \AA}$, $V = 2990 \text{ \AA}^3$].

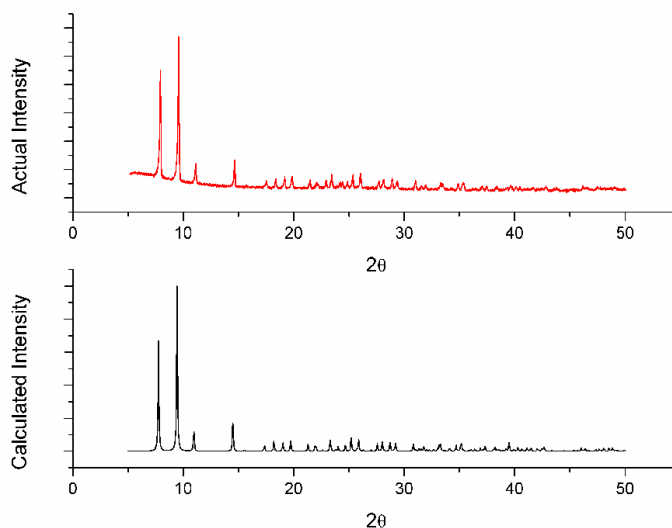


Figure 2-1 – Powder diffraction pattern of $[\text{C}(\text{NH}_2)_3]_8\{\text{Co}_4(\text{cit})_4\} \cdot 4\text{H}_2\text{O}$ collected at 130 K (upper) and calculated from CSD structure CEHVAN 130 K data (lower).

2.1.2 – Structure of $[\text{C}(\text{NH}_2)_3]_8\{\text{Co}_4(\text{cit})_4\} \cdot 4\text{H}_2\text{O}$

The $\{\text{Co}_4(\text{cit})_4\}^{8-}$ anion is a cubane with S_4 symmetry that consists of four cobalt(II) ions coordinated by four tetradeprotonated citrate ligands $[\text{C}(\text{O}^-)(\text{CO}_2^-)(\text{CH}_2\text{CO}_2^-)_2 = \text{cit}^{4-}]$. The citrate alkoxide group provides the corner bridging oxygen of the cubane, with the citrate carboxylate arms capping the cobalt(II) centres (Figure 2-2). The short α -carboxylate arm of citrate imparts a twisted trigonal-prismatic geometry to the six coordinate metal centres. The cubane Co- $\hat{\text{O}}$ -Co bridging angles are in the range 97.18 - 99.24° with Co-O bond lengths of 2.090 - 2.136 \AA .

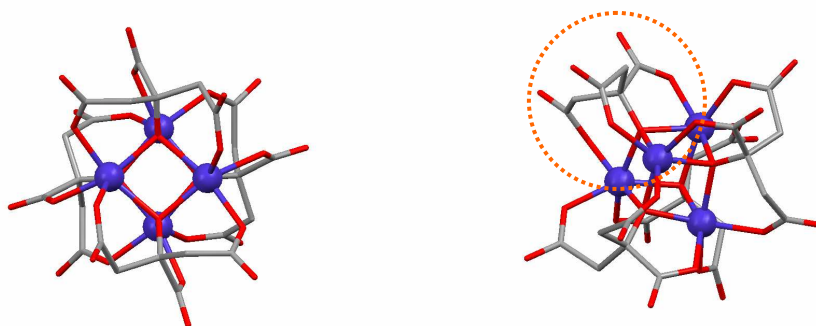


Figure 2-2 – Structure of the $\{\text{Co}_4(\text{cit})_4\}^{8-}$ anion with the structural role of an individual citrate ligand highlighted on right (Co blue, O red, C grey, H omitted).

The guanidinium counterions create an extensive hydrogen bonding network within the crystal lattice, where each cubane makes around 40 hydrogen bonds [1], as shown in Figure 2-3. When viewed along the crystallographic c axis, four of the guanidinium cations per cluster are seen to arrange into square columns that run through the crystal, while the remaining four are located around the cubane cluster. The hydrogen bonding network not only makes the Co_4 cubane the single dominant product from the cobalt(II)/citrate/guanidinium system, but unfortunately makes the crystals so stable and insoluble that they cannot be used as a starting material for further reactions using a ‘building-block’ synthesis approach.

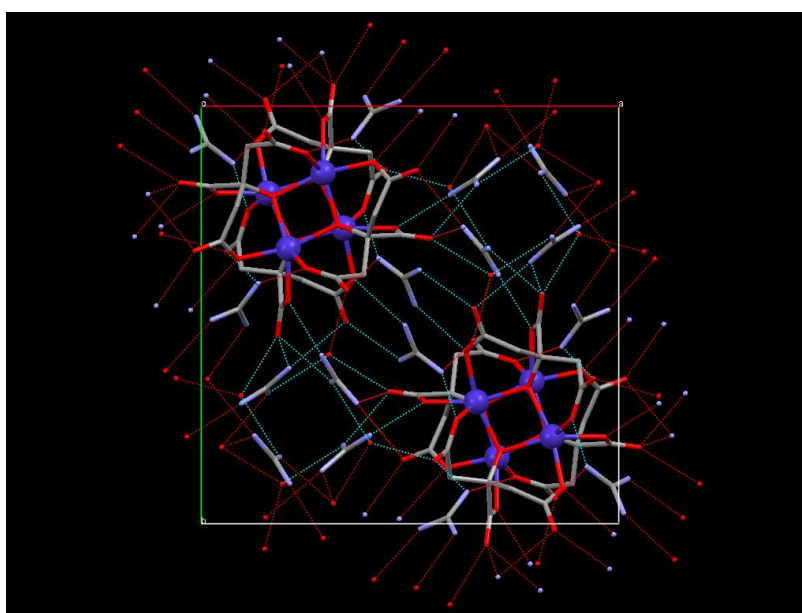


Figure 2-3 – Co_4 cubane and guanidinium counterion hydrogen bonding, shown as one unit cell viewed along the c axis (Co blue, O red, C grey, N pale blue, H omitted).

Related reactions using the methyl and ethyl derivatives of guanidinium (Figure 2-4) did not give any product crystals, with only solid residues formed after evaporation. Presumably the bulkier nature of these cations and their reduced symmetry prevents the close packing as seen for Co_4 above and reduces their hydrogen bonding abilities.

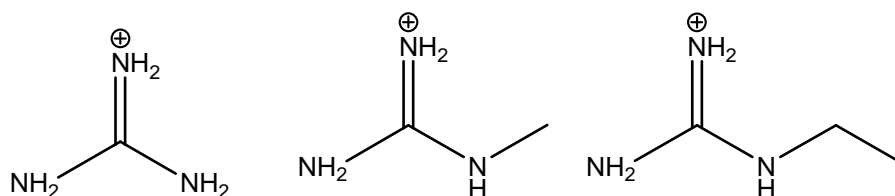


Figure 2-4 – Structure diagrams of guanidinium (left), methylguanidinium (centre) and ethylguanidinium (right).

2.1.3 – Electronic Spectroscopy of $[\text{C}(\text{NH}_2)_3]_8\{\text{Co}_4(\text{cit})_4\} \cdot 4\text{H}_2\text{O}$

The electronic spectrum of $[\text{C}(\text{NH}_2)_3]_8\{\text{Co}_4(\text{cit})_4\} \cdot 4\text{H}_2\text{O}$ dispersed in a KBr disc at ~ 20 K is shown in Figure 2-5. The most striking feature of the spectrum is the large intensity of the ${}^4\text{T}_1 \rightarrow {}^4\text{A}_2$ transition, which is very weak in most octahedral or pseudo-octahedral Co(II) compounds [4]. The cobalt centres in the cubane have C_1 symmetry and the highest reasonable symmetry description is distorted C_3 . In C_3 symmetry the ground and excited ${}^4\text{T}_1$ states and the ${}^4\text{T}_2$ state all split into ${}^4\text{E}$ and ${}^4\text{A}$ states. With either a ${}^4\text{A}$ or ${}^4\text{E}$ ground state the ${}^4\text{A}({}^4\text{A}_2)$ transition becomes allowed, acquiring intensity by mixing (principally) with the ${}^4\text{A}({}^4\text{T}_1(\text{P}))$ state.

Extracting the values of Δ_0 and B for such distorted species is of limited value. However due to the clear appearance of the ${}^4\text{T}_1 \rightarrow {}^2\text{T}_1$, ${}^2\text{T}_2$ transitions, B can be accurately found. The best fit values of $\Delta_0 = 8150 \text{ cm}^{-1}$ and $B = 840 \text{ cm}^{-1}$ reproduce the energies of all the transitions fairly well with the exception of the ${}^4\text{T}_1 \rightarrow {}^4\text{A}_2$ transition which is slightly overestimated. This is consistent with its energy being lowered due mixing with the ${}^4\text{A}({}^4\text{T}_1(\text{P}))$, state as mentioned above.

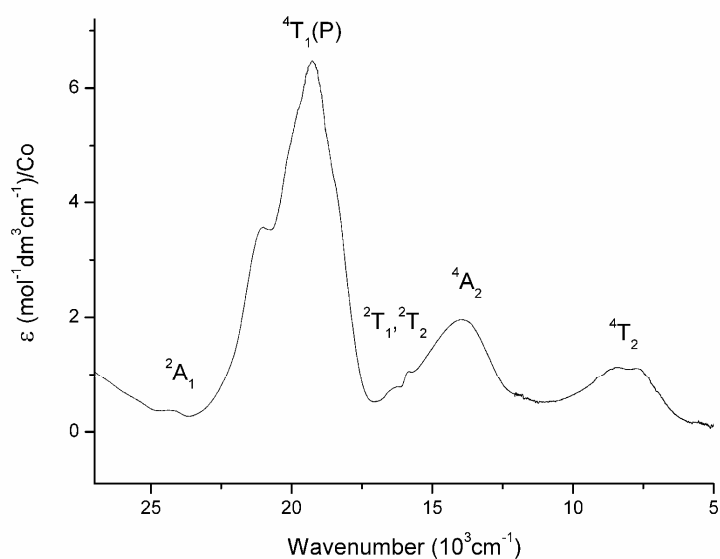


Figure 2-5 – Solid state electronic spectrum of $[\text{C}(\text{NH}_2)_3]_8\{\text{Co}_4(\text{cit})_4\} \cdot 4\text{H}_2\text{O}$ at 20 K (a baseline correction has been applied).

2.1.4 – Magnetic Properties of $[\text{C}(\text{NH}_2)_3]_8\{\text{Co}_4(\text{cit})_4\} \cdot 4\text{H}_2\text{O}$

The magnetic susceptibility of the Co_4 cluster, measured in a 1 kOe field, is shown in Figure 2-6. The value of χT at 290 K ($11.65 \text{ cm}^3 \text{ mol}^{-1} \text{ K}$) is consistent with four non-interacting $\text{Co}(\text{II})$ centres with $S_i = 3/2$ and $g = 2.49$. χT shows a gradual increase to a broad maximum value of $12.7 \text{ cm}^3 \text{ mol}^{-1} \text{ K}$ at 80 K, then decreases with temperature, with a more rapid decline below 10 K. This broad maximum is typical for $\text{Co}(\text{II})$ compounds and arises from single-ion spin-orbit coupling. The decrease in χT at low temperature is consistent with the presence of intramolecular antiferromagnetic exchange coupling and the sharp drop below 10 K due to zero-field splitting effects. However, due to the large orbital contribution of cobalt(II) it is difficult to perform a quantitative analysis of the susceptibility data. The magnetisation curve measured at 2 K is shown in the inset of Figure 2-6. There is a rapid increase from 0 to 0.7 T, and then the magnetisation starts to plateau before increasing again above 2 T ($M/N\beta = 4.8$ at 2 Tesla). Clearly, the ground state is magnetic in contrast to the previous report [1]. However, the subsequent rise in the magnetisation above 2 Tesla is consistent with the presence of low-lying excited states, in agreement with Hudson *et al.* [1]

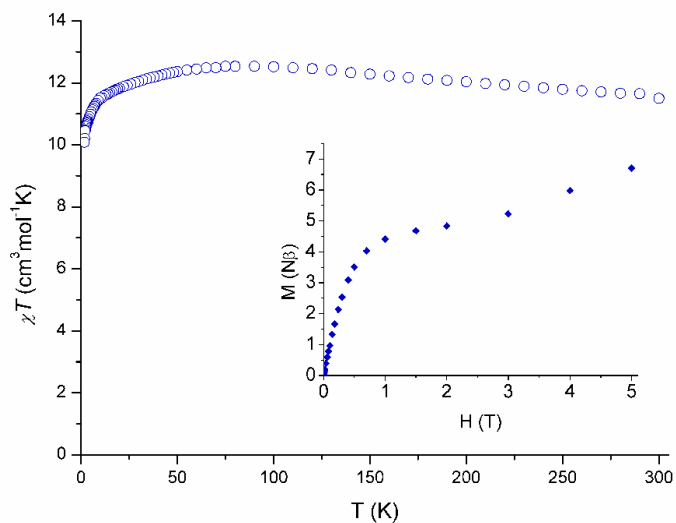


Figure 2-6 – Temperature dependence of χT for $[\text{C}(\text{NH}_2)_3]_8\{\text{Co}_4(\text{cit})_4\} \cdot 4\text{H}_2\text{O}$ measured in a 1000 Oe field. Inset shows the field dependence of the magnetisation at 2 K.

Ac susceptibility data measured between 130 and 9997 Hz is shown in Figure 2-7. Distinct, frequency dependent peaks are seen in the out-of-phase (χ'') component of the ac susceptibility. The observation of such ac peaks is indicative of slow relaxation and an Arrhenius analysis gives an energy barrier $\Delta E/k_B = 24$ K, and $\tau_0 = 3.4 \times 10^{-8}$ s for frequencies between 225 and 1267 Hz. At higher frequencies the plot of $\ln(\tau)$ vs $1/T$ shows curvature (see Figure 2-8) suggesting a different relaxation pathway as seen for Mn_{12} acetate [5].

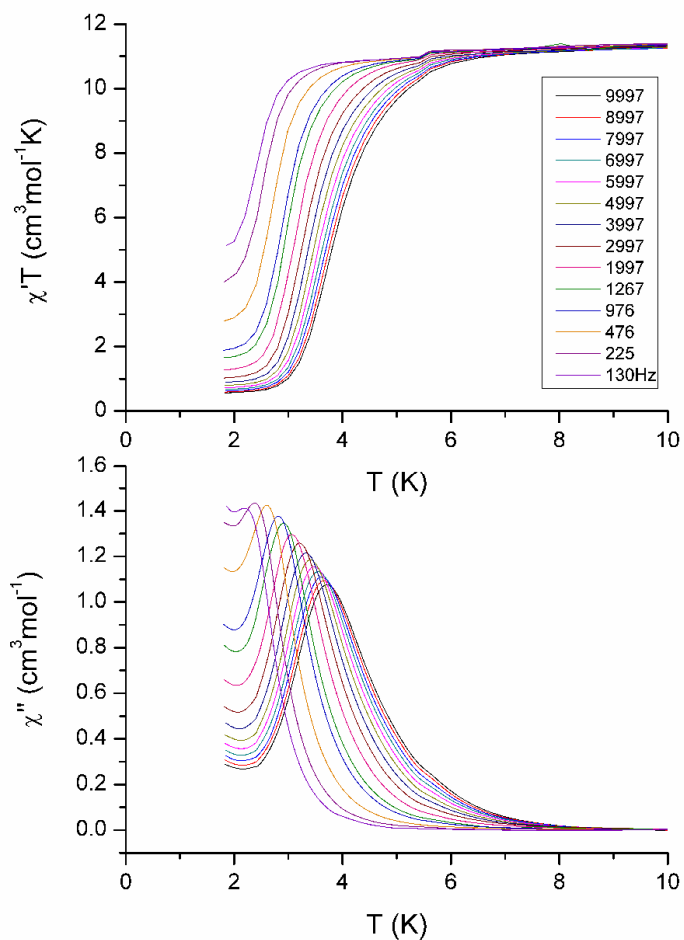


Figure 2-7 – The in-phase and out-of-phase components of the ac susceptibility for $[\text{C}(\text{NH}_2)_3]_8\{\text{Co}_4(\text{cit})_4\} \cdot 4\text{H}_2\text{O}$ shown as $\chi' T$ versus T (upper) and χ'' versus T (lower).

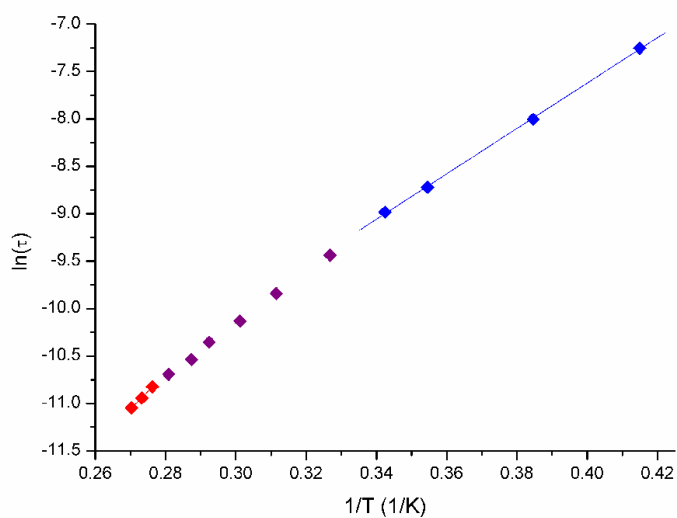


Figure 2-8 – Arrhenius plot. Colour scheme: blue linear region 225-1267 Hz, purple (1997-6997 Hz), red linear region 7997-9997 Hz.

The SMM behaviour of the Co_4 cluster is confirmed by the observation of magnetisation versus field hysteresis loops that are temperature and sweep rate dependent (Figure 2-9). The loops collapse at zero field due to very fast quantum tunnelling of the magnetisation (QTM) and have almost no coercivity. There is an effective direct relaxation pathway between the ground state levels, which arises from the strong orbital contribution. It is interesting to note that the SMM $[\text{Mn}^{\text{III}}_2\text{Dy}^{\text{III}}_2(\text{tmp})_2(\text{O}_2\text{CMe}_3)_4(\text{NO}_3)_4]^{2-}$ containing Dy(III), and hence a significant orbital contribution to the magnetic properties, has been found to possess similar fast QTM at zero field [6]. Single crystal dc relaxation data was measured in an applied field of 0.1 T (see Figure 2-10), to avoid the $H = 0$ fast tunnelling transition. An Arrhenius analysis yields the parameters $\Delta E/k_B = 21$ K, and $\tau_0 = 8 \times 10^{-7}$ s, which are consistent with those obtained from the ac data above.

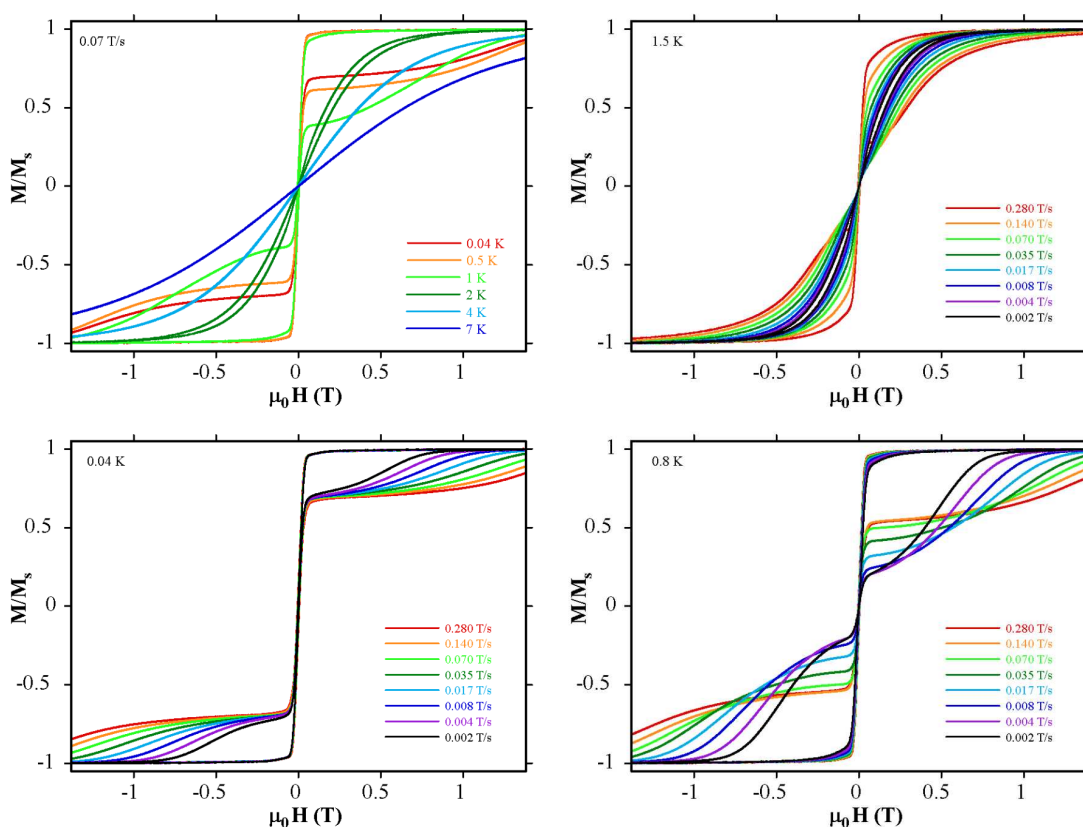


Figure 2-9 – Temperature dependence of Co_4 single crystal magnetisation versus field hysteresis loops (upper left), and sweep rate dependence measured at 1.5 K (upper right), 0.8 K (lower right) and 0.04 K (lower left).

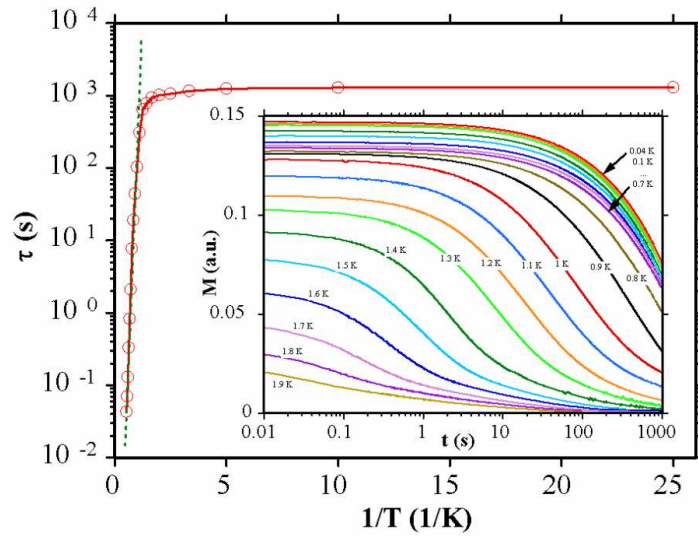


Figure 2-10 – Arrhenius plot using single-crystal (dc) data, measured in an applied field of 0.1 T. Inset shows the magnetisation measured as a function of time at the indicated temperatures.

It is interesting to note that after the publication of this work [7] a follow-up publication by Hudson and co-workers [8] reported an ac study of the Co_4 cubane with a calculated $\Delta E/k_B = 13$ K, and $\tau_0 = 8.4 \times 10^{-7}$ s, which is considerably smaller than that found by our ac study with $\Delta E/k_B = 24$ K, and $\tau_0 = 3.4 \times 10^{-8}$ s. The source of this discrepancy is unknown; however the ac data that was reported in the follow up publication [8] was measured over a smaller frequency range (10-1500 Hz) and the few resolved peaks were far less distinct than those reported in our publication [7]. We are confident in the values we have reported [7] due to the consistent ac peak shape and positions obtained from multiple samples from several separate syntheses. The same sample has been measured on both a Quantum Design MPMS XL SQUID magnetometer and a PPMS SQUID magnetometer giving the same results. Crucially, a single crystal from this synthesis gave an energy barrier of $\Delta E/k_B = 21$ K, and $\tau_0 = 8 \times 10^{-7}$ s from the independent technique of microSQUID dc magnetisation relaxation measurements, and these values are consistent with our ac studies.

2.1.5 – Co₄ High Pressure Structural Study

The Co₄ SMM is a good candidate for high pressure X-ray crystallography studies as it readily forms large, stable crystals that diffract well. The hydrogen bonding network is also an interesting feature, as on application of hydrostatic pressure all of the components should interact with one another, and there are no large flexible organic regions in the structure that would tend to compress in preference to more rigid clusters. The Co₄ cluster magnetic behaviour is consistent with intramolecular antiferromagnetic exchange coupling at low temperatures (see Figure 2-6) and pressure induced distortions to the cubane geometry could provide more ferromagnetic exchange pathways by reducing the Co- \hat{O} -Co bridging angles.

On application of pressure the structure becomes compressed, and the unit cell dimensions and volume are reduced. Figure 2-11 illustrates the reduction in the Co₄ unit cell volume. A small increase in volume is observed between ambient pressure and 1.8 kbar, most likely due to thermal contraction since the literature CSD structure CEHVAN [1] was collected at 130K, whereas the pressure cell data was collected at ambient temperature. The volume reduces steadily on increasing the pressure from 1.8 kbar to 21.8 kbar, followed by a smaller rate of change to 26.4 kbar. It can be seen from the values in Table 2-1 that the unit cell a dimension changes the most, with a smooth decrease of 0.88 Å over the measured pressure range, while the c dimension only decreases by 0.22 Å with several jumps. The unit cell a length also inherently has a much greater effect on the unit cell volume as in the tetragonal Co₄ unit cell the length a = b and so the volume V is given by: $V = a \times b \times c = a^2 c$.

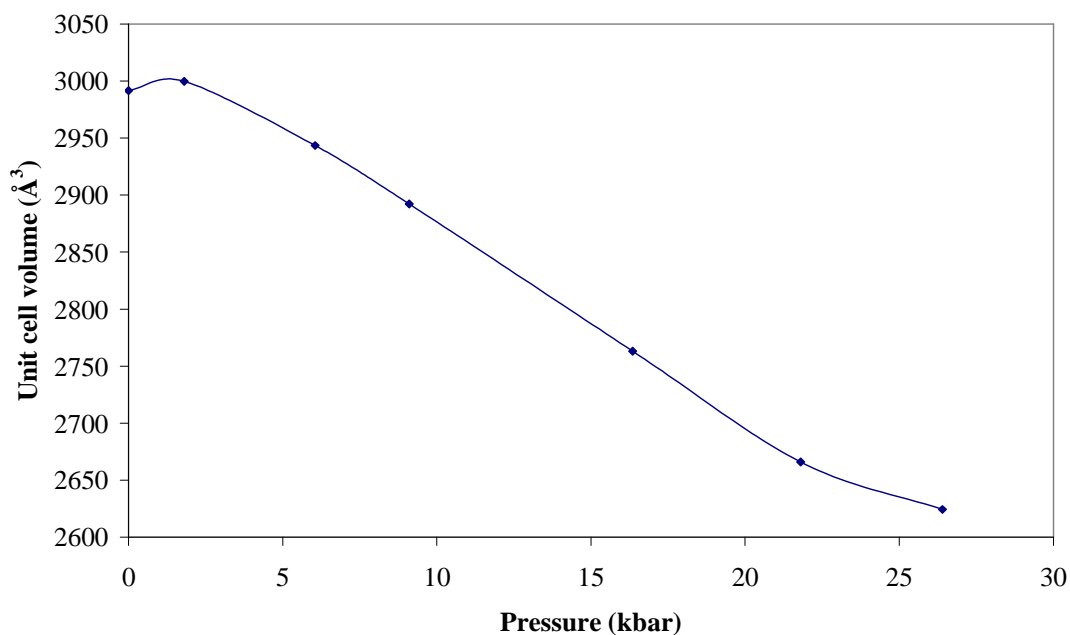


Figure 2-11 – Effect of pressure on Co₄ unit cell volume. 0 kbar data measured at 130 K, all other diamond anvil pressure cell measurements at ambient temperature.

Pressure (kbar)			Unit cell dimensions (Å)		Unit cell volume (Å ³)
Before	After	Average	a	c	
0	0	0	16.1224(8)	11.509(1)	2991.5(4)
1.8	1.8	1.8	16.1073(2)	11.5621(2)	2999.73(7)
5.5	6.6	6.1	16.0336(2)	11.4494(2)	2943.37(7)
9.1	9.1	9.1	15.9663(3)	11.3454(6)	2892.2(2)
16.4	16.3	16.4	15.5853(3)	11.3753(5)	2763.1(1)
21.8	21.8	21.8	15.346(1)	11.3195(9)	2665.9(5)
25.5	27.3	26.4	15.245(1)	11.292(1)	2624.3(6)

Table 2-1 – Reduction in unit cell dimensions on application of pressure, measured at ambient temperature with the exception of 0 kbar at 130 K.

An interesting feature revealed by this pressure study is a phase transition seen at 16.4 kbar at which point two key changes occur. Firstly, the number of water molecules in the unit cell is reduced, and secondly, half of the guanidinium counterions become disordered. Figure 2-12 illustrates how the eight molecules of water in the Phase I unit cell are located near to guanidinium counterions, whereas in the Phase II unit cell only two water molecules are present, and these are located in cavities between the stacks of cubanes (on the S_4 axis of the Co₄ unit).

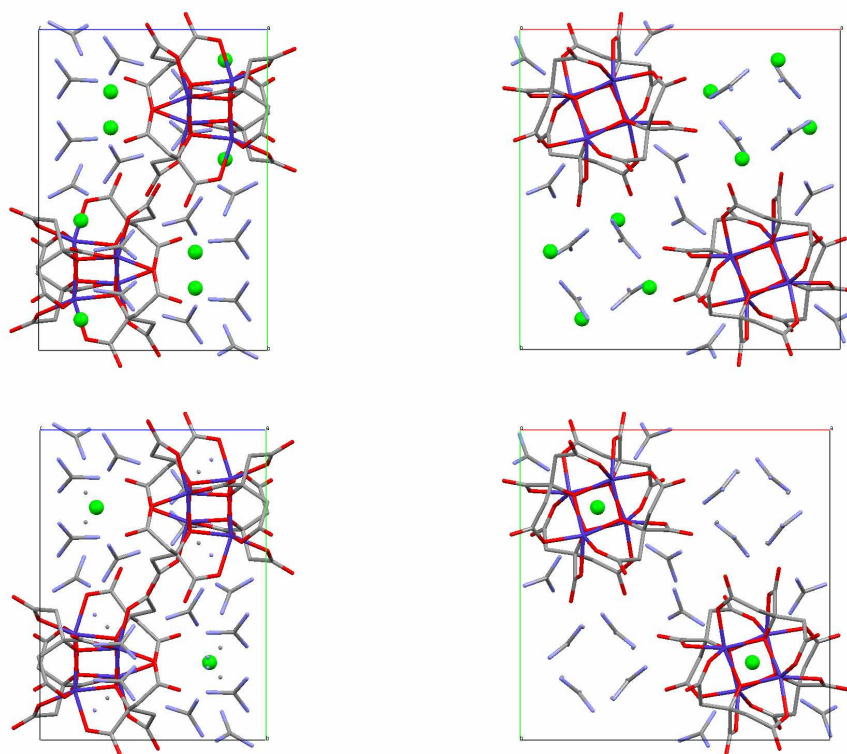


Figure 2-12 – Comparison of the Co_4 unit cells in Phase I at ambient pressure (upper) and Phase II at 16.4 kbar (lower), seen along the a (left) and c (right) axes. (Co blue, O red, C grey, N pale blue, H omitted. Water oxygen atoms are highlighted in green).

Presumably the other water molecules must either leave the crystals or become disordered to the point where they cannot be found (complicated by the unavoidable lower completeness of the pressure cell data). The water molecules in Phase I form part of the extensive hydrogen bonding network between the guanidinium and the Co_4 oxygens (discussed earlier in Section 2.1.2), but the water molecules in the cavities in the Phase II unit cell do not take part in the hydrogen bonding network. A consequence of this seems to be that the guanidinium counterions can become disordered, as they will be less rigidly held with fewer hydrogen bonds. This is a very unusual result as disorder has been created by applying pressure, whereas it would be expected that high pressure would lead to compression of the crystal packing and a more ordered structure.

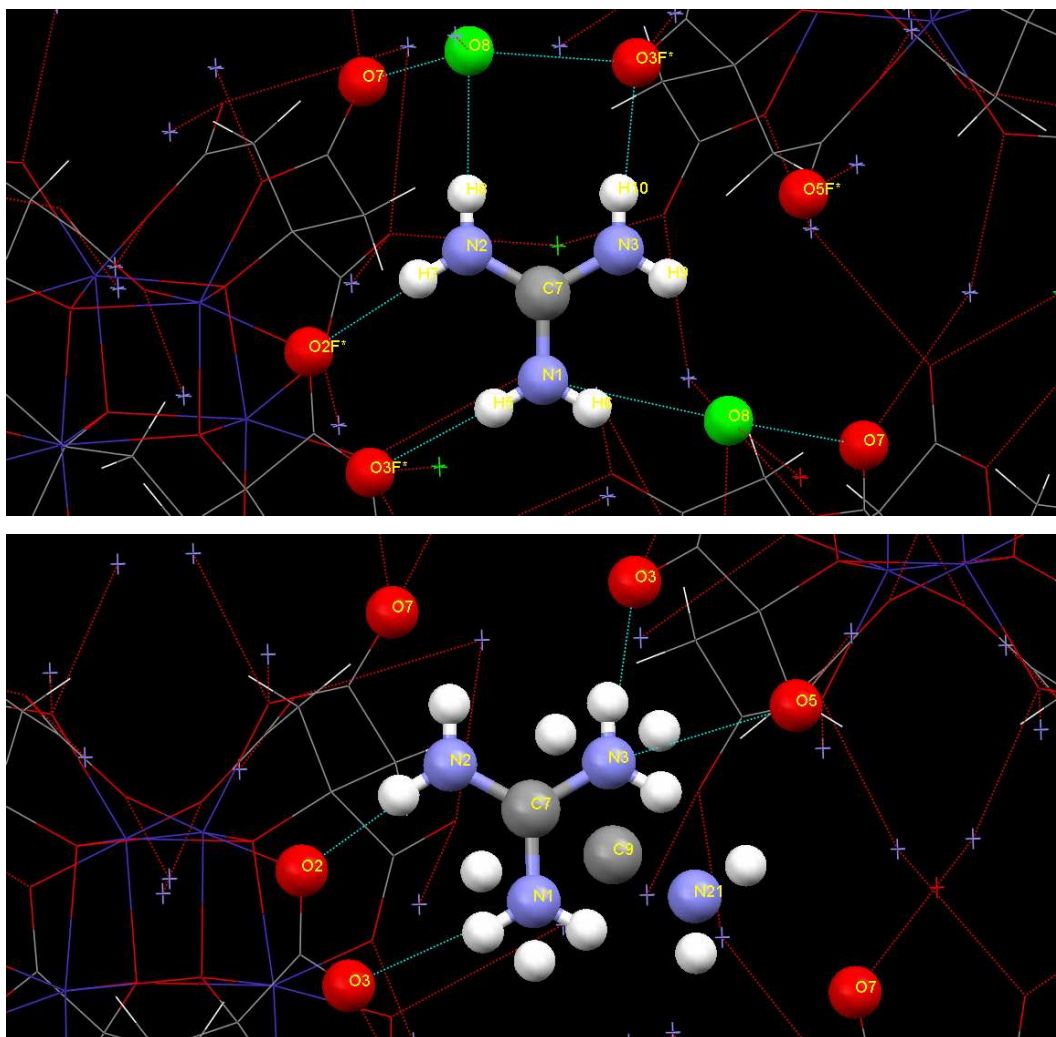


Figure 2-13 – Guanidinium hydrogen bonding in Phase I (upper) and II (lower) (Co blue, O red, C grey, N pale blue, H white, Water atoms O8 highlighted in green).

Figure 2-13 compares the guanidinium ion comprising C7 N1 N2 N3 that is fixed in Phase I and disordered in Phase II. This disorder can be visualised as flipping the molecule on the N1 N3 axis so that N2 moves to the N21 position and C7 moves to C9. In the ambient pressure Phase I structure a hydrogen atom of N2 hydrogen bonds to a water molecule oxygen O8, which is in turn hydrogen bonded to neighbouring Co₄ carboxylate oxygens O3 and O7, with a similar arrangement also seen for a hydrogen atom of N1 (via the symmetry related O8 in Figure 2-13). In Phase II the disorder means that N2 can be in the N21 position which then allows hydrogen bonding between a hydrogen atom of N3 and the Co₄ carboxylate O5. Although this change also means that a hydrogen of N2 is no longer hydrogen bonded to the carboxylate oxygen O2, it is facilitated by the other hydrogen atom of N2 not having to hydrogen bond to the Phase I water O8 that is removed in Phase II.

It is interesting to note that powdered samples of Co₄ were found to be slightly hygroscopic, with microanalysis results indicating a pentahydrate (see Section 2.1.1). This additional water could be present in the cavity positions between the cubanes (where the water is seen to reside in Phase II) since it would not be involved in the hydrogen bonding and so could absorb and desorb readily.

When studying the structure of the Co₄ cubane itself, it is discovered that the bond distances and angles change very little between 0 and 9.1 kbar (Table 2-2). This may be explained by the observation that on increasing the pressure, the square stacks of cubanes rotate in one sense while the square columns of guanidinium rotate in the opposite sense, when viewed along the *c* axis. Therefore the structure reorganises due to the applied pressure but the robust cubane units remain largely unchanged. The biggest difference is observed around the phase transition when the spread of Co-O bond length values is reduced. The magnetic properties of the Co₄ cluster are therefore unlikely to change considerably in the pressure range 0-9.1 kbar, but may alter at 16.4 kbar in Phase II, if the reduction in bond lengths alters the metal oxygen orbital overlap. However, since the bridging angles remain similar this change may be very small.

Pressure (kbar)	Co- \hat{O} -Co Angles (°)			Co-O Bond Lengths (Å)		
0.0	97.2(1)	99.2(1)	98.6(1)	2.093(2)	2.136(2)	2.090(2)
1.8	97.0(1)	99.0(1)	98.3(1)	2.100(4)	2.139(3)	2.096(3)
6.1	97.0(1)	99.3(1)	98.5(1)	2.097(4)	2.133(3)	2.084(3)
9.1	96.9(1)	99.2(1)	98.5(1)	2.094(3)	2.130(3)	2.078(3)
16.4	97.6(3)	99.4(3)	97.6(3)	2.087(7)	2.081(8)	2.082(8)

Table 2-2 – Co₄ cubane Co- \hat{O} -Co bridging angles and Co-O bond distances.

0 kbar data measured at 130 K, all other measurements at ambient temperature.

Magnetic measurements at high pressure have not yet been carried out due to the current technical limitations of the developmental SQUID pressure cell. The most obvious difference at high pressure is expected to be observed in the shape and position of the peaks in out-of-phase component of the ac susceptibility (χ'' versus *T* plot as in Figure 2-7). However, the sample size in the SQUID pressure cell is very small (in comparison to a normal gelatine capsule) and gives only a small signal which is also masked by the high background of the metal cell. This is further complicated by the restriction to low frequencies below 1000 Hz, and since the Co₄

cubane only gives resolved χ'' peaks above 130 Hz, the available frequency range is small. This could perhaps be countered by ac measurements with a fixed applied dc field to shift the peaks to higher temperatures (i.e. to shift the peaks below 130 Hz to a temperature that is accessible to the SQUID), however this would require an extensive set of measurements to determine the best measurement conditions, and recollection of the gelatine capsule data under similar applied fields. Application of a dc field to the metal pressure cell could also increase the background levels. Due to these complications and the expected small differences in magnetic properties, the high pressure magnetic characterisation of the Co₄ cubane remains for future study.

2.1.6 – Heterometallic Cubane Systems

Note that the formulae given in this section refer to the overall stoichiometry, as the compounds are not necessarily pure species (see Section 2.1.6.2).

2.1.6.1 – Heterometallic Cubane Syntheses

Cobalt and Zinc (1:1) - To a solution of citric acid monohydrate (0.27g, 1.3mmol), Co(NO₃)₂·6H₂O (0.19g, 0.65mmol) and Zn(NO₃)₂·6H₂O (0.19g, 0.65mmol) in water (50mL) was added a solution of guanidinium carbonate (0.94g, 5.2mmol) in water (25mL). The solution was stirred and left to stand, producing a large yield of pale purple crystals, selected IR data (cm⁻¹): 3337 (m), 3137 (m), 1656 (m), 1605 (w), 1536 (s), 1427 (m), 1379 (s), 1233 (m), 1083 (w), 959 (m), 924 (m), 848 (m). Analysis, calculated (found) for, [C(NH₂)₃]₈Co₂Zn₂(cit)₄·7H₂O, C₃₂H₇₈Co₂Zn₂N₂₄O₃₅: C, 23.90 (24.01); H, 4.89 (4.79); N, 20.91 (20.88).

Cobalt and Manganese (1:1) - To a solution of citric acid monohydrate (0.27g, 1.3mmol), Co(NO₃)₂·6H₂O (0.19g, 0.65mmol) and Mn(NO₃)₂·4H₂O (0.16g, 0.65mmol) in water (50mL) was added a solution of guanidinium carbonate (0.94g, 5.2mmol) in water (25mL). The solution was stirred and left to stand, producing a large yield of dark purple crystals, selected IR data (cm⁻¹): 3337 (m), 3133 (m), 1660 (m), 1605 (w), 1537 (s), 1426 (m), 1378 (s), 1231 (m), 1078 (w), 958 (m), 921 (m), 847 (m). Analysis, calculated (found) for, [C(NH₂)₃]₈Co₂Mn₂(cit)₄·7H₂O, C₃₂H₇₈Co₂Mn₂N₂₄O₃₅: C, 24.22 (24.25); H, 4.95 (4.73); N, 21.18 (21.06).

Cobalt and Nickel (1:1) - To a solution of citric acid monohydrate (0.27g, 1.3mmol), $\text{Co}(\text{NO}_3)_2 \cdot 6\text{H}_2\text{O}$ (0.19g, 0.65mmol) and $\text{Ni}(\text{NO}_3)_2 \cdot 6\text{H}_2\text{O}$ (0.19g, 0.65mmol) in water (50mL) was added a solution of guanidinium carbonate (0.94g, 5.2mmol) in water (25mL). The solution was stirred and left to stand, producing a large yield of orange crystals, selected IR data (cm^{-1}): 3335 (m), 3127 (m), 1659 (m), 1536 (s), 1427 (m), 1377 (s), 1234 (m), 1093 (w), 959 (m), 927 (m), 849 (m). Analysis, calculated (found) for, $[\text{C}(\text{NH}_2)_3]_8\text{Co}_2\text{Ni}_2(\text{cit})_4 \cdot 7\text{H}_2\text{O}$, $\text{C}_{32}\text{H}_{78}\text{Co}_2\text{Ni}_2\text{N}_{24}\text{O}_{35}$: C, 24.11 (24.05); H, 4.93 (4.78); N, 21.08 (20.82).

Cobalt and Iron (1:1) - To a solution of citric acid monohydrate (0.27g, 1.3mmol), $\text{CoSO}_4 \cdot 7\text{H}_2\text{O}$ (0.18g, 0.65mmol) and $\text{FeSO}_4 \cdot 7\text{H}_2\text{O}$ (0.18g, 0.65mmol) in water (50mL) was added a solution of guanidinium carbonate (0.94g, 5.2mmol) in water (25mL). The solution was stirred and left to stand. A cloudy brown solution formed with a moderate yield of suspended purple/brown crystals, selected IR data (cm^{-1}): 3329 (m), 3140 (m), 1656 (m), 1539 (s), 1426 (m), 1379 (s), 1233 (m), 1082 (w), 958 (m), 923 (m), 848 (m).

2.1.6.2 – Discussion of Heterometallic Cubane Syntheses

The remarkable structural similarity of the series of metal citrate cubanes with guanidinium [1] presented the opportunity to synthesise heterometallic examples. Reactions were carried out with a 1:1 mixture of cobalt with zinc, manganese, nickel, and iron, as described in Section 2.1.6.1. In all cases extended prism type crystals of similar appearance to those of Co_4 were formed overnight and the reaction solutions became colourless, suggesting that both metals had crystallised out (the exceptional case being Co/Fe where the solution was cloudy brown, most likely due to oxidation of Fe(II) to Fe(III) in water, which could not be included into the cubane crystal structure for charge balance reasons). The mixed cobalt nickel synthesis was particularly striking as the product crystals were a dark orange colour. Figure 2-14 shows samples of pure cobalt, pure nickel and the 1:1 metal mixture crystals. Grinding samples of purple Co_4 and green Ni_4 together in a mortar and pestle was found to give a similar orange colour to that of the powdered Co/Ni mixture crystals.



Figure 2-14 – Photograph of cubane crystal samples, purple Co₄ (left), dark orange Co/Ni 1:1 mix (centre) and green Ni₄ (right).

param	Co	Fe	Mg	Mn	Ni	Zn
formula	C ₈ H ₂₀ CoN ₆ O ₉	C ₈ H ₂₀ FeN ₆ O ₉	C ₈ H ₂₀ MgN ₆ O ₉	C ₈ H ₂₀ MnN ₆ O ₉	C ₈ H ₂₀ Ni ₆ O ₉	C ₈ H ₂₀ N ₆ O ₉ Zn
fw	403.23	400.15	368.61	399.24	403.01	409.67
cryst syst	tetragonal	tetragonal	tetragonal	tetragonal	tetragonal	tetragonal
space group	<i>P</i> 4 ₂ / <i>n</i>	<i>P</i> 4 ₂ / <i>n</i>	<i>P</i> 4 ₂ / <i>n</i>			
<i>T</i> (K)	130	130	130	130	130	130
<i>a</i> (Å)	16.1224(8)	16.2542(8)	16.1405(6)	16.2890(12)	16.0562(8)	16.1337(5)
<i>c</i> (Å)	11.5088(11)	11.5350(10)	11.5809(8)	11.5022(17)	11.6135(12)	11.6460(7)
<i>V</i> (Å ³)	2991.5(4)	3047.5(3)	3017.0(3)	3051.9(6)	2994.0(4)	3031.4(2)
<i>Z</i>	8	8	8	8	8	8
<i>d</i> _{calc} (g cm ⁻³)	1.791	1.744	1.623	1.738	1.788	1.795
<i>μ</i> (mm ⁻¹)	1.210	1.051	0.180	0.927	1.359	1.682
R1 ^a [<i>I</i> > 2σ(<i>I</i>)]	0.0579	0.0815	0.0900	0.0862	0.0487	0.0442
wR2 ^b [<i>I</i> > 2σ(<i>I</i>)]	0.1425	0.1990	0.2410	0.1973	0.1307	0.1262

^a R1 = $\sum ||F_o| - |F_c|| / \sum |F_o|$. ^b wR2 = $\{\sum [w(F_o^2 - F_c^2)^2] / \sum [w(F_o^2)]\}^{1/2}$, $w = 1 / [\sigma^2(F_o^2) + (aP)^2 + bP]$ and $P = [(F_o^2) + 2(F_c^2)] / 3$.

Table 2-3 - Similarity of the metal citrate cubane crystal structures [1].

The crystallographic similarity of the metal citrate cubane series is highlighted in Table 2-3. Although this similarity allows the easy synthesis of the heterometallic examples, it also causes considerable difficulty in establishing the structural nature of the metal distribution. Assuming a 1:1 ratio between the two metals Co and M, the possible structures are:

- (A) – Co₄ packed together with M₄
- (B) – Co₃M₁ packed together with Co₁M₃
- (C) – Co₂M₂
- (D) – Random mix of Co_xM_y packed together (where x + y = 4)

The situation is complicated still further by the fact that due to the high symmetry of the cubane cluster, the cubanes in (B) and (C) could be packed such that differing orientations of the cubane (with respect to the metal positions) could create the overall effect of the two metals being disordered over all sites, which would appear to be the same as (D). For this reason, investigation of the heterometallic crystals by single crystal X-ray diffraction has met with very limited success in determining the metal dispersion; however it has confirmed the expected cubane structure. Magnetic characterisation of the mixed metal cubanes is also of limited utility, though the Co/Zn sample can be used to establish if case (A) is present.

2.1.6.3 – Magnetic Properties of $[\text{C}(\text{NH}_2)_3]_8\text{Co}_2\text{Zn}_2(\text{cit})_4 \cdot 7\text{H}_2\text{O}$

A comparison of the magnetic susceptibility of the mixed metal Co_2Zn_2 cluster with the single metal Co_4 cluster, both measured in a 1 kOe field, is shown in Figure 2-15. For Co_2Zn_2 the value of χT at 290 K ($5.70 \text{ cm}^3\text{mol}^{-1}\text{K}$) is consistent with two non-interacting Co(II) centres with $S_i = 3/2$ and $g = 2.47$, and is it also approximately half of value for Co_4 ($11.65 \text{ cm}^3\text{mol}^{-1}\text{K}$ with $g = 2.49$). On cooling χT shows a gradual increase to a very broad maximum value of $6.20 \text{ cm}^3\text{mol}^{-1}\text{K}$ at 100 K, then decreases steadily with temperature until a plateau between ~ 22 and 8.89 K with $\chi T \sim 5.83 \text{ cm}^3\text{mol}^{-1}\text{K}$, followed by a more rapid decrease with temperature. The χT curve for Co_2Zn_2 shows some important differences with that of Co_4 , as the broad maxima in the curves occur at different temperatures (100 K and 80 K) and Co_4 does not display a plateau at low temperature, although both curves do show a similar rapid decline below 10 K.

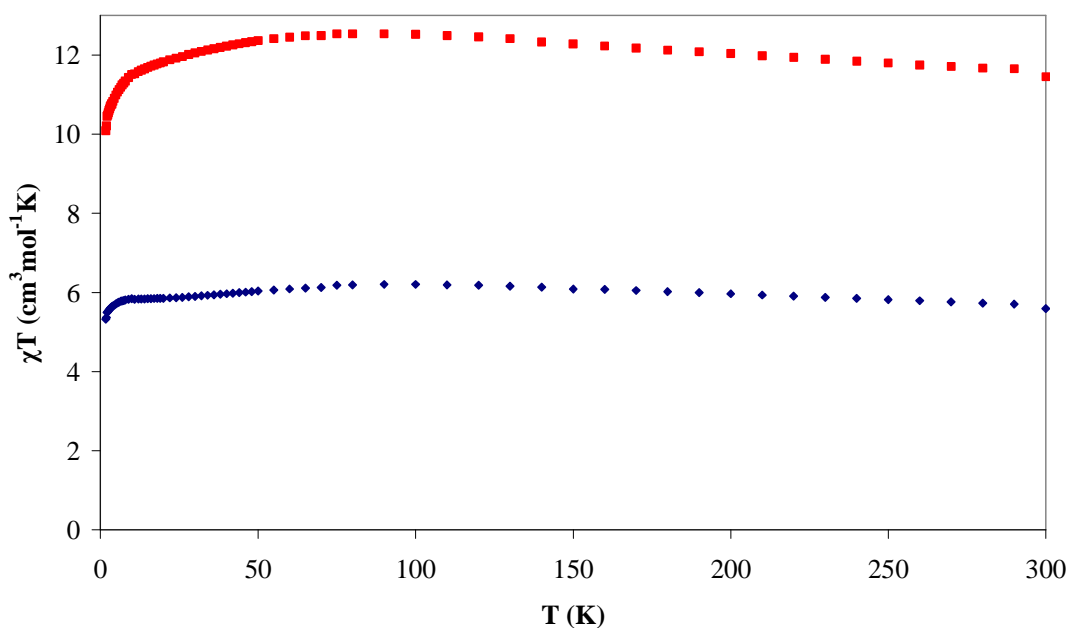


Figure 2-15 – Comparison of the temperature dependence of χT for $[\text{C}(\text{NH}_2)_3]_8\text{Co}_2\text{Zn}_2(\text{cit})_4 \cdot 7\text{H}_2\text{O}$ (Blue) and $[\text{C}(\text{NH}_2)_3]_8\{\text{Co}_4(\text{cit})_4\} \cdot 4\text{H}_2\text{O}$ (Red), measured in a 1000 Oe field.

A comparison of the magnetisation curves measured at 2 K for Co_2Zn_2 and Co_4 is shown in Figure 2-16. Both show a rapid increase from 0 to 1 T, but above this point the Co_2Zn_2 curve continues in a smooth curve to a (not saturated) value of $M/N\beta = 4.0$

at 5 Tesla, whereas the Co_4 curve plateaus before increasing again above 2 T due to low-lying excited states (see Section 2.1.4). The mixed metal cubane does not display such a feature in the magnetisation curve.

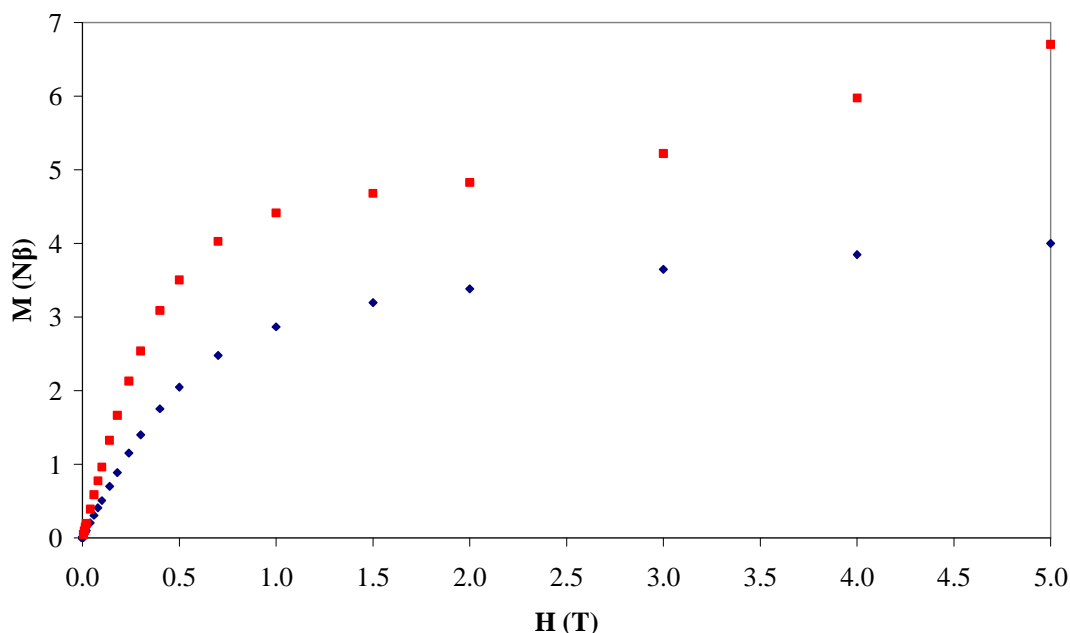


Figure 2-16 – Comparison of the field dependence of the magnetisation at 2 K for $[\text{C}(\text{NH}_2)_3]_8\text{Co}_2\text{Zn}_2(\text{cit})_4 \cdot 7\text{H}_2\text{O}$ (Blue) and $[\text{C}(\text{NH}_2)_3]_8\{\text{Co}_4(\text{cit})_4\} \cdot 4\text{H}_2\text{O}$ (Red).

The ac magnetic susceptibility of the Co_2Zn_2 cluster is shown in Figures 2-17 and 2-18. The out-of-phase component of the Co_2Zn_2 ac susceptibility displays the onset of a frequency dependent signal, unlike the distinct χ'' peaks seen for Co_4 above 130 Hz (see Figure 2-7). At low temperature the 1267 Hz curve appears to cross the 976 Hz curve (probably an experimental error). The magnitude of the χ'' signal for Co_2Zn_2 is also small, with a maximum of $0.40 \text{ cm}^3 \text{ mol}^{-1}$ compared to $1.45 \text{ cm}^3 \text{ mol}^{-1}$ for Co_4 .

Overall, when comparing the Co_2Zn_2 and Co_4 clusters it can be seen that there are differences in the dc χT curve shape, magnetisation curve shape and ac χ'' curves. Consequently it can be concluded that the possible structure (A), with Co_4 clusters packed together with Zn_4 clusters, is not present since magnetically this would behave as a diluted Co_4 sample, and so would display the same curve shapes as seen for Co_4 but with half of the magnitude. The cubane clusters formed are therefore definitely heterometallic in nature, but the locations of the two metals within the cubanes remains unknown.

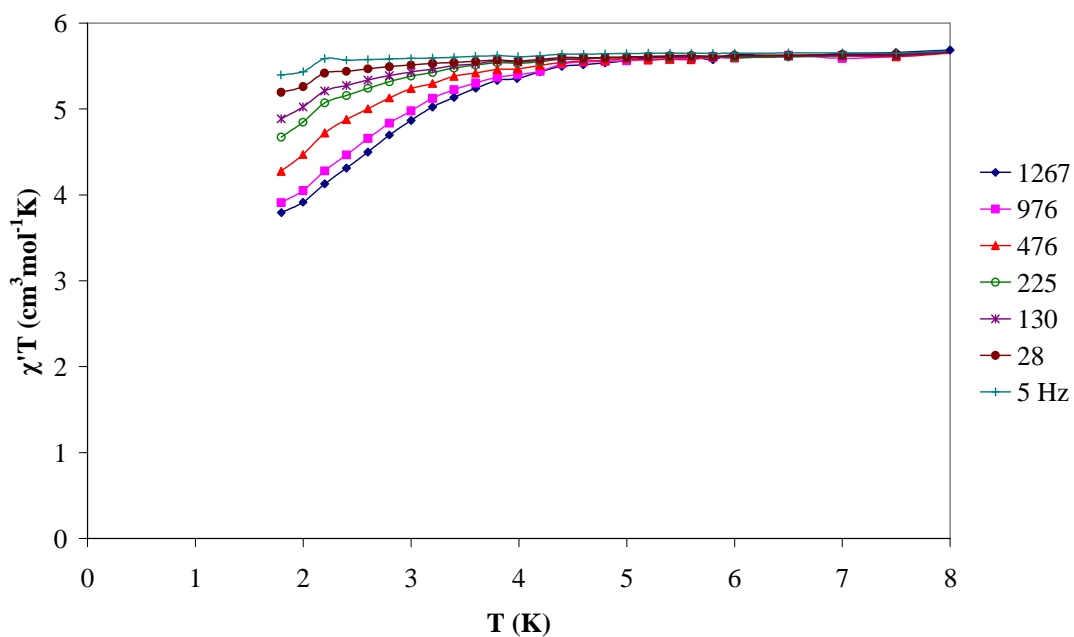


Figure 2-17 – The in-phase component of the ac susceptibility for $[\text{C}(\text{NH}_2)_3]_8\text{Co}_2\text{Zn}_2(\text{cit})_4 \cdot 7\text{H}_2\text{O}$ shown as $\chi'T$ versus T .

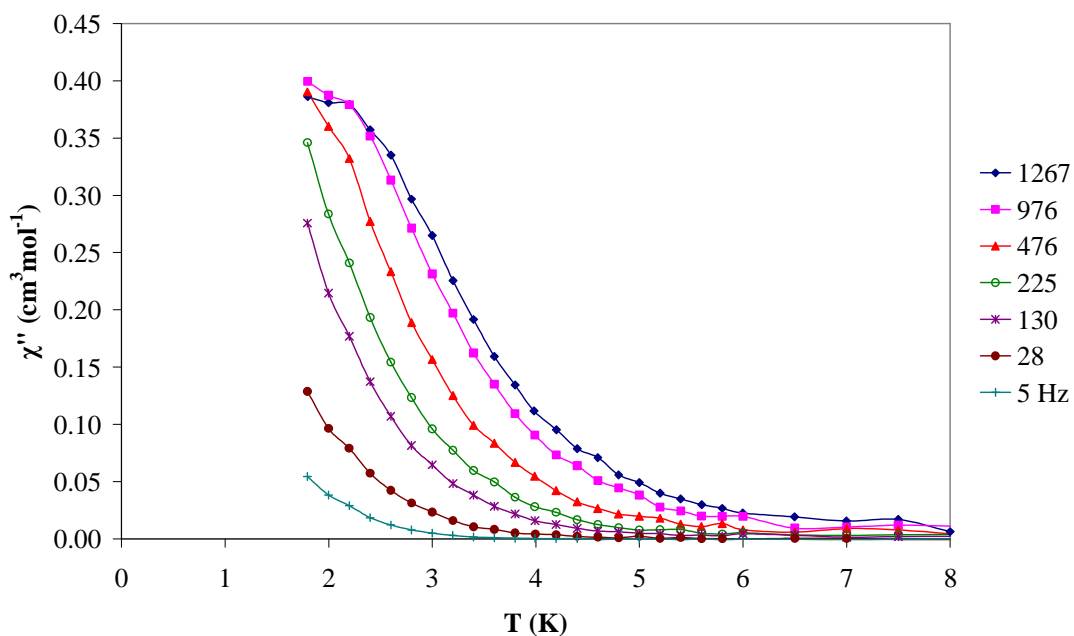


Figure 2-18 – The out-of-phase component of the ac susceptibility for $[\text{C}(\text{NH}_2)_3]_8\text{Co}_2\text{Zn}_2(\text{cit})_4 \cdot 7\text{H}_2\text{O}$ shown as χ'' versus T .

2.2 – The Co₆ Cluster {Co₄(cit)₄[Co(H₂O)₅]₂}⁴⁻

2.2.1 – Synthesis of [NMe₄]₃Na{Co₄(cit)₄[Co(H₂O)₅]₂}.11H₂O

Original literature synthesis [2] using solvent layering for crystallisation

CoSO₄·7H₂O (2.030 g, 7.2 mmol) and citric acid monohydrate (1.518 g, 7.2 mmol) were combined in solution in 10 ml H₂O. NMe₄OH·5H₂O (~4.62 g) was added until pH 7.00 was obtained. 16 ml of solution was diluted with 16 ml H₂O and 0.803g Na₂SO₄ added. 0.4 ml aliquots were layered with 1.6 ml EtOH in narrow tubes. After 1 month, pink rod-type crystals of product formed, with colourless salt impurity crystals and oil. Pink crystals, selected IR data (cm⁻¹): 3214 (m), 1551 (s), 1487 (m), 1376 (s), 1237 (m), 1089 (m), 951 (w), 921 (w). Yield of 16% based on cobalt.

Improved ‘superhedgehog’ synthesis using solvent mixing for crystallisation

CoSO₄·7H₂O (2.031 g, 7.2 mmol) and citric acid monohydrate (1.519 g, 7.2 mmol) were combined in solution in 10 ml H₂O. NMe₄OH·5H₂O (~4.70 g) was added until pH 7.50 was obtained. 15 ml of solution was diluted with 15 ml H₂O and 0.1875 g Na₂SO₄ added. 1.0 ml aliquots were then mixed with between 1.9-3.0 ml EtOH and kept in sealed vials. After ten days, pink crystals were produced in characteristic hedgehog formations. Selected data (cm⁻¹): 3221 (m), 1550 (s), 1487 (m), 1380 (s), 1285 (w), 1237 (m), 1091 (m), 1061 (w), 952 (m), 923 (m). Yield of 19.5% based on cobalt. Unit cell of (NMe₄)₃Na{Co₆} confirmed by single crystal X-ray diffraction.

The cluster was previously produced by slow diffusion of ethanol into a neutral solution containing Co²⁺, cit⁴⁻, NMe₄⁺, and Na⁺ using solvent layering [2]; however the small yield per capillary and colourless salt impurity crystals were not ideal. We now report an improved synthesis at higher pH and reduced Na⁺ concentration that uses direct mixing with ethanol to obtain the Co₆ cluster as the sole product from the reaction in under half the time compared to solvent diffusion. Improved yields have also allowed much larger sample sizes to be used for the magnetic measurements in this study. The product crystallises in characteristic ‘hedgehog’ formations of rod crystals joined at a point to form a hemisphere as shown in Figure 2-19. The original synthesis produced hedgehogs of a diameter of approximately 2 mm, and the small rod crystals required a synchrotron source for single crystal X-ray diffraction studies,

whereas the new synthesis produces much larger ‘superhedgehogs’ of 9 mm diameter which provide individual rod crystals of sufficiently large size to be studied using conventional lab based X-ray sources.

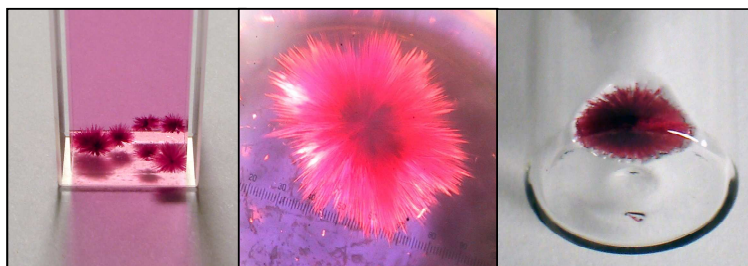


Figure 2-19 – Photographs of 2 mm ‘hedgehog’ Co₆ crystal formations in a cuvette (left), enlarged photo (centre) and a 9 mm ‘superhedgehog’ in a 16 mm vial (right).

2.2.2 – Structure of [NMe₄]₃Na{Co₄(cit)₄[Co(H₂O)₅]₂}.11H₂O

The structure of the Co₆ anion is shown in Figure 2-20. The cluster has a central {Co₄(cit)₄}⁸⁻ unit where the cubane corner bridging oxygen is provided by the citrate alkoxide group, while the carboxylate arms cap the remaining cobalt coordination sites, with the same structure as Co₄ (see Section 2.1.2). The shorter citrate α -carboxylate imparts a twisted trigonal-prismatic geometry to the six coordinate cobalt centres, while also providing oxygen coordination sites for the two peripheral [Co(H₂O)₅]²⁺ units. The cubane Co- \hat{O} -Co bridging angles are in the range 96.46-100.33° with Co-O bond lengths of 2.070-2.142 Å. Charge balance of the anion is provided by one sodium and three tetramethylammonium counterions.

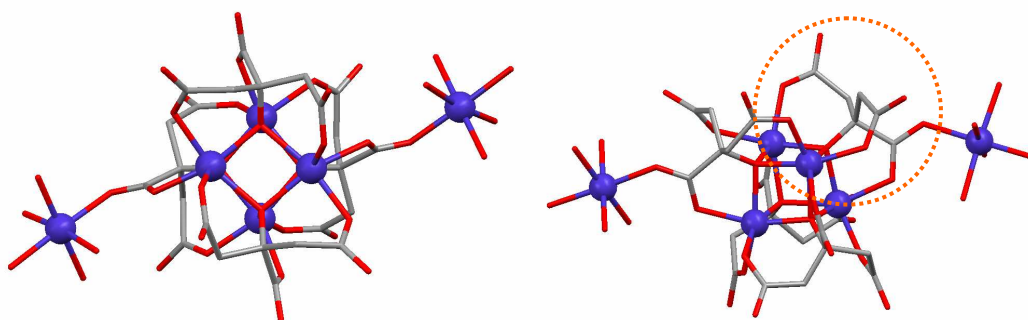


Figure 2-20 – Structure of the {Co₄(cit)₄[Co(H₂O)₅]₂}⁴⁻ anion with the structural role of an individual citrate ligand highlighted on right (Co blue, O red, C grey, H omitted).

The Co₆ clusters pack together within the crystal in a ‘herring bone’ chain pattern with the peripheral [Co(H₂O)₅]²⁺ units interlaced. Significant hydrogen bonding occurs between the clusters in the chain via the water molecules of the peripheral cobalt centres and the outer carboxylate oxygens of the cubane citrates, as highlighted in Figure 2-21. There is also hydrogen bonding to a lesser extent between the chains, which can be seen parallel with the (red) *a* axis in Figure 2-21, and more obviously in Figure 2-22 which views the clusters along the chains on the *a* axis. Figure 2-22 also highlights how the tetramethylammonium counterions are arranged in the rectangular channels between the chains of clusters. The sodium counterions are located close in to the Co₆ clusters and are disordered over two sites, coordinated to the citrate oxygens and cobalt bound water.

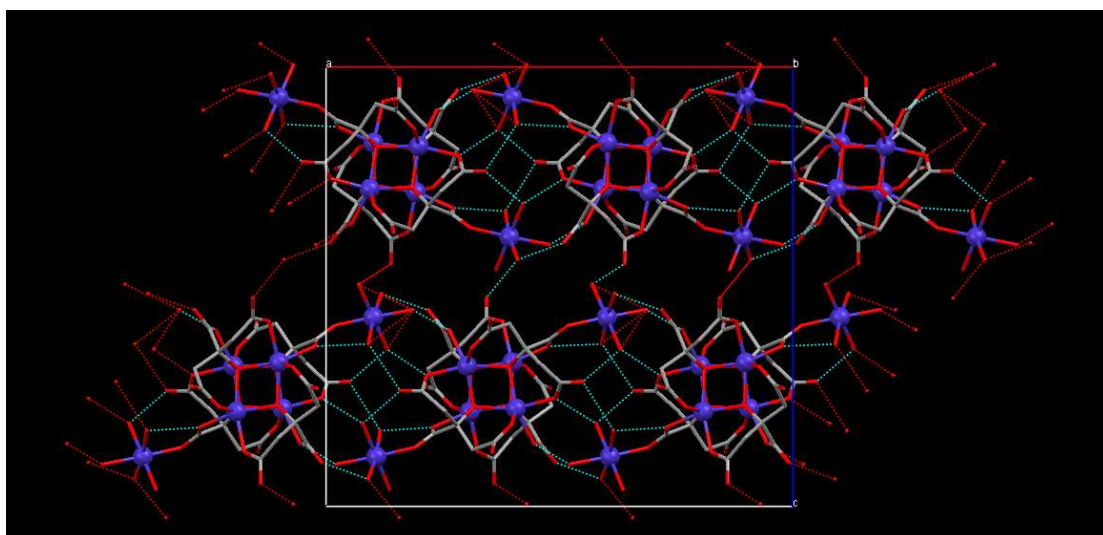


Figure 2-21 – Co₆ anion crystal packing and hydrogen bonding viewed along the *b* axis, with Na⁺ and NMe₄⁺ counterions omitted for clarity (Co blue, O red, C grey, H omitted).

Note that for convenience in this chapter a full compound formula such as [NMe₄]₃Na{Co₄(cit)₄[Co(H₂O)₅]₂}.11H₂O is simplified to Na{Co₆}. The simplified formula should be taken to include the {Co₄(cit)₄[Co(H₂O)₅]₂}⁴⁻ anion, three [NMe₄]⁺ counterions and the fourth counterion stated. Unless indicated as dehydrated, it should also be taken to include the total number of lattice water given in the compound synthesis section.

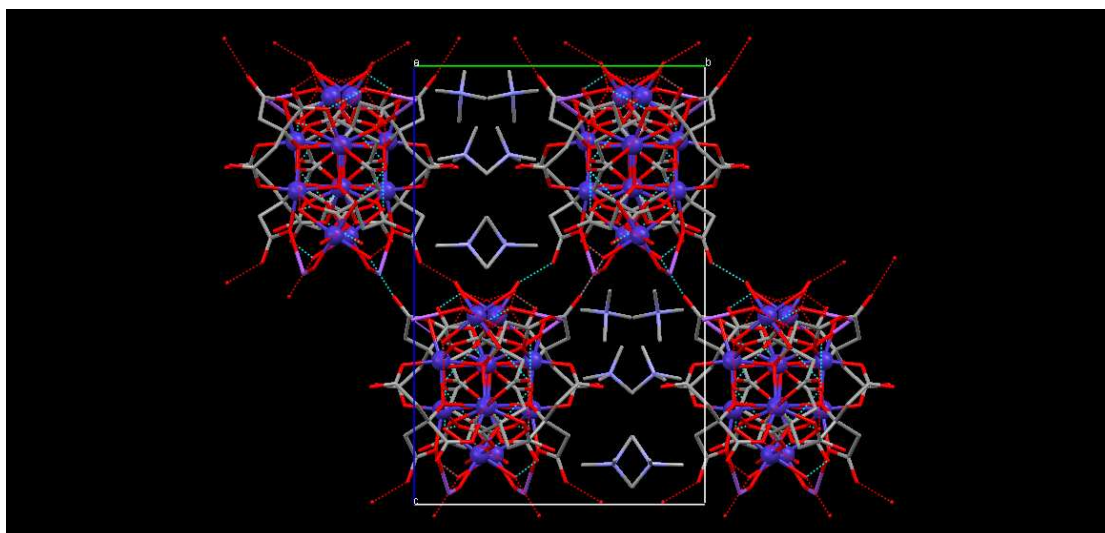


Figure 2-22 – Co₆ anion crystal packing and hydrogen bonding viewed along the *a* axis, highlighting the chain like arrangement of the clusters with NMe₄⁺ counterions in the space between them (Co blue, O red, C grey, N pale blue, Na violet, H omitted).

2.2.3 – Co₆ Reaction Solution Spectroscopic Study

As part of the efforts to improve the Co₆ synthesis and also to explore new product formation, a spectroscopic investigation of the reaction solution was undertaken. This followed the superhedgehog experimental synthesis described in Section 2.2.1, but in this case a sample of the solution was taken at regular intervals as the pH was increased over the range 2 to 12. The electronic spectra of these samples were then measured, the results of which are shown in Figure 2-23.

Initially the reaction solution at low pH will contain protonated citrate, and at pH 3 the electronic spectrum consists of one peak at 512 nm corresponding to simple cobalt species that will be present such as [Co(H₂O)₆]²⁺. As can be seen in Figure 2-23, on increasing the pH this principal peak shifts to longer wavelength and increases in absorbance, while a second broad peak appears around 725 nm. The peak shift indicates the coordination of the cobalt centres by the deprotonated citrate ligands as the pH increases (due to the changing crystal field splitting), and can be more easily seen in Figure 2-24 which shows the peak shift as a function of solution pH. This displays a sinusoidal curve centred on pH 7, with an almost linear increase from pH 6 to 8. It is within this linear region that the second broad band appears at around 725 nm, and it increases in absorbance with increasing pH. Comparing the Co₆ reaction

solution spectra with that of Co_4 in Figure 2-5 (Section 2.1.3) the peaks can be assigned as the principal ${}^4\text{T}_1$ (~525 nm) with the appearance of the broad ${}^4\text{A}_2$ (~725 nm) suggesting the formation of the cubane unit in solution due to the structural distortion applied to the cobalt centres as discussed previously in Section 2.1.3. At very high pH of 11 and 12, additional small peaks appear at 647 nm, but these samples were unstable and oxidised to dark, cloudy solutions within a few hours.

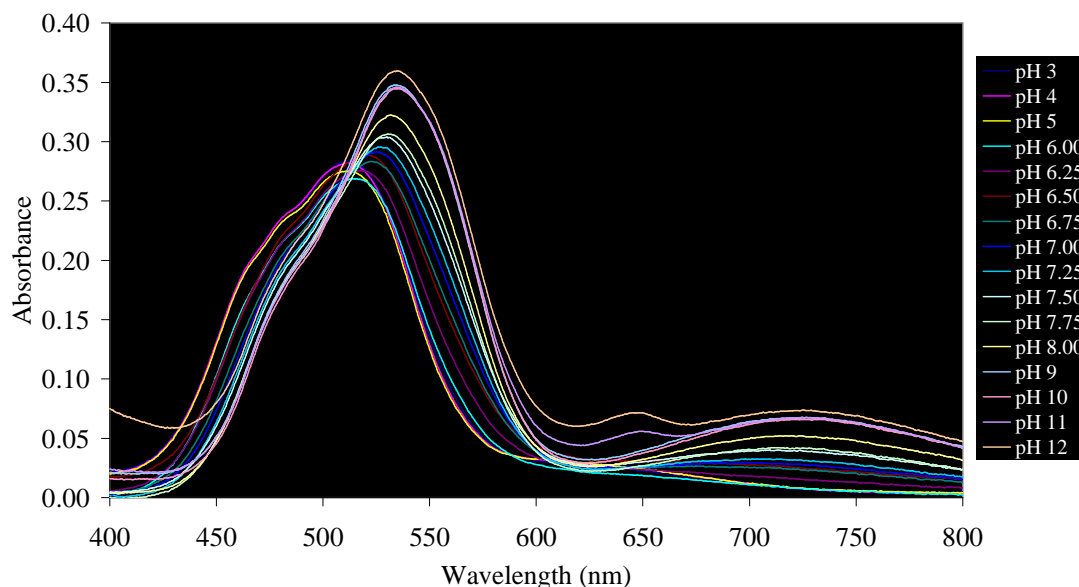


Figure 2-23 – pH dependence of the Co_6 reaction solution electronic spectrum.

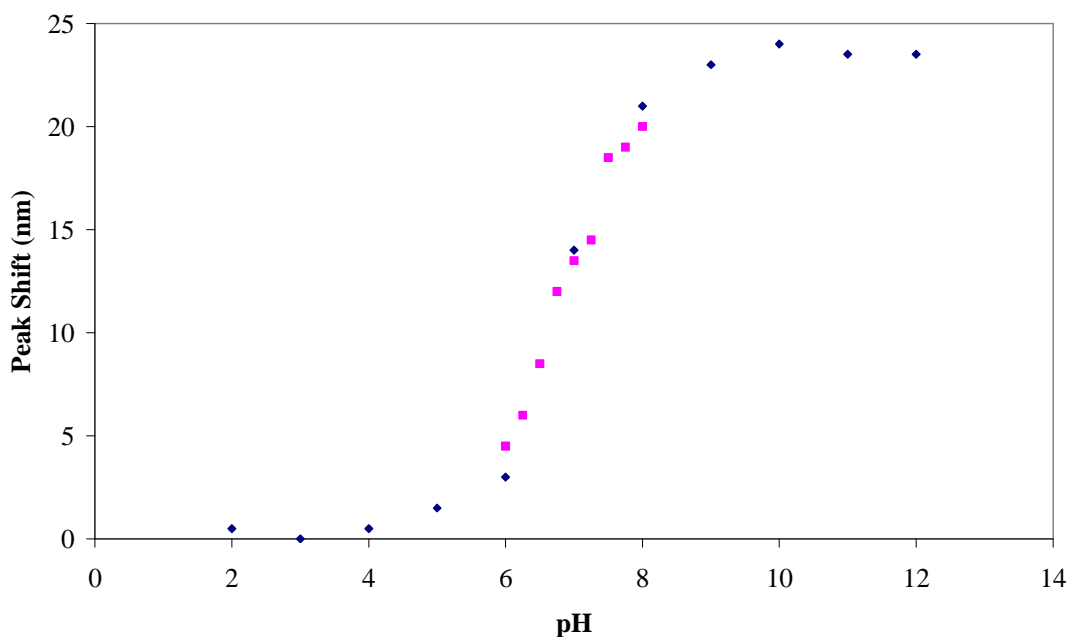


Figure 2-24 – Peak shift (from 512 nm) of the cobalt ${}^4\text{T}_1$ peak as a function of pH.

It is interesting to note that the pH 6-8 region is observed as a rapid change from red to dark purple. Previous studies at pH 6 allowed the formation of three products from solution via control of the counterion [3], these being the double salts $[\text{Co}(\text{H}_2\text{O})_6][\text{NMe}_4]_2[\text{SO}_4]_2 \cdot 4\text{H}_2\text{O}$, $[\text{Co}(\text{H}_2\text{O})_6][\text{NEt}_4]_2[\text{SO}_4]_2 \cdot 4\text{H}_2\text{O}$, and the 1D coordination polymer $[\text{NBu}_4]_2[\text{Co}_2(\text{Hcit})_2(\text{H}_2\text{O})_4] \cdot 4\text{H}_2\text{O}$. This example demonstrates how the size of the counterion used not only affects the structure, but also whether the ligand is present in the product, in one case as the Hcit^{3-} form with the three carboxylate groups deprotonated and the central alkoxy group still protonated. Removal of the proton from the alkoxy group (which plays a vital bridging role in the cubane structure) occurs at higher pH with the Co_6 cluster accessible around pH 7 using the original literature synthesis [2].

The improved ‘superhedgehog’ synthesis is at a higher pH of 7.5, where both peaks in the spectra are seen to be of higher absorbance (and ${}^4\text{T}_1$ peak shift) compared with pH 7. The important role of the counterion appears again, as with the Na_2SO_4 concentration of the literature synthesis a novel 3D network based on Co_4 units is obtained (discussed later in Section 2.4), whereas with one quarter of the Na_2SO_4 concentration, the pure Co_6 superhedgehogs are formed. Since the peak shift and increase in absorbance continues at higher pH, further study would be of interest; however it is found that as the pH increases it becomes much more difficult to crystallise products out of solution, either by solvent mixing or slow evaporation. The highest pH that has produced solid product is pH 8.00 reactions, which gave either the 3D network or poor quality hedgehog crystals in small yield.

2.2.4 – Magnetic Properties of $\text{Na}\{\text{Co}_6\}$

Figure 2-25 illustrates the dc magnetic susceptibility of the hydrated $\text{Na}\{\text{Co}_6\}$ cluster $[\text{NMe}_4]_3\text{Na}\{\text{Co}_4(\text{cit})_4[\text{Co}(\text{H}_2\text{O})_5]_2\} \cdot 11\text{H}_2\text{O}$ measured in a 100 Oe field. At 290 K the value of χT is $18.05 \text{ cm}^3\text{mol}^{-1}\text{K}$ which is consistent with six noninteracting $\text{Co}(\text{II})$ centres with $S_i = 3/2$ and an average $g = 2.53$. On cooling from 300 K to 120 K the value of χT remains reasonably constant, followed by a gradual decrease to a shallow local minimum of $16.8 \text{ cm}^3\text{mol}^{-1}\text{K}$ at 34 K. On further cooling there is a rapid upward curvature in χT indicating ferromagnetic interactions, which peaks at a maximum value of $18.8 \text{ cm}^3\text{mol}^{-1}\text{K}$ at 7.4 K. There is then a rapid decrease at lower

temperatures to a value of $15.0 \text{ cm}^3 \text{ mol}^{-1} \text{ K}$ at 1.8 K, which is consistent with zero-field splitting or the effects of intermolecular antiferromagnetic exchange. The field dependence of the magnetisation at 2 K shows an increase from 0 to 0.5 T followed by a gradual curve until 3 T after which there is a slow increase. The magnetisation is not saturated at 5 T with $M/N\beta = 12.3$. The dc magnetic characterisation is consistent with our previously reported data [2], however in this case the maximum in χT is more pronounced as a result of measuring in a smaller applied field.

For comparison, the discrete Co_4 SMM cubane ([7] - see Figure 2-6 in Section 2.1.4) shows a gradual increase in χT on cooling with a maximum at 80 K followed by a decrease which becomes more rapid below 20 K. It is proposed that the magnetic coupling within the Co_4 cubane is antiferromagnetic in nature (consistent with the χT curve of Figure 2-6), but that the exchange interactions are weak (consistent with the literature study of the metal citrate cubane series [1]) and so the spin arrangement can be approximated as two spin 'up' centres and two spin 'down' centres for ease of discussion (see the pictorial representation of Figure 2-30 in Section 2.2.5). It is suggested that each peripheral spin 'up' Co(II) centre of the Co_6 cluster can couple ferromagnetically to the neighbouring Co(II) centre of the cubane, transforming the two spin 'down' centres into additional spin 'up' centres, thus generating the overall ferromagnetic behaviour observed as a peak in the χT curve for the Co_6 cluster. This hypothesis will be discussed further in Section 2.2.5.

The magnetisation curve of Co_4 increases rapidly from 0 to 0.7 T with a plateau around 2 T before a further increase indicating the presence of low-lying excited states, however such features are not evident in the magnetisation curve of $\text{Na}\{\text{Co}_6\}$.

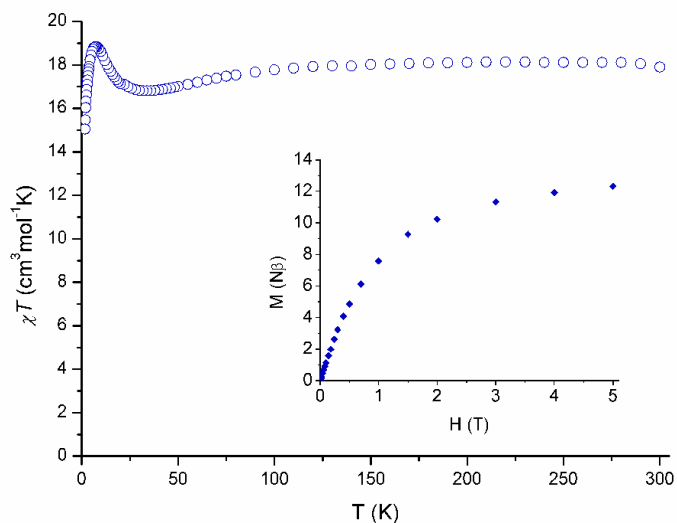


Figure 2-25 – Temperature dependence of χT for hydrated $\text{Na}\{\text{Co}_6\}$ measured in a 100 Oe field. Inset shows field dependence of the magnetisation at 2 K.

The high frequency ac susceptibility data of $\text{Na}\{\text{Co}_6\}$ is shown in Figure 2-26. The out-of-phase component in the range 130-1997 Hz shows the onset of a peak as had been observed previously at low frequency [2]. Interestingly, this new study has revealed the presence of an unusual step-like plateau between 2.5 and 3.5 K at high frequency. Above 2997 Hz the χ'' curve separation reduces and the step becomes more pronounced until 6997-9997 Hz where the curves are very close together. The magnitude of χ'' increases with frequency and so the curves do not cross. An equivalent measurement of the Co_4 SMM displays distinct peaks at all frequencies between 130 and 9997 Hz (Figure 2-7 in Section 2.1.4). Figure 2-56.

The presence of a frequency dependent signal in the out-of-phase component of the ac susceptibility suggests that some form of slow relaxation of the magnetisation is occurring. It is proposed that the step-like plateau is the result of two overlapping signals, with the onset of the peak-like feature attributed to a cluster relaxation process. This feature is thought to be obscured at low temperatures by a second signal that increases below ~ 3.75 K which is possibly due to intermolecular interactions (see comparison in Figure 2-57 and discussion in Section 2.2.5).

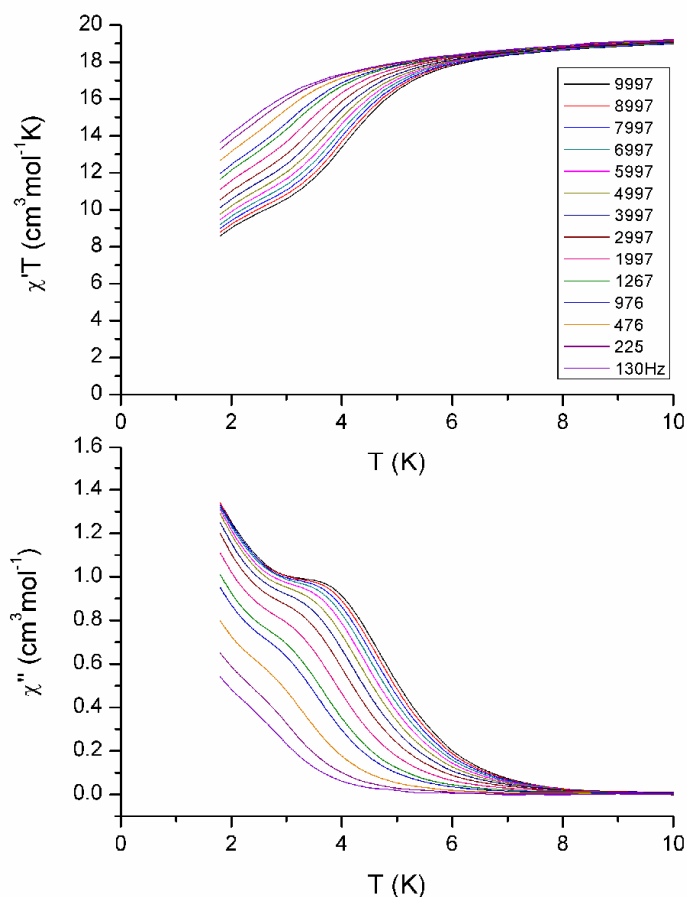


Figure 2-26 – The in-phase and out-of-phase components of the ac susceptibility of hydrated $\text{Na}\{\text{Co}_6\}$ shown as $\chi'T$ versus T (upper) and χ'' versus T (lower).

To investigate further, single crystal measurements were carried out using a micro-SQUID in order to look for magnetisation versus field hysteresis loops. As can be seen in Figure 2-27, with a sweep rate of 0.14 mT/s hysteresis loops are observed at 0.5 K, which widen on cooling as expected. The loops show a small dependence of the sweep rate and broaden slightly on increasing the rate, as would be expected for a single molecule magnet with an Ising type easy axis anisotropy. The curves display a ‘leaning’ orientation that would suggest intermolecular interactions, most likely the result of hydrogen bonding between the clusters, particularly in the area of neighbouring peripheral cobalt units which are arranged together due to the herring bone packing of the Co_6 cluster in the crystal (see Section 2.2.2). The discrete Co_4 cubane SMM hysteresis loops collapse at zero field due to very fast quantum tunnelling of the magnetisation (Figure 2-9), but show a larger sweep rate dependence compared with the $\text{Na}\{\text{Co}_6\}$ measurements.

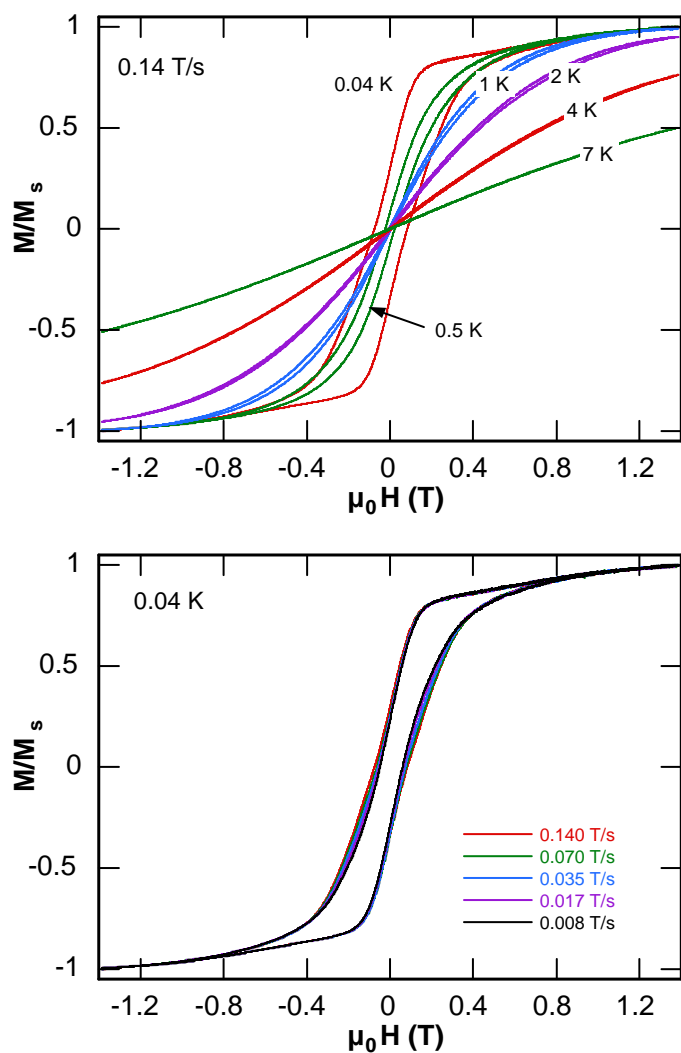


Figure 2-27 – Temperature (upper) and sweep rate (lower) dependence of single crystal magnetisation versus field hysteresis loops of hydrated $\text{Na}\{\text{Co}_6\}$.

The hydrated $\text{Na}\{\text{Co}_6\}$ cluster has therefore been shown by ac and hysteresis measurements to be single molecule magnet complicated by intermolecular interactions.

2.2.5 – Hydration Dependent Magnetic Properties of Na{Co₆}

Magnetic measurements were made on fresh samples of mass c.a. 22 mg consisting of crystals lightly ground to give a randomly oriented polycrystalline sample and loaded into a gelatin capsule. The sample was restrained by compression with the inverted top half of the capsule. After measuring the fresh, hydrated sample, the capsule was removed and placed into a vacuum system (rotary pump and oil diffusion pump attached to a stainless steel manifold) at ambient temperature followed by evacuation for one hour, reaching a final pressure of 2×10^{-4} torr. The capsule was then re-inserted into SQUID and re-measured. This process was then repeated with a further two hours of dehydration, to bring the total vacuum dehydration time to three hours.

Figure 2-28 compares the dc magnetic susceptibility of the hydrated Na{Co₆} cluster with dehydrated samples measured after 1 hour and 3 hours in vacuum. At 290 K the value of χT is $16.8 \text{ cm}^3 \text{ mol}^{-1} \text{ K}$ which is consistent with six noninteracting Co(II) centres with $S_i = 3/2$ and an average $g = 2.44$. The high temperature curve shape of the dehydrated sample is similar to that when hydrated, as in both cases the value of χT remains reasonably constant on cooling from 300 K to 120 K, followed by a gradual decrease. In the case of the 3 hour dehydrated measurements, this gradual decrease continues on cooling and there is no peak as seen for the fresh sample. The data collected after 1 hour of dehydration in the vacuum shows intermediate properties, as the curve does not decrease as rapidly below 100 K, and still shows minor remnants of the peak seen at 7.4 K in the fully hydrated data. The minimum value of χT at 1.8 K for the fresh hydrated sample is $15.0 \text{ cm}^3 \text{ mol}^{-1} \text{ K}$, which is reduced to $11.0 \text{ cm}^3 \text{ mol}^{-1} \text{ K}$ after 1 hour of vacuum dehydration, and finally to $9.21 \text{ cm}^3 \text{ mol}^{-1} \text{ K}$ after 3 hours. The χT curve shapes observed are consistent with those previously reported for the hydrated $[\text{NMe}_4]_3\text{Na}\{\text{Co}_4(\text{cit})_4[\text{Co}(\text{H}_2\text{O})_5]_2\} \cdot 11\text{H}_2\text{O}$ and 3 hour dehydrated $[\text{NMe}_4]_3\text{Na}\{\text{Co}_4(\text{cit})_4[\text{Co}(\text{H}_2\text{O})_5]_2\} \cdot 7\text{H}_2\text{O}$ [2].

On dehydration the field dependence of the magnetisation at 2 K shows a curve which is reduced in magnitude as time in vacuum increases (Figure 2-29). There is significantly more curvature at lower fields when dehydrated and a larger gradient at high field compared with the fresh sample. The magnetisation is not saturated at 5 T with $M/N\beta = 8.75$ after 1 hour and $M/N\beta = 8.05$ after 3 hours.

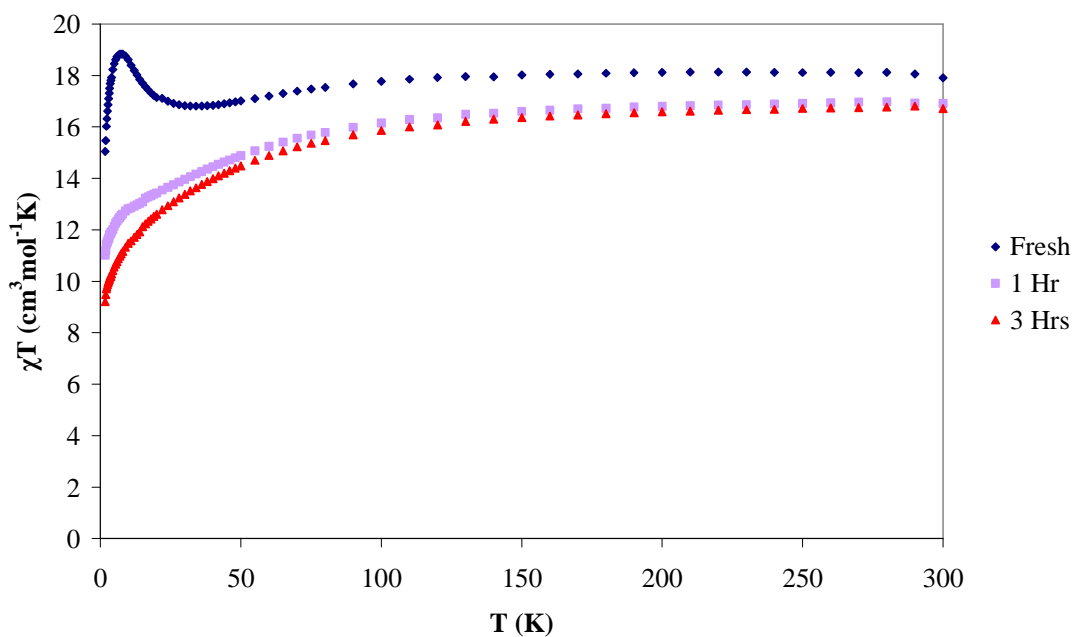


Figure 2-28 – Hydration dependence of the χT curve of $\text{Na}\{\text{Co}_6\}$ measured in a 100 Oe field. A comparison of the fresh hydrated sample (blue diamonds) with the dehydrated sample measured after 1 hour (lavender squares) and 3 hours (red triangles) in vacuum.

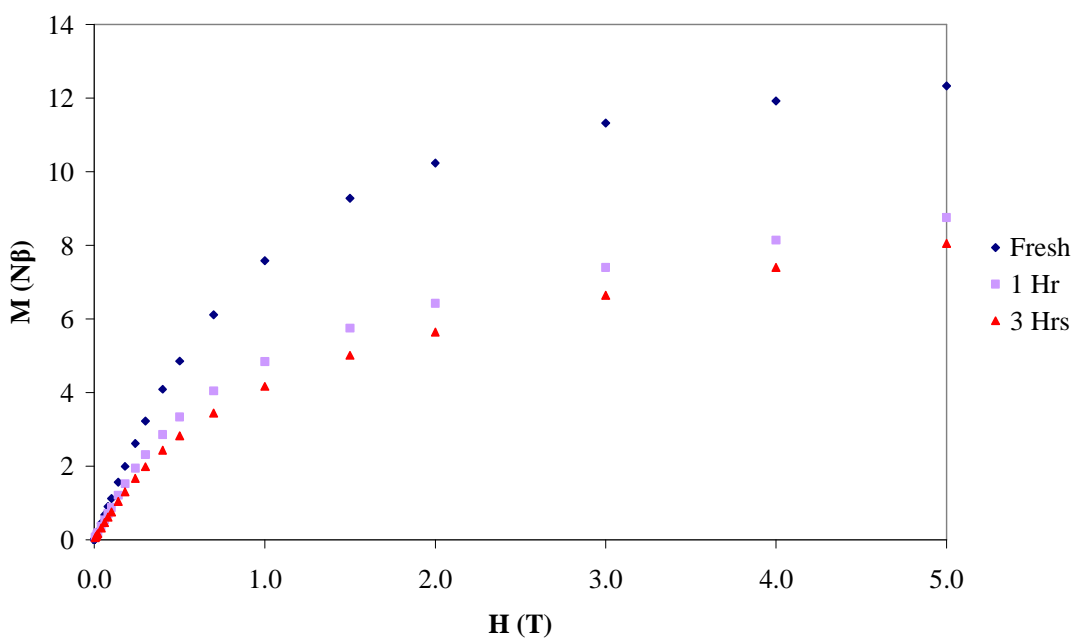


Figure 2-29 – Hydration dependence of the magnetisation curve of $\text{Na}\{\text{Co}_6\}$. A comparison of the fresh hydrated sample (blue diamonds) with the dehydrated sample measured after 1 hour (lavender squares) and 3 hours (red triangles) in vacuum.

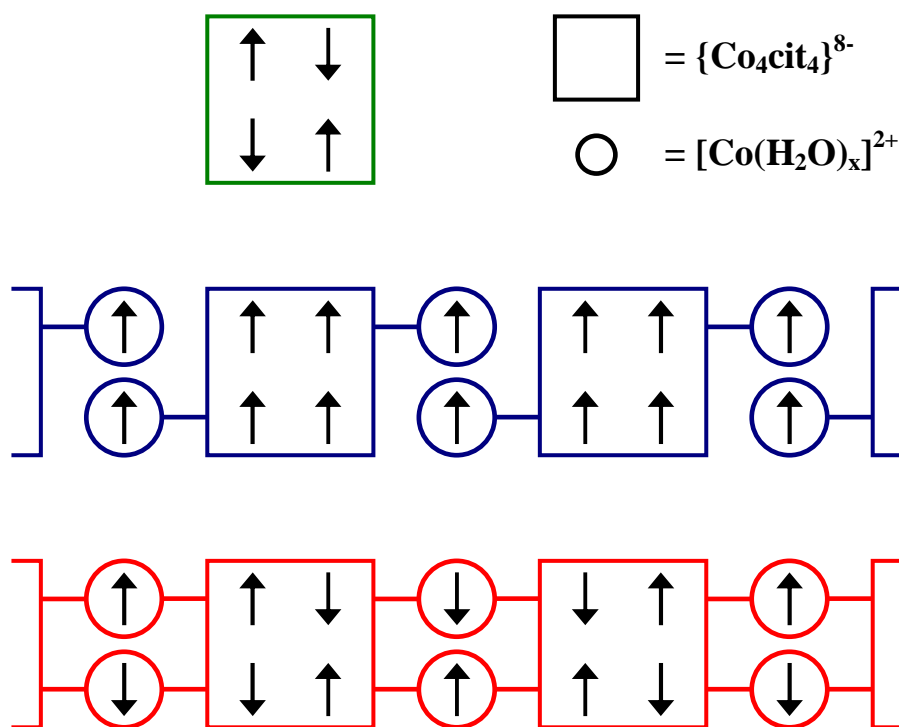


Figure 2-30 – Pictorial representation of the proposed cobalt(II) centre spin orientations in the discrete Co_4 cluster (green), the hydrated Co_6 cluster (blue, where $x = 5$) and the dehydrated, polymerised Co_6 cluster (red, where $x = 4$). $x =$ number of water molecules coordinated to the peripheral cobalt(II) centre.

The hypothesis for the nature of the spin interactions in the cobalt(II) citrate compounds is shown in Figure 2-30. It is suggested that there is a ferromagnetic interaction between the peripheral cobalt(II) centre and the neighbouring cobalt(II) centre of the cubane unit. In the case of the hydrated $\text{Na}\{\text{Co}_6\}$ cluster, these ferromagnetic interactions could overcome the weak antiferromagnetic exchange within the cubane such that all six spin centres of the cluster couple ferromagnetically. This would result in an increase in the χT curve, consistent with the peak feature observed for hydrated $\text{Na}\{\text{Co}_6\}$. On dehydration it is proposed that the clusters could polymerise via the peripheral cobalt(II) centres to form chains with two linker units between each cubane, as shown in Figure 2-30. If the exchange interactions between the linker cobalt(II) centres and neighbouring cubane cobalt(II) centres remain ferromagnetic in character, then the overall effect (in combination with the intracubane exchange) could be antiferromagnetic behaviour, which is consistent with the downwards curvature observed in the χT curve for dehydrated samples.

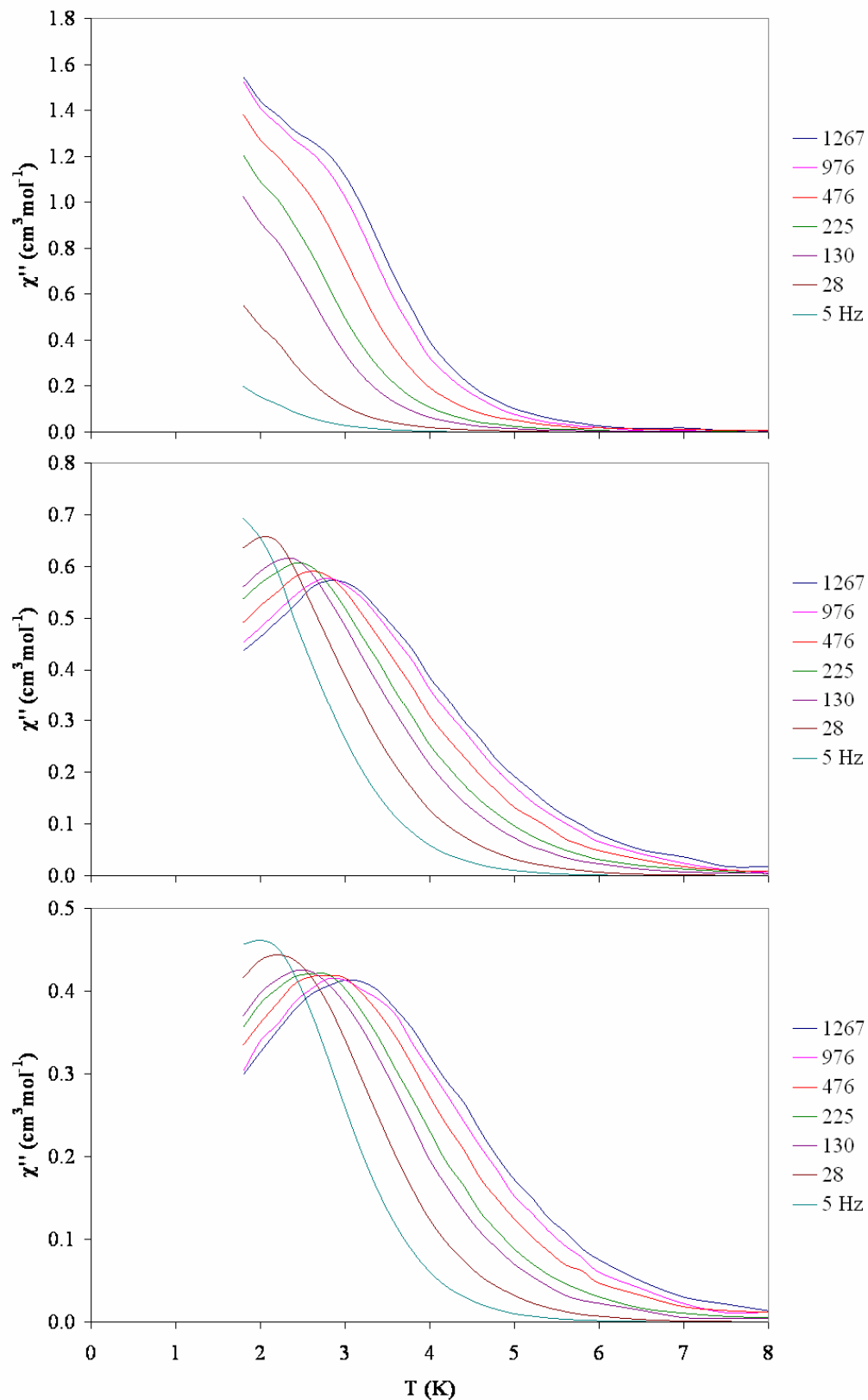


Figure 2-31 – The hydration dependence of the out-of-phase component of the ac susceptibility of $\text{Na}\{\text{Co}_6\}$, shown as fresh, hydrated sample (upper), after 1 hour of dehydration (middle) and after 3 hours (lower).

The hydration dependence of the magnetic behavior is most prominent in the out-of-phase component of the ac magnetic susceptibility (χ''). Figure 2-31 illustrates how the onset of a frequency dependent signal in the out-of-phase susceptibility is transformed into distinct peaks after dehydration for 1 hour. An Arrhenius analysis of the peak positions gives an energy barrier to the reorientation of the magnetisation of $\Delta E/k_B = 28$ K with $\tau_0 = 8.2 \times 10^{-9}$ s for 28-1267 Hz. Further dehydration to three hours total vacuum time shifts the peak positions to higher temperatures, including that for 5 Hz which can now be seen in the temperature range accessible with the SQUID. An Arrhenius analysis for 28-1267 Hz gives an increased energy barrier of $\Delta E/k_B = 31$ K with $\tau_0 = 5.3 \times 10^{-9}$ s. This energy barrier is higher than that previously reported ($\Delta E/k_B = 26$ K with $\tau_0 = 8.2 \times 10^{-9}$ s) [2], however the new value should be more accurate due to the larger sample sizes and greater range of measured frequencies. It is proposed that the appearance of the distinct peaks on dehydration is the result of a reduction in the second (overlapping) low temperature χ'' signal that was proposed earlier in Section 2.2.4. If the second signal is the result of intermolecular interactions, then it would be expected to alter significantly on polymerisation of the clusters. The apparent shift of the χ'' peaks on dehydration is both interesting and unusual. A lattice solvent dependent magnetic behaviour has also been observed for manganese based SMMs, which was attributed to varying degrees of intermolecular antiferromagnetic exchange interactions mediated by the hydrogen bonding network and π -stacking (observed in the crystal structure of the fully solvated form) [9].

The dehydration of the $\text{Na}\{\text{Co}_6\}$ crystals is accompanied by a striking colour change from hydrated pink crystals to dark purple dehydrated crystals, and so an investigation of the changes in the electronic spectrum was carried out. The fresh, hydrated crystals were ground and pressed into a disc of pure material. The spectrum was measured and the disc placed under vacuum for dehydration under the same conditions as for the SQUID capsule. The spectrum of the dehydrated disc was then re-measured.

By comparing the two spectra of Figure 2-32 it can be seen that the major difference is the large reduction of the ${}^4\text{A}_2$ peak ($14 \times 10^3 \text{ cm}^{-1}$) on dehydration. There is also a small shift and broadening of the ${}^4\text{T}_1$ peak ($19 \times 10^3 \text{ cm}^{-1}$). The water combination peak ($\sim 5 \times 10^3 \text{ cm}^{-1}$) indicates the amount of water present (as confirmed by equivalent

measurements on Co(II) doped silica gel – Figure 2-33), and can be seen to decrease considerably on vacuum dehydration. The overall similarity of the two spectra (in particular the similar intensity) shows that the cobalt centres remain octahedral, and so the colour change is not due to the peripheral cobalt centres changing to tetrahedral coordination (this being a possible hypothesis since a mix of octahedral pink cobalt with tetrahedral blue cobalt would produce a purple colour).

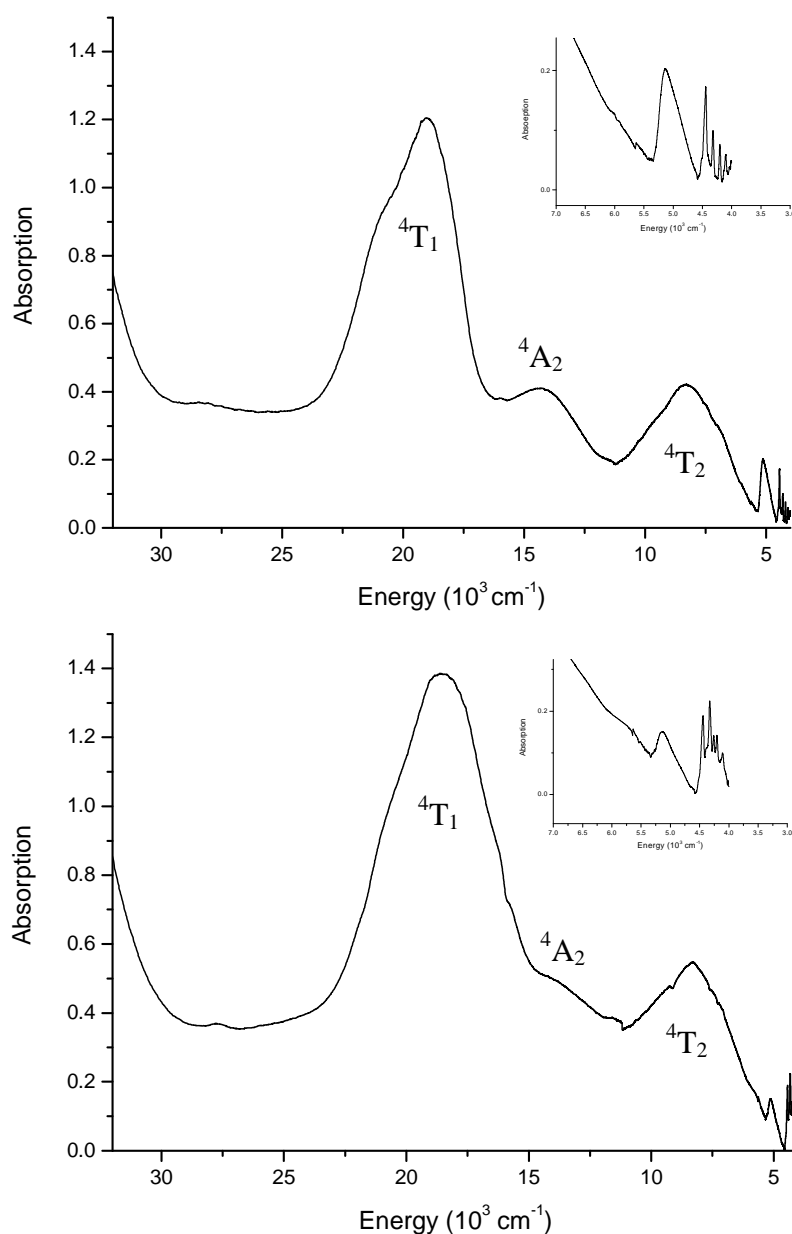


Figure 2-32 – Electronic spectra of hydrated (upper) and dehydrated (lower) $\text{Na}\{\text{Co}_6\}$. Inset is enlarged region of water combination band located at far right of full spectrum. A baseline correction has been applied.

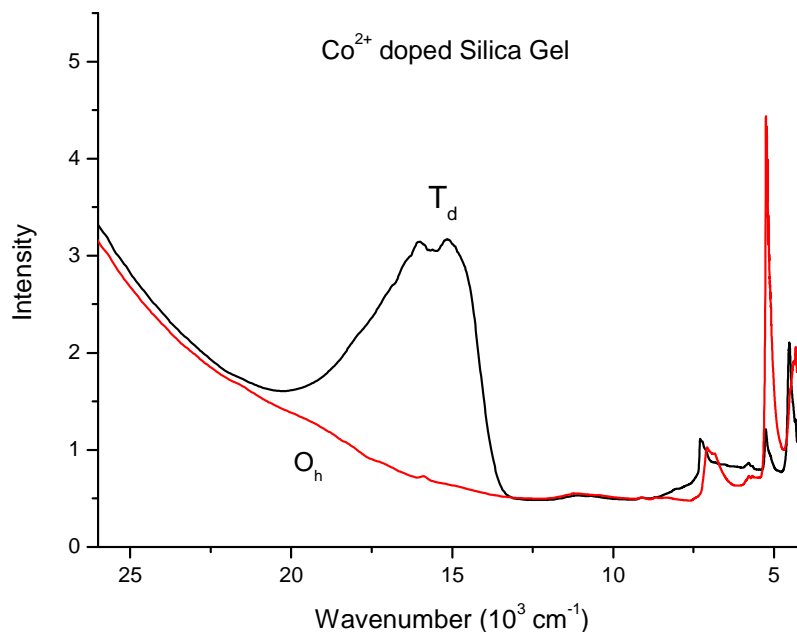


Figure 2-33 – Hydration dependence of the electronic spectrum of Co(II) doped silica gel. Black line is dehydrated tetrahedral coordination; red line is hydrated octahedral coordination. Note that the dehydrated tetrahedral Co(II) spectrum has a greater intensity, but a smaller water combination peak ($\sim 5 \times 10^3 \text{ cm}^{-1}$) compared with the octahedral Co(II) spectrum.

The electronic spectra provide useful clues as to what is occurring at the molecular level during the dehydration process; however a single crystal X-ray diffraction study of the dehydrated crystals would be the optimum solution. Unfortunately all attempts to date have been unsuccessful due to extremely poor diffraction of the crystals that have been placed in the vacuum. As previously mentioned, significant improvements have been made to the crystal size and quality; however the diffraction of the hydrated crystals is still comparatively weak on lab-based diffractometers. Diffraction studies of the dehydrated crystals have proven unobtainable on lab equipment even though the crystals remain intact (as shown in Figure 2-34) and appear of good quality by microscopy study. Related powder diffraction experiments investigating changes in unit cell dimensions and sample crystallinity have also been unsuccessful for similar reasons.

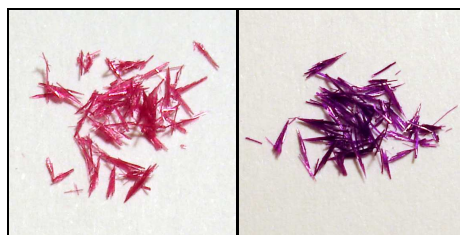


Figure 2-34 – Photograph of hydrated pink crystals (left) and dark purple dehydrated crystals (right) of Na{Co₆}.

We note a recent report by Campo *et al.* of a 1D chain of cobalt(II) citrate cubanes linked by octahedral cobalt(II) centres [10], which shares many common structural features with our Na{Co₆} cluster. Interestingly the 1D chain has been shown to undergo a thermally induced single-crystal-to-single-crystal cross-linking to form a 2D network by coordination through the peripheral cobalt(II) centres, as determined by single crystal X-ray diffraction. The process involves water egress and therefore bears many similarities to the behaviour of Na{Co₆}. Indeed, due to the previously mentioned close proximity of the peripheral cobalt centres of Na{Co₆} within the crystal packing, linking the discrete clusters into chains is the hypothetical explanation for the hydration dependent behaviour of the sample. If these polymer chains form with varying lengths throughout the crystal by local reorganisation, this could explain why the crystals do not diffract X-rays after dehydration even though the crystals remain intact. The linking of the clusters into chains via the peripheral cobalt(II) centres could possibly explain the reduction in the intensity of the ${}^4T_1 \rightarrow {}^4A_2$ transition seen in the electronic spectrum on dehydration. The peripheral -OCO(H₂O)₅ units have C_{4v} symmetry which is non centrosymmetric, and if on dehydration these were to become linking trans -OCO(H₂O)₄O- units these would have D_{4h} symmetry which is centrosymmetric and so the intensity would be reduced.

One key difference of the Na{Co₆} behaviour compared with the thermally induced results of Campo *et al.* [10] is that although a pink to purple colour change is observed by heating samples of Na{Co₆}, we have found so far that they do not show χ'' peaks in the ac susceptibility as in samples from vacuum dehydration, however this may be due to decomposition of the sample at the temperatures required to drive the water fully out of the SQUID capsule.

2.3 – Alkali Metal Analogues of Na{Co₆}

Due to the location of the Na⁺ counterions close in to the Co₆ clusters in the crystal structure, studies of similar syntheses with other alkali metals of different sizes was of interest. Li⁺, K⁺, Rb⁺ and Cs⁺ analogues of the Na{Co₆} reaction (Section 2.2.1) were carried out to investigate possible differences in crystal packing. These used the literature synthesis with the addition of the various metal sulphate salts in place of Na₂SO₄. Solvent layering was used for crystallisation as per the literature [2]. Unfortunately these experiments were of limited success. The Li⁺ experiment oiled, and the Rb⁺ and Cs⁺ experiments gave very few crystals, most of which were small blocks of salts (IR showed no citrate peaks) with only a handful of very small hedgehogs. Although the K⁺ experiment produced a reasonable yield, the hedgehogs obtained were so small and delicate that they simply disintegrated when any attempt was made to harvest them. Clearly these were not feasible routes to these compounds given the quantities required for analysis, and most crucially, a viable SQUID sample.

Fortunately, experiments using the novel superhedgehog synthesis (increased final pH of 7.50, ¼ literature salt concentration) were successful and have given large hedgehogs using Li⁺, K⁺, Rb⁺ and Cs⁺ salts. These experiments provide crystals in good yield. Interestingly, products were also obtained using Mg²⁺ and Ca²⁺ salts, however the hedgehogs were extremely small and delicate, and so no further analysis was feasible.

For direct comparison with the following sections, the temperature dependence of χT for the hydrated and dehydrated Na{Co₆} measured in a 1000 Oe field is shown in Figure 2-35. The features of the χT curves are similar to those seen in 100 Oe in Figure 2-28, with the hydrated data displaying a peak at low temperature around 7.4 K, which in this case is less distinct and more like a plateau. The dehydrated data after 1 hour in vacuum shows a decreasing curve around that temperature with a small peak feature at 2.9 K. In the more linear region at high temperature, the value of χT at 290 K is 18.10 cm³mol⁻¹K for the hydrated sample and 16.89 cm³mol⁻¹K for the dehydrated sample.

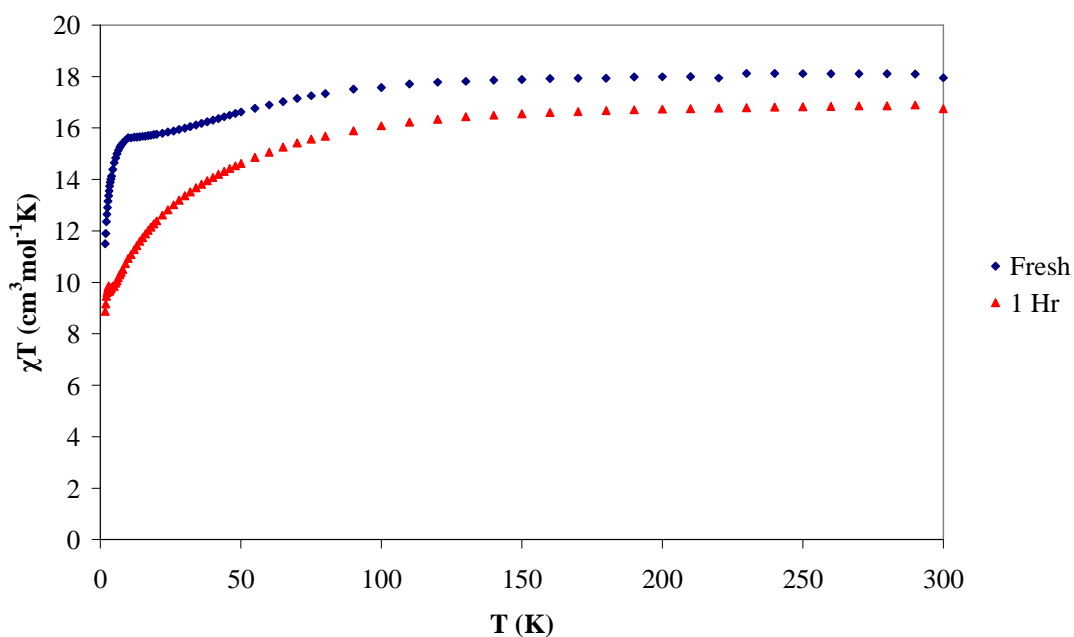


Figure 2-35 – Hydration dependence of the χT curve of $\text{Na}\{\text{Co}_6\}$, measured in a 1000 Oe field. A comparison of the fresh hydrated sample (blue diamonds) with the dehydrated sample measured after 1 hour (red triangles) in vacuum.

2.3.1 – Lithium Analogue

2.3.1.1 – Synthesis of $[\text{NMe}_4]_3\text{Li}\{\text{Co}_4(\text{cit})_4[\text{Co}(\text{H}_2\text{O})_5]_2\} \cdot 16\text{H}_2\text{O}$

$\text{CoSO}_4 \cdot 7\text{H}_2\text{O}$ (2.030 g, 7.2 mmol) and citric acid monohydrate (1.518 g, 7.2 mmol) were combined in solution in 10 ml H_2O . $\text{NMe}_4\text{OH} \cdot 5\text{H}_2\text{O}$ (~4.93 g) was added until pH 7.50 was obtained. 15 ml of solution was diluted with 15 ml H_2O and 0.145 g Li_2SO_4 added. 1.0 ml aliquots were mixed with 3.1-4.0 ml EtOH or layered with 5.0 ml EtOH. Small pink hedgehogs formed in moderate yield, selected IR data (cm^{-1}): 3209 (m), 1549 (s), 1487 (m), 1378 (s), 1287 (w), 1239 (m), 1090 (w), 1060 (w), 952 (w), 923 (w). Analysis, calculated (found) for $\text{C}_{36}\text{H}_{104}\text{Co}_6\text{N}_3\text{O}_{54}\text{Li}$: C, 23.97 (23.78); H, 5.81 (5.59); N, 2.33 (2.33).

2.3.1.2 – Structure of $[\text{NMe}_4]_3\text{Li}\{\text{Co}_4(\text{cit})_4[\text{Co}(\text{H}_2\text{O})_5]_2\} \cdot 16\text{H}_2\text{O}$

The $\text{Li}\{\text{Co}_6\}$ structure is very similar to that of $\text{Na}\{\text{Co}_6\}$. Both structures are in the $Pna2_1$ space group and have unit cell dimensions of $a = 23.093(3)$, $b = 14.3843(18)$, $c = 21.691(3)$ Å for Na^+ and slightly longer dimensions of $a = 23.240(5)$, $b = 14.527(3)$, $c = 22.523(5)$ Å for Li^+ . The packing of the Co_6 clusters in $\text{Li}\{\text{Co}_6\}$ is the same ‘herring bone’ pattern as previously seen for $\text{Na}\{\text{Co}_6\}$ (Figure 2-21), with the tetramethylammonium ions filling the channels between the clusters when seen along the a axis, as shown in Figure 2-36. The $\text{Li}\{\text{Co}_6\}$ cubane bridging angles are in the range 94.43 - 101.37° with Co-O bond lengths of 2.066 - 2.174 Å, which are broader ranges than those found for $\text{Na}\{\text{Co}_6\}$ (Section 2.2.2).

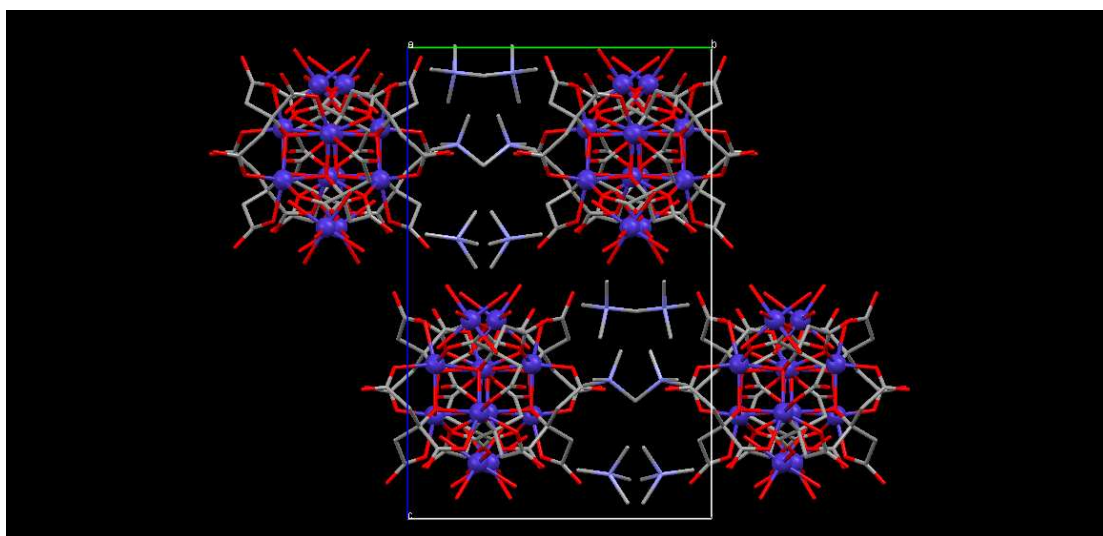


Figure 2-36 – Cluster packing in $\text{Li}\{\text{Co}_6\}$ crystal structure, viewed along the a axis (Co blue, O red, C grey, N pale blue, H and lattice water omitted).

The diffraction study was complicated by the fact that the crystal used was multiple twinned, a problem previously encountered with the sodium version. The Li^+ cations could not be found in the structure due to their small electron density and the fact that they were likely to be disordered over several sites like the sodium analogue. However due to the similar positions of the tetramethylammonium counterions in the two structures it is likely that the Li^+ ions could be present in same regions as the Na^+ seen in Figure 2-22. Multiple twinning of the crystals was a particular problem with $\text{Li}\{\text{Co}_6\}$ and they proved to be relatively unstable, as within a few weeks the hedgehog formations shattered and were reduced to a crystalline carpet of shards.

2.3.1.3 – Magnetic Properties of Li{Co₆}

In Figure 2-37 the value of χT at 290 K for Li{Co₆} is 17.5 cm³mol⁻¹K, and it remains reasonably constant on cooling to 100 K, after which a gradual decrease occurs that is indicative of antiferromagnetic interactions. The decrease is almost linear between 50 and 24 K, with a region of increasing downward curvature centred on ~8 K, which is followed by another rapid linear decrease from 3.7 to 1.8 K. Although there is no prominent peak or plateau as seen for the hydrated Na{Co₆} it is interesting to note that the region of the curve with the greatest change of gradient occurs at similar temperature. Overall, the Li{Co₆} χT curve shape resembles the dehydrated Na{Co₆} rather than the hydrated Na{Co₆} data of Figure 2-35.

The magnetisation curve of Li{Co₆} (Figure 2-38) is also similar to that of Na{Co₆}. The magnetisation is not saturated in a field of 5 T with a value of $M/N\beta = 9.74$, which is of a magnitude closer to the dehydrated Na{Co₆} data. By contrast the Li{Co₆} out-of-phase ac susceptibility data shown in Figure 2-39 has the onset of a frequency dependent signal that was previously seen for the hydrated Na{Co₆}, and there are no distinct peaks present.

This apparent mixture of similarities may be explained by the fact that this sample was restrained in eicosane wax to prevent torquing of the crystals. It is possible that the heat from the molten eicosane and the heating of the sample to ensure that the wax was evenly dispersed may have partially dehydrated the sample before it was fully sealed from the air. This may have affected the dc susceptibility without being sufficient to cause a colour change or the appearance of χ'' peaks. Measurements of Na{Co₆} in eicosane wax have also shown similar effects, with a reduced χT curve. It should also be noted that as previously mentioned in Section 2.2.5, the application of heat to Na{Co₆} did not give χ'' peaks, which could be due to decomposition of the sample or shattering of the crystals due to thermal shock.

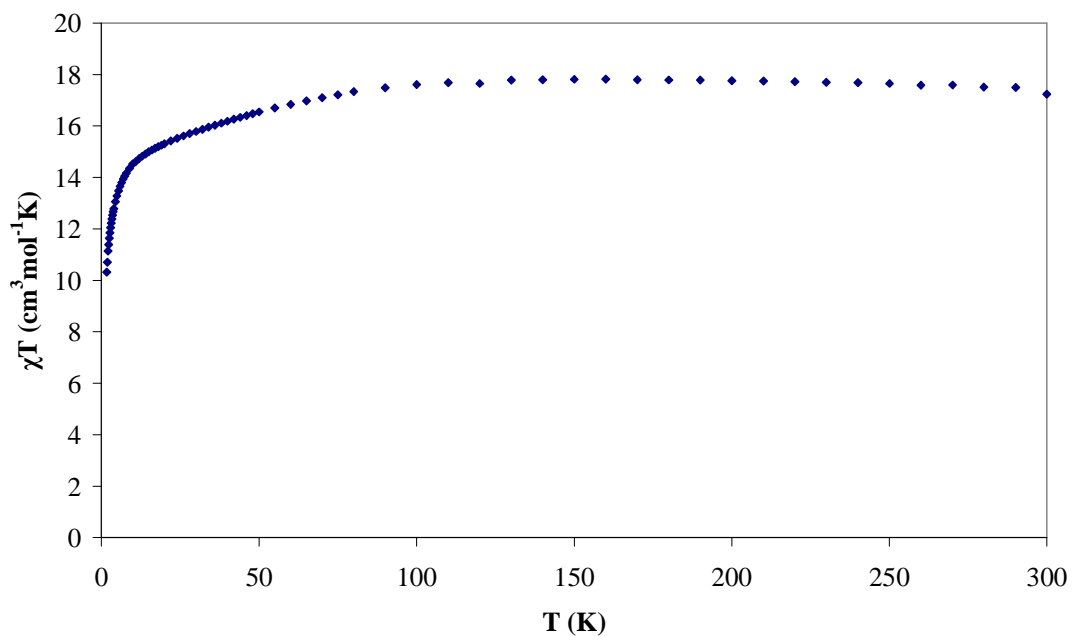


Figure 2-37 – Temperature dependence of χT for hydrated $\text{Li}\{\text{Co}_6\}$ measured in a 1000 Oe field.

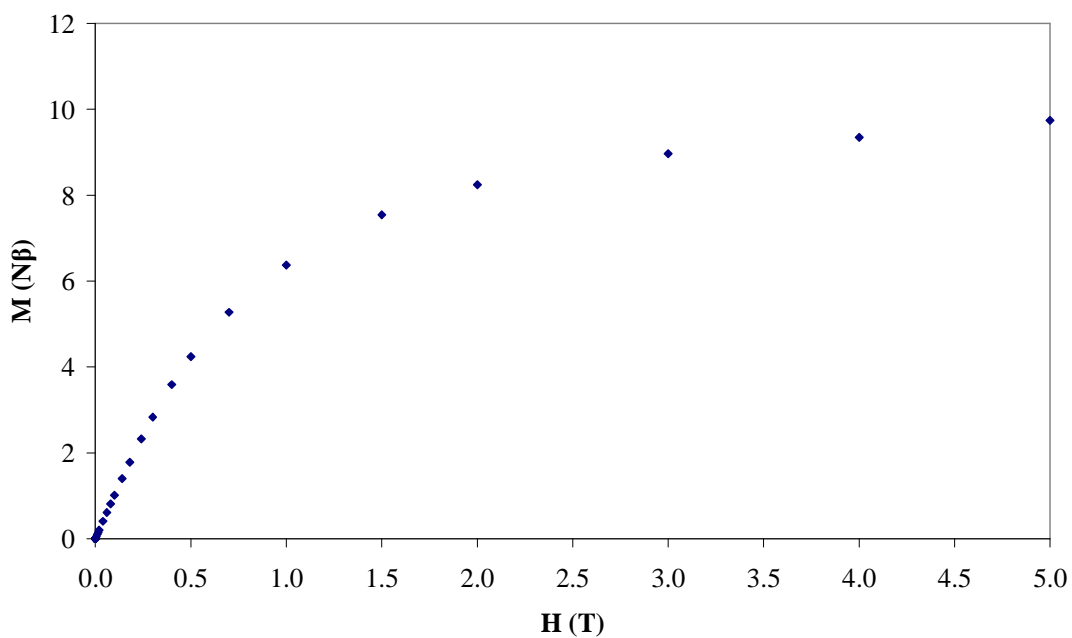


Figure 2-38 – Field dependence of the magnetisation at 2 K for $\text{Li}\{\text{Co}_6\}$.

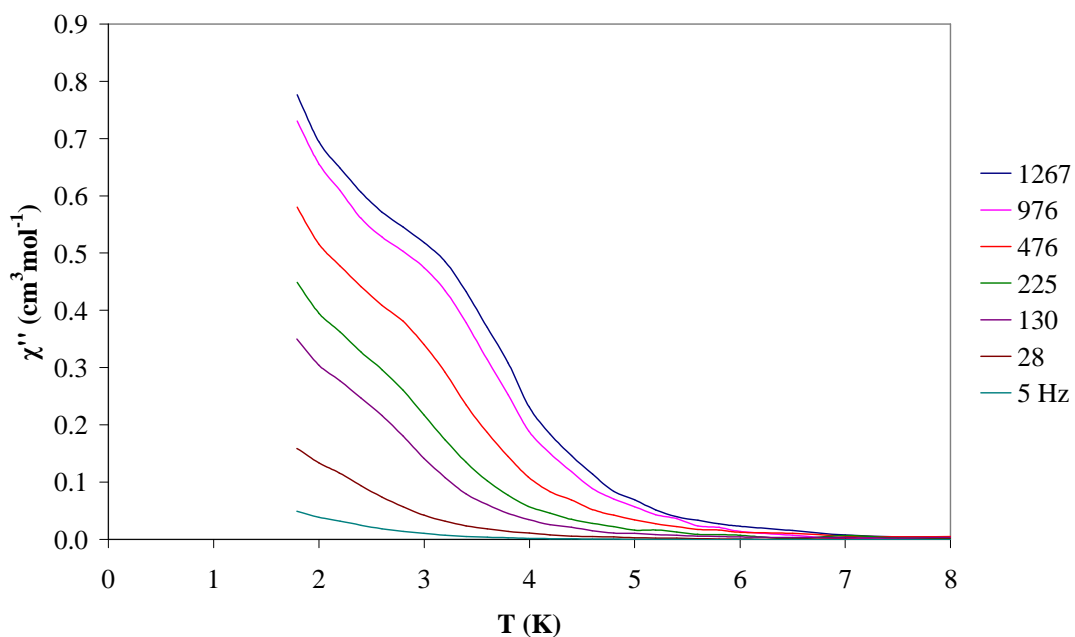


Figure 2-39 – The out-of-phase component of the ac susceptibility for $\text{Li}\{\text{Co}_6\}$.

2.3.2 – Potassium Analogue

2.3.2.1 – Synthesis of $[\text{NMe}_4]_3\text{K}\{\text{Co}_4(\text{cit})_4[\text{Co}(\text{H}_2\text{O})_5]_2\} \cdot 14\text{H}_2\text{O}$

$\text{CoSO}_4 \cdot 7\text{H}_2\text{O}$ (2.030 g, 7.2 mmol) and citric acid monohydrate (1.518 g, 7.2 mmol) were combined in solution in 10 ml H_2O . $\text{NMe}_4\text{OH} \cdot 5\text{H}_2\text{O}$ (~4.93 g) was added until pH 7.50 was obtained. 15 ml of solution was diluted with 15 ml H_2O and 0.230 g K_2SO_4 added. 1.0 ml aliquots were mixed with 4.1-5.0 ml EtOH or layered with 5.0 ml EtOH. Small pink hedgehogs formed in low yield, along with fine colourless salt. Hedgehog crystals, selected IR data (cm^{-1}): 3219 (m), 1551 (s), 1486 (m), 1377 (s), 1288 (w), 1239 (m), 1091 (m), 1058 (w), 951 (m), 922 (w).

The potassium analogue of the $\text{Na}\{\text{Co}_6\}$ superhedgehog synthesis was the least successful at producing crystals. The hedgehog formations obtained were very small (approximately the size of the $\text{Na}\{\text{Co}_6\}$ hedgehogs produced using the original literature synthesis), and the rods appeared very rough and of poor quality by microscopy. There was also a significant problem with very finely divided colourless salt impurities which tended to coat all surfaces. Indeed it was not uncommon for the hedgehog to be partially submerged in a heavy salt suspension layer. Collection of the crystals without the salt impurity was very difficult, and even after water washes

the microanalysis still suggested the presence of salt, with a formula of $[\text{NMe}_4]_3\text{K}\{\text{Co}_4(\text{cit})_4[\text{Co}(\text{H}_2\text{O})_5]_2\} \cdot 14\text{H}_2\text{O} \cdot \frac{1}{4}([\text{NMe}_4]_2\text{SO}_4)$. Analysis, calculated (found) for $\text{C}_{37}\text{H}_{103}\text{Co}_6\text{N}_{3.25}\text{O}_{52.5}\text{KS}_{0.125}$: C, 24.27 (24.07); H, 5.67 (5.22); N, 2.49 (2.92). A single crystal X-ray diffraction study was attempted, but was unsuccessful as the diffraction was very poor due to the low crystal quality. Due to the problems with the product crystals no further analysis of the K^+ analogue was carried out.

2.3.3 – Caesium Analogue

2.3.3.1 – Synthesis of $[\text{NMe}_4]_3\text{Cs}\{\text{Co}_4(\text{cit})_4[\text{Co}(\text{H}_2\text{O})_5]_2\} \cdot 16\text{H}_2\text{O}$

$\text{CoSO}_4 \cdot 7\text{H}_2\text{O}$ (2.030 g, 7.2 mmol) and citric acid monohydrate (1.518 g, 7.2 mmol) were combined in solution in 10 ml H_2O . $\text{NMe}_4\text{OH} \cdot 5\text{H}_2\text{O}$ (~4.93 g) was added until pH 7.50 was obtained. 15 ml of stock solution was diluted with 15 ml H_2O and 0.478 g Cs_2SO_4 added. 1.0 ml aliquots were mixed with 4.8-5.8 ml EtOH or layered with 6.0 ml EtOH. Pink hedgehogs/rods formed in moderate yield, selected IR data (cm^{-1}): 3226 (m), 1550 (s), 1487 (m), 1379 (s), 1287 (w), 1238 (m), 1090 (w), 1059 (w), 951 (m), 923 (w). Analysis, calculated (found) for $\text{C}_{36}\text{H}_{104}\text{Co}_6\text{N}_3\text{O}_{54}\text{Cs}$: C, 22.40 (22.41); H, 5.43 (5.41); N, 2.18 (2.54).

2.3.3.2 – Structure of $[\text{NMe}_4]_3\text{Cs}\{\text{Co}_4(\text{cit})_4[\text{Co}(\text{H}_2\text{O})_5]_2\} \cdot 16\text{H}_2\text{O}$

The caesium analogue crystallises in the $Pna2_1$ space group with unit cell dimensions of $a = 23.049(13)$, $b = 14.6342(8)$, $c = 20.9420 \text{ \AA}$. The a and c dimensions are smaller than those of $\text{Na}\{\text{Co}_6\}$ and the b dimension is longer, giving an overall unit cell volume of 7063.81 \AA^3 that is smaller than the $\text{Na}\{\text{Co}_6\}$ volume of 7205.24 \AA^3 . The Co_6 cluster packing is the same as that for the Na^+ and Li^+ analogues, but the counterion positions are different. The Cs^+ counterions are located close in to the Co_6 clusters as seen previously with Na^+ , but in this case they are disordered over three sites rather than two, and the larger Cs^+ can coordinate to a greater number of the oxygens of the cluster. The tetramethylammonium ions are also in new positions, with the greatest difference seen for the pair of ions at the top of the channels in Figure 2-40 which are shifted towards the clusters, very close to one of the Cs^+ sites. Within the cluster the $\text{Cs}\{\text{Co}_6\}$ cubane bridging angles are in the range 95.86 - 101.01° with Co-O bond lengths of 2.074 - 2.134 \AA .

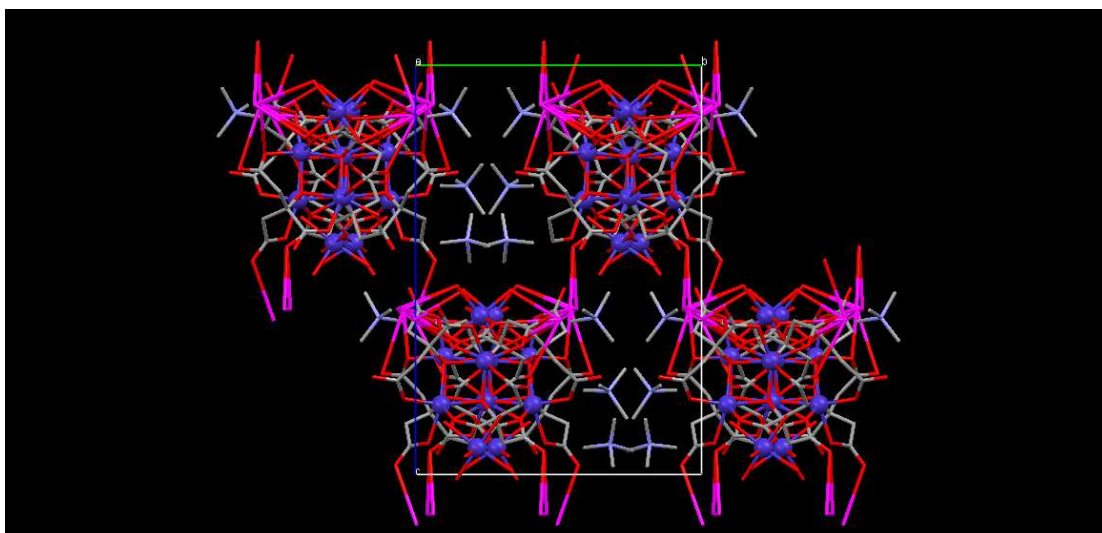


Figure 2-40 – Cluster packing in Cs{Co₆} crystal structure, viewed along the *a* axis (Co blue, O red, C grey, N pale blue, Cs pink, H and lattice water omitted).

2.3.3.3 – Hydration Dependent Magnetic Properties of Cs{Co₆}

The χT curves for both hydrated and dehydrated Cs{Co₆} are shown in Figure 2-41. At 290 K the value of χT for Cs{Co₆} is 17.2 cm³mol⁻¹K when hydrated and 16.8 cm³mol⁻¹K after one hour of dehydration in vacuum. Both curves once again display a relatively constant region between 300 and 150 K followed by a decrease on further cooling, which becomes more rapid and linear between 50 and 24 K. A very broad feature is seen at lower temperatures (which is more prominent in the hydrated data) with a rapid decrease in χT below 8 K. The reduction in the χT curve at low temperatures on dehydration is not as great as that seen for Na{Co₆} and this may be due to the larger number of lattice water molecules (16 rather than 11) resulting in less water removal in the same vacuum time. The Cs{Co₆} magnetisation curve of Figure 2-42 shows a reduction in magnitude on dehydration, with an unsaturated value of $M/N\beta = 11.3$ when fresh and $M/N\beta = 8.45$ after 1 hour in vacuum.

The onset of a frequency dependent signal in the out-of-phase component of the ac susceptibility for the hydrated Cs{Co₆} (Figure 2-43) is transformed into distinct peaks on dehydration (Figure 2-44). There is an anomaly with the greater magnitude of the dehydrated χ'' peak at 1267 Hz which could be due to an instrumental error (see Figure 2-18). An Arrhenius analysis of 130-1267 Hz gives an energy barrier of $\Delta E/k_B = 22$ K with $\tau_0 = 5.7 \times 10^{-8}$ s, which is smaller than found for Na{Co₆} after 1 hour.

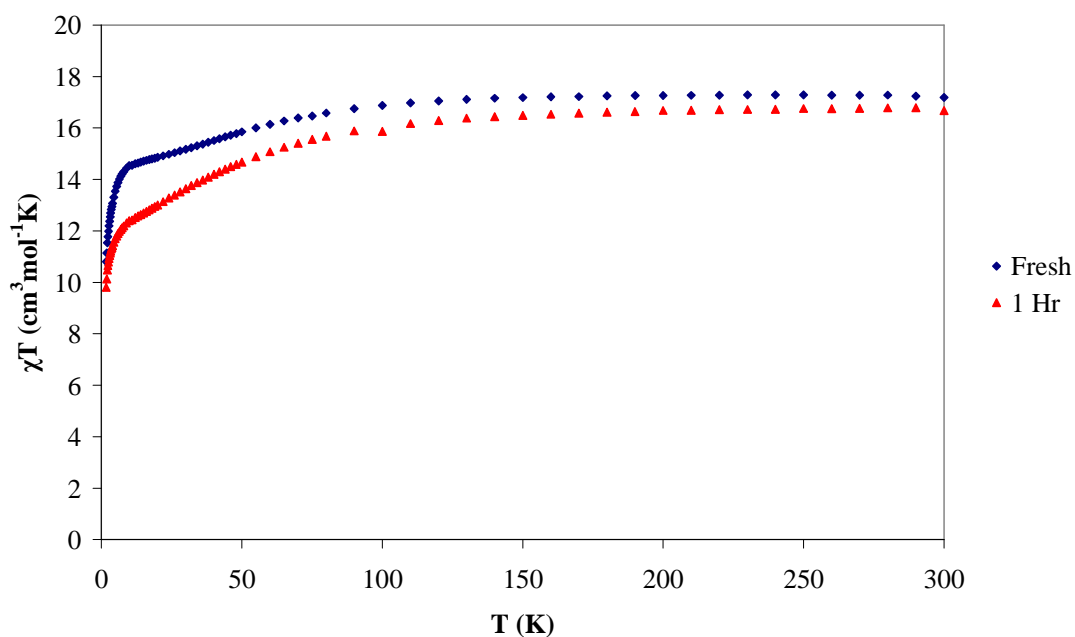


Figure 2-41 – Hydration dependence of the χT curve of $\text{Cs}\{\text{Co}_6\}$ measured in a 1000 Oe field. A comparison of the fresh hydrated sample (blue diamonds) with the dehydrated sample measured after 1 hour (red triangles) in vacuum.

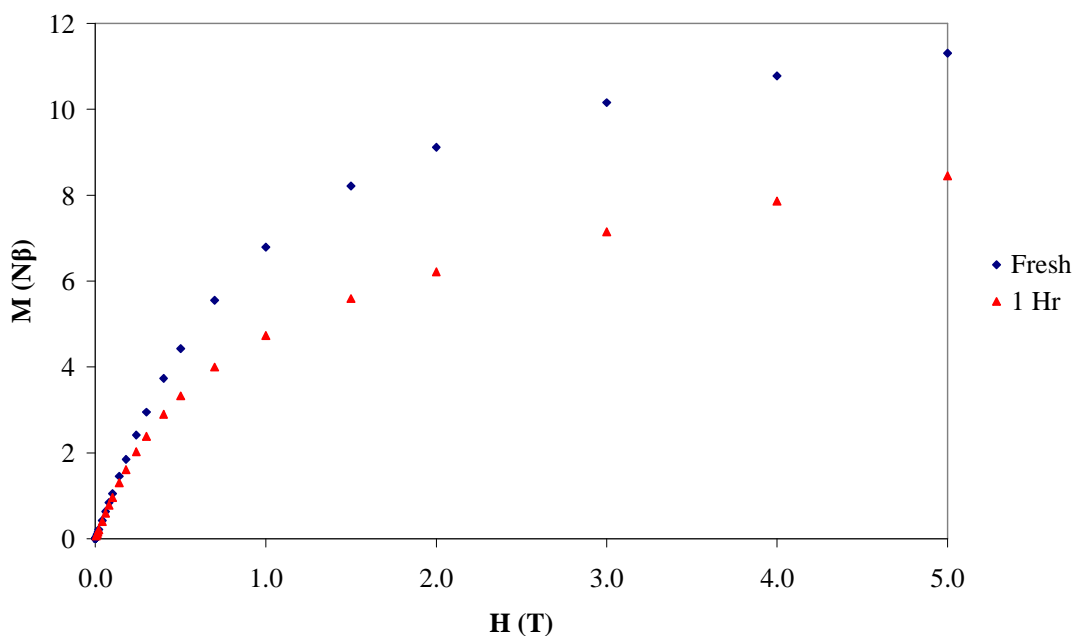


Figure 2-42 – Hydration dependence of the magnetisation curve of $\text{Cs}\{\text{Co}_6\}$. A comparison of the fresh hydrated sample (blue diamonds) with the dehydrated sample measured after 1 hour (red triangles) in vacuum.

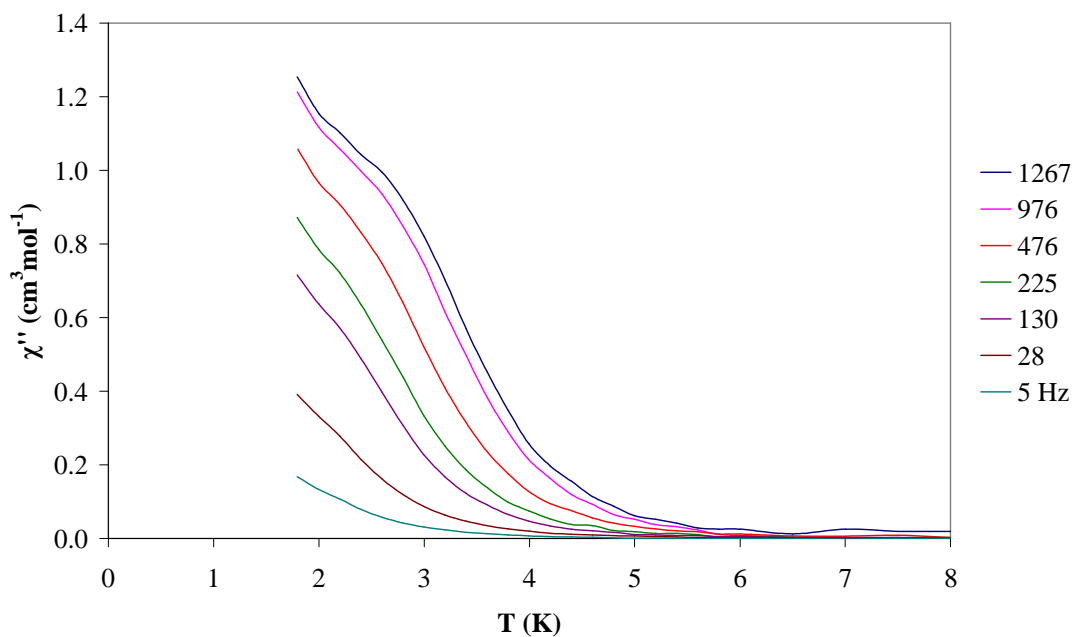


Figure 2-43 – The out-of-phase component of the ac susceptibility for the fresh hydrated sample of $\text{Cs}\{\text{Co}_6\}$.

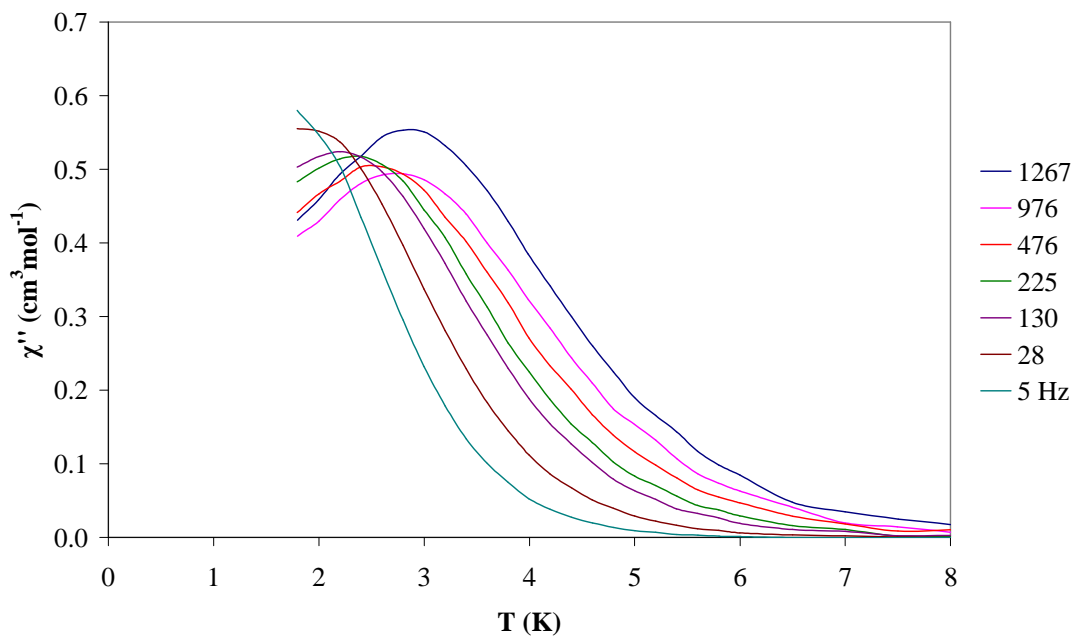


Figure 2-44 – The out-of-phase component of the ac susceptibility for the dehydrated sample of $\text{Cs}\{\text{Co}_6\}$ measured after 1 hour in vacuum.

2.3.4 – Attempted Rubidium Analogue

2.3.4.1 – Synthesis of $[\text{NMe}_4]_4\{\text{Co}_4(\text{cit})_4[\text{Co}(\text{H}_2\text{O})_5]_2\} \cdot 18\text{H}_2\text{O}$

$\text{CoSO}_4 \cdot 7\text{H}_2\text{O}$ (2.030 g, 7.2 mmol) and citric acid monohydrate (1.518 g, 7.2 mmol) were combined in solution in 10 ml H_2O . $\text{NMe}_4\text{OH} \cdot 5\text{H}_2\text{O}$ (~4.93 g) was added until pH 7.50 was obtained. 15 ml of stock solution was diluted with 15 ml H_2O and 0.355 g Rb_2SO_4 added. 1.0 ml aliquots were mixed with 4.3-5.1 ml EtOH or layered with 5.0 ml EtOH. Large, chunky hedgehog crystals formed in good yield, selected IR data (cm^{-1}): 3229 (m), 1550 (s), 1486 (m), 1378 (s), 1287 (w), 1239 (m), 1091 (m), 1054 (w), 951 (m), 922 (w). Analysis, calculated (found) for $\text{C}_{40}\text{H}_{120}\text{Co}_6\text{N}_4\text{O}_{56}$: C, 25.19 (25.16); H, 6.34 (6.08); N, 2.94 (2.96).

The rubidium analogue of the superhedgehog synthesis proved to be an exceptional case. The product crystallisation required several weeks longer than others in the series, and the hedgehogs formed were noticeably different to the naked eye. Figure 2-45 illustrates how the hedgehog formations consist of much larger rectangular rods rather than the much finer needle-like rods seen earlier for $\text{Na}\{\text{Co}_6\}$ in Figure 2-19. Also visible are some colourless salt crystals, however due to the large size and robust nature of the hedgehogs the separation of the two was not difficult.

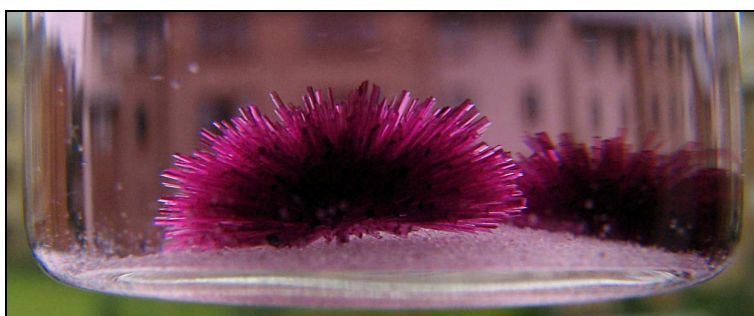


Figure 2-45 – Photograph of the hedgehog crystals obtained from the rubidium synthesis, seen in a 16 mm vial.

Microanalysis revealed that the product crystals were not the expected $\text{Rb}\{\text{Co}_6\}$ and were in fact the Co_6 cluster with charge balance provided only by tetramethylammonium counterions, with the formula $[\text{NMe}_4]_4\{\text{Co}_4(\text{cit})_4[\text{Co}(\text{H}_2\text{O})_5]_2\} \cdot 18\text{H}_2\text{O}$. This result was initially surprising, and it

was thought that the absence of rubidium in the product must have been the result of a subtle solubility effect in the crystallisation solution. To investigate this possibility, further experiments were carried out using the original literature synthesis of $\text{NMe}_4\{\text{Co}_6\}$ at pH 7 [2], which was modified to include additional Rb_2SO_4 for crystallisation. As mentioned in the introduction to Section 2.3, such experiments had previously shown major problems with salt impurities and very low hedgehog yields. To reduce the salt impurities, bulk addition of EtOH was used to rapidly precipitate the salt, which was then removed by filtration. The filtrate was divided into aliquots in sealed vials for crystallisation. It was found that the yield of hedgehogs was improved, although the formations were still very small and delicate. This approach was therefore not an improvement over the original reported synthesis of $\text{NMe}_4\{\text{Co}_6\}$ [2] which gave hedgehogs of a similar size.

Modified literature $\text{NMe}_4\{\text{Co}_6\}$ synthesis

$\text{CoSO}_4 \cdot 7\text{H}_2\text{O}$ (2.031 g, 7.2 mmol) and citric acid monohydrate (1.519 g, 7.2 mmol) were combined in solution in 10 ml H_2O . $\text{NMe}_4\text{OH} \cdot 5\text{H}_2\text{O}$ (~4.67 g) was added until pH 7.05 was obtained. 15 ml of this stock solution was diluted with 15 ml H_2O and 1.411 g $\text{Rb}_2\text{SO}_4 \cdot 7\text{H}_2\text{O}$ added. The solution was mixed with 120 ml EtOH to precipitate excess salt that was separated by filtration and the filtrate divided into 5 ml aliquots in sealed vials. Small pink hedgehogs formed, selected IR data (cm^{-1}): 3210 (m), 1550 (s), 1486 (m), 1378 (s), 1287 (w), 1239 (m), 1091 (m), 1058 (w), 950 (m), 920 (w).

2.3.4.2 – Structure of $[\text{NMe}_4]_4[\text{Co}_4(\text{cit})_4[\text{Co}(\text{H}_2\text{O})_5]_2] \cdot 18\text{H}_2\text{O}$

From the initial indexing of the unit cell by single crystal X-ray diffraction it became apparent that the structure was considerably different to those seen in the rest of the series. The unit cell dimensions included a long axis which presented a problem due to the proximity of the diffraction spots to one another on the detector image. The diffraction was also very weak for lab based equipment, and so the full dataset was collected using a synchrotron source. Even so, the diffraction remained weak and to low angle. It was discovered that the rod crystal from the hedgehog used for the diffraction study was single, and did not suffer the twinning problems found for the $\text{Na}\{\text{Co}_6\}$ family, which is interesting given the large size of the crystal and the overall

similarity of the joined crystal formations. The unit cell dimensions for $\text{NMe}_4\{\text{Co}_6\}$ are $a = 23.0160(17)$, $b = 24.4060(18)$, $c = 57.227(4)$ Å with a volume of 32146 Å³ and so it is much larger compared to $\text{Na}\{\text{Co}_6\}$ with $a = 23.093(3)$, $b = 14.3843(18)$, $c = 21.691(3)$ Å and a volume of 7205 Å³.

In this case there are no alkali metal ions located close to the clusters as they have been replaced with much bulkier tetramethylammonium ions and so a new packing arrangement is required. Figure 2-46 illustrates how the clusters are arranged in square formations of chains in $\text{NMe}_4\{\text{Co}_6\}$ as opposed to the parallelogram formations seen for $\text{Na}\{\text{Co}_6\}$ in Figure 2-22. This has interesting consequences for the hydrogen-bonding between clusters, which now only occurs within the layers of clusters in the a b plane which are separated from each other by the counterions, as shown in Figure 2-47. Within the layers the clusters adopt a similar ‘herring bone’ pattern to that seen for $\text{Na}\{\text{Co}_6\}$ (Figure 2-48 compared to Figure 2-21). The $\text{NMe}_4\{\text{Co}_6\}$ cubane $\text{Co}-\hat{\text{O}}-\text{Co}$ bridging angles are in the range 94.40 - 100.44° with $\text{Co}-\text{O}$ bond lengths of 2.022 - 2.153 Å, which are broader ranges than those of $\text{Na}\{\text{Co}_6\}$ which has $\text{Co}-\hat{\text{O}}-\text{Co}$ bridging angles of 96.46 - 100.33° and $\text{Co}-\text{O}$ bond lengths of 2.070 - 2.142 Å.

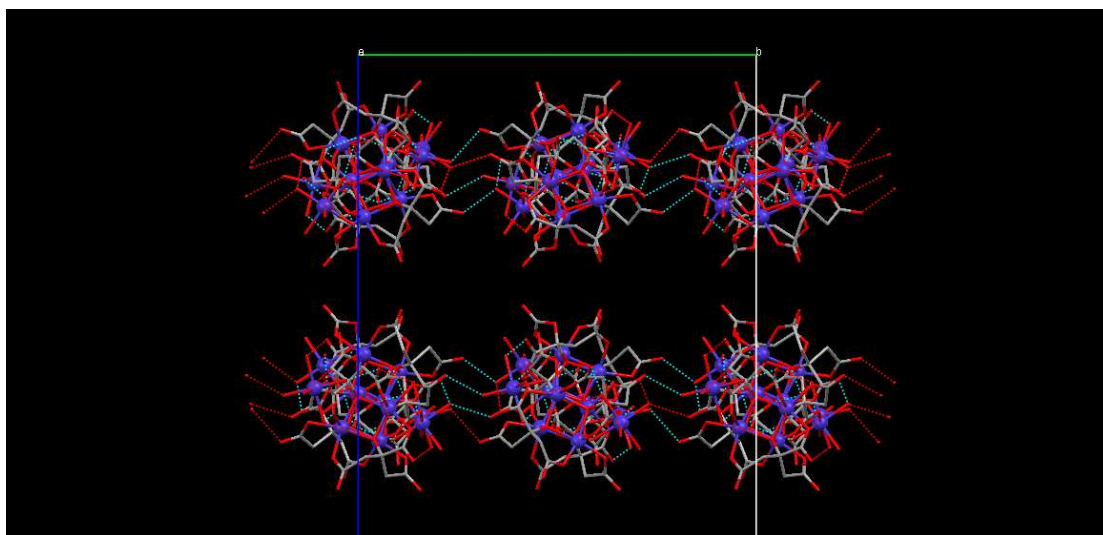


Figure 2-46 – $\text{NMe}_4\{\text{Co}_6\}$ crystal packing and hydrogen bonding viewed along the a axis, highlighting the square arrangement of the cluster chains (Co blue, O red, C grey, N pale blue. Hydrogen, NMe_4^+ and lattice water omitted for clarity).

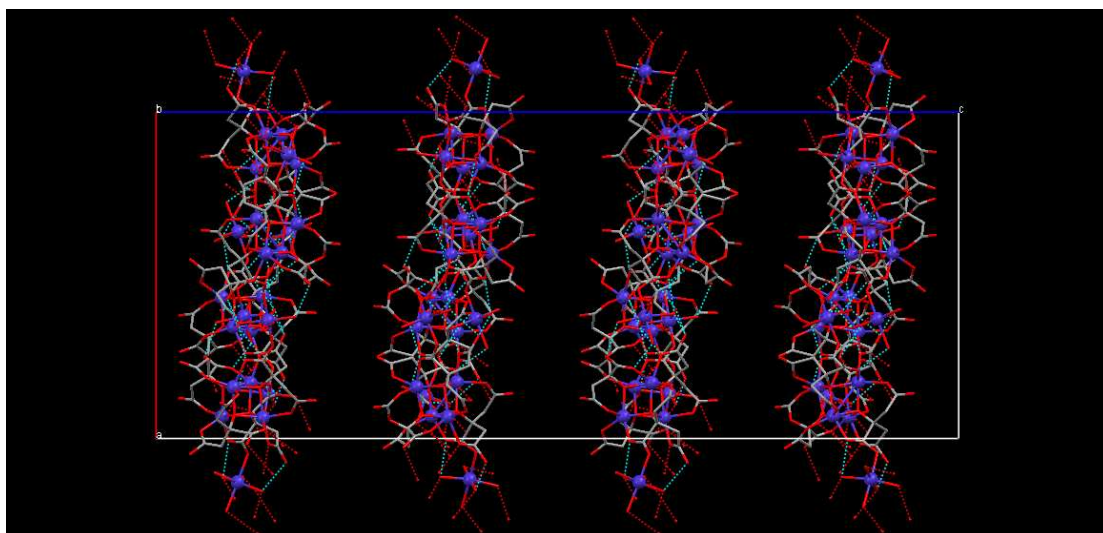


Figure 2-47 – $\text{NMe}_4\{\text{Co}_6\}$ crystal packing and hydrogen bonding viewed along the b axis, showing the hydrogen bonded layers and the long unit cell b length (Co blue, O red, C grey. Hydrogen, NMe_4^+ and lattice water omitted for clarity).

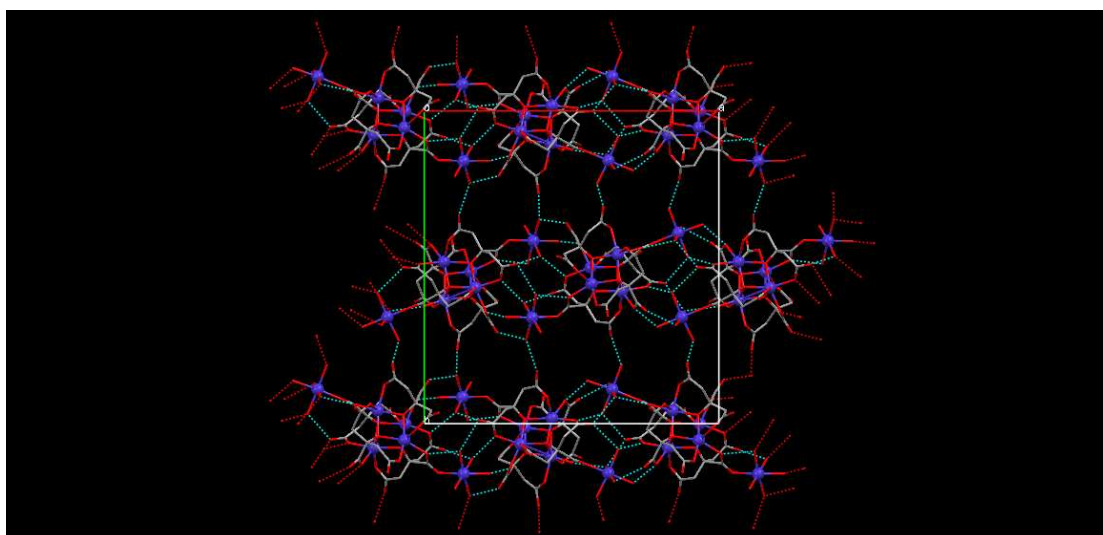


Figure 2-48 – $\text{NMe}_4\{\text{Co}_6\}$ crystal packing and hydrogen bonding viewed along the c axis, showing 'herring bone' cluster packing (Co blue, O red, C grey. Hydrogen, NMe_4^+ and lattice water omitted for clarity).

This is the first time that the crystal structure of $\text{NMe}_4\{\text{Co}_6\}$ has been determined as although a synthesis was previously reported [2], the crystals obtained were multiple twinned and of very small size and so were unsuitable for diffraction studies. It is interesting to compare $\text{Na}\{\text{Co}_6\}$ with $\text{NMe}_4\{\text{Co}_6\}$ since the intermolecular interactions in the form of hydrogen bonds has been reduced from a three dimensional bonding network in $\text{Na}\{\text{Co}_6\}$ to two dimensional planes in $\text{NMe}_4\{\text{Co}_6\}$.

2.3.4.3 – Hydration Dependent Magnetic Properties of $\text{NMe}_4\{\text{Co}_6\}$

The temperature dependence of χT for hydrated and dehydrated samples of $\text{NMe}_4\{\text{Co}_6\}$ is shown in Figure 2-49. At 290 K the value of χT is $19.0 \text{ cm}^3\text{mol}^{-1}\text{K}$ when hydrated and $17.5 \text{ cm}^3\text{mol}^{-1}\text{K}$ when dehydrated, which is consistent with six noninteracting Co(II) centres with $S_i = 3/2$ and average g values of 2.60 and 2.49 respectively. The value of χT for both curves remains reasonably constant on cooling from 300 to 150 K followed by a gradual decrease. Below this temperature the hydrated curve shows a gradual decline to shallow local minimum of $17.2 \text{ cm}^3\text{mol}^{-1}\text{K}$ at 240 K, followed by an increase (indicative of ferromagnetic interactions) to a maximum peak value of $17.6 \text{ cm}^3\text{mol}^{-1}\text{K}$ at 8.9 K before falling away sharply to final value of $13.7 \text{ cm}^3\text{mol}^{-1}\text{K}$ at 1.8 K. Meanwhile the dehydrated curve changes from an initial gradual decline to much more rapid decrease below 50 K which continues to a local minimum of $12.1 \text{ cm}^3\text{mol}^{-1}\text{K}$ at 5.9 K before increasing in a small, sharp peak to $12.5 \text{ cm}^3\text{mol}^{-1}\text{K}$ at 2.9 K, before falling rapidly to $11.0 \text{ cm}^3\text{mol}^{-1}\text{K}$ at 1.8 K.

Comparing the hydration dependence of the χT curves of $\text{NMe}_4\{\text{Co}_6\}$ and $\text{Na}\{\text{Co}_6\}$ (Figures 2-49 and 2-35) it can be seen that both compounds display very similar profiles. The constant regions from 300 to 150 K are followed by decreases with a broad peak feature around 8.9 K when hydrated, or a small peak around 2.9 K when dehydrated, although these features are considerably more pronounced in the $\text{NMe}_4\{\text{Co}_6\}$ data.

As can be seen from Figure 2-50, the magnetisation curve of $\text{NMe}_4\{\text{Co}_6\}$ displays the reduction in magnitude on dehydration that is typical of the Co_6 family. Neither curves are saturated in a 5 T field and have values of $M/N\beta = 11.5$ when fresh and $M/N\beta = 8.27$ after dehydration. When comparing the difference between the hydrated and dehydrated magnetisation values at 5 T, it is found that $\text{NMe}_4\{\text{Co}_6\}$ shows a smaller reduction (3.22), compared to $\text{Na}\{\text{Co}_6\}$ (3.58).

The out-of-phase component of the ac susceptibility for $\text{NMe}_4\{\text{Co}_6\}$ changes from the onset of a signal seen when hydrated in Figure 2-51 to the well formed, distinct χ'' peaks of Figure 2-52 when dehydrated. The peaks in this case are far sharper than the broad peaks found for $\text{Na}\{\text{Co}_6\}$. It is also noteworthy that both Figure 2-51 and 2-52 have the same scale and so the χ'' signals are not reducing in size upon dehydration as had previously been seen for $\text{Na}\{\text{Co}_6\}$ (Figure 2-31). These observations are consistent with the hypothesis of a second overlapping χ'' signal at low temperature due to intermolecular interactions, since these should be reduced in $\text{NMe}_4\{\text{Co}_6\}$ due to the packing arrangement as two dimensional planes of hydrogen bonded clusters rather than the three dimensional hydrogen bonding network found in $\text{Na}\{\text{Co}_6\}$. An Arrhenius analysis of the peak positions for 28-1267 Hz gives an energy barrier to the reorientation of the magnetisation of $\Delta E/k_B = 31$ K with $\tau_0 = 2.8 \times 10^{-9}$ s. This value is close to the previously reported value of $\Delta E/k_B = 32$ K with $\tau_0 = 2.1 \times 10^{-9}$ s for $[\text{NMe}_4]_4\{\text{Co}_4(\text{cit})_4[\text{Co}(\text{H}_2\text{O})_5]_2\} \cdot 6\text{H}_2\text{O}$ [2], and is also close to the $\text{Na}\{\text{Co}_6\}$ value after 3 hours in vacuum with $\Delta E/k_B = 31$ K with $\tau_0 = 4.1 \times 10^{-9}$ s.

The similarities in the behaviour of $\text{Na}\{\text{Co}_6\}$ and $\text{NMe}_4\{\text{Co}_6\}$ are very interesting considering the different packing of the clusters. Since both reside in ‘herring bone’ patterns, the consistent curve shapes observed are perhaps to be expected. The reduction of the intermolecular interactions via hydrogen bonds in $\text{NMe}_4\{\text{Co}_6\}$ due to the layered structure could possibly explain the more prominent ferromagnetic peak features. Future work could investigate this further using single crystal magnetisation versus field hysteresis loops measured on a microSQUID, for comparison with the ‘leaning’ $\text{Na}\{\text{Co}_6\}$ loops of Figure 2-27. The reduced hydrogen bonding may also facilitate the egress of water from the crystals, giving larger and sharper ac peaks in a smaller vacuum time for $\text{NMe}_4\{\text{Co}_6\}$ compared with $\text{Na}\{\text{Co}_6\}$, even though it has more lattice water when hydrated (18 and 11 respectively). Probably the most interesting feature is the coincident values for the energy barrier, which could indicate a similar dehydrated species is formed in each case, even though the overall packing is different. The proposal of linking the clusters into chains of random length is still feasible within the layers of $\text{NMe}_4\{\text{Co}_6\}$ structure, and indeed may be easier to accomplish with fewer nearest neighbours to impede reorganisation.

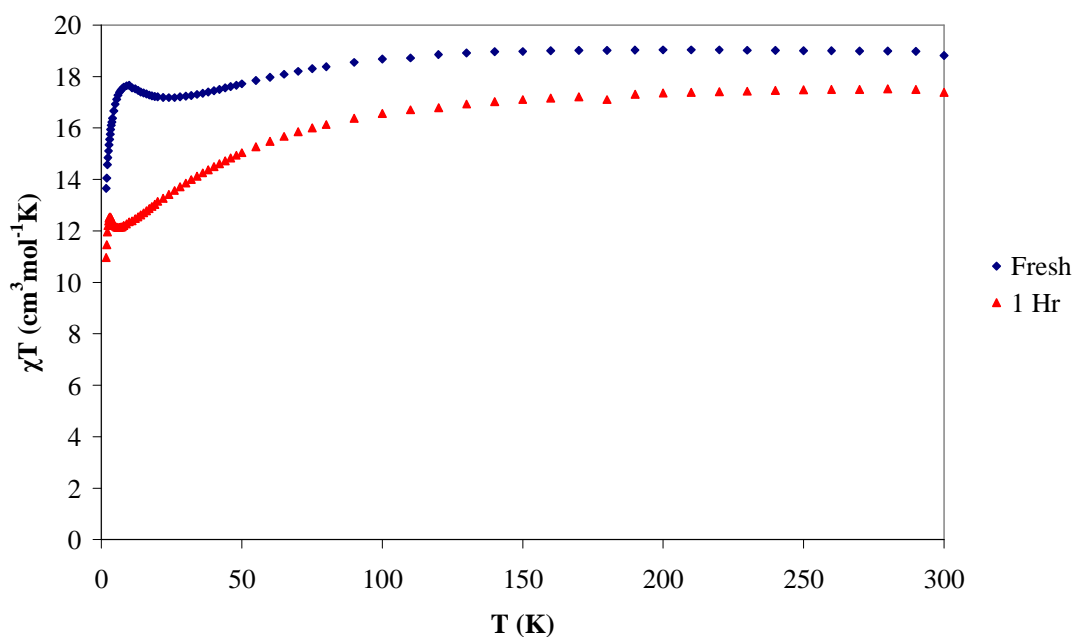


Figure 2-49 – Hydration dependence of the χT curve of $\text{NMe}_4\{\text{Co}_6\}$ measured in a 1000 Oe field. A comparison of the fresh hydrated sample (blue diamonds) with the dehydrated sample measured after 1 hour (red triangles) in vacuum.

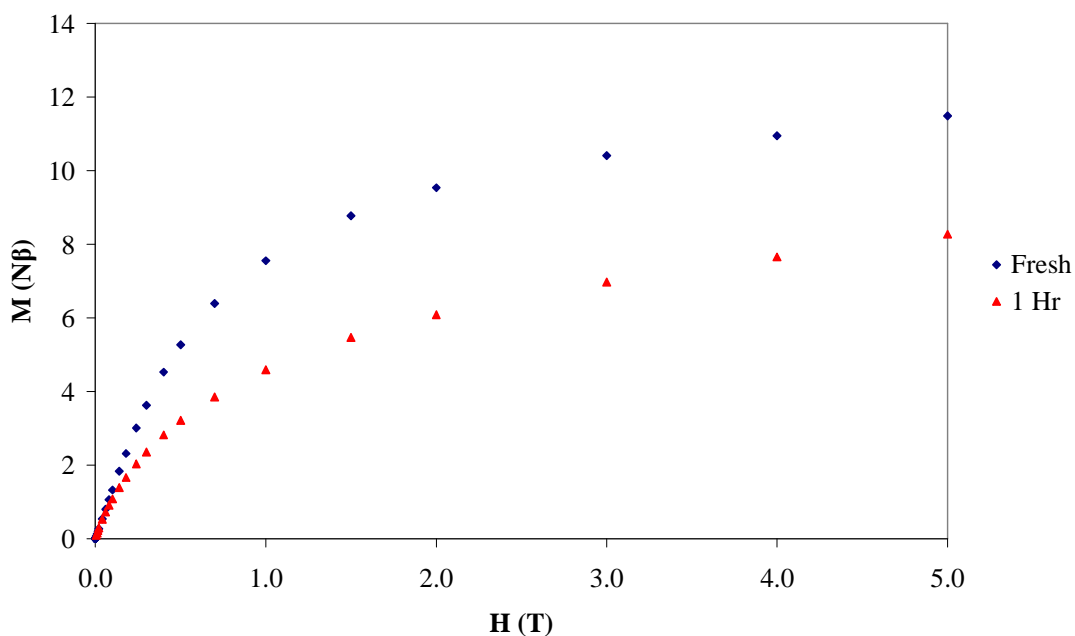


Figure 2-50 – Hydration dependence of the magnetisation curve of $\text{NMe}_4\{\text{Co}_6\}$. A comparison of the fresh hydrated sample (blue diamonds) with the dehydrated sample measured after 1 hour (red triangles) in vacuum.

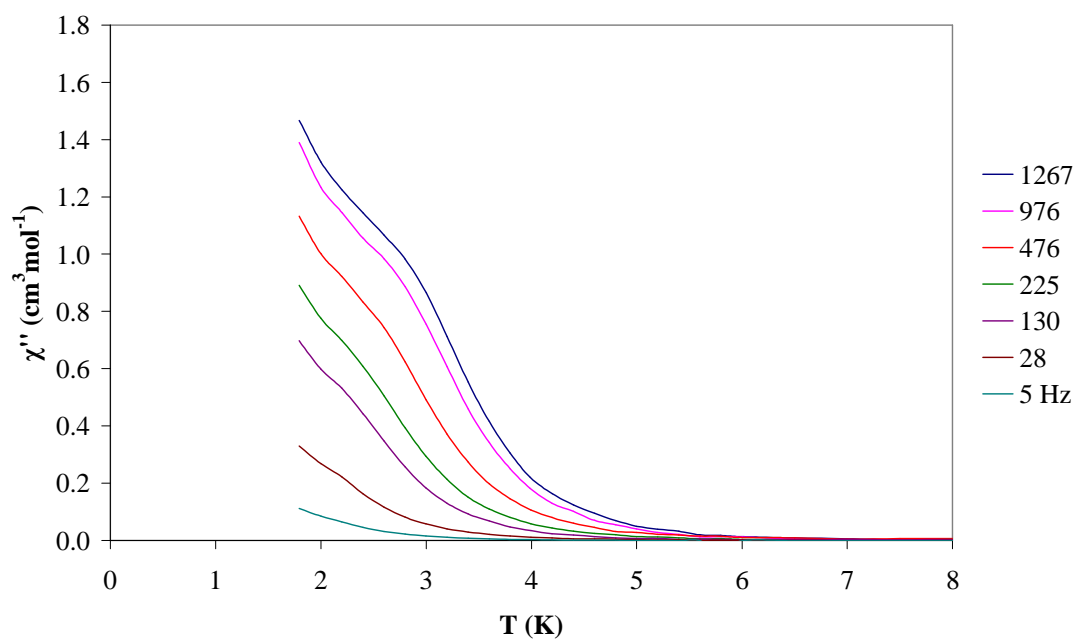


Figure 2-51 – The out-of-phase component of the ac susceptibility for the fresh hydrated sample of $\text{NMe}_4\{\text{Co}_6\}$.

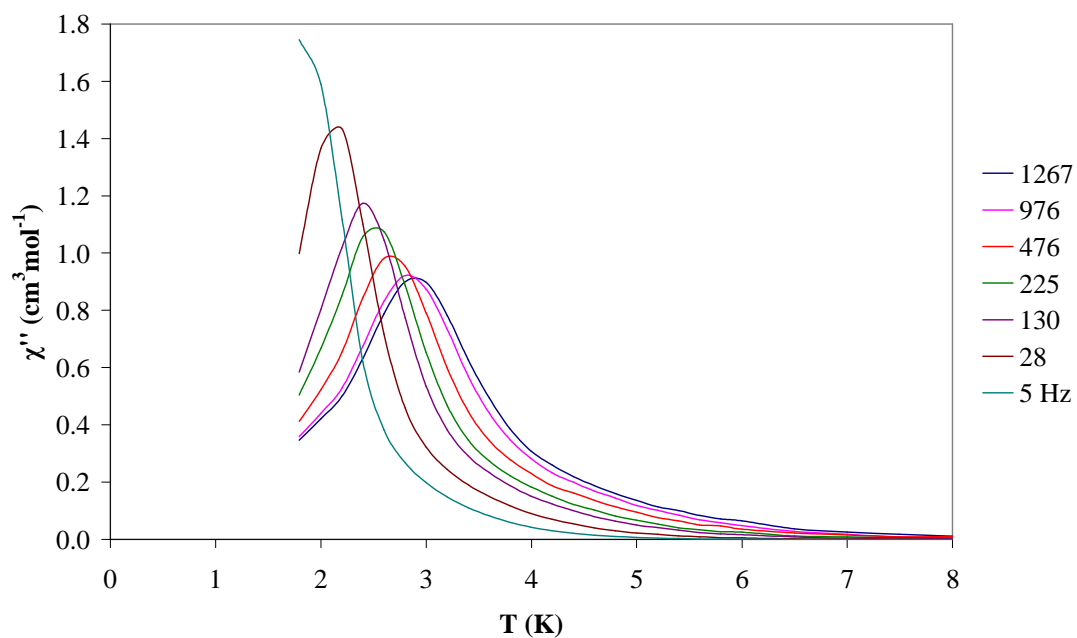


Figure 2-52 – The out-of-phase component of the ac susceptibility for the dehydrated sample of $\text{NMe}_4\{\text{Co}_6\}$ measured after 1 hour in vacuum.

2.4 – The 3D Network $\{\text{Na}_4\text{Co}_4(\text{cit})_4[\text{Co}(\text{H}_2\text{O})_3]_2(\text{H}_2\text{O})_{15}\} \cdot 3\text{H}_2\text{O}$

We have a particular interest in cobalt citrate chemistry, which often features the cobalt(II) citrate cubane $\{\text{Co}_4(\text{cit})_4\}^{8-}$ as a structural unit, and has itself been shown to be a single molecule magnet as $[\text{C}(\text{NH}_2)_3]_8\{\text{Co}_4(\text{cit})_4\} \cdot 4\text{H}_2\text{O}$ (Section 2.1) [7]. The large number of carboxylate oxygen atoms around the outside of this cubane provide coordination sites that make it an ideal candidate for linking into networks. Previously in Section 2.2 the Co_6 SMM was discussed, which consists of the cobalt(II) citrate cubane with two peripheral octahedral cobalt(II) centres $[\text{NMe}_4]_3\text{Na}\{\text{Co}_4(\text{cit})_4[\text{Co}(\text{H}_2\text{O})_5]_2\} \cdot 11\text{H}_2\text{O}$ [2]. Campo *et al.* have reported a 1D chain of cobalt(II) citrate cubanes with peripheral octahedral cobalt(II) centres $\{\text{Cs}_2[\text{Co}_7(\text{cit})_4(\text{H}_2\text{O})_{13.5}]\}_2 \cdot 15\text{H}_2\text{O}$ which can be transformed into a 2D network $[\text{Co}(\text{H}_2\text{O})_6]\{\text{Cs}_2[\text{Co}_{6.5}(\text{cit})_4(\text{H}_2\text{O})_9]\}_2 \cdot 3\text{H}_2\text{O}$ by crosslinking [10]. We now report a 3D structural network of cobalt(II) citrate cubanes linked by octahedral cobalt(II) centres $\{\text{Na}_4\text{Co}_4(\text{cit})_4[\text{Co}(\text{H}_2\text{O})_3]_2(\text{H}_2\text{O})_{15}\} \cdot 3\text{H}_2\text{O}$ thus completing this dimensional set of networks. We note that a 3D network based on cobalt(II) cubanes with citrate has been reported by Xiang *et al.* [11] $[\text{KCo}_3(\text{cit})(\text{Hcit})(\text{H}_2\text{O})_2] \cdot 8\text{H}_2\text{O}$, however the bonding between cubanes differs due to the tetrahedral coordination of the linking cobalt(II) centres. We would also stress that it is only since our recent report of the SMM behaviour of the discrete Co_4 citrate cubane [7] that the significance of this family of linked networks has become apparent, which adds further value to both existing magnetic characterisation and measurements yet to be reported (1D ribbon, 2D net). Lin *et al.* have reported a 3D net of cobalt(II) cubanes [12], $\text{Co}_4(\text{CH}_3\text{O})_4(\text{CH}_3\text{OH})_4(\text{dcn})_4$, however these do not include citrate ligands and the discrete cubane subunit has not been shown to function as a SMM.

2.4.1 – Synthesis of $\{\text{Na}_4\text{Co}_4(\text{cit})_4[\text{Co}(\text{H}_2\text{O})_3]_2(\text{H}_2\text{O})_{15}\} \cdot 3\text{H}_2\text{O}$

$\text{CoSO}_4 \cdot 7\text{H}_2\text{O}$ (2.031 g, 7.2 mmol) and citric acid monohydrate (1.519 g, 7.2 mmol) were combined in solution in 10 ml H_2O . $\text{NMe}_4\text{OH} \cdot 5\text{H}_2\text{O}$ (~4.80 g) was added until pH 7.50 was obtained. 15 ml of solution was diluted with 15 ml H_2O and 0.375 g Na_2SO_4 added. 1.0 ml aliquots were then mixed with 1.2-2.3 ml EtOH. After 7 months in a sealed vial, pink crystals were produced in very low yield. Selected IR data (cm^{-1}): 3226 (m), 1543 (s), 1382 (s), 1294 (w), 1241 (m), 1091 (m), 954 (w), 922 (m), 851 (m).

2.4.2 – Structure of $\{\text{Na}_4\text{Co}_4(\text{cit})_4[\text{Co}(\text{H}_2\text{O})_3]_2(\text{H}_2\text{O})_{15}\}.3\text{H}_2\text{O}$

The structure of the 3D network is shown in Figure 2-53. Coordination to the cubane for linking can occur on either the α -carboxylate or β -carboxylate oxygen sites of the citrate ligand. In this case, the linking octahedral cobalt(II) centres are coordinated only to the β -carboxylate sites. Two citrate ligands of the cubane have two linkers coordinated, and the other two citrates coordinate one linker each. Each linking centre connects to three carboxylates of neighboring cubanes in a T formation, with the other three sites filled by water molecules. From Figure 2-53 it can be seen that when viewed along the a and b axes the cubanes are arranged in crosslinked chains. The parallelogram shaped channels between the chains are filled by sodium counterions that are coordinated to cubane oxygens and water molecules. In the network, the cubane Co- $\hat{\text{O}}$ -Co angles are in the range 96.77 - 99.76° with Co-O bond lengths of 2.049 - 2.135 Å, which is similar to the discrete Co_4 cubane SMM which has Co- $\hat{\text{O}}$ -Co angles in the range 97.18 - 99.24° with Co-O bond lengths of 2.090 - 2.136 Å.

The variety of available coordination sites surrounding the cubane provides the flexibility for the synthesis of the different coordination networks. The discrete Co_6 SMM cluster has two peripheral octahedral cobalt(II) centres attached via α -carboxylates on opposite sides of the cubane. In the 1D and 2D networks [10] the peripheral centres are coordinated to both the α -carboxylate and β -carboxylate sites, while our 3D network features only β -carboxylate coordination. In the structures of the Co_6 cluster family and the 1D, 2D and 3D networks, the packing arrangements result in ‘bands’ of cubanes and peripheral/linker octahedral cobalt(II) centres that are separated by the counterions (see Figures 2-53, 2-21, 2-22, 2-46, 2-48). In the tetrahedral linker 3D network [11] each citrate of the cubane has two linkers coordinated only through the β -carboxylates, with a much more regimented rectangular packing arrangement of the cubanes that is dissimilar to the octahedrally linked cases.

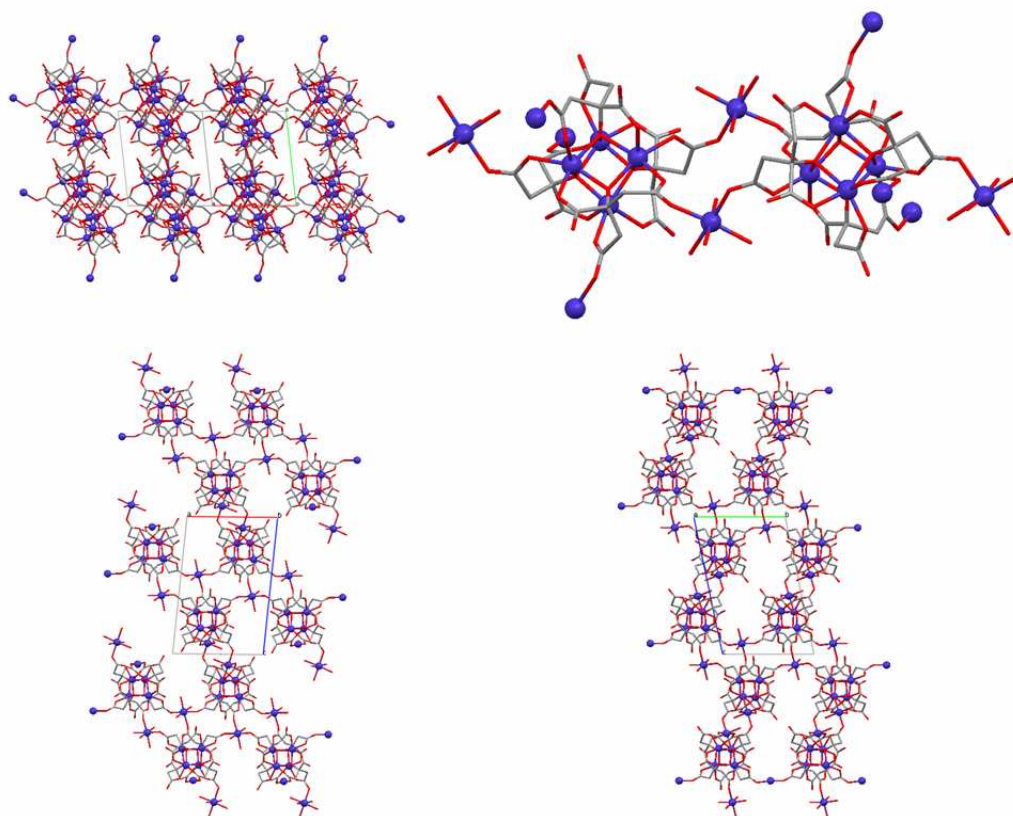


Figure 2-53 – 3D network structure, shown as an enlarged fragment (upper right), viewed along cubane chains (upper left) and seen along *b* (lower left) and *a* (lower right) crystallographic axes (Co blue, O red, C grey, H and Na⁺ counterions/water omitted for clarity).

2.4.3 – Magnetic Properties of the 3D Network

Figure 2-54 illustrates the dc magnetic susceptibility of the 3D network measured in a 1 kOe field. On cooling from 300 K χT shows a very gradual increase to a maximum of value of $19.7 \text{ cm}^3 \text{ mol}^{-1} \text{ K}$ at around 120 K, followed by a gradual decrease to a minimum of $18.4 \text{ cm}^3 \text{ mol}^{-1} \text{ K}$ at 20 K, then increases rapidly to $22.1 \text{ cm}^3 \text{ mol}^{-1} \text{ K}$ at 1.7 K. The increase below 20 K is indicative of ferromagnetic coupling. The high temperature behaviour is similar to the discrete Co_4 cubane which shows a gradual increase in χT on cooling, with a maximum at 80 K followed by a decrease, however at temperatures below 20 K the χT curve decreases, in contrast to the 3D network. Like Co_4 , the Co_6 cluster also displays a broad maximum and decrease at low temperature.

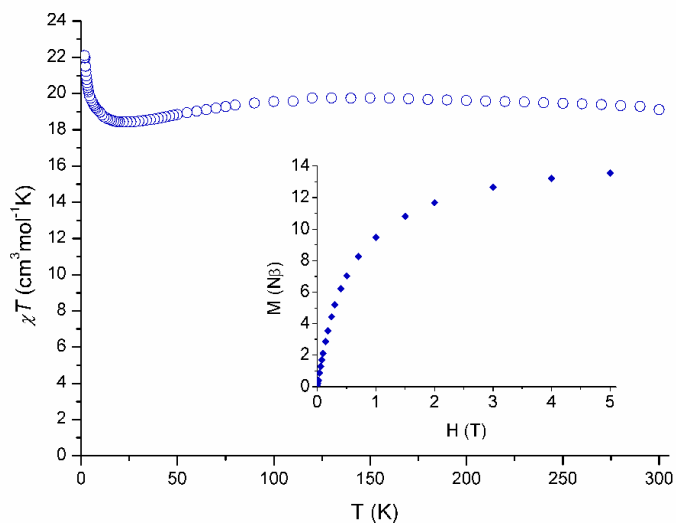


Figure 2-54 – Temperature dependence of χT for 3D network measured in a 1000 Oe field. Inset shows field dependence of the magnetisation at 2 K.

The field dependence of the magnetisation of the 3D network at 2 K reaches a value of $M/N\beta = 13.6$ at 5 T. No hysteresis was observed at 2 K. Further investigation was carried out using a single crystal measurement on a micro-SQUID, the results of which are shown in Figure 2-55. With a sweep rate of 2 mT/s hysteresis loops are seen below 0.6 K. These broaden on further cooling, with a step feature appearing at 0.1 K which is distinct at 0.04 K. In the case of a single molecule magnet with an Ising type (easy axis) anisotropy, increasing the sweep rate of the magnetisation should increase the width of the hysteresis loops. However, inspection of the sweep rate dependence of the 3D network reveals that on increasing the sweep rate the loops narrow, suggesting an easy plane magnetic anisotropy. The step feature in the loop also disappears at higher sweep rates. For comparison, the discrete Co_4 cubane SMM hysteresis loops collapse at zero field due to very fast quantum tunnelling of the magnetisation. The Co_6 SMM hysteresis loops do not show fast quantum tunnelling, but they are complicated by the presence of intermolecular interactions and display only small sweep rate dependence.

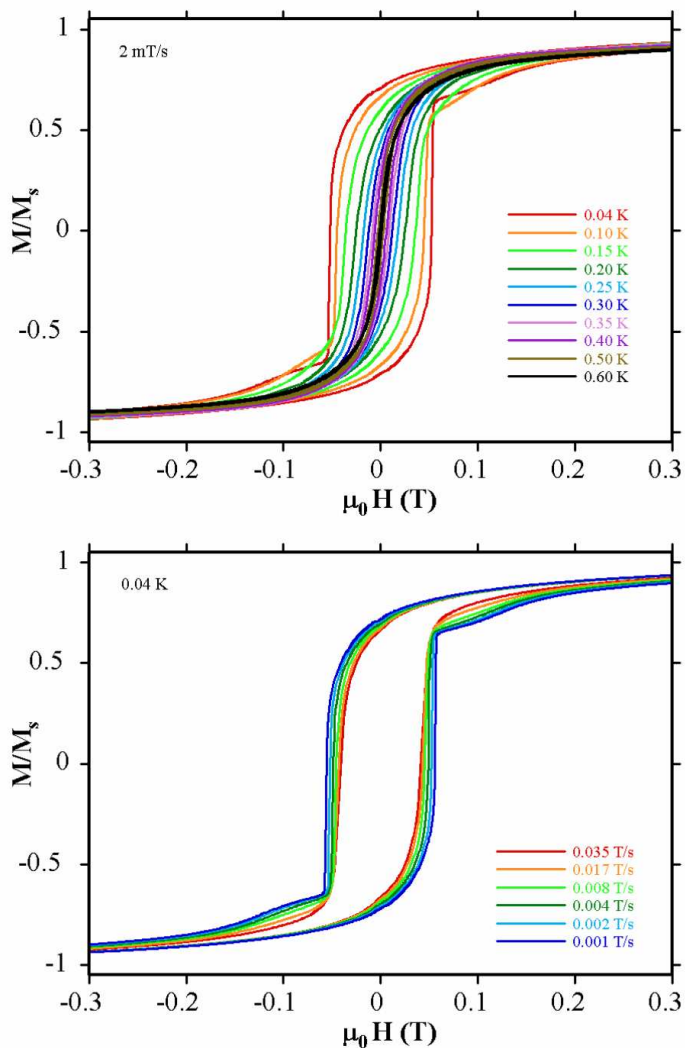


Figure 2-55 – Temperature (upper) and sweep rate (lower) dependence of single crystal magnetisation versus field hysteresis loops for the 3D network.

The ac susceptibility data of the 3D network is shown in Figure 2-56. The out-of-phase component in the range 130-1997 Hz shows the onset of a peak that is similar to the curve shape of χ'' seen for the hydrated Co_6 cluster (Figure 2-57). At higher frequencies in the range 2997-9997 Hz the network χ'' curves show an unusual crossover in the region of ~ 3 -4.5 K. The shape of the χ'' curve plateau at the crossover is reminiscent of the high frequency behaviour of the hydrated Co_6 cluster which displays a step-like plateau between 2.5 and 3.5 K. At frequencies above 2997 Hz the $\text{Co}_6 \chi''$ curve separation reduces and the step becomes more pronounced until 6997-9997 Hz where the curves are very close together. Crucially, the curves do not cross as the magnitude of χ'' increases with frequency unlike the behaviour observed for the 3D network. By contrast, the Co_4 SMM displays distinct peaks at all

frequencies between 130 and 9997 Hz (Figure 2-57). It is suggested that the crossover in the 3D network curves is caused by a second overlapping χ'' signal, in a similar manner to that discussed earlier for the Co_6 cluster (Sections 2.2.4 and 2.2.5). Similar effects to the hypothetical intermolecular interactions of the Co_6 case would be expected to be present in some form in the 3D network due to the similarity of the structural components.

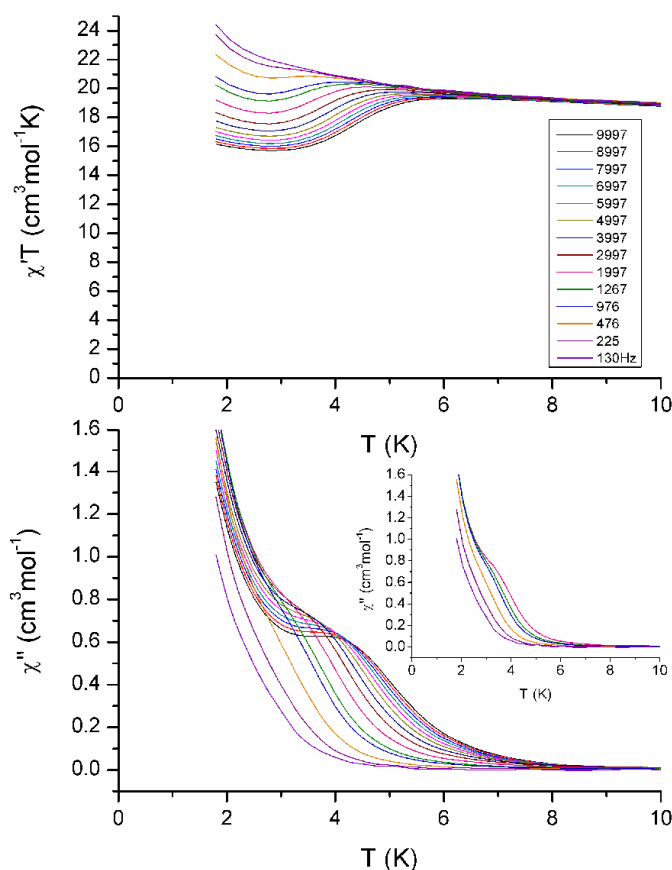


Figure 2-56 – The in-phase and out-of-phase components of the ac susceptibility shown as $\chi'T$ versus T (upper) and χ'' versus T (lower), with inset expansion of 130-1997 Hz.

A crossover of χ'' curves has been seen for the 2D Mn_4 network $[\text{Mn}_4(\text{hmp})_4\text{Br}_2(\text{OMe})_2(\text{dcn})_2] \cdot \frac{1}{2}\text{H}_2\text{O} \cdot 2\text{THF}$ reported by Miyasaka *et al.* [13] that displays complex magnetic behaviour between the limits of the SMM and classical regimes. However, for the manganese network all measured frequencies 50-1488 Hz underwent the crossover, unlike in this 3D cobalt network where it is observed only at higher frequencies. For the 2D Mn_4 network, a plot of the frequency dependence of

χ'' revealed peaks indicative of a changeover between two different relaxation pathways, however a similar analysis of the data for the 3D cobalt network did not give any analogous peaks.

Comparing this 3D network with octahedral linkers to that of Xiang *et al.* [11] with tetrahedral linkers it is found that the χT curves are similar as they both show no major slope between 300 and ~50 K and an increase below 20 K. However an interesting difference is that the net with octahedral linkers does not display the reported antiferromagnetic decrease between 43 and 20 K which is seen using tetrahedral linkers. The tetrahedral linker net is reported to display hysteresis loops at 2 K, however these appear to be extremely narrow.

In summary, the structure and magnetic properties of a novel three dimensional structural network based on single molecule magnet cobalt citrate cubane subunits has been determined. This completes a dimensional set of discrete cluster and 1D, 2D and 3D linked networks that are accessible due to the variety of coordination sites provided by the citrate ligand. The network displays ferromagnetic interactions at low temperature, and magnetisation versus field hysteresis loops that are temperature and sweep rate dependent consistent with an easy-plane magnetic anisotropy. This highlights the changeover from the single molecule magnet behavior of the discrete Co_4 cubane to long range ordering by linking these subunits into a 3D network. AC susceptibility measurements show an unusual crossover that may be the result of overlapping signals from several relaxation pathways. Future work will include specific heat capacity measurements to investigate magnetic ordering.

Section	Compound	ΔE (K)	τ_0 (s)	$M/N\beta$ at 5T
2.1.4	Co_4	24	3.4×10^{-8}	6.78
2.2.5	dehydrated $\text{Na}\{\text{Co}_6\}$	28	8.2×10^{-9}	8.75
2.3.3.3	dehydrated $\text{Cs}\{\text{Co}_6\}$	22	5.7×10^{-8}	8.45
2.3.4.3	dehydrated $\text{NMe}_4\{\text{Co}_6\}$	31	2.8×10^{-9}	8.27
2.4.3	3D network	-	-	13.6

Table 2-4 – Comparison of selected magnetic data for compounds based on Cobalt(II) citrate cubane units (data shown for 1 hour of vacuum dehydration).

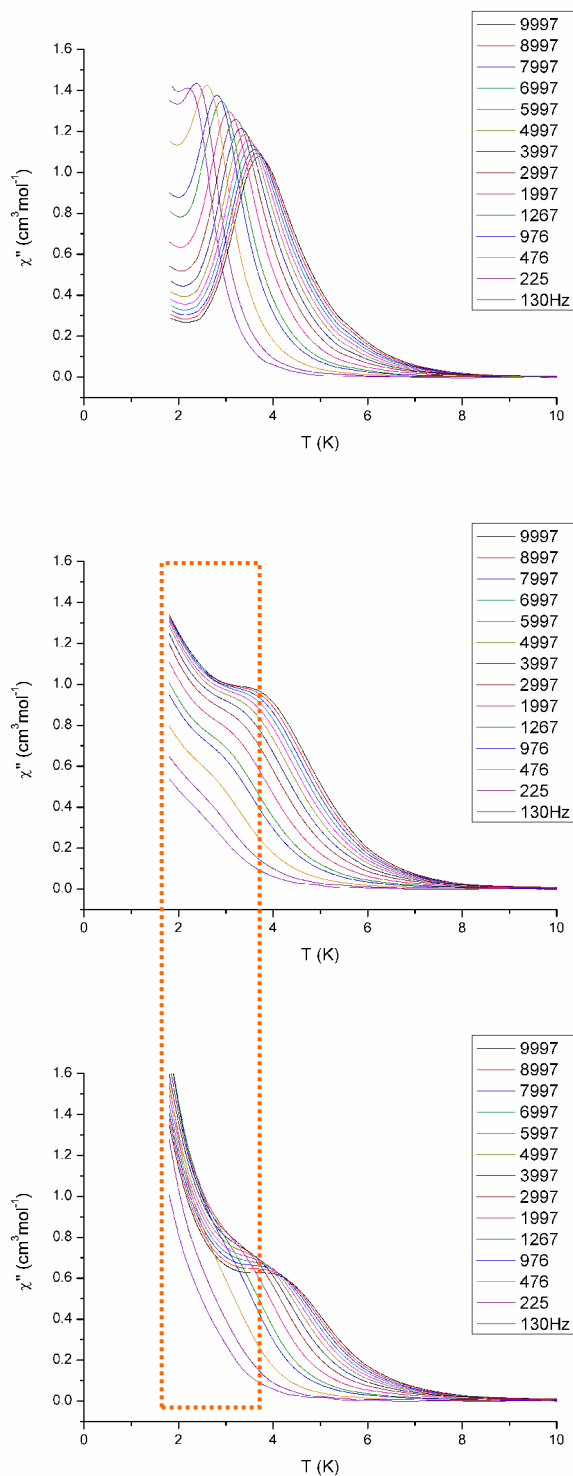


Figure 2-57 – Comparison of the out-of-phase component of the ac susceptibility shown as χ'' versus T for $[\text{C}(\text{NH}_2)_3]_8\{\text{Co}_4(\text{cit})_4\} \cdot 4\text{H}_2\text{O}$ (top), $[\text{NMe}_4]_3\text{Na}\{\text{Co}_4(\text{cit})_4[\text{Co}(\text{H}_2\text{O})_5]_2\} \cdot 11\text{H}_2\text{O}$ (middle) and $\{\text{Na}_4\text{Co}_4(\text{cit})_4[\text{Co}(\text{H}_2\text{O})_3]_2(\text{H}_2\text{O})_{15}\} \cdot 3\text{H}_2\text{O}$ (bottom) with the proposed region affected by a second overlapping χ'' signal highlighted.

- [1] Hudson, T. A.; Berry, K. J.; Moubaraki, B.; Murray, K. S.; Robson, R. *Inorg. Chem.* 2006, 45, 3549.
- [2] Murrie, M.; Teat, S. J.; Stöckli-Evans, H.; Gudel, H. U. *Angew. Chem. Int. Ed.* 2003, 42, 4653.
- [3] Galloway, K. W.; Parkin, A.; Harte, S. M.; Ferguson A.; Murrie, M. *Cryst. Eng. Comm.* 2006, 8, 346.
- [4] Lever, A. B. P. *Inorganic Electronic Spectroscopy 2nd Ed*, Elsevier, Amsterdam, 1984.
- [5] Novak, M. A.; Folly, W. S. D.; Sinnecker, J. P.; Soriano, S. *J. Mag. Mat.* 2005, 294, 133.
- [6] Mishra A.; Wernsdorfer, W.; Parsons, S.; Christou, G.; Brechin, E. K. *Chem. Commun.* 2005, 2086.
- [7] Galloway, K. W.; Whyte, A. M.; Wernsdorfer, W.; Sanchez-Benitez, J.; Kamenev, K. V.; Parkin, A.; Peacock, R. D.; Murrie, M. *Inorg. Chem.* 2008, 47, 7438.
- [8] Moubaraki, B.; Murray, K. S.; Hudson, T. A.; Robson, R. *Eur. J. Inorg. Chem.* 2008, 4525.
- [9] Boskovic, C.; Brechin, E. K.; Streib, W. E.; Folting, K.; Bollinger, J. C.; Hendrickson, D. N.; Christou, G. *J. Am. Chem. Soc.* 2002, 124, 3725.
- [10] Campo, J.; Falvello, L. R.; Mayoral, I.; Palacio, F.; Soler, T.; Tomás, M. *J. Am. Chem. Soc.* 2008, 130, 2932.
- [11] Xiang, S.; Wu, X.; Zhang, J.; Fu, R.; Hu, S.; Zhang, X. *J. Am. Chem. Soc.* 2005, 127, 16352.
- [12] Lin, Z.; Li, Z.; Zhang, H. *Crys. Growth Des.* 2007, 7, 589.
- [13] Miyasaka, H.; Nakata, K.; Lecren, L.; Coulon, C.; Nakazawa, Y.; Fujisaki, T.; Sugiura, K.; Yamashita, M.; Clérac, R. *J. Am. Chem. Soc.* 2006, 128, 3770.

3.0 – The Copper Guanidinium System

The study of the copper guanidinium system was initiated by a heterometallic experiment that was based on the Co₄ cluster synthesis.

Copper and cobalt heterometallic synthesis

To a solution of citric acid monohydrate (0.55 g, 2.6 mmol) in water (50 mL) was added a solution of Co(NO₃)₂·6H₂O (0.38 g, 1.3 mmol) and Cu(NO₃)₂·3H₂O (0.31 g, 1.3 mmol) in water (50 mL) followed by a solution of guanidinium carbonate (1.87 g, 10.4 mmol) in water (50 mL). The solution was stirred and then left to stand. After three hours pink prism crystals appeared (single crystal XRD confirms Co₄ cluster unit cell). These were collected by filtration and the remaining blue solution slowly evaporated, giving large numbers of blue crystals after one month.

This experiment highlights the remarkable ability of the guanidinium ion to template specific dominant products. In the space of hours the cobalt(II) was separated from the dark purple solution by crystallisation as the Co₄ cluster, leaving a blue solution that on slow evaporation gave crystals of a novel copper(II) dimer [C(NH₂)₃]₄{Cu₂(cit)₂}.H₂O (Section 3.1) after a month. Once again the hydrogen bonding ability of the guanidinium ion is an important factor, since the rapid removal of cobalt from the solution as the very stable and insoluble Co₄ crystals is responsible for the ease of separation of the two metal species. This straightforward metal separation is most dramatically illustrated by the colours of two types of product crystals as shown in Figure 3-1. The technique was also found to be robust, and was able to prove the presence of cobalt in a cobalt/copper mixed metal species prepared by Marta Martinez-Belmonte (Price Research Group). A sample was treated with acid to remove the bound oxalate ligand, followed by addition of citric acid and guanidinium carbonate, which produced small, pink, elongated prism crystals of Co₄ overnight.



Figure 3-1 – Photographs of the crystals of [C(NH₂)₃]₈{Co₄(cit)₄}.4H₂O (left) and [C(NH₂)₃]₄{Cu₂(cit)₂}.H₂O (right) from the heterometallic synthesis.

3.1 – Copper Citrate Dimer [C(NH₂)₃]₄{Cu₂(cit)₂}.H₂O

3.1.1 – Synthesis of [C(NH₂)₃]₄{Cu₂(cit)₂}.H₂O

To a solution of citric acid monohydrate (1.09 g, 5.2 mmol) in water (50 mL) was added a solution of Cu(NO₃)₂.3H₂O (1.26 g, 5.2 mmol) in water (50 mL) followed by a solution of guanidinium carbonate (3.75 g, 20.8 mmol) in water (50 mL). The solution was then left to stand uncovered. After 1 month of slow evaporation, a large yield of blue rectangular crystals formed, selected IR data (cm⁻¹): 3315 (m), 3140 (m), 3093 (m), 1676 (s), 1650 (s), 1603 (s), 1577 (s), 1546 (m), 1429 (m), 1371 (s), 1291 (w), 1245 (s), 1133 (m), 1069 (m), 950 (w), 920 (s), 842 (m), 742 (m). The crystals were collected by filtration and recrystallised by dissolving in minimal water and then slowly evaporating the solution. The powdered samples used for analysis were found to be slightly hygroscopic and analyse as the dihydrate, calculated (found) for C₁₆H₃₆Cu₂N₁₂O₁₆: C, 24.65 (21.54); H, 4.65 (4.63); N, 21.56 (21.32).

Somewhat unusually for a guanidinium product, the copper citrate dimer was found to be water soluble, thus allowing recrystallisation of the product in this case. This solubility also explains why the copper citrate dimer only crystallises on slow evaporation in the mixed metal separation where it was first discovered. The pure copper synthesis described above was used to generate samples for further analysis.

3.1.2 – Structure of [C(NH₂)₃]₄{Cu₂(cit)₂}.H₂O

The copper citrate dimer crystallises in the *Pbca* space group and consists of two copper centres bound by two citrate ligands as shown in Figure 3-2. The central alkoxide group of the citrate bridges the two copper centres, with further coordination by the β-carboxylate groups to impart a distorted square planar geometry, with a notable twist towards tetrahedral. The Cu-Ô-Cu bridging angles are 95.16° and the bridging Cu-O bond distances are 1.92 and 1.93 Å. An interesting feature of the structure is the alignment of each of the α-carboxylate groups towards one of the copper centres, with a long contact distance of 2.63 Å. This is considerably longer than the bridging bonds, though as will be discussed later, the long contact plays an important structural role.

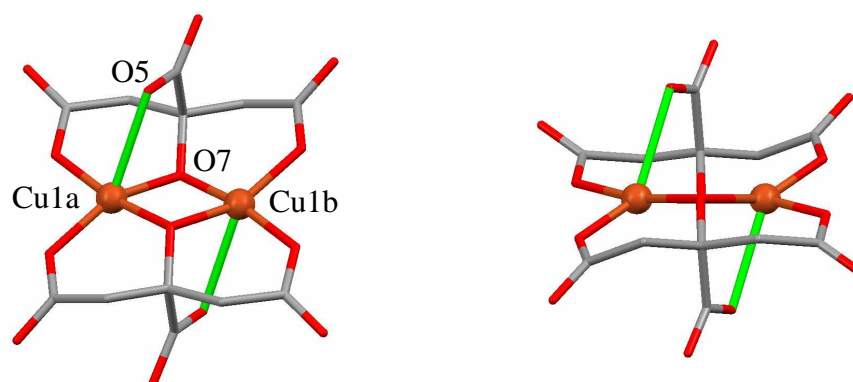


Figure 3-2 – Copper citrate dimer structure (left) and bridging plane view (right), (Cu orange, O red, C grey, H omitted, long contact highlighted in green).

The guanidinium counterions are arranged in columns through the copper citrate dimer crystal, as had previously been seen in the Co_4 cubane structure (compared in Figure 3-3), and are involved in hydrogen bonding with the citrate carboxylate oxygens. An examination of the crystal lattice (Figure 3-4) also reveals that the citrate alkoxide oxygen and α -carboxylate oxygen of the dimer units are hydrogen bonded via intermediate water molecules.

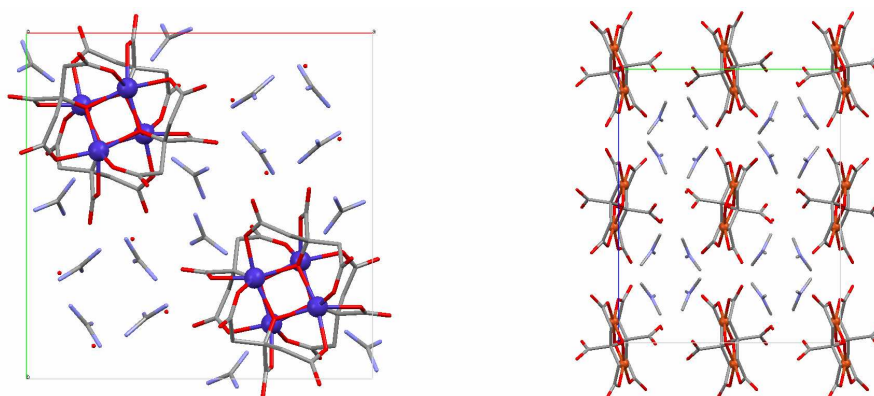


Figure 3-3 – Column arrangement of the guanidinium counterions in the Co_4 (left) and copper citrate dimer (right) crystal lattice, shown as unit cells viewed along the c and a axes respectively (Co blue, Cu orange, O red, C grey, N pale blue, H omitted).

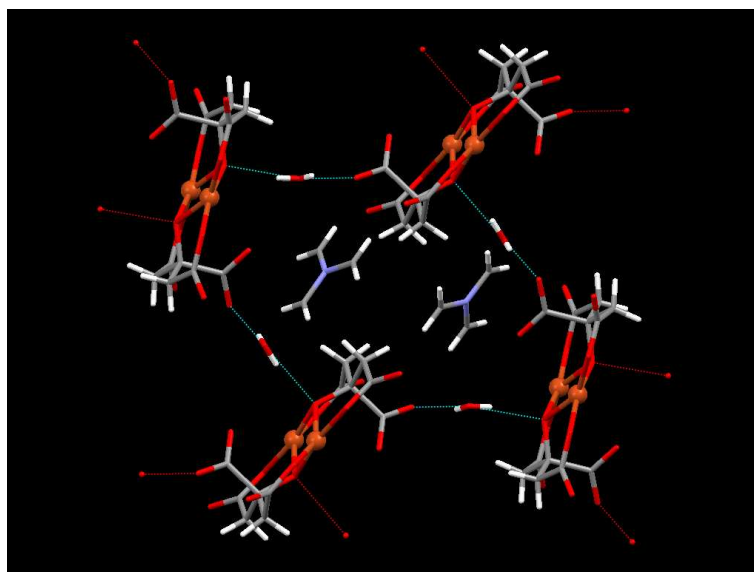


Figure 3-4 – Hydrogen bonding between copper citrate dimers via water (Cu orange, O red, C grey, N pale blue, H white, guanidinium hydrogen bonding omitted).

3.1.3 – Magnetic Properties of $[\text{C}(\text{NH}_2)_3]_4\{\text{Cu}_2(\text{cit})_2\} \cdot \text{H}_2\text{O}$

The dc magnetic properties of the copper citrate dimer are illustrated by Figures 3-5 and 3-6. Figure 3-5 shows the temperature dependence of χT measured in a 1000 Oe field. This gradually increases on cooling from 300 to ~50 K at which point the curve plateaus, reaching a maximum value of $1.16 \text{ cm}^3 \text{ mol}^{-1} \text{ K}$ before decreasing at temperatures below 10 K. The magnetisation curve shown in Figure 3-6 increases steadily between 0-1 T, followed by a gradual curve that obtains a final value of $M/N\beta = 2.12$ at 5 T.

The χT curve data was fitted using CAMMAG, using a one J model ($\hat{H} = -2JS_1S_2$) for the coupling between the two $S_i = 1/2$ centres. The best fit was obtained using the parameters $g = 2.16$ and $J = +86.5 \text{ K}$ and this reproduces the curve reasonably well over the temperature range 300-10 K, as shown in Figure 3-5. The increase of χT on cooling is indicative of ferromagnetic coupling between the two copper centres of the dimer, and the maximum in χT and the magnetisation curve are consistent with a $S = 1$ ground state.

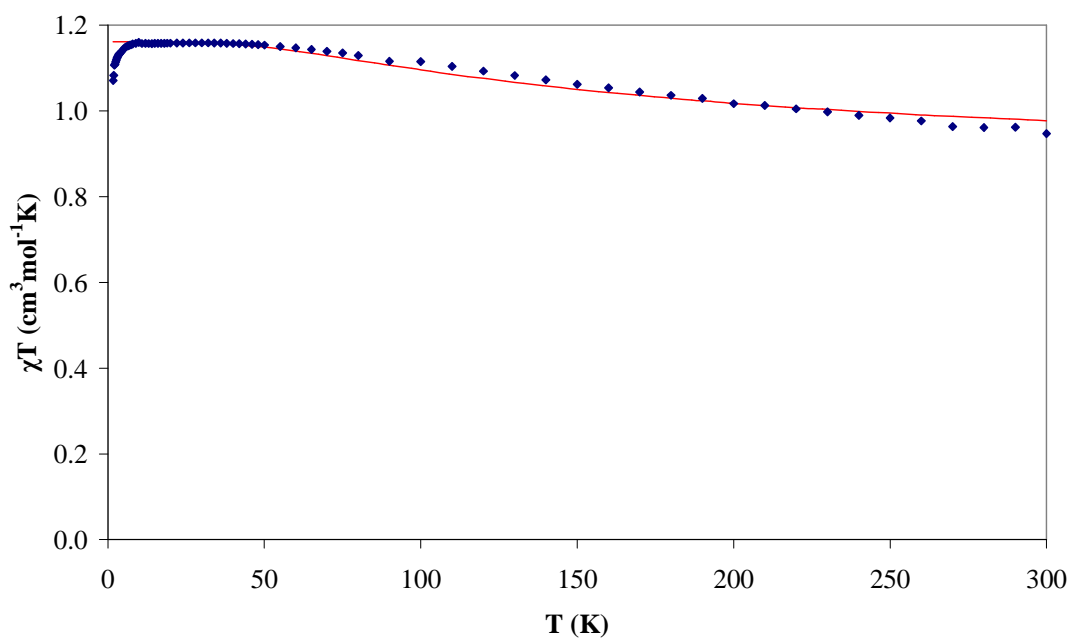


Figure 3-5 – Temperature dependence of χT for $[\text{C}(\text{NH}_2)_3]_4\{\text{Cu}_2(\text{cit})_2\} \cdot \text{H}_2\text{O}$ measured in a 1000 Oe Field, with the curve fit shown as a red line ($J = +86.5$ K, $g = 2.16$).

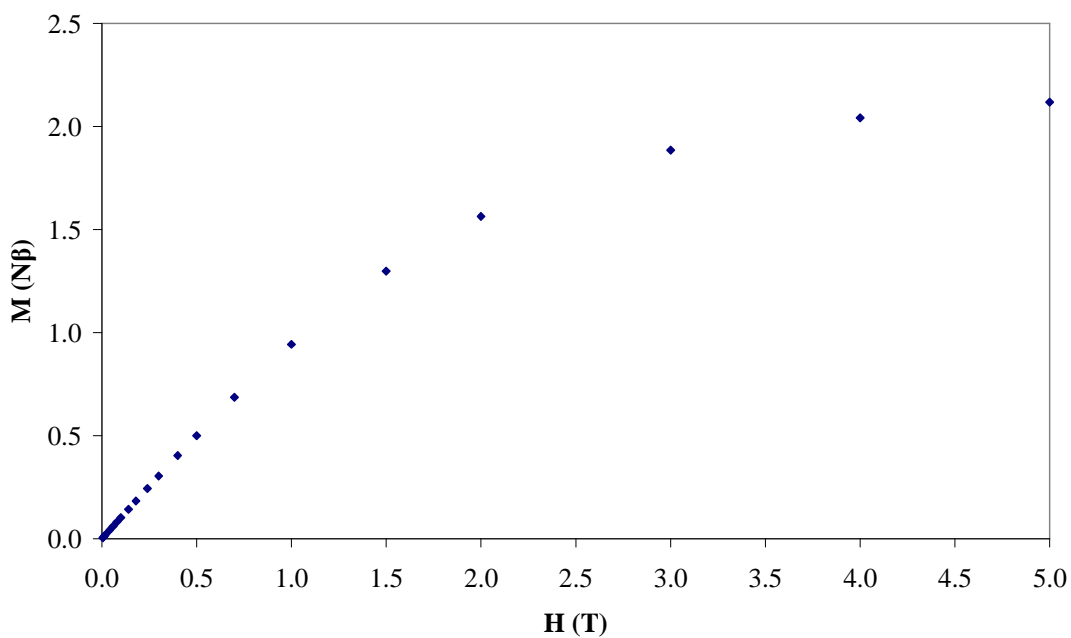


Figure 3-6 – Field dependence of the magnetisation at 2 K for $[\text{C}(\text{NH}_2)_3]_4\{\text{Cu}_2(\text{cit})_2\} \cdot \text{H}_2\text{O}$.

The ferromagnetic interaction determined by the magnetic measurements is in agreement with structural considerations, as the bridging angles of 95.16° are below the ferromagnetic to antiferromagnetic changeover at 97.6° seen in previous studies of planar hydroxo-bridged dimers (Section 1.2) [2,3]. There is a linear relationship between the value of $2J$ and the bridging angle for hydroxide bridged dimers [2] and a linear relationship is also observed for alkoxide bridges, with an offset in the changeover angle to a smaller value of 95.8° [3,4]. The bridging angle of the copper citrate dimer is therefore smaller than both of these critical angles.

However, care must be taken with comparisons to existing experimental magnetostructural research, since by their very nature these studies focus on families of compounds with closely related structures. Although the behavioural trends may indeed be consistent over many families of compounds, such as the relation between bridging angle and $2J$, the studies cannot easily determine the effect of a component part of a distortion on the overall magnetic character of the full compound structure. Combination of different studies also presents the problem of chemical differences between the product families, which may have complications such as intermolecular interactions or other unidentified effects.

Instead it may be useful to consider computational studies of the systems where the effect of a variety of distortion types can be investigated on the same structure system. Relevant publications to the research in this chapter include a report by Hu *et al.* which considered the effect of structural and chemical parameters on magnetic coupling in hydroxo-bridged copper(II) dimers [5]. Studies by Ruiz *et al.* modelled both hydroxide and alkoxide bridges, compared the results obtained by the various computational methods available against real experimental values [6] and also considered the effect of coordination by counterions [7]. These papers used Density Functional Theory (DFT) with a broken symmetry approach to investigate the effects of the copper environment, non-bridging ligands and Cu_2O_2 core geometry distortions including asymmetric bridging. The general conclusions of these papers are relevant for the distortions observed in the novel copper(II) dimers throughout this chapter.

The modelling studies [5,6,7] suggest that the coordination environment of the copper centre is important and that a distortion from square planar towards a tetrahedral geometry (as found in the copper citrate dimer) reduces the antiferromagnetic contribution. Increasing the electronegativity of the non-bridging groups was found to enhance ferromagnetic coupling, and in this dimer the copper centres are bound by the electronegative oxygen atoms of the citrate ligand.

The geometry of the bridging oxygen group was discovered to have a great effect on the magnetic coupling, with an out-of-plane displacement of the bridging group biased towards ferromagnetic interactions. The discovery of this important contribution to the magnetic properties highlights the utility of computational methods, since previous experimental studies [2] could not determine this effect, particularly due to the uncertainty in the position of the hydrogen of the bridging ligand obtained using X-ray diffraction. The hydrogen position can also be affected by interactions with counterions [6]. Inspection of the copper citrate dimer reveals that the α -carboxylate long contact pulls the attached alkoxide groups away from the bridging plane (Figure 3-2) and so this is likely to increase the ferromagnetic character.

Unsurprisingly the DFT studies found that a small Cu-O-Cu angle is the most important factor to favour ferromagnetic coupling (see Section 1.2). Again, the copper citrate dimer has a small bridging angle due to the α -carboxylate long contact pulling the attached alkoxide groups further apart. The magnetostructural features of the copper citrate dimer are therefore consistent with both the experimental results [2,4] and theoretical modelling studies [5,6,7].

3.1.4 – Copper Citrate Dimer High Pressure Structural Study

A high pressure single crystal X-ray diffraction study of the copper citrate dimer crystals was carried out. Table 3-1 illustrates the reduction in the unit cell volume as the pressure is increased. In this case the unit cell *c* length elongates on increasing pressure while the *a* and *b* lengths contract.

Pressure (kbar)	Unit cell dimensions (Å)			Volume (Å ³)
	a	b	c	
Ambient	11.716(7)	14.713(9)	17.93(1)	3092(3)
3	11.5200(4)	14.4315(7)	18.012(3)	2994.5(5)
11	11.2728(8)	13.868(1)	18.219(4)	2848.2(6)
22	11.1332(5)	13.4098(7)	18.367(2)	2742.1(4)

Table 3-1 – Effect of pressure on the unit cell dimensions of $[\text{C}(\text{NH}_2)_3]_4\{\text{Cu}_2(\text{cit})_2\} \cdot \text{H}_2\text{O}$.

Table 3-2 shows the effects of the applied pressure on the bridging structure and the long contact distance. This reveals that the long contact distance between the α -carboxylate and the copper(II) centre decreases considerably on application of pressure, with a reduction of 0.22 Å at 22 kbar compared to ambient conditions. It is interesting to note that the citrate α -carboxylate groups of the stacked dimers are arranged approximately aligned with the crystallographic *b* axis (horizontal green axis in Figure 3-3), which is seen to undergo the largest reduction in Table 3-1. On increasing the applied pressure, the Cu- $\hat{\text{O}}$ -Cu bridging angles are reduced, with a change of 1.2° over the 0-22 kbar range. The Cu1a-O7 bond distance is seen to elongate with increased pressure (Figure 3-7). This is the bridging bond that forms a coordination ‘loop’ between the citrate ligand and the copper centre Cu1a via the long contact (Figure 3-2). The Cu1b-O7 distance varies but does not display an overall trend. These features can be explained by the α -carboxylate bending over to shorten the long contact, which pulls the connected alkoxide group further out from the Cu-Cu plane, lengthening the bridging bond Cu1a-O7 and producing a more acute bridging angle.

Pressure (kbar)	Cu- \hat{O} -Cu Angles (°) Cu1a- \hat{O} 7-Cu1b	Cu-O Bond Lengths (Å)		α -CO ₂ ⁻ Long Contact Cu1a-O5
		Cu1a-O7	Cu1b-O7	
Ambient	95.16(9)	1.934(2)	1.924(2)	2.628(3)
3	95.0(2)	1.938(4)	1.919(4)	2.567(4)
11	94.4(1)	1.942(3)	1.922(3)	2.470(3)
22	94.0(1)	1.956(3)	1.917(3)	2.407(4)

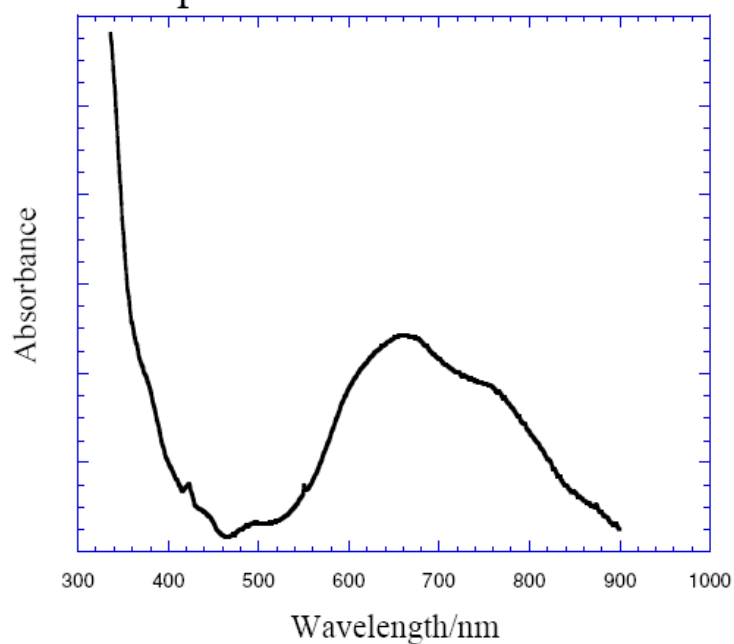
Table 3-2 – Effect of pressure on the Cu- \hat{O} -Cu bridging structure and the α -carboxylate long contact of [C(NH₂)₃]₄{Cu₂(cit)₂}.H₂O.

Since the Cu- \hat{O} -Cu bridging angles become more acute under pressure, it would be expected that the dimer exchange interactions would become more ferromagnetic in character. Future work that would be of interest includes a magnetism study under high pressure to observe changes in magnetic behaviour as a result of altering the bridging angles and bond lengths. Unfortunately this study was not possible within this research timeframe.

3.1.5 – Copper Citrate Dimer High Pressure Electronic Spectroscopy

A colour change of blue to green was also observed at high pressure, which may be the result of the changing coordination environment of copper centres due to the decreasing long contact distance. To investigate further, electronic spectra were measured at ambient conditions and at high pressure, as shown in Figure 3-7. A preliminary analysis of the results suggests that electronic spectra differ due to a change in the coordination number, as the spectrum appears to change from two allowed transitions in the pseudo-tetrahedral (D_{2d}) 4-coordinate unit to (mainly) a single allowed transition in the 5-coordinate unit (C_{4v}) (i.e. in D_{2d} symmetry the $E \rightarrow B_2$ and $A_1 \rightarrow B_2$ transitions are allowed, and in C_{4v} only the $E \rightarrow B_1$ transition is allowed). It was found that on increasing the pressure, the maximum in the peak at 640 nm is shifted to 670 nm and then an abrupt change takes place to a high energy phase that could involve a coordination change. At room temperature the main effects in the electronic spectra could be explained in terms of monomer copper units, suggesting that the crystal-field interaction is more important than the copper exchange coupling in the 0-64 kbar range. There is a band at around 320 nm (probably a charge transfer band) that moves to higher energies upon increasing the pressure. The visible colour change is due to the reduction of the absorption in the 550-700 nm region at high pressure. (See also Section 3.2.3)

Ambient pressure in the DAC



P = 54 kbar

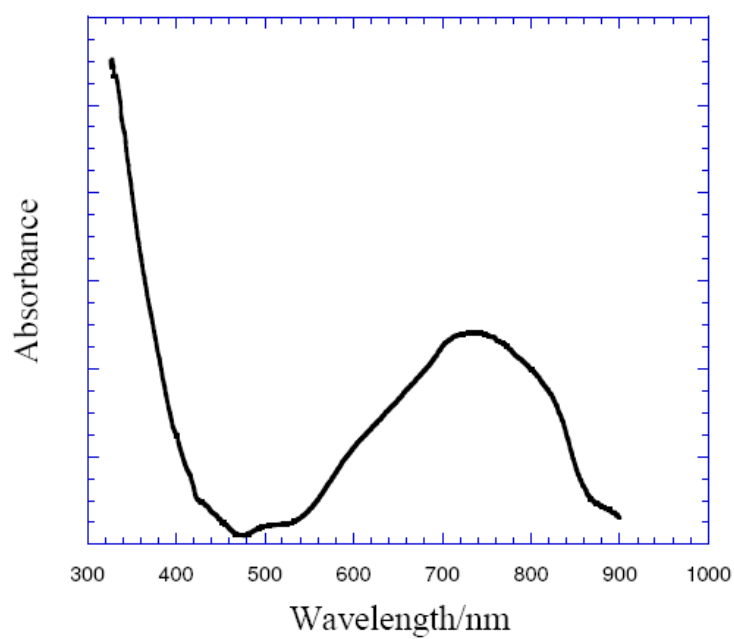


Figure 3-7 – The electronic spectra of $[\text{C}(\text{NH}_2)_3]_4\{\text{Cu}_2(\text{cit})_2\} \cdot \text{H}_2\text{O}$ measured in a diamond anvil cell (DAC) at ambient pressure (upper) and at 54 kbar (lower). (See also Figure 3-13 in Section 3.2.3)

3.2 – Hydroxy Bridged Dimer [C(NH₂)₃]{Cu₂cit[C(NH₂)₂NH]₂(OH)}

Based on the interesting copper citrate dimer structure already seen in the copper citrate guanidinium system, it was considered of interest to investigate higher reaction pH values. This was achieved by the use of additional NaOH, which is a stronger base than carbonate and also provides the opportunity to incorporate bridges.

3.2.1 – Synthesis of [C(NH₂)₃]{Cu₂cit[C(NH₂)₂NH]₂(OH)}

Original synthesis

To a solution of citric acid monohydrate (0.55 g, 2.6 mmol) in water (25 ml) was added a solution of Cu(NO₃).3H₂O (0.63 g, 2.6 mmol) in water (25 ml) followed by a solution of guanidinium carbonate (1.87 g, 10.4 mmol) in water (25 ml). To the resulting blue solution was added NaOH (0.52 g, 13 mmol) and a darkening of the colour of the solution was observed (pH = 13.74). The solution was then left to stand uncovered. Dark blue crystals appeared within one hour and a very large yield formed overnight. Selected IR data (cm⁻¹): 3350 (m), 3189 (m), 1630 (s), 1558 (s), 1425 (s), 1402 (s), 1251 (m), 1076 (m), 909 (m), 643 (s). Analysis, calculated (found) for C₉H₂₁Cu₂N₉O₈: C, 21.18 (21.29); H, 4.15 (4.15); N, 24.70 (27.74).

The formation of the hydroxy bridged dimer was characterised by a sudden darkening of the solution to a deep royal blue. Although the synthesis above was the first to produce the novel dimer, for experimental reasons that will be discussed later, a carbonate free synthesis was also developed.

Carbonate free synthesis

To a solution of citric acid monohydrate (0.55 g, 2.6 mmol) in water (25 ml) was added a solution of Cu(NO₃).3H₂O (0.63 g, 2.6 mmol) in water (25 ml) followed by a solution of guanidinium nitrate (1.27 g, 10.4 mmol) in water (25 ml). To the resulting blue solution was added NaOH (~0.56 g). The product formed extremely rapidly from solution and so to obtain the highest quality crystals the NaOH was added very gradually until the solution colour change point had just been reached. This effectively reduced the amount of product formed and the lower concentration gave a slower overnight crystallisation that produced a large yield of well formed crystals. The identity of the product was confirmed by single crystal X-ray diffraction.

3.2.2 – Structure of $[C(NH_2)_3]\{Cu_2cit[C(NH_2)_2NH]_2(OH)\}$

The novel dimer $[C(NH_2)_3]\{Cu_2cit[C(NH_2)_2NH]_2(OH)\}$ crystallises in the *Pnma* space group and has the structure illustrated in Figure 3-8. In this case, a hydroxide bridge and two terminal guanidine ligands have replaced one of the citrate ligands of the copper citrate dimer discussed in the previous Section 3.1.2.

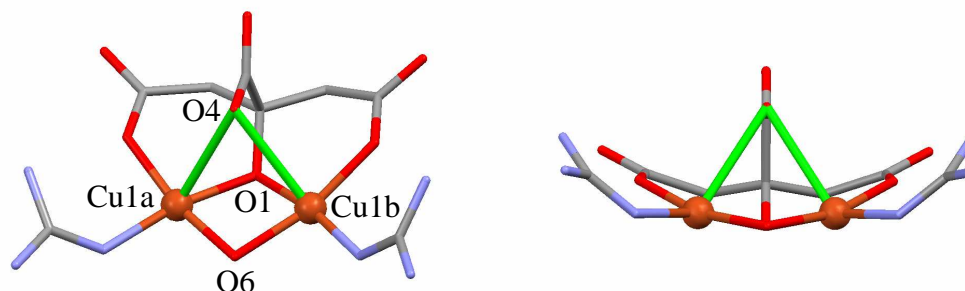


Figure 3-8 – Hydroxy bridged copper dimer structure (left) and bridging view (right), (Cu orange, O red, C grey, H omitted, long contact highlighted in green).

A search of version 5.29 of the Cambridge Structural Database reveals this to be the first structure with guanidine directly bound to a transition metal ion (however guanidine derivatives bonded to transition metal ions are known). It is also interesting to note that both the protonated (guanidinium counterion) and neutral (guanidine ligand) forms are present in the same product, with the guanidinium counterion (Figures 3-9) bisected by the vertical mirror plane of the dimer (Figure 3-10). Considering the pK_a of guanidine is 13.71, and the reaction solution pH is 13.74, the Henderson-Hasselbalch equation ($pH = pK_a + \log_{10}\{[Base]/[Acid]\}$) reveals that the two forms are present in solution in approximately equal concentrations as $[Base]/[Acid] = 1.07$.

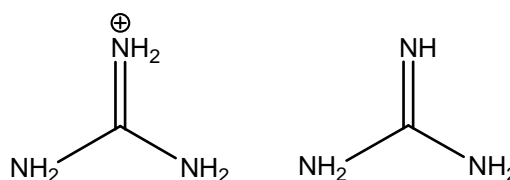


Figure 3-9 – Structure diagrams of guanidinium (left) and guanidine (right).

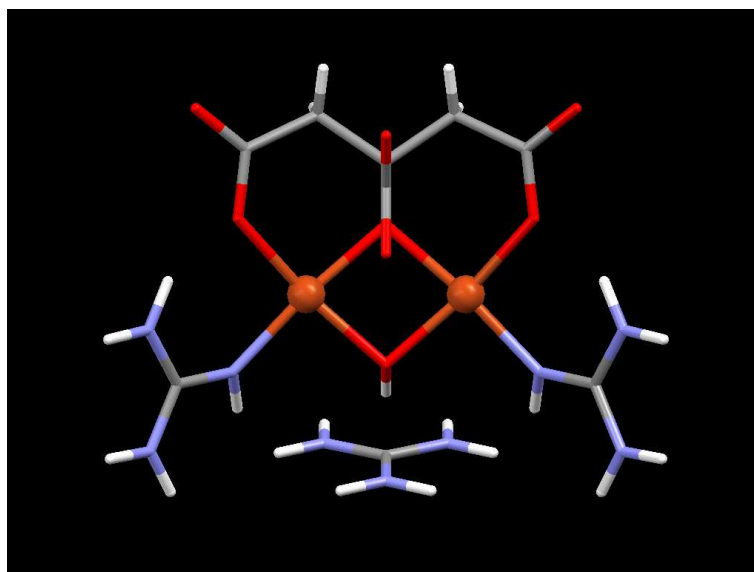


Figure 3-10 – Hydroxy bridged copper dimer structure, illustrating location of the guanidinium counterion on the vertical mirror plane of the dimer (Cu orange, O red, C grey, N pale blue, H white).

In comparison to the copper citrate dimer of Section 3.1, the hydroxy bridged copper dimer has larger bridging angles with $\text{Cu}-\hat{\text{O}}(\text{citrate})-\text{Cu} = 95.65^\circ$, $\text{Cu}-\hat{\text{O}}(\text{H})-\text{Cu} = 96.77^\circ$, and the Cu-O bond distances are longer at 1.95 (Cu-O citrate) and 1.94 (Cu-OH) Å. The removal of the second citrate gives an overall curved structure and bridging as seen in Figure 3-8, and the α -carboxylate now has a long contact to both coppers centres with a distance of 2.74 Å. This curved structure gives a very interesting crystal packing, where the dimers and counterions adopt a tubular arrangement within the crystal as shown in Figure 3-11. This is a result of the hydrogen bonding between the dimers, where the hydrogen atoms of the NH_2 groups of the guanidine ligands hydrogen bond in pairs with the α -carboxylate oxygen pair of citrate, while the β -carboxylate oxygen bonds with the NH_2 group hydrogen atoms of the guanidinium counterion, as highlighted in Figure 3-12. Hydrogen bonds also occur between the tubular chains via the hydroxide bridge hydrogen atoms and the α -carboxylate oxygens, and between the hydrogen atoms of guanidine ligands and the citrate β -carboxylate oxygens. A consequence of the extensive hydrogen bonding network is that the product crystallises very rapidly, giving large crystals that are insoluble once formed.

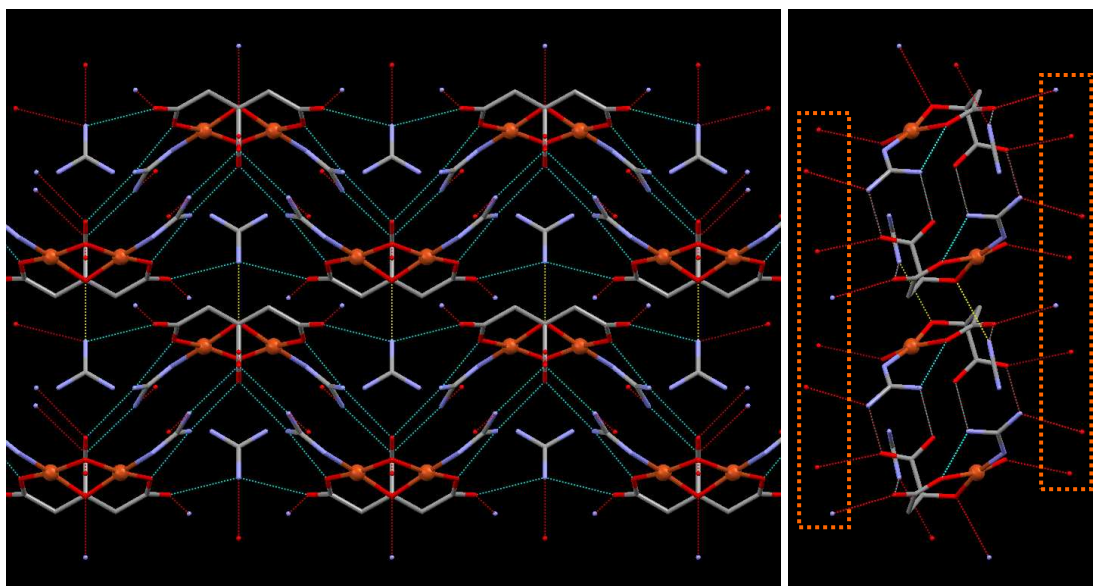


Figure 3-11 – Hydrogen bonding within dimer chains (blue) and short contact region between chains (yellow), shown in front and end elevation. Highlighted boxes indicate the hydrogen bonds between neighbouring tubular chains (Cu orange, O red, C grey, N pale blue, H omitted for clarity).

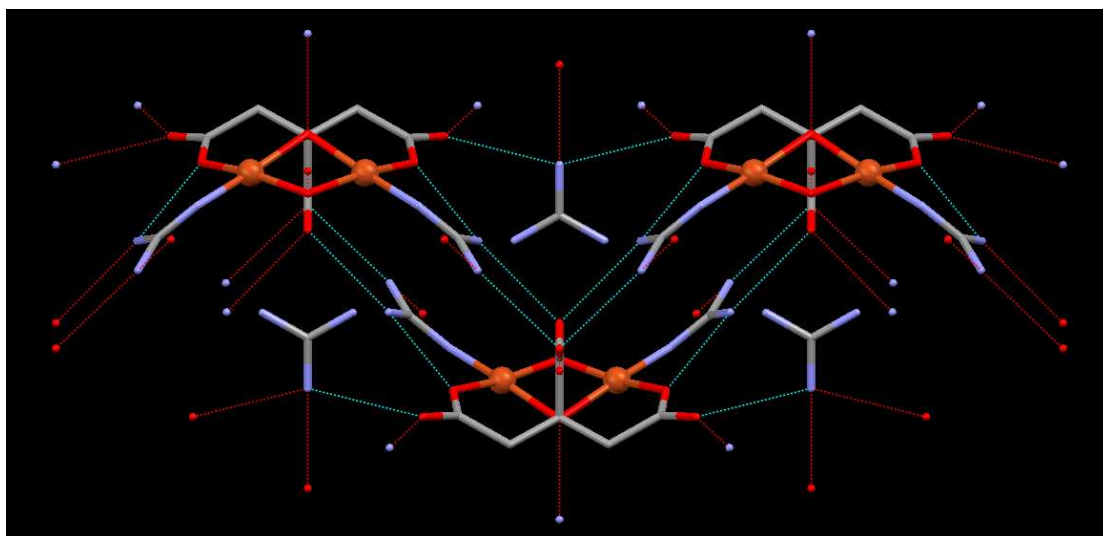


Figure 3-12 – Detail of hydrogen bonding between dimers via guanidine and guanidinium (Cu orange, O red, C grey, N pale blue, H omitted for clarity).

3.2.3 – Comparison of Citrate Based Dimer Electronic Spectra

The dark blue colour indicative of the changeover from $[\text{C}(\text{NH}_2)_3]_4\{\text{Cu}_2(\text{cit})_2\} \cdot \text{H}_2\text{O}$ to the nitrogen coordination of $[\text{C}(\text{NH}_2)_3]\{\text{Cu}_2\text{cit}[\text{C}(\text{NH}_2)_2\text{NH}]_2(\text{OH})\}$ was investigated by measurement of the electronic spectra. A comparison of the solid state spectra of the two dimers is shown in Figure 3-13. The product crystals were dispersed in a KBr disc and spectra collected at room temperature and also with Displex cooling to ~ 20 K. The room temperature spectra show indistinct overlapping peaks, but the cooled spectra reveal three peak features as would be expected for distorted square planar d^9 copper centres. The peak positions for $[\text{C}(\text{NH}_2)_3]_4\{\text{Cu}_2(\text{cit})_2\} \cdot \text{H}_2\text{O}$ are approximately 621, 672 and 740 nm, compared to 568, 604 and 716 nm for $[\text{C}(\text{NH}_2)_3]\{\text{Cu}_2\text{cit}[\text{C}(\text{NH}_2)_2\text{NH}]_2(\text{OH})\}$. The peak positions are therefore shifted to lower wavelength (higher energy) in $[\text{C}(\text{NH}_2)_3]\{\text{Cu}_2\text{cit}[\text{C}(\text{NH}_2)_2\text{NH}]_2(\text{OH})\}$ which is consistent with a larger crystal field splitting due to the nitrogen coordination of the copper centres by the guanidine ligands.

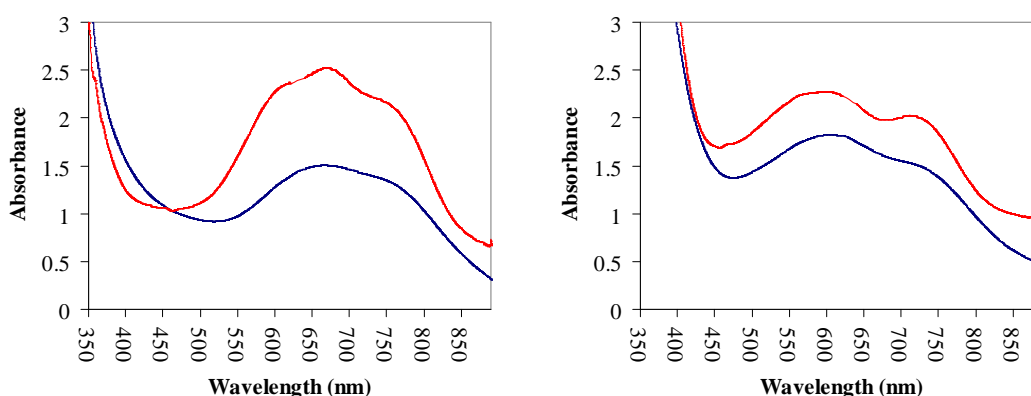


Figure 3-13 – Electronic spectra of $[\text{C}(\text{NH}_2)_3]_4\{\text{Cu}_2(\text{cit})_2\} \cdot \text{H}_2\text{O}$ (left), and $[\text{C}(\text{NH}_2)_3]\{\text{Cu}_2\text{cit}[\text{C}(\text{NH}_2)_2\text{NH}]_2(\text{OH})\}$ (right), measured at room temperature (blue) and at ~ 20 K (red).

3.2.4 – Magnetic Properties of $[\text{C}(\text{NH}_2)_3]\{\text{Cu}_2\text{cit}[\text{C}(\text{NH}_2)_2\text{NH}]_2(\text{OH})\}$

The dc magnetic properties of the hydroxy bridged dimer are shown in Figure 3-14. The value of χT at 290 K is $0.83 \text{ cm}^3 \text{ mol}^{-1} \text{ K}$ and on cooling χT remains reasonably constant until 200 K, at which point a long decreasing curve begins which eventually approaches $0 \text{ cm}^3 \text{ mol}^{-1} \text{ K}$ at 0 K. The curve was fitted using a one J model ($\hat{H} = -2JS_1S_2$) in CAMMAG, with the best parameters found to be $g = 2.16$ and $J = -27.8 \text{ K}$ which can be seen to be in good agreement over the temperature range measured.

The observed antiferromagnetic coupling between the copper centres is perhaps to be expected considering that the bridging angles in this case of 95.65° (citrate) and 96.77° (OH) are very close to the expected changeover values at 95.8° (alkoxide) and 97.6° (hydroxide) [2,3,4]. However this comparison is complicated by the non-planar bridging and presence of two unequal bridging angles and bond lengths in this dimer. The DFT modelling studies [5,7] suggest that such a hinge distortion of the Cu_2O_2 core should reduce the antiferromagnetic character. The calculations also show that the effect of asymmetric bridging is slight, and can be estimated using an average of the two bridging angles. The DFT models therefore seem to suggest ferromagnetic contributions, also favoured by the replacement of citrate oxygen coordination by the more electronegative guanidine nitrogen, however these components must be minor compared to the dependence on the bridging angle. It also interesting to note that the DFT studies show that in antiferromagnetic examples there is a remarkably large spin delocalisation from the metal centres onto the surrounding ligands. Since the hydroxy bridged dimer ligands have already been shown to be involved in an extensive hydrogen bonding network (Figure 3-11) it is possible that the observed magnetic behaviour is complicated by intermolecular interactions, or indeed that the DFT model may not be applicable to this case.

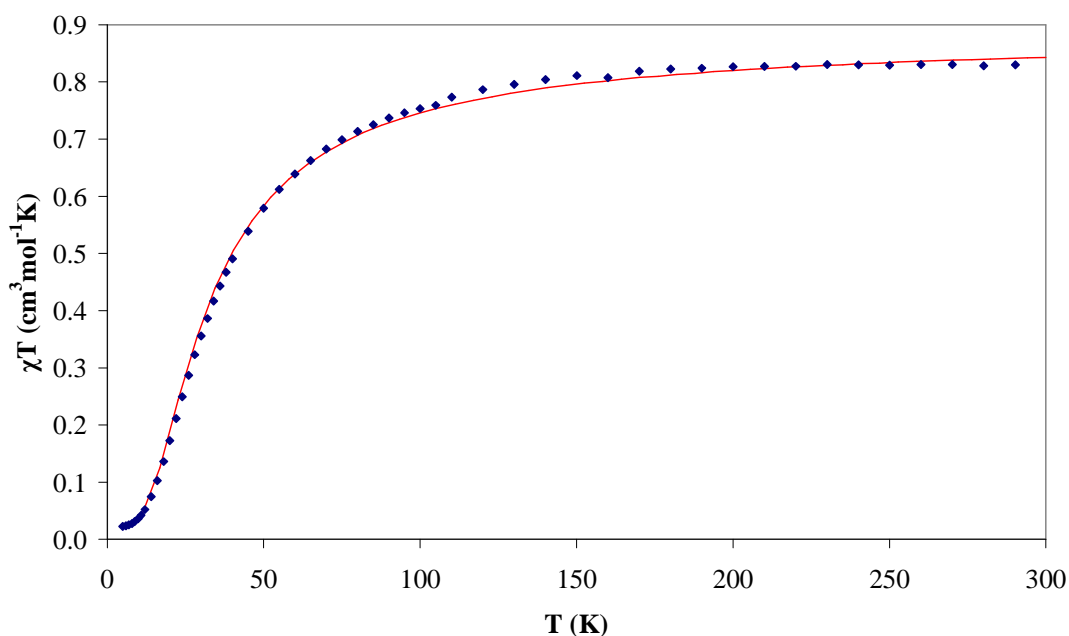


Figure 3-14 – Temperature dependence of χT for $[\text{C}(\text{NH}_2)_3]\{\text{Cu}_2\text{cit}[\text{C}(\text{NH}_2)_2\text{NH}]_2(\text{OH})\}$ measured in a 1000 Oe field, with the fit shown as a red line ($J = -27.8$ K, $g = 2.16$).

3.2.5 – Hydroxy Bridged Dimer High Pressure Structural Study

A high pressure single crystal X-ray diffraction study was carried out on $[\text{C}(\text{NH}_2)_3]\{\text{Cu}_2\text{cit}[\text{C}(\text{NH}_2)_2\text{NH}]_2(\text{OH})\}$ due to the presence of the long contact (similar to that seen for $[\text{C}(\text{NH}_2)_3]_4\{\text{Cu}_2(\text{cit})_2\}.\text{H}_2\text{O}$) and also because of the interesting packing of the hydrogen bonded dimers. Table 3-3 shows the reduction in the unit cell dimensions and volume on increasing the applied pressure, along with two high pressure phases with changes to crystal space group. Note that the Phase III volume is much larger as there are two different dimer species in the unit cell, compared with one in the other phases.

Pressure (kbar)	Phase	Space Group	Unit cell dimensions (Å)			Volume (Å ³)
			a	b	c	
Ambient	I	<i>Pnma</i>	15.679(4)	12.699(3)	8.932(2)	1778.43
8	I	<i>Pnma</i>	15.6012(9)	12.5198(3)	8.8557(2)	1729.73
18	I	<i>Pnma</i>	15.434(2)	12.3617(6)	8.7439(4)	1668.3
29	II	<i>P2₁2₁2₁</i>	15.083(1)	12.1396(3)	8.7075(3)	1594.39
42	III	<i>P2₁/c</i>	16.303(1)	11.9204(5)	17.1330(8)	3030.57

Table 3-3 – Effect of pressure on the unit cell dimensions of $[\text{C}(\text{NH}_2)_3]\{\text{Cu}_2\text{cit}[\text{C}(\text{NH}_2)_2\text{NH}]_2(\text{OH})\}$.

The high pressure crystallography studies reveal that within Phase I from 0-18 kbar, there are only small changes to the hydroxy bridged dimer structure (Table 3-4). The bridging angles alter, with a decrease in Cu1a- $\hat{\text{O}}1$ -Cu1b (citrate) and decrease in Cu1a- $\hat{\text{O}}6$ -Cu1b (hydroxide). The Cu-O1 (citrate) and Cu-O6 (hydroxide) bond distances remain relatively constant, while the long contact decreases. Overall, the changes are smaller than those observed for $[\text{C}(\text{NH}_2)_3]_4\{\text{Cu}_2(\text{cit})_2\}.\text{H}_2\text{O}$ in Section 3.1.4. The change in symmetry in Phase II and III removes the mirror plane seen on the centre of the dimer in Phase I (Figure 3-8) and so the four bridging bonds can therefore have independent lengths (note that a single numbering scheme is used in Table 3-4, however the copper centres Cu1a and Cu1b are not symmetry equivalent in Phases II and III). There are also two different long contact distances, as the α -carboxylate twists towards one of the copper centres (Cu1a) thus decreasing one contact while increasing the other. Although the bridging structure displays larger changes in Phases II and III, intermolecular interactions also play a major role.

Pressure (kbar)	Phase	Cu- \hat{O} -Cu Angles (°)		Cu-O Bond Lengths (Å)				α -CO ₂ ⁻ Long Contact	
		Cu1a- \hat{O} 1-Cu1b	Cu1a- \hat{O} 6-Cu1b	Cu1a-O1	Cu1a-O6	Cu1b-O1	Cu1b-O6	Cu1a-O4	Cu1b-O4
Ambient	I	95.65(2)	96.77(2)	1.955(2)	<i>1.938(2)</i>	1.955(2)	<i>1.938(2)</i>	2.74(3)	2.740(3)
8	I	95.34(1)	96.20(1)	1.953(2)	<i>1.940(4)</i>	1.953(2)	<i>1.940(4)</i>	2.729(3)	2.729(3)
18	I	95.16(1)	95.84(1)	1.950(2)	<i>1.940(4)</i>	1.950(2)	<i>1.940(4)</i>	2.701(3)	2.701(3)
29	II	95.1(2)	96.6(3)	1.936(5)	<i>1.920(8)</i>	1.956(6)	<i>1.927(8)</i>	2.664(7)	2.738(7)
42 (A)	III	96.3(3)	95.4(3)	1.924(9)	<i>1.93(1)</i>	1.911(8)	<i>1.93(1)</i>	2.680(7)	2.723(7)
(B)		92.6(2)	96.3(3)	1.962(6)	<i>1.88(1)</i>	1.919(7)	<i>1.89(1)</i>	2.50(1)	2.82(1)

Table 3-4 – Effect of pressure on the Cu- \hat{O} -Co bridging structure and the α -carboxylate long contact of [C(NH₂)₃]{Cu₂cit[C(NH₂)₂NH]₂(OH)} (numbers in italics refer to the hydroxide bridge). Note that two species are present at 42 kbar.

The hydroxy bridged dimer has been found to undergo an unusual two-stage polymerisation to form chains at high pressure, with two associated phase changes (see Figure 3-15). Phase I is present at ambient conditions up to moderately high pressures and has discrete dimer units. At 29 kbar Phase II is observed, where one of the β -carboxylate arms of the citrate on each dimer coordinates to a copper centre of one neighbouring dimer, on the opposite side to the long contact. On further increase of pressure to 42 kbar Phase III is observed, where *in one species* (A) both of the β -carboxylate arms now coordinate to copper centres on both neighbouring dimers. Figure 3-14 shows the new bonds created under pressure in purple, which have a long contact length of ~ 2.6 Å compared to an equivalent separation in Phase I of ~ 3.2 Å. In Phase II each dimer has one bond to the next dimer in the chain, and in Phase III, two bonds to the next dimer in the chain. The result of this coordination coupled with the long contact, means that the copper centres are effectively becoming six coordinate. The changes can be visualised as the tubes of dimers described earlier being compressed together until the outer dimer faces can coordinate to each other (i.e. compression in the yellow bond region of Figure 3-11).

In addition to the polymer chain where each dimer makes two bonds to the next dimer in the chain, *the second species* (B) in Phase III remains similar to the Phase II polymer with only one bond to the next dimer in the chain. The α -carboxylate of the second species leans heavily to one side, making the Cu1b-O4 distance extremely long compared to Cu1a-O4 for (B) in Table 3-4. The two different polymer chain species are arranged in alternating bands in the crystal structure, as highlighted in orange and yellow in Figure 3-16.

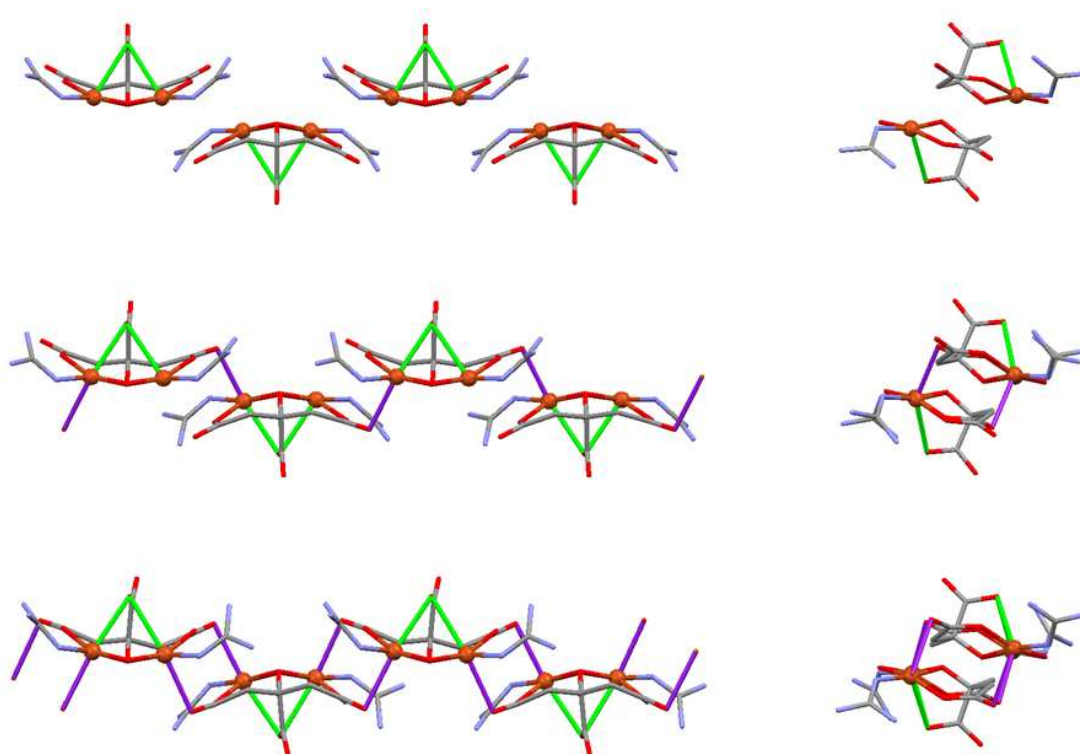


Figure 3-15 – Hydroxy bridged dimer in Phase I at ambient pressure (top), Phase II at 29 kbar (middle) and Phase III (A) at 42 kbar (bottom), shown in front and end elevation of polymer chains with long contact shown in green and pressure induced bonds in purple, (Cu orange, O red, C grey, N pale blue, H omitted).

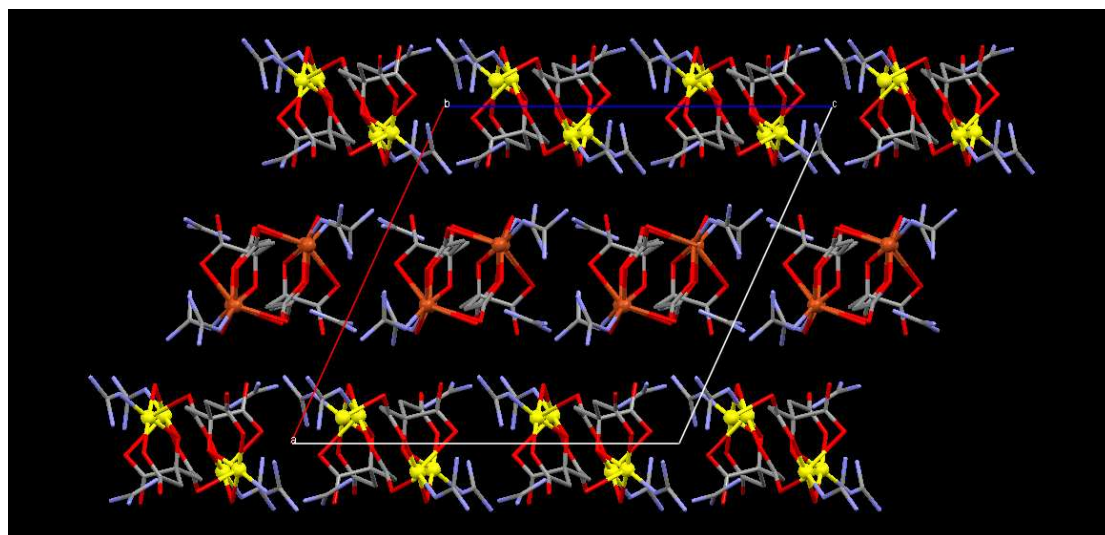


Figure 3-16 – Alternating bands of Phase III dimer polymer species, viewed along the *b* axis. ‘Orange’ dimers have two bonds to next in the chain (A), whereas ‘yellow’ copper dimers have one bond (B), (Cu orange and yellow, O red, C grey, N pale blue, H omitted).

An investigation of the magnetic properties at high pressure would be of interest in order to determine the effects of the both the intramolecular changes to the bridging structure in Phase I and also the intermolecular changes of the polymerisation in Phases II and III. Unfortunately the currently available SQUID pressure cell cannot withstand the high pressures required for the polymerisation, but it may be capable of measuring the onset of these effects. Such measurements were not possible during this research, not only due to extensive time such pressure measurements require, but also because of complications with the hydroxy bridged copper dimer possessing only a small spin (two $S_i = 1/2$) and antiferromagnetic coupling. Since the SQUID pressure cell is still in early development, investigations of this multiphase dimer may become practical in the future.

3.3 – Copper Citrate Trimer $\{Cu_3(cit)_3Na(OH)\}^{6-}$

A full compound formula for the copper citrate trimer could not be determined due to problems with inconsistent microanalysis results caused by impurities from the synthesis. The trimer anion formula was determined from the X-ray crystallography studies, but a full formula could not be obtained due to disorder in the structure.

3.3.1 – Synthesis of Copper Citrate Trimer

Na⁺ Synthesis - To a solution of citric acid monohydrate (1.09 g, 5.2 mmol) and CuSO₄·5H₂O (1.30 g, 5.2 mmol) in water (15 mL) was added guanidinium carbonate (1.87 g, 10.4 mmol) with rapid stirring, producing bubbles and a darkening of the blue solution. NaOH (0.43 g, 10.4 mmol) was added giving an instant dark blue precipitate (IR of hydroxy bridged dimer) which was removed by filtration. The light blue filtrate was then left to stand uncovered. After slow evaporation, hexagonal needle crystals formed in very low yield, selected IR data (cm⁻¹): 3348 (m), 3127 (m), 1650 (s), 1574 (s), 1440 (w), 1380 (s), 1281 (w), 1246 (m), 1105 (s), 1007 (w).

Li⁺ Synthesis - To a solution of citric acid monohydrate (1.09 g, 5.2 mmol) and CuSO₄·5H₂O (1.30 g, 5.2 mmol) in water (15 mL) was added guanidinium carbonate (1.87 g, 10.4 mmol) with rapid stirring, producing bubbles and a darkening of the blue solution. LiOH (0.25 g, 10.4 mmol) was added giving an instant dark blue precipitate which was removed by filtration. The light blue filtrate was then left to stand

uncovered. After evaporation, the residue was dissolved in 1 ml of water, placed in a tall, narrow vial, and left to slowly evaporate. A very small yield of blue crystals formed with colourless residue. Blue crystals, selected IR data (cm^{-1}): 3339 (m), 3154 (m), 1654 (s), 1577 (s), 1377 (s), 1247 (w), 1246 (m), 1097 (s), 921 (w), 842 (w).

K⁺ Synthesis - To a solution of citric acid monohydrate (1.09 g, 5.2 mmol) and $\text{CuSO}_4 \cdot 5\text{H}_2\text{O}$ (1.30 g, 5.2 mmol) in water (15 mL) was added guanidinium carbonate (1.87 g, 10.4 mmol) with rapid stirring, producing bubbles and a darkening of the blue solution. KOH (0.57 g, 10.4 mmol) was added giving an instant dark blue precipitate which was removed by filtration. The light blue filtrate was then left to stand uncovered. After evaporation, the residue was dissolved in 1 ml of water, placed in a tall, narrow vial, and left to slowly evaporate. A small number of blue crystals formed with a colourless organic residue. Blue crystals, selected IR data (cm^{-1}): 3344 (m), 3118 (m), 1648 (s), 1542 (s), 1437 (w), 1378 (s), 1247 (m), 1124 (m), 1070 (w), 905 (w), 842 (w).

A second new product obtained by addition of NaOH to the original copper citrate dimer synthesis (Section 3.1.1) is a copper citrate trimer. The trimer formation appears to be pH dependent, in a pH region between that of the two dimers already discussed. It is also very soluble in water and requires careful slow evaporation to obtain crystals, although these tend to be in low yield and accompanied by large amounts of colourless crystals/residue from the very concentrated solutions. The trimer crystals are also very unusual in that they form hollow, hexagonal needles as seen in Figure 3-17. The crystals also appear to crystallise from the outside in, with the central channel becoming increasingly narrow, which in some cases continues until a solid hexagonal prism is obtained.

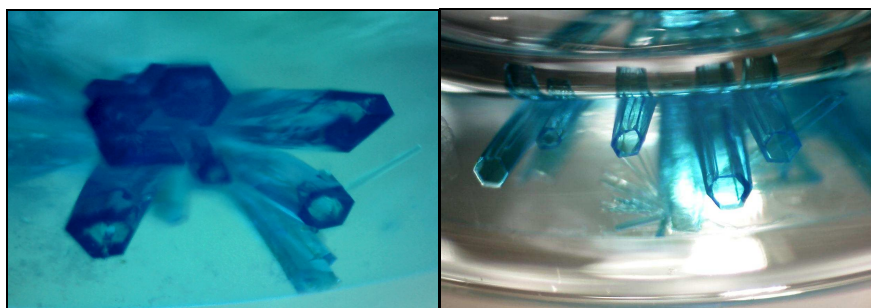


Figure 3-17 – Photographs of the copper trimer crystals illustrating the unusual hollow hexagonal needle form, which appear to crystallise from the outside inwards.

The nature of the crystals presents several problems, particularly in harvesting a sample for analysis. Even when carefully collected and manually separated from any colourless impurity crystals present, there remains the problem of residual concentrated solution remaining inside the needles. To try and minimise this effect the needles were gently crushed between two sheets of filter paper, but even so problems with inconsistent microanalysis of the samples suggests the presence varying amounts of residual impurities.

3.3.2 – Structure of $\{\text{Cu}_3(\text{cit})_3\text{Na}(\text{OH})\}^{6-}$

The copper citrate trimer crystallises in the $P\bar{3}$ space group which is consistent with the shape of the crystals. The Na^+ trimer structure is shown in Figure 3-18 and this reveals that the copper(II) centres are bridged by the citrate alkoxide group and each is bound by one α - and one β -carboxylate arm. The remaining β -carboxylate arm completes the coordination of a sodium centre that is also bound to the alkoxide groups. A bridging hydroxide is bound at the bottom of the trimer, giving an overall geometry of a distorted $\{\text{Cu}_3\text{NaO}_4\}$ cubane. The copper centres in the trimer are in a square-based pyramidal coordination environment, which can be seen in the side elevation of Figure 3-18.

There are two bridging pathways between the copper(II) centres of the trimer. The citrate alkoxide bridge has a large angle with $\text{Cu}-\hat{\text{O}}(\text{citrate})-\text{Cu} = 104.35^\circ$, but short bonds of 1.97 Å, whereas the hydroxide bridge has an acute angle of $\text{Cu}-\hat{\text{O}}(\text{H})-\text{Cu} = 75.64^\circ$ with much longer bonds of 2.54 Å. The large citrate bridging angles would be expected to tend towards antiferromagnetic coupling, but the effect of the small hydroxide bridging angles with long bond lengths is less clear.

Similar copper(II) trimer structures with a central hydroxide bridge have been reported, but these have tended to be based on long chain ligands with oxygen and nitrogen donors that adopt a propeller like arrangement [8-14, Appendix]. None of the structures feature a central sodium centre as found in the citrate case. The literature trimers also feature square based pyramidal coordination of the copper(II) centres, but have a shallower bowl shape with wider hydroxide bridging angles of over 100° (and shorter Cu-OH bonds) and display antiferromagnetic interactions.

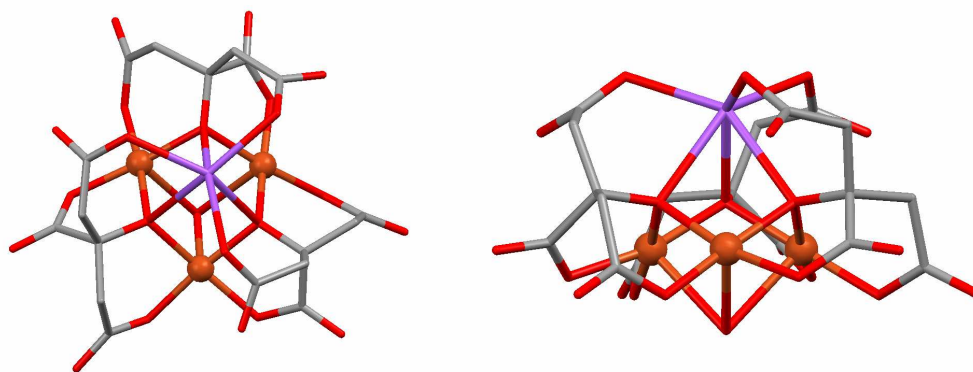


Figure 3-18 – $\{\text{Cu}_3(\text{cit})_3\text{Na}(\text{OH})\}^{6-}$ anion structure from above (left) and in side elevation (right), (Cu orange, O red, C grey, Na violet, H omitted).

The trimer structure incorporates the additional base in the coordinated Na^+ and the OH^- bridge on the central C_3 axis of the cluster. Analogous syntheses with LiOH and KOH were carried out to investigate whether the different sizes of metal centres would result in structural distortions that could alter the magnetic properties. Small numbers of crystals were obtained for each, however only the potassium crystals were suitable for single crystal X-ray diffraction. The K^+ analogue was found to have the same structure as the Na^+ version, with differences in the hydroxide bridge bond distances and angles and K^+ - β -carboxylate bond distances. Comparison between the analogues is complicated due to the large R factors (see Appendix) that are the result of disorder within the structures.

The copper(II) citrate trimer packing consists of two contrasting regions. The trimer units and three guanidinium ions per cluster form hexagonal honeycomb layers that are rigidly bound by hydrogen bonding (Figure 3-19). The layers are stacked together such that the trimers are aligned in columns, which results in large channels along the c axis. The contents of the channels are highly disordered, in sharp contrast to the highly ordered hydrogen bonded framework. Presumably the other guanidinium or sodium counterions and solvent water are disordered within the channels, coordinating or hydrogen bonding to the large number of citrate oxygens that are seen to point inward from the channel walls. The shape of the trimer and guanidinium hydrogen bonding network is reminiscent of the hollow hexagonal shape of the crystals (Figure 3-17).

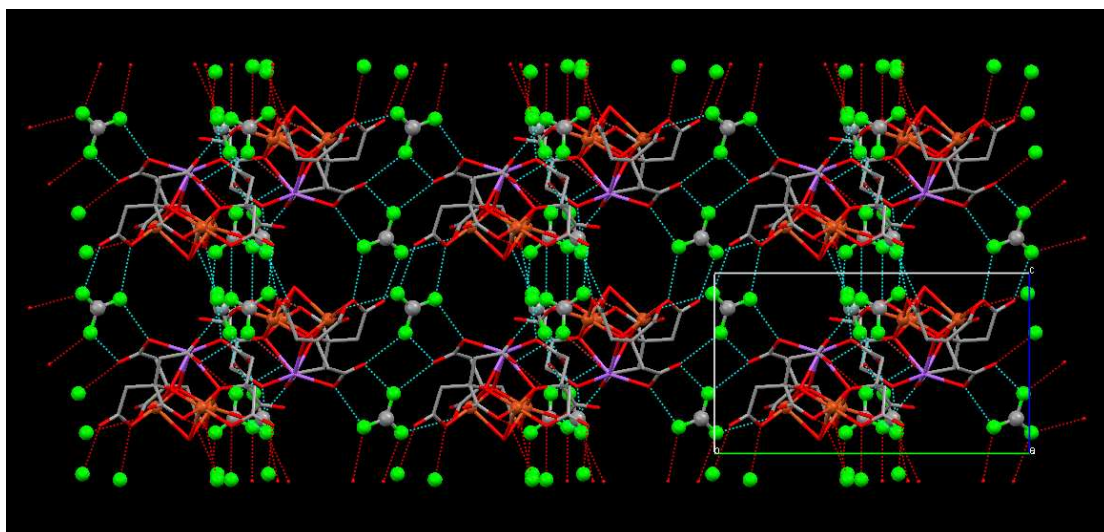
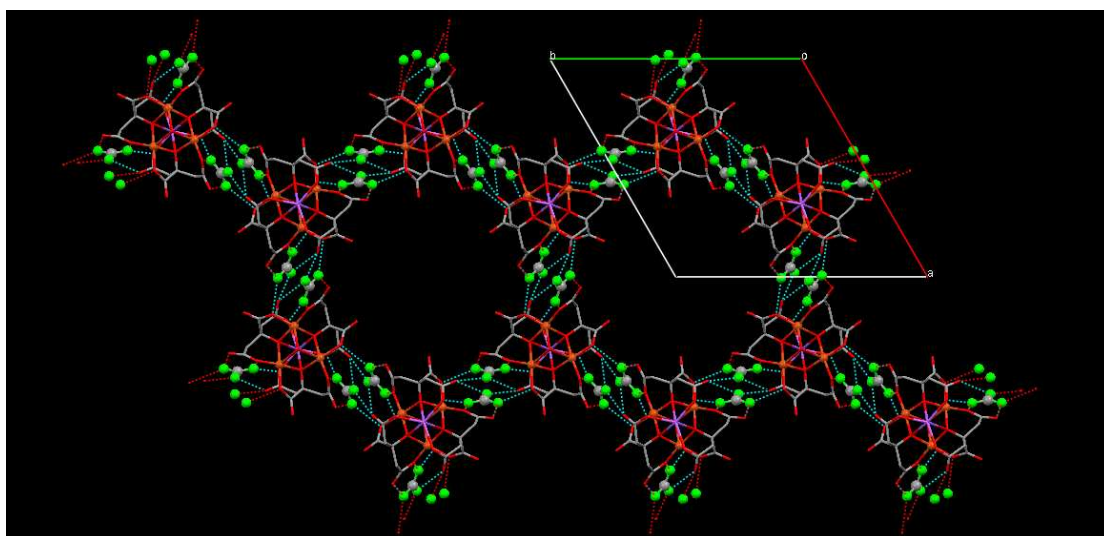


Figure 3-19 – $\{\text{Cu}_3(\text{cit})_3\text{Na}(\text{OH})\}^{6-}$ crystal packing, illustrating the hydrogen bonding in the hexagonal layers of copper trimers and guanidinium counterions. The three $[\text{C}(\text{NH}_2)_3]^+$ per trimer cluster that are involved in the hydrogen bonding network are highlighted using a ball and stick representation with green nitrogen atoms. The view along the c axis (upper) shows the large channels, which are thought to contain the other disordered counterions (not shown). The view along the b axis (lower) shows the stacking of the layers, (Cu orange, O red, C grey, N green, Na violet, H omitted).

3.3.2 – Magnetic Properties of Na⁺ Copper Citrate Trimer

A formula weight was not available for the analysis of the magnetic data since microanalysis results were inconsistent due to impurities and a full formula could not be found from the crystallography studies due to the disorder. To address this issue, CAMMAG was used to simulate a χT curve of an equivalent shape to that seen in Figure 3-20 based on a model of three $S_i = 1/2$ centres with one positive J for the coupling of the spins in the equilateral triangle ($\hat{H} = -2J(S_1S_2 + S_2S_3 + S_1S_3)$). The experimental χT data was then scaled to the magnitude of the simulation using an estimated molecular weight of 1700 gmol⁻¹ giving a g value of ~2.2. The curve fit following the scaling used the parameters $g = 2.18$ with $J = 30$ K.

From a value of 1.47 cm³mol⁻¹K at 290 K, the χT curve steadily increases on cooling with a more rapid increase below 100 K. This upwards curvature continues to a maximum peak value of 2.24 cm³mol⁻¹K at 9.9 K, before decreasing at lower temperatures. The magnetisation curve of Figure 3-21 levels out towards 5 T where it has a value of $M/N\beta = 3.44$, which is consistent with a spin ground state $S_T = 3/2$. Since the trimer displays ferromagnetic interactions between the copper(II) centres, the acute bridging via the hydroxide must dominate over the wide bridging angles provided by the citrate alkoxide groups, even though the hydroxide bridge has longer bonds.

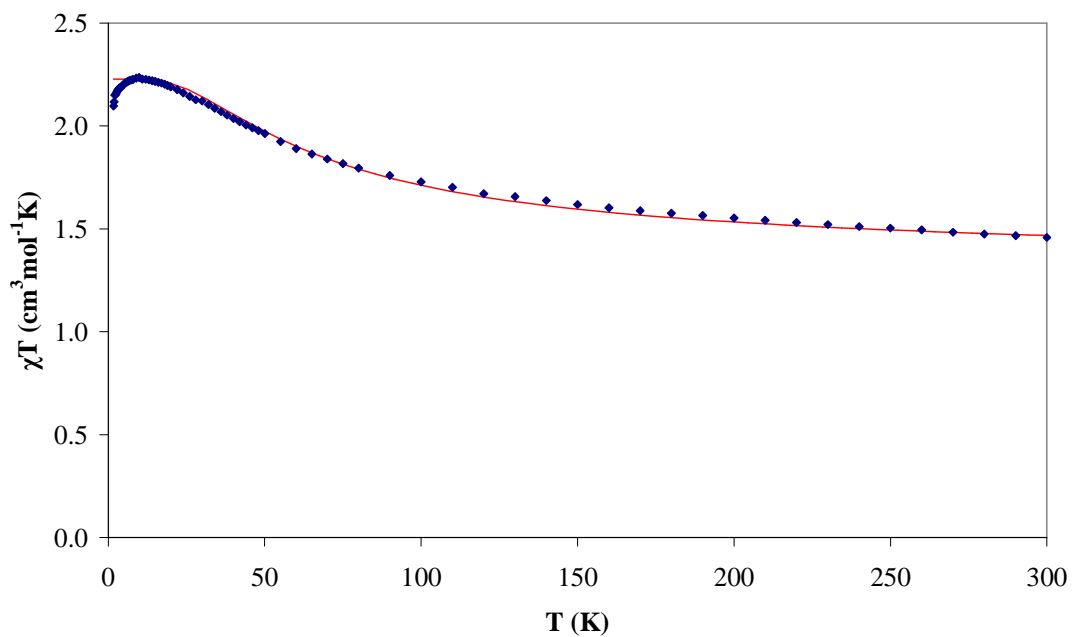


Figure 3-20 – Temperature dependence of χT for the Na^+ copper trimer, measured in a 1000 Oe field, with the fit shown as a red line ($J = 30$ K, $g = 2.18$).

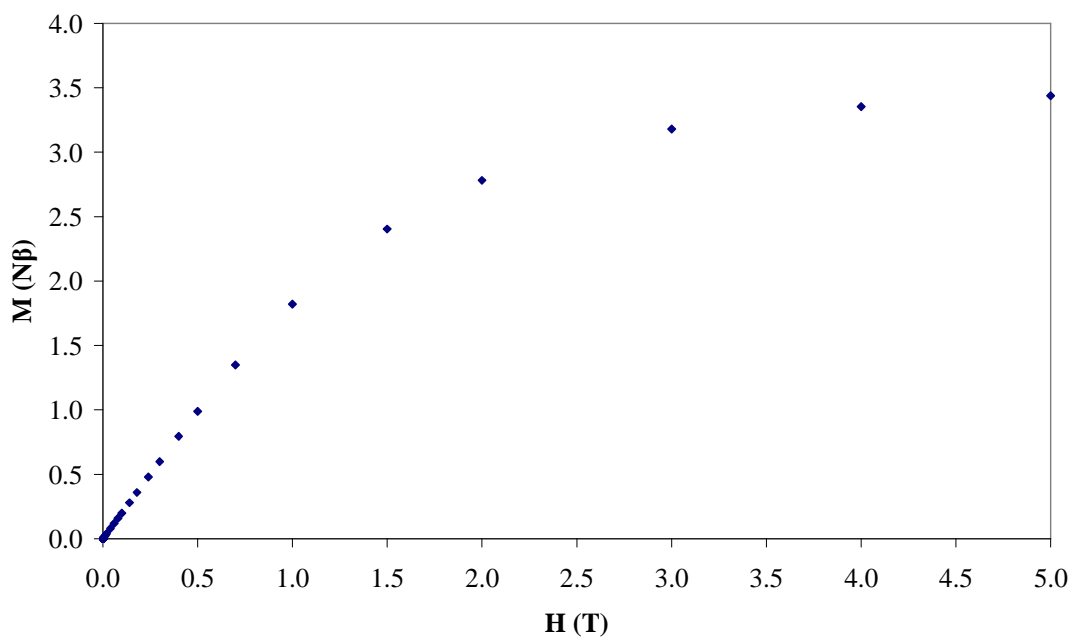


Figure 3-21 – Field dependence of the magnetisation at 2 K for the Na^+ copper trimer.

3.4 – Related Ligand Systems

The interesting results obtained from the study of the copper dimers prompted further investigation of the syntheses using related ligands, with the aim of creating comparable structures or other novel products. The first experiments looked at replacing the guanidinium with the derivatives methylguanidinium and ethylguanidinium. The analogues of the two copper dimer syntheses using the reagents of Figure 3-22 (with hydroxide base) did not produce any product crystals. This is most likely the result of the bulky methyl and ethyl groups preventing the neat packing displayed by the counterions in the copper dimer structures. The reduction in the opportunities for hydrogen bonding is also a consideration given the important role that these interactions have been shown to play. Guanidineacetic acid was selected for study in the hydroxide bridged dimer synthesis, in an effort to replace the terminal guanidine ligands. If this was successful the attached carboxylic acid groups could provide further copper coordination points on the sides of the dimer unit in order to promote the formation of larger clusters. Unfortunately this reagent proved to be insoluble and unreactive in the aqueous conditions employed.

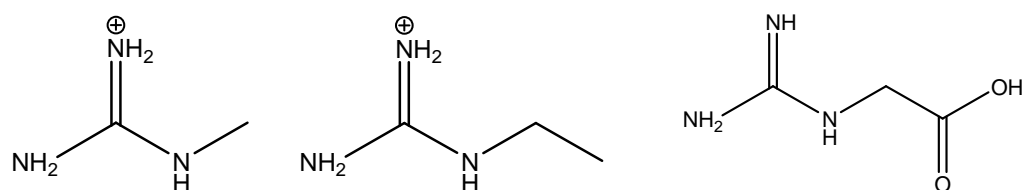


Figure 3-22 – Structure diagrams of methylguanidinium (left), ethylguanidinium (centre) and guanidineacetic acid (right).

The second approach looked at ligands with structures related to citric acid. These were chosen to maintain the five carbon backbone of citric acid, while allowing investigation of the effect of varying the functional groups available for coordination to the metal centres. The ligands that were selected are shown in Figure 3-23.

Tricarballic acid has the structure of citric acid with the central alcohol group removed. Reactions using this ligand were largely unsuccessful due to a tendency of the solutions to precipitate. This is not surprising given the key bridging role the central alkoxide group has been shown to play in the products reported, and so the ligand is likely to form complex polymers. It may be useful in future syntheses with mixed ligands, in order to promote outward growth to form larger clusters in

conjunction with ligands such as citrate that can wrap around and cap, however initial reactions met with limited success.

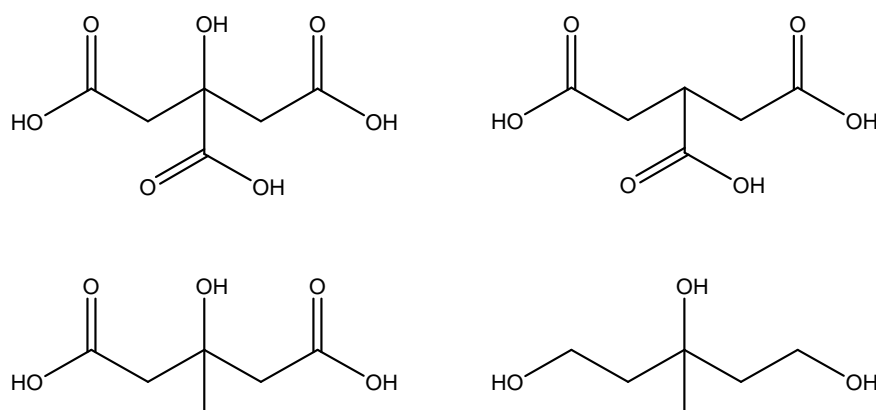


Figure 3-23 – Ligand structure diagrams, citric acid (upper left), tricarballic acid (upper right), 3-hydroxy-3-methylglutaric acid (lower left) and 3-methyl-1,3,5-pentanetriol (lower right).

3-hydroxy-3-methylglutaric acid (H₃L₂) has the structure of citric acid with the central carboxylic acid replaced by a methyl group. 3-methyl-1,3,5-pentanetriol (H₃L₁) is the doubly reduced form of 3-hydroxy-3-methylglutaric acid. In theory these ligands should be able to provide the central bridging alkoxide group and two terminal oxygens for the copper coordination seen in the dimers. Since the dimers only have a long contact rather than a bond with the α -carboxylate, it was hoped that new analogous dimers would be accessible, allowing for the resulting difference in charge balance.

However it was found that reactions using 3-hydroxy-3-methylglutaric acid or 3-methyl-1,3,5-pentanetriol with guanidinium carbonate lead to the formation of a three dimensional network [C(NH₂)₃]₂Cu(CO₃)₂, the structure of which had previously been reported in the literature [15]. This proved to be a very stable and dominant product, which would even readily crystallise from the residual solution absorbed on a filter paper. Consequently the copper(II), carbonate and guanidinium ions were rapidly removed from solution, without reaction or coordination with the new ligands. As will be discussed later, the development of carbonate free syntheses in alternative solvents does indeed allow access to comparable novel dimer structures using these ligands.

3.4.1 – Copper Carbonate Network $[\text{C}(\text{NH}_2)_3]_2\text{Cu}(\text{CO}_3)_2$

3.4.1.1 – Synthesis of $[\text{C}(\text{NH}_2)_3]_2\text{Cu}(\text{CO}_3)_2$

Analogue of the hydroxy bridged dimer synthesis

To a solution of 3-methyl-1,3,5-pentanetriol (0.70 g, 5.2 mmol) in water (50 ml) was added a solution of $\text{Cu}(\text{NO}_3)_2 \cdot 3\text{H}_2\text{O}$ (1.26 g, 5.2 mmol) in water (50 ml) followed by a solution of guanidinium carbonate (4.70 g, 26 mmol) in water (50 ml). The solution was then left to stand uncovered overnight producing a very large yield of blue crystals. Selected IR data (cm^{-1}): 3414(m), 3334(m), 3173(m), 1649(s), 1569(w), 1497(s), 1302(s), 1055(m), 847(s). Analysis calculated (found) for $\text{C}_3\text{H}_6\text{CuN}_3\text{O}_6$: C 15.82 (15.89); H, 3.98 (3.93); N, 27.67 (27.46).

For further magnetic characterisation, the copper carbonate network was selected for study by powder neutron diffraction. A new synthesis was required that would allow for deuteration of the samples. Since the 3-methyl-1,3,5-pentanetriol in the synthesis above acted as a spectator and was not present in the product, it was decided to investigate the direct reaction of copper(II), carbonate and guanidinium ions. The reaction was studied as an array of conditions covering solution concentrations and the number of equivalents of carbonate, since these were important limiting factors in the rapid formation and crystallisation of the product. Guanidinium chloride was found to be the only salt commercially available as the fully deuterated form, and so this was used as the guanidinium ion source. Copper(II) chloride was chosen in order to maintain common counterions and also to prevent any possible instances of crystal defects where a nitrate anion could take the place of a similarly shaped guanidinium cation. The optimised reaction conditions are given below.

Direct stoichiometric synthesis

To a solution of CuCl_2 (0.70 g, 5.2 mmol) and guanidinium chloride (0.99 g, 10.4 mmol) in water (5.2 ml for 1 M $\text{Cu}(\text{II})$ solution), was added a solution of K_2CO_3 (1.44 g, 10.4 mmol) in water (10.4 ml for 1 M CO_3^{2-} solution) under rapid stirring. An instant blue precipitate formed, which rapidly darkened on stirring. The very large yield of crystalline precipitate was collected by filtration and washed with copious water. The identity of the product was confirmed by powder X-ray diffraction.

3.4.1.2 – Structure of $[\text{C}(\text{NH}_2)_3]_2\text{Cu}(\text{CO}_3)_2$

The structure of $[\text{C}(\text{NH}_2)_3]_2\text{Cu}(\text{CO}_3)_2$ consists of copper(II) centres that are linked into a three dimensional network by carbonate with charge balance provided by guanidinium ions. Each carbonate ion binds to two copper centres while the third oxygen remains uncoordinated. The guanidinium counterions are located in the spaces within the copper carbonate framework (shown in Figure 3-24) and hydrogen bond with carbonate oxygen atoms. The copper(II) centres have two coordination geometries in the network, with both square planar centres and distorted centres that are between square planar and tetrahedral coordination, as highlighted in Figure 3-25.

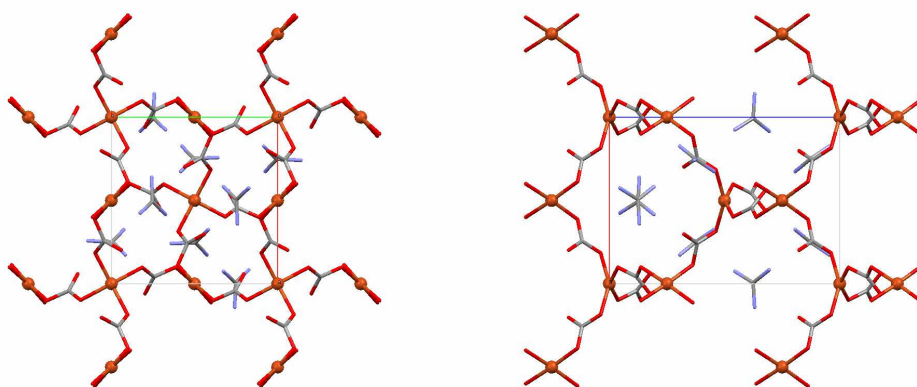


Figure 3-24 – Structure of copper carbonate 3D network, viewed along *c* axis (left) and *b* axis (right), (Cu orange, O red, C grey, N pale blue, H omitted).

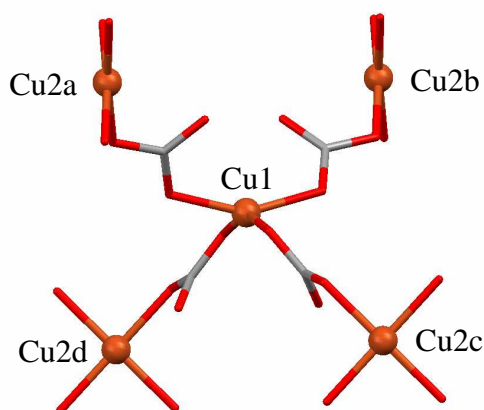


Figure 3-25 – Enlarged view of the two types of copper coordination environments in the 3D network illustrating the square planar (Cu2) and tetrahedrally distorted geometries (Cu1), (Cu orange, O red, C grey).

3.4.1.3 – Magnetic Properties of $[\text{C}(\text{NH}_2)_3]_2\text{Cu}(\text{CO}_3)_2$

The previous report in the literature [15] had only considered the copper(II) carbonate network from a structural perspective, and so a sample was prepared for magnetic characterisation. This revealed that the copper carbonate network behaves as a ferrimagnet, and the temperature dependence of the magnetisation in Figure 3-26 shows a notably high ordering temperature of 65 K. The zero field cooled magnetisation curve is lower than that of the field cooled, with the two curves merging at 50 K.

An initial rationalisation of the magnetic properties can be proposed based on structural considerations involving the two types of copper coordination environment. It is thought that the crystal behaves as two interpenetrating nets of the two types of copper ions which couple together antiferromagnetically. Since the copper environments are different there is an incomplete cancellation of the small orbital moments and therefore a net moment remains and the compound is ferrimagnetic. Further magnetic investigation of this product was carried out by powder neutron diffraction on instruments D2b and D20 at the Institut Laue Langevin, however at the time of writing the results of these experiments had not yet been received or modelled.

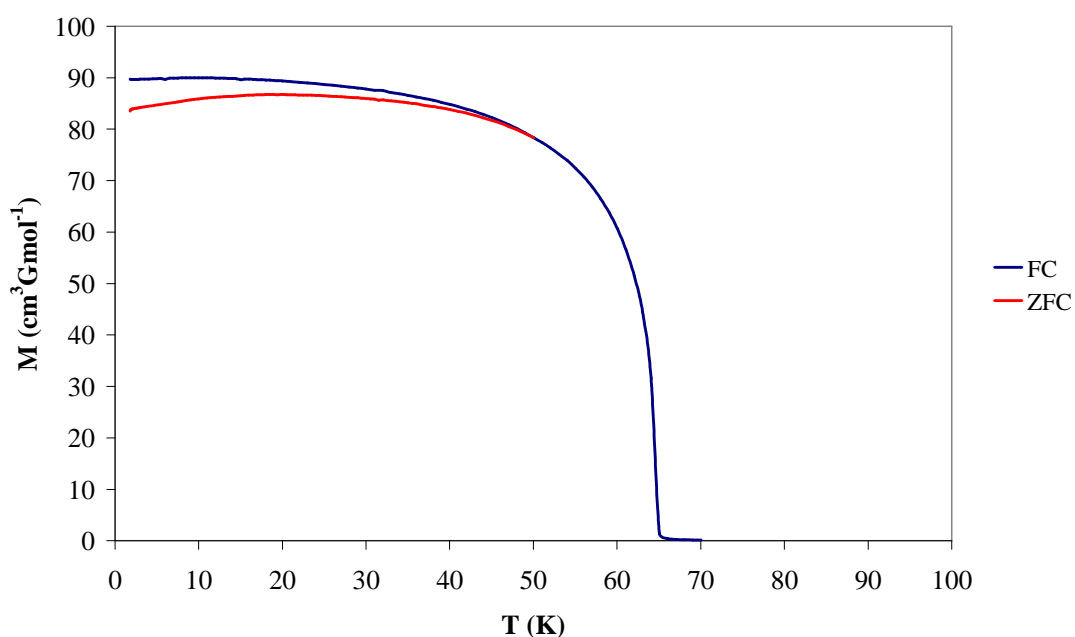


Figure 3-26 – Field Cooled and Zero Field Cooled temperature dependence of the magnetisation for $[\text{C}(\text{NH}_2)_3]_2\text{Cu}(\text{CO}_3)_2$.

3.4.2 – Copper Triol Dimer $\{\text{Cu}_2(\text{H}_2\text{L1})_2\}(\text{NO}_3)_2$

3.4.2.1 – Synthesis of $\{\text{Cu}_2(\text{H}_2\text{L1})_2\}(\text{NO}_3)_2$

3-methyl-1,3,5-pentanetriol ($\text{H}_3\text{L1}$) (0.70 g, 5.2 mmol), $\text{Cu}(\text{NO}_3)_2 \cdot 3\text{H}_2\text{O}$ (1.26 g, 5.2 mmol) and guanidinium nitrate (1.27 g, 10.4 mmol) were combined in MeOH (75 ml). NaOH (0.21 g, 5.25 mmol) was gradually added with rapid magnetic stirring, which gave green trailing precipitate and eventually a dark green solution. For crystallisation, the solution was filtered and set up for vapour diffusion in a small vial placed inside a larger sealed vial containing ether. Large blue crystals formed in very low yield, selected IR data (cm^{-1}): 2726 (m), 1415 (m), 1377 (w), 1354 (w), 1291 (s), 1197 (w), 1155 (w), 1131 (m), 1072 (s), 1041 (w), 992 (w), 924 (m), 868 (w), 827 (m).

3.4.2.2 – Structure of $\{\text{Cu}_2(\text{H}_2\text{L1})_2\}(\text{NO}_3)_2$

The copper triol dimer crystallises in the $C2/m$ space group and consists of two copper(II) centres coordinated by two monodeprotonated 3-methyl-1,3,5-pentanetriol ligands. The central alcohol group of each ligand is deprotonated and bridges between the copper(II) centres. The general appearance of the triol dimer is similar to the copper citrate dimer discussed earlier, with the methyl group replacing the α -carboxylate of citrate (compare Figure 3-27 with Figure 3-2 of Section 3.1.2). In this case long contacts occur between the copper centres and nitrate counterions located above and below the bridging plane.

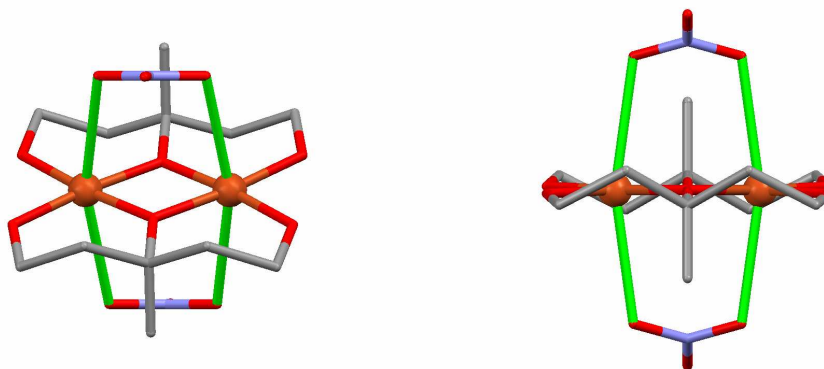


Figure 3-27 – Copper triol dimer structure (left) and bridging view (right) also showing nitrate ions with long contacts highlighted in green, (Cu orange, O red, C grey, N pale blue, H omitted).

The removal of the α -carboxylate group from the ligand backbone has a variety of implications for the copper bridging in this triol dimer. Since the long contact between the ligand and copper(II) centre seen for citrate is no longer present, the triol ligand in this case can be disordered over two orientations with the methyl group pointing up or down relative to the bridging plane. Note that in Figure 3-27 the dimer is illustrated with the predominant orientations (ratio $\sim 70/30$). The result of only three contact points between the ligand and copper(II) centres and the orientational disorder is that coordination geometry is very planar as can be seen in Figure 3-28. The copper(II) centres are therefore square planar and do not have the tetrahedral twist distortion seen with citrate.

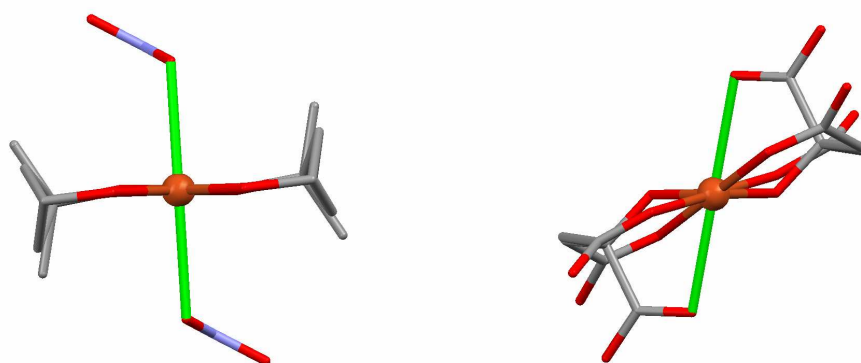


Figure 3-28 – Comparison of the ligand positions relative to the (horizontal) bridging plane in $\{\text{Cu}_2(\text{H}_2\text{L1})_2\}(\text{NO}_3)_2$ (left) and $[\text{C}(\text{NH}_2)_3]_4\{\text{Cu}_2(\text{cit})_2\}$ (right), (Cu orange, O red, C grey, N pale blue, H omitted, long contact highlighted in green).

In the copper triol dimer the $\text{Cu}-\hat{\text{O}}-\text{Cu}$ bridging angles are 100.38° and the bridging Cu-O bond distances are 1.90 \AA . The bridging angle is therefore larger than that of the copper citrate dimer (95.16°) and the bridge bonds are shorter. This can again be explained by the absence of a ligand long contact, as Figure 3-28 shows that the citrate α -carboxylate contact with the copper(II) centre pulls the ligand out of the bridging plane, which separates the alkoxide bridging oxygens and produces longer bridging bonds and a smaller angle. These effects are absent in the case of the copper triol dimer which has an alkoxide oxygen separation of 2.43 \AA compared to the larger 2.60 \AA for the copper citrate dimer. The copper(II) long contact distance to the nitrate ions are 2.73 \AA compared with the shorter 2.62 \AA to the citrate α -carboxylate.

The 3-methyl-1,3,5-pentanetriol ligand in the dimer has only the bridging alkoxide group deprotonated and the terminal coordinating groups remain as protonated alcohols. These hydrogen bond to the nitrate ions of neighbouring dimer units as shown in Figure 3-29. The synthesis of the $\{\text{Cu}_2(\text{H}_2\text{L1})_2\}(\text{NO}_3)_2$ dimer only included enough hydroxide to deprotonate one of the three alcohols. A comparable synthesis with three equivalents of hydroxide per one equivalent of ligand did not give any product crystals. This is interesting, since if the triply deprotonated 3-methyl-1,3,5-pentanetriol was to form an equivalent dimer there would no longer be the possibility of forming such a hydrogen bonding network due to the removal of the alcohol protons. However in this case the theoretical dimer would have an overall charge of minus two, so the nitrate counterions would most likely be replaced by sodium or guanidinium ions and the opportunity for oxygen long contacts with the copper centres would be removed. It is also noteworthy that guanidinium is present in the synthesis of the $\{\text{Cu}_2(\text{H}_2\text{L1})_2\}(\text{NO}_3)_2$ dimer but not included in the product (charge balance considerations being the most obvious explanation). Nonetheless, the hydrogen bonding network via the alcohol hydrogen is an important bonding interaction between the copper triol dimers. Figure 3-30 shows the packing arrangement with bands of hydrogen bonded dimers separated by organic layers of the ligand backbone. Note that if the dimer unit is taken to include the two ‘bound’ nitrates, then it has a neutral overall charge.

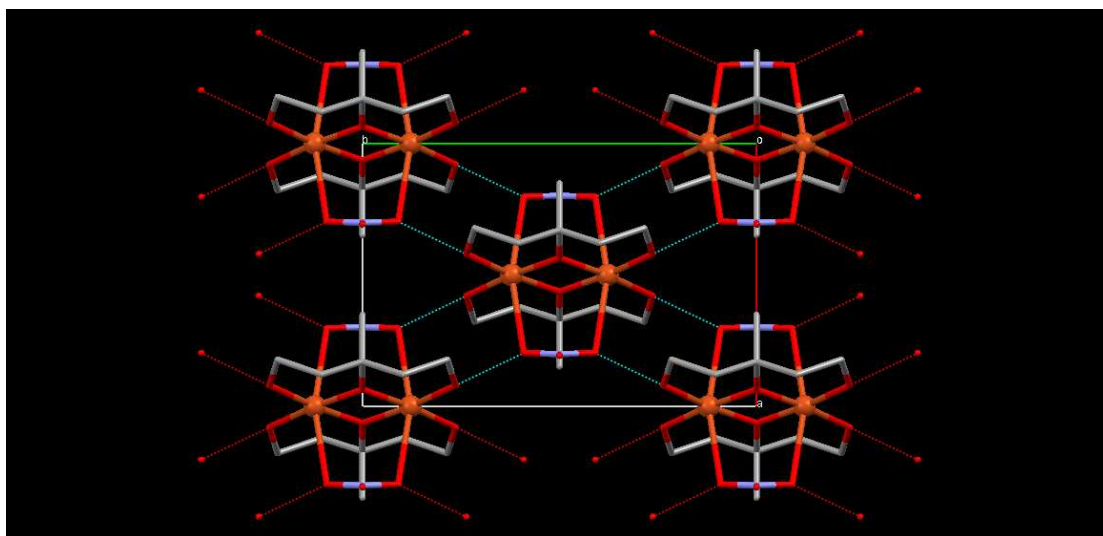


Figure 3-29 – Hydrogen bonding between the copper triol dimer alcohol groups and nitrate ions, viewed along the *c* axis with only the predominant ligand orientation shown for clarity, (Cu orange, O red, C grey, N pale blue, H omitted).

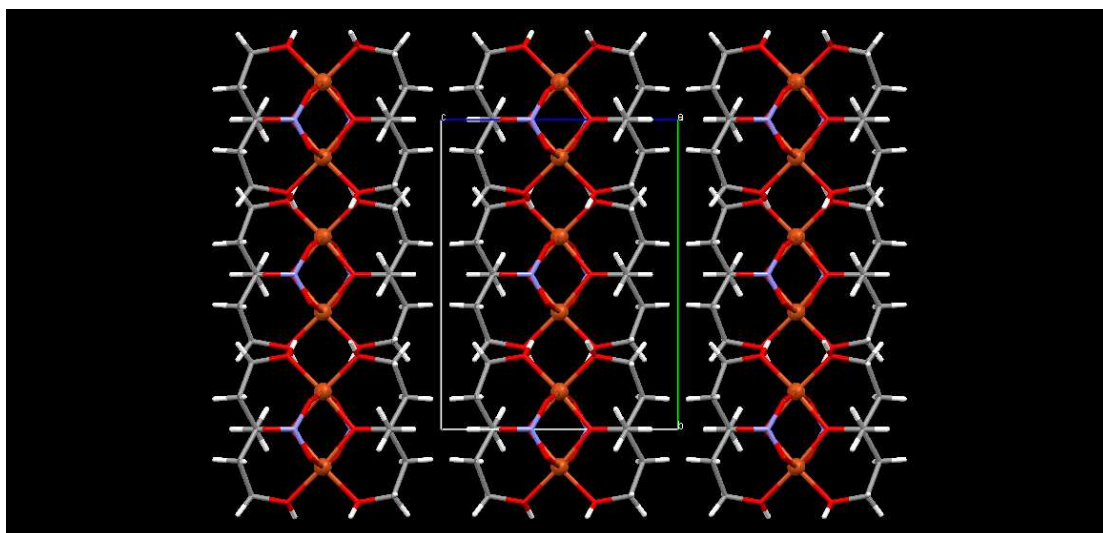


Figure 3-30 – Arrangement of the triol dimers into bands of copper centres separated by the organic ligands, viewed along the *a* axis with only the predominant ligand orientation shown for clarity, (Cu orange, O red, C grey, N pale blue, H white).

3.4.2.3 – Magnetic Properties of $\{\text{Cu}_2(\text{H}_2\text{L1})_2\}(\text{NO}_3)_2$

Unfortunately due to the very low yield of the syntheses, it was not possible to obtain a large enough sample to measure reliable magnetic data. From a structural perspective it is likely that the triol dimer would display antiferromagnetic coupling due to the large bridging angles (100.38°) that are present [2,3,4]. Since the bridging and the copper environments are planar in nature, there is no tetrahedral distortion or displacement of the oxygen bridge that DFT modelling studies [5,6,7] suggest would favour ferromagnetic interactions, as was found in the related copper citrate dimer. Thus the structural effect of the removal of the citrate long contact is likely to have important consequences for the magnetic properties. It should also be noted that the bound nitrate counterions may also have an effect on the value of the coupling constant, as found in modelling studies of the dimer $[\text{Cu}(\text{bipy})(\text{OH})_2(\text{NO}_3)_2]$, where neglecting the weakly coordinated counterions caused a decrease of 34 cm^{-1} in the calculated $2J$ value [7].

3.4.3 – Copper Tetramer

{Cu₄(L2)₂[C(NH₂)₂NH]₄(OMe)₂}.2MeOH.3H₂O

3.4.3.1 – Synthesis of {Cu₄(L2)₂[C(NH₂)₂NH]₄(OMe)₂}.2MeOH.3H₂O

Previous synthesis and ligand recovery

To a solution of 3-hydroxy-3-methyl-glutaric acid (H₃L2) (0.21 g, 1.3 mmol) in water (6.25 mL) was added a solution of Cu(NO₃)₂.3H₂O (0.31 g, 1.3 mmol) in water (6.25 mL) followed by a solution of guanidinium carbonate (0.94g, 5.2 mmol) in water (6.25 ml). The solution was then covered and left to stand. After 15 minutes, blue crystals formed in large yield, selected IR data (cm⁻¹): 3166 (m), 1570 (s), 1498 (s), 1307 (s), 1056 (m), 849 (s). (Identified as [C(NH₂)₃]₂Cu(CO₃)₂ of Section 3.4.1)

Due to the expensive nature of the ligand it was necessary to recover it from the previous synthesis, where it was presumably left in solution when the copper(II), guanidinium and carbonate ions crystallised out as the dominant network product. After several months in the sealed beaker, the solution was filtered to remove the carbonate network crystals and the filtrate solvent removed on a rotary evaporator, giving small blue crystals and organic residue. 10 ml of water was added, the solution was filtered to remove the second batch of insoluble blue crystals, and the filtrate solvent removed again using the rotary evaporator. Colourless organic residue was obtained, which for the purposes of the following reaction was assumed to contain 1.3 mmol 3-hydroxy-3-methyl-glutaric acid.

Subsequent copper tetramer synthesis

3-hydroxy-3-methyl-glutaric acid (1.3 mmol), Cu(NO₃)₂.3H₂O (0.31 g, 1.3 mmol) and guanidinium nitrate (0.32g, 2.6 mmol) were combined in MeOH (18.75 ml). NaOH (0.156 g, 3.9 mmol) was gradually added with rapid magnetic stirring, producing a change from pale to intense dark blue. For crystallisation, the solution was set up for vapour diffusion in a small vial placed inside a larger sealed vial containing ether. Blue crystals formed in moderate yield, selected IR data (cm⁻¹): 3339 (m), 3185 (m), 1624 (m), 1553 (s), 1523 (w), 1377 (s), 1277 (m), 1178 (w), 1146 (w), 1097 (w), 984 (w), 919 (w). Analysis calculated (found) for C₂₀H₅₄Cu₄N₁₂O₁₇: C 24.29 (24.45); H, 5.50 (5.30); N, 17.00 (16.88).

3.4.3.2 – Structure of $\{\text{Cu}_4(\text{L2})_2[\text{C}(\text{NH}_2)_2\text{NH}]_4(\text{OMe})_2\} \cdot 2\text{MeOH} \cdot 3\text{H}_2\text{O}$

The copper tetramer crystallises in the $C2/c$ space group, with a structure that consists of two offset copper(II) dimer subunits, as shown in Figure 3-31. It incorporates two trideprotonated 3-hydroxy-3-methyl-glutaric acid ligands which bridge and also terminally coordinate to the Cu1 and Cu2 centres. Methoxide ions provide bridges between the Cu1 and Cu2 of each dimer subunit, and also bridge between the two subunits to link them into a tetramer. Each copper(II) centre has a terminal guanidine ligand bound in a similar manner to that seen earlier for the hydroxide bridged dimer (Figure 3-8 in Section 3.2.2). The coordination geometry of Cu1 is square-based pyramidal, while Cu2 is square planar.

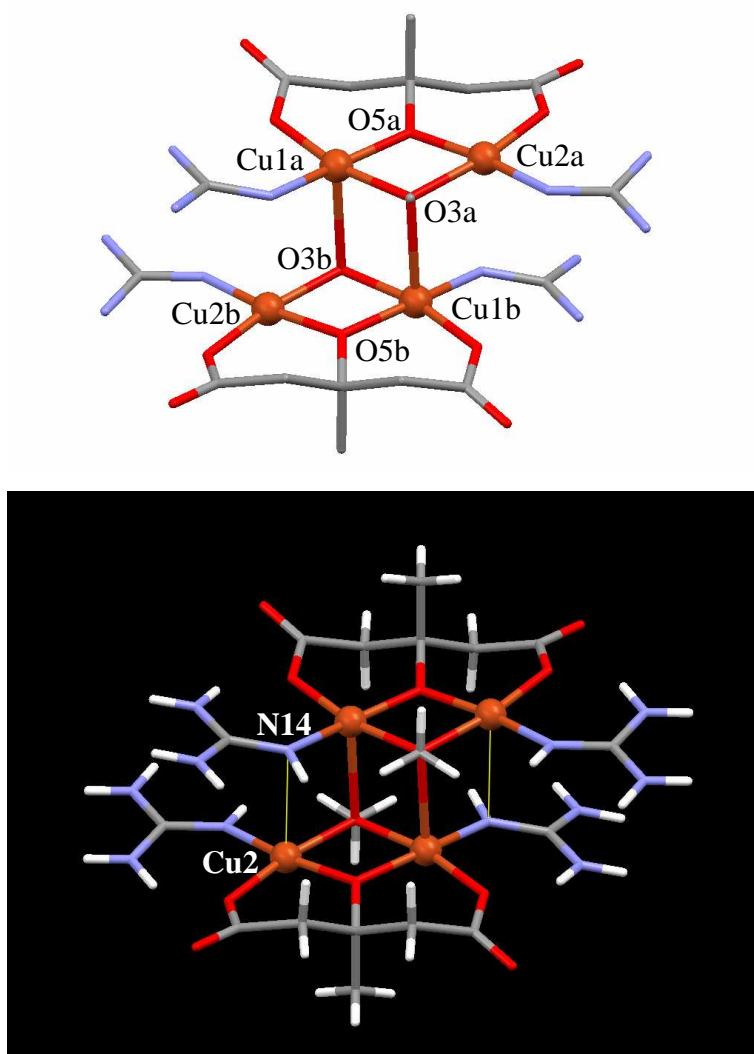


Figure 3-31 – Copper tetramer structure with only the predominant ligand orientations shown for clarity, (Cu orange, O red, C grey, N pale blue, H white (lower) and omitted (upper), long contact interactions highlighted in yellow).

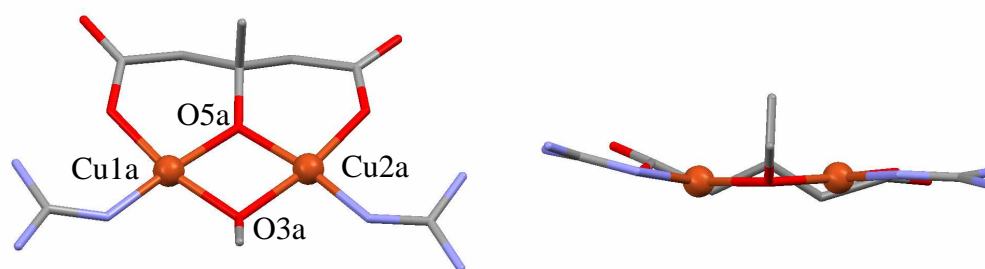


Figure 3-32 – Dimer subunit structure of the copper tetramer (left) and bridging view (right), (Cu orange, O red, C grey, N pale blue, H omitted).

For the purposes of comparison with the other products discussed in this chapter, it is useful to consider the structure of one of the symmetry equivalent dimer subunits of the tetramer, as shown in Figure 3-32. The trideprotonated ligand (L2)³⁻ is disordered over two orientations (methyl group pointing up or down) as was previously seen in the case of the triol dimer (Section 3.4.2.2). The absence of a ligand long contact (such as the α -carboxylate of the citrate) once again leads to a more planar dimer structure as shown in the comparison with the curved hydroxy bridged dimer in Figure 3-33. In the copper tetramer the bridging angles are $\text{Cu1a}-\hat{\text{O}}5\text{a}-\text{Cu2a} = 104.77^\circ$, $\text{Cu1a}-\hat{\text{O}}3\text{a}-\text{Cu2a} = 101.09^\circ$, with bond distances of 1.93 Å (Cu1a-O5a), 1.92 Å (Cu2a-O5a), 1.98 Å (Cu1a-O3a) and 1.97 Å (Cu2a-O3a). These angles are therefore larger than those found for the hydroxide bridged dimer with $\text{Cu}-\hat{\text{O}}(\text{citrate})-\text{Cu} = 95.65^\circ$, $\text{Cu}-\hat{\text{O}}(\text{H})-\text{Cu} = 96.77^\circ$, Cu-O distances 1.95 (citrate) and 1.94 (OH) Å.

When comparing these two structures consideration must also be given to the interactions occurring with other dimers. The hydroxy bridged dimer has a curved structure generated by the citrate ligand, but the position of the guanidine ligands is due to the tubular packing of the dimers within the crystal and the extensive hydrogen bonding (Figure 3-11 in Section 3.2.2). In this tetramer there are long contact interactions between Cu2 and N14 (2.74 Å) which cause the guanidine ligand to bend away (seen Figure 3-31 and the bridging view of Figure 3-32). The Cu1-O3 bonds that link the dimer units into a tetramer have a length of 2.44 Å, with bridging angles of $\text{Cu1a}-\hat{\text{O}}3\text{a}-\text{Cu1b} = 93.65^\circ$ and $\text{Cu2a}-\hat{\text{O}}3\text{a}-\text{Cu1b} = 95.03^\circ$ (and equivalently with a and b reversed).

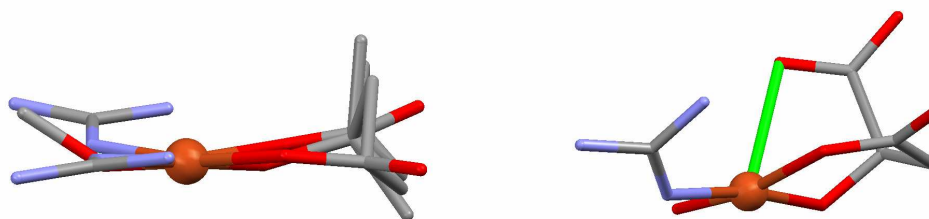


Figure 3-33 – Comparison of the ligand positions relative to the bridging plane in the dimer subunit of the copper tetramer (left) and $[\text{C}(\text{NH}_2)_3]\{\text{Cu}_2\text{cit}[\text{C}(\text{NH}_2)_2\text{NH}]_2(\text{OH})\}$ (right), (Cu orange, O red, C grey, N pale blue, H omitted, long contact highlighted in green).

The $\{\text{Cu}_4(\text{L}2)_2[\text{C}(\text{NH}_2)_2\text{NH}]_4(\text{OMe})_2\}$ species is neutral (since the 3-hydroxy-3-methyl-glutaric acid has central methyl group instead of the carboxylic acid group of citrate), and so no guanidinium counterions are required as found for the hydroxide bridged dimer. The hydrogen bonding network between the tetramers is therefore not quite as extensive, but still involves the $(\text{L}2)^{3-}$ carboxylate oxygen atoms, guanidine ligand hydrogen atoms and includes the lattice solvent.

3.4.3.3 – Magnetic Properties of

$\{\text{Cu}_4(\text{L}2)_2[\text{C}(\text{NH}_2)_2\text{NH}]_4(\text{OMe})_2\} \cdot 2\text{MeOH} \cdot 3\text{H}_2\text{O}$

From structural considerations, antiferromagnetic interactions may occur within the dimer subunits due to the very large bridging angles involved (104.77 and 101.09°) and the planar bridging (much like the triol dimer in Section 3.4.2.3). The smaller bridging angles between the subunits (93.65 and 95.03°) may favour ferromagnetic interactions, but this is complicated by the long bond distances involved (2.44 \AA). Problems were encountered with the stability of the crystals when removed from the mother liquor as the samples were observed to change colour from blue to green-blue on standing in air. This could be due to loss of volatile methanol solvent or absorption of water by the crystals. A magnetic characterisation of the tetramer remains for future work.

- [1] Hudson, T. A.; Berry, K. J.; Moubaraki, B.; Murray, K. S.; Robson, R. *Inorg. Chem.* 2006, 45, 3549.
- [2] Crawford, V. H.; Richardson, H. W.; Wasson, J. R.; Hodgson D. J.; Hatfield, W. E. *Inorg. Chem.* 1976, 15, 2107.
- [3] Astheimer, H.; Haase, W. *J. Chem. Phys.* 1986, 85, 1427.
- [4] Merz, L.; Haase, W. *J. Chem. Soc. Dalton Trans.* 1980, 875.
- [5] Hu, H.; Liu, Y.; Zhang, D.; Liu, C. *Journal of Molecular Structure (Theochem)* 2001, 546, 73.
- [6] Ruiz, E.; Alemany, P.; Alvarez, S.; Cano, J. *J. Am. Chem. Soc.* 1997, 119, 1297.
- [7] Ruiz, E.; Alemany, P.; Alvarez, S.; Cano, J. *Inorg. Chem.* 1997, 36, 3683.
- [8] Ray, M. S.; Chattopadhyay, S.; Drew, M. G. B.; Figuerola, A.; Ribas, J.; Diaz, C.; Ghosh, C. *Eur.J.Inorg.Chem.* 2005, 4562. (CSD structures LAYYAM, LAYYEQ, LAYYIU, LAYYOA)
- [9] Sarkar, B.; Ray, M. S.; Drew, M. G. B.; Figuerola, A.; Diaz, C.; Ghosh, A. *Polyhedron* 2006, 25, 3084. (CSD structures RETDOK, RETDUQ)
- [10] Chumakov, Y. M.; Tsapkov, V. I.; Simonov, Y. A.; Antosyak, B. Y.; Bocelli, G.; Perin, M.; Starikova, Z. A.; Samus, N. M.; Gulya A. P. *Koord.Khim.(Russ.)(Coord.Chem.)* 2005, 31, 621. (CSD structure SEBZAB)
- [11] Bian, H.; Xu, J.; Gu, W.; Yan, S.; Cheng, P.; Liao, D.; Jiang, Z. *Polyhedron* 2003, 22, 2927. (CSD structures ULOSAP, ULOSET)
- [12] Kwiatkowski, E.; Kwiatkowski, M.; Dettlaff-Weglikowska, U.; Ho, D. M. *J.Crystallogr.Spectrosc.Res.* 1992, 22, 411. (CSD structure YAHHUK)
- [13] Costes, J.; Dahan, F.; Laurent, J. *Inorg. Chem.* 1986, 25, 413. (CSD structure DOKJES)
- [14] Kwiatkowski, M.; Kwiatkowski, E.; Olechnowicz, A.; Ho, D. M.; Deutsch, E. *Inorganica Chimica Acta* 1988, 150, 65. (CSD structure GOHVAA)
- [15] Abrahams, B. F.; Haywood, M. G.; Robson R.; Slizys, D. A. *Angew. Chem. Int. Ed.* 2003, 42, 1112.

CAMMAG – Rawson, J. M. *Cammag version 4.1*, University of Cambridge, 2005.

MAGPACK – Borrás-Almenar, J. J.; Clemente-Juan, J. M.; Coronado, E.; Tsukerblat, B. S. *Journal of Computational Chemistry* 2001, 22, 985.

4.0 – 3d-4f Reaction Systems

Since a large spin and anisotropy are important properties for the generation of SMM behaviour, the use of lanthanide ions in cluster syntheses is desirable [1,2]. The large coordination numbers of the lanthanide ions can also help to encourage the formation of larger clusters with more spin centres. 3d-4f systems are attractive since they can be developed from existing synthetic methodology. The cobalt(II) and copper(II) systems described in the previous chapters are good candidates for further studies including lanthanide ions since the citrate ligands have been shown to provide a variety of coordination sites around the outside of the product clusters that are useful for binding additional metal centres.

4.1 – Addition of Lanthanide Ions to the Cobalt Citrate System

4.1.1 – Discussion of Reaction Methodology

The cobalt citrate system is a particularly attractive target for study with lanthanide ions due to the $\{\text{Co}_4(\text{cit})_4\}^{8-}$ cobalt cubane structural motif that is present through the product family. This discrete unit has been shown to function as a single molecule magnet in the case of the Co_4 cluster (Section 2.1) and so it is therefore an ideal building block for the synthesis of larger clusters. The citrate carboxylate oxygens have already demonstrated their capability for binding additional metal centres to form larger clusters in the case of the Co_6 cluster (Section 2.2) and in the 3D network (Section 2.3).

From a synthetic perspective, the most obvious route would involve providing the $\{\text{Co}_4(\text{cit})_4\}^{8-}$ cubane unit in solution using the Co_4 synthesis (Section 2.1.1) followed by the addition of a lanthanide salt for further reaction. Unfortunately the stability of the Co_4 crystals makes $[\text{C}(\text{NH}_2)_3]_8\{\text{Co}_4(\text{cit})_4\} \cdot 4\text{H}_2\text{O}$ the dominant product, even in reactions involving lanthanide(III) ions. A second approach looked at including the lanthanide salt with the cobalt salt and citric acid at the start of the reaction before the base was added. This would allow the lanthanide(III) ions to be present on deprotonation of the ligand and to compete with the cobalt(II) ions for binding. Alternatively, the lanthanide salt was added and the ligand deprotonated before the addition of the cobalt salt. A similar approach was reported for the addition of

lanthanide(III) ions to the synthesis of a stable copper(II) cubane, which was successful in producing *3d-4f* species [3]. Nonetheless, the only crystalline product obtained from our cobalt(II) experiments was found to be $[\text{C}(\text{NH}_2)_3]_8\{\text{Co}_4(\text{cit})_4\}\cdot 4\text{H}_2\text{O}$. Other approaches investigated include varying the metal to ligand ratio and the use of secondary capping ligands (discussed later), yet the cobalt cubane crystals remained the only isolated product. It rapidly became apparent that the syntheses would have to be free of the guanidinium counterion so as not to form the Co_4 cluster crystals, and so the focus was switched to the Co_6 synthesis (Section 2.2.1).

The addition of lanthanide salts to the Co_6 reaction solutions gave a corresponding drop in the solution pH. Since the final solution pH has been shown to be an important factor in the formation of products from this system (Section 2.2.3), various methods were devised for control of the pH after the lanthanide salt addition. The general reaction schemes employed are summarised as follows:

- (A) - 7.2 mmol Co(II) salt and 7.2 mmol citric acid were combined in solution in 10 ml H_2O . The selected base was slowly added until the desired final pH was obtained. (Co_6 reference synthesis)
- (B) - 7.2 mmol Co(II) salt, 7.2 mmol citric acid and 3.6 mmol of Ln(III) salt were combined in solution in 10 ml H_2O . The selected base was slowly added until the desired final pH was obtained.
- (C) - 7.2 mmol Co(II) salt and 7.2 mmol citric acid were combined in solution in 10 ml H_2O . The selected base was added until pH 7 was obtained and then 3.6 mmol of Ln(III) salt was gradually added to the solution under rapid stirring. If required, additional base was slowly added until the desired final pH was obtained.
- (D) - 7.2 mmol Co(II) salt and 7.2 mmol citric acid were combined in solution in 10 ml H_2O . The selected base was added until pH 8 was obtained and then 3.6 mmol of Ln(III) salt was gradually added to the solution under rapid stirring. The resulting solution had a final pH~7.
- (E) - 7.2 mmol Co(II) salt and 7.2 mmol citric acid were combined in solution in 10 ml H_2O . The selected base was added until pH 7 was obtained. Ln(III) salt (3.6 mmol) and capping ligand (3.6 mmol) were dissolved in 10 ml H_2O ,

followed by deprotonation by addition of base (ratio as appropriate). The Ln(III) solution was stirred for 15 mins and then added dropwise to the Co(II) solution. Further base was then added until the desired final pH was obtained.

The reactions were set up for crystallisation by mixing aliquots of solution of varying dilution with MeOH, EtOH or ⁱPrOH, and by associated vapour diffusion techniques. If the reactant solutions were found to be miscible with these alcohols, Na₂SO₄ was added. Slow evaporation in Petri dishes was also used where appropriate.

The metal salts used were either the sulphate or nitrate. Sulphate salts were initially chosen since this was the counterion originally used in the synthesis of the Co₆ cluster [4], but it was discovered that the lanthanide sulphates had a low solubility in the reaction solutions. Although the nitrate salts were much more soluble, the solutions had a tendency to form oils when attempts were made to crystallise them. Reactions using NaHCO₃ also often formed oils and NMe₄OH.5H₂O was the preferred base.

The experiments involving addition of Gd(III) salts often suffered from problems with precipitation, which prevented attempts to obtain crystals by the traditional techniques previously described. Initially this problem had been countered to some extent by either holding the reaction solution pH at a point lower than that of precipitation, by adding less Gd(III) salt than ideally desired, or by filtering the solution and attempting to crystallise a product from the filtrate. The later approach seemed to be the most promising, as a product may still have been present in the solution even if the majority of it had precipitated. Indeed, a lower concentration in the solution can lead to slower crystallisation and better crystals.

However, a problem with this approach was that there was no convenient, routine way to prove that Gd(III) was present in the filtrate solution, or in the precipitate. To resolve this issue the Gd(III) was replaced with Er(III), which can be easily detected by measuring the electronic spectrum. At reaction solution concentrations the Er(III) peaks are visible in the spectrum along with the broad Co(II) peak, as shown in Figure 4-1. The Er(III) peaks not only show that the lanthanide ion is present, but also allow calculation of the concentration present in solution, which is useful in characterising filtrate solutions. In addition, the absorbance of the hypersensitive peak of Er(III)

(521 nm) relative to the reference peak (654 nm) indicates the coordination environment of the lanthanide ion, which is useful in determining if the ligand has successfully bound [5]. The increase in the ratio of hypersensitive peak absorbance to reference peak absorbance from the uncoordinated Er(III) salt solution peak ratio of ~ 2.2:1 to values of between 4:1 and 8:1 suggest that the lanthanide ions are indeed successfully binding to the ligands in the reactions. It was thought that if a cluster could be produced containing Er(III), an analogous product could be obtained using other lanthanide ions such as Gd(III).

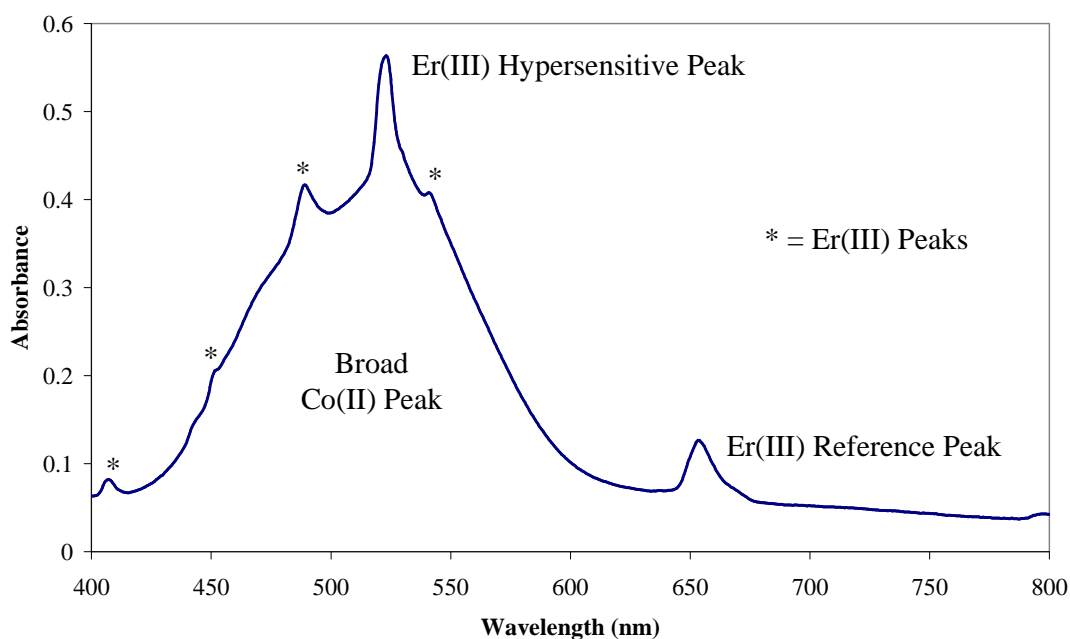


Figure 4-1 – An example of a spectrum from a reaction solution containing Co(II) and Er(III) illustrating the clearly visible peaks from the lanthanide(III) ion.

The vast majority of the lanthanide(III) ions were found to be removed in the precipitation, and since the precipitates were also pink, this would indicate a mixed cobalt(II)/lanthanide(III) product. It was thought that the precipitation could be the result of polymerisation through the high coordination number lanthanide sites, creating large insoluble species. To try and prevent this, additional capping ligands were included in the reactions in order to reduce the available coordination sites on the lanthanide ions. The most effective method (E) was found to involve combining the capping ligand and lanthanide salt in solution, then adding base to deprotonate the ligand for coordination before it was added to the pH 7 Co_6 reaction solution. A variety of capping ligands were trialled including diglycolic acid, d-mandelic acid,

bis-tris, acetylacetonone and acetic acid (Figure 4-2). Acetylacetonone and acetic acid could be conveniently included in the synthesis by using their cobalt salts as starting materials, while diglycolic acid was the most successful additional ligand for preventing precipitation. Even so, no products were obtained from the crystallisation attempts of the reactions involving capping ligands.

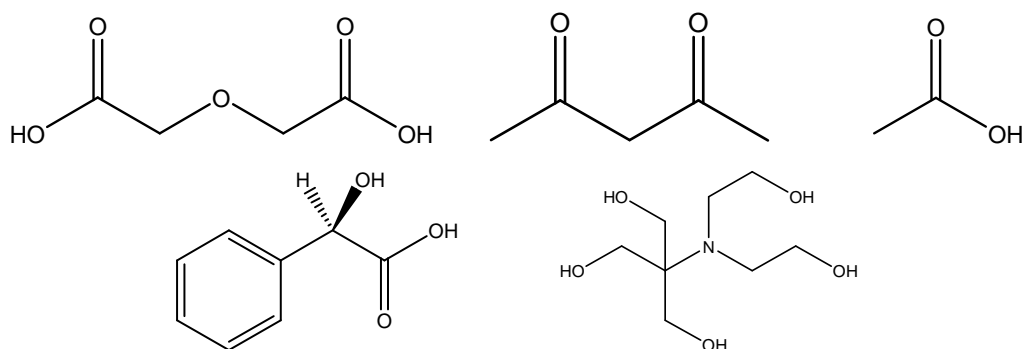


Figure 4-2 – Structure diagrams of the capping ligands, diglycolic acid (upper left), acetylacetonone (upper centre), acetic acid (upper right), d-mandelic acid (lower left) and bis-tris (lower right).

It was later discovered that the cobalt/lanthanide precipitates redissolved on further addition of base to the reaction mixture. This could indicate the presence of a neutral intermediate which would be insoluble in water and lead to precipitation. On further addition of base the intermediate could become charged once again and so return to solution. A consequence of including a greater amount of base is that the final solution pH is around 8. Such a high final pH had previously been problematic for crystallisation in the standard Co₆ reaction at pH 7.5, and required the addition of Na₂SO₄ to obtain product crystals. A reference reaction using the standard Co₆ synthesis with the final pH increased to 8 only gave a few crystals of very poor quality (Section 2.2.3). Crystallisation at such high pH values is therefore very difficult, possibly due to complex hydroxide species that could be formed. Evidence for this theory is based on experiments where, after dissolving the precipitates at high pH, acid was added to adjust the pH back to 7 for crystallisation. Although the products present remained in solution (no precipitation) as the pH was reduced, the crystallisation attempts were again unsuccessful suggesting that additional hydroxide species had been retained. Future investigation of these reactions in alternative solvents may allow the formation of crystalline products.

4.2 – Addition of Lanthanide Ions to the Copper Citrate System

The addition of lanthanide ions to the copper guanidinium citrate system was of interest due to the ability of the guanidinium counterion to rapidly crystallise products from solution. The reaction methodology employed was along similar lines to that already discussed for the cobalt citrate system, but without the use of capping ligands in this case. The coordinative flexibility displayed by copper in the products of Chapter 3 is a particularly useful property for further reactions with lanthanide(III) ions, since ligand reorganisation and a variety of coordination geometries are likely to be important factors in the creation of new heterometallic species.

Unfortunately very few crystals were obtained from the heterometallic syntheses, and those that did form on slow evaporation tended to be encased in excessive colourless residue, which hampered attempts to separate and characterise them. The lack of readily formed crystals from the reaction system is surprising, however it is possible that heterometallic species involving citrate, copper(II) and lanthanide(III) ions may have an overall positive charge, and would therefore not require a positive counterion such as $[\text{C}(\text{NH}_2)_3]^+$. However, some novel negatively charged products which include guanidinium counterions were isolated, including a *3d-4f* product.

4.2.1 – Copper(II) Monomer $[\text{C}(\text{NH}_2)_3]_2\{\text{Cu}(\text{H}_2\text{cit})_2\}$

4.2.1.1 – Synthesis of $[\text{C}(\text{NH}_2)_3]_2\{\text{Cu}(\text{H}_2\text{cit})_2\}$

To a solution of citric acid monohydrate (0.55 g, 2.6 mmol) in water (25 ml) was added a solution of guanidinium carbonate (1.87 g, 10.4 mmol) in water (25 ml) followed by $\text{Gd}(\text{NO}_3)_3 \cdot 6\text{H}_2\text{O}$ (0.59 g, 1.3 mmol). To the resultant solution was slowly added $\text{Cu}(\text{NO}_3)_2 \cdot 3\text{H}_2\text{O}$ (0.63 g, 2.6 mmol) in water (25 ml). After half of the $\text{Cu}(\text{NO}_3)_2 \cdot 3\text{H}_2\text{O}$ was added a white precipitate began to form and persisted even after the full amount of $\text{Cu}(\text{NO}_3)_2 \cdot 3\text{H}_2\text{O}$ was added. To the solution containing the precipitate was then added an excess of citric acid monohydrate to reduce the pH of the solution from pH 9 to pH 6 at which point the precipitate dissolved. Pale blue crystals of $[\text{C}(\text{NH}_2)_3]_2\{\text{Cu}(\text{H}_2\text{cit})_2\}$ formed in moderate yield after three weeks of slow evaporation. Selected IR data (cm^{-1}): 3349 (m), 3140 (m), 1713 (m), 1653 (s), 1562 (s), 1438 (m), 1380 (s), 1244 (s), 1064 (m), 899 (m).

4.2.1.2 – Structure of $[\text{C}(\text{NH}_2)_3]_2\{\text{Cu}(\text{H}_2\text{cit})_2\}$

The copper(II) monomer $[\text{C}(\text{NH}_2)_3]_2\{\text{Cu}(\text{H}_2\text{cit})_2\}$ crystallises in the $P2_1/n$ space group and consists of one copper(II) centre bound by two doubly deprotonated citrate ligands with charge balance provided by two guanidinium ions. The monomer structure is similar to that of a literature example with formula $[\text{NH}_4]_4\{\text{Cu}(\text{Hcit})_2\}$, which has triply deprotonated citrate ligands and ammonium counterions [6]. A comparison of the two monomers is given in Figure 4-3.

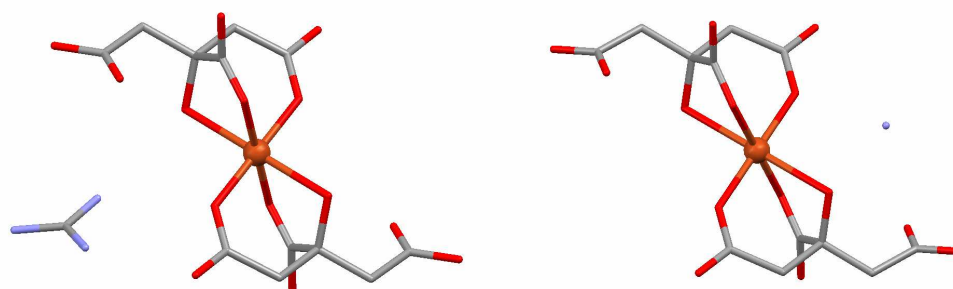


Figure 4-3 – Comparison of the copper(II) citrate monomer structures $[\text{C}(\text{NH}_2)_3]_2\{\text{Cu}(\text{H}_2\text{cit})_2\}$ (left) and $[\text{NH}_4]_4\{\text{Cu}(\text{Hcit})_2\}$ (right), (Cu orange, O red, C grey, N pale blue, H omitted). Ammonium example is CSD structure JOCNEU [6].

Both structures contain distorted octahedral copper(II) centres coordinated by the citrate alcohol group, one α -carboxylate and one β -carboxylate. The copper geometry is distorted as a result of the short α -carboxylate, which binds with a $\text{O}-\hat{\text{C}}\text{u}-\text{O}$ angle of 78° (guanidinium) or 74° (ammonium) relative to the alcohol, rather than at 90° . A Jahn-Teller elongation is seen in both monomers along the copper alcohol bonds.

It should be noted that in the literature example with ammonium ions [6], only the citrate alcohol group is protonated, while in this case with guanidinium ions both the alcohol and the trailing uncoordinated β -carboxylic acid groups are protonated. In this structure both of the protons were located as Q peaks in the Fourier difference map using CRYSTALS. Charge balance arguments based on the number of counterions also supports this formulation. The double protonation of citrate in the monomer may be unusual, however $[\text{C}(\text{NH}_2)_3]_2\{\text{Cu}(\text{H}_2\text{cit})_2\}$ was formed as a side product due to excess addition of citric acid to the copper(II)/gadolinium(III) system to lower the pH (amusingly, the ammonium copper(II) monomer was also formed as a

side product in the attempted synthesis of a copper(II)/antimony(III) citrate [6]. Additional evidence for the β -carboxylate protonation of the citrate in the guanidinium copper(II) monomer comes from the hydrogen bonding pattern between the monomers which displays the distinctive carboxylic acid hydrogen bonding dimer motif, as shown in Figure 4-4. This arrangement is not seen for the literature structure of $[\text{NH}_4]_4\{\text{Cu}(\text{Hcit})_2\}$ with ammonium counterions and triply deprotonated citrate [6].

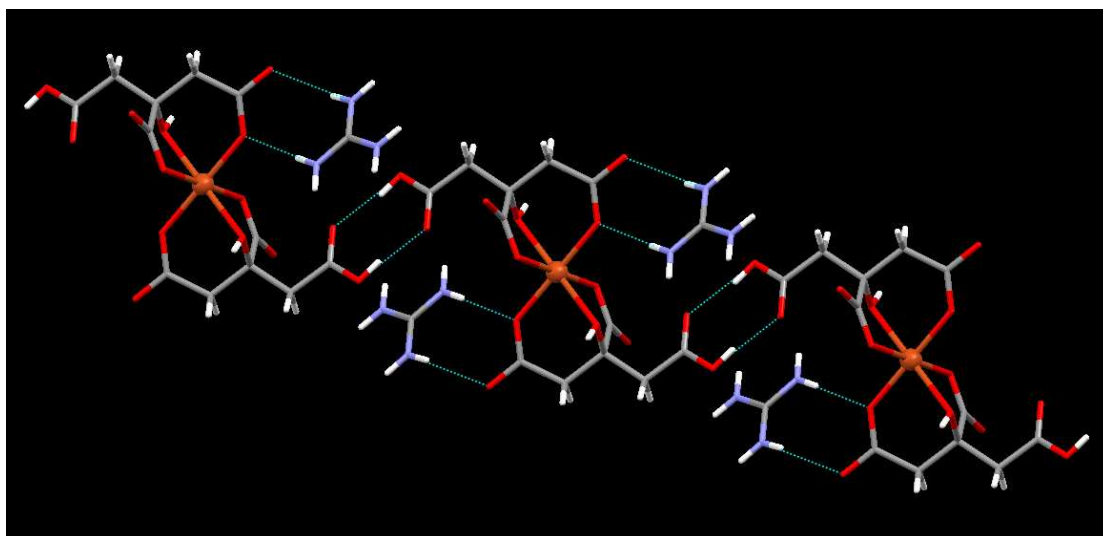


Figure 4-4 – The carboxylic acid hydrogen bonding dimer motif seen between the copper(II) monomers $[\text{C}(\text{NH}_2)_3]_2\{\text{Cu}(\text{H}_2\text{cit})_2\}$, (Cu orange, O red, C grey, N pale blue, H white).

It is also interesting to compare the structure of the guanidinium copper(II) citrate monomer $[\text{C}(\text{NH}_2)_3]_2\{\text{Cu}(\text{H}_2\text{cit})_2\}$ with the cobalt(II) and nickel(II) monomers, $[\text{C}(\text{NH}_2)_3]_4\{\text{Co}(\text{Hcit})_2\} \cdot 2\text{H}_2\text{O}$ and $[\text{C}(\text{NH}_2)_3]_4\{\text{Ni}(\text{Hcit})_2\} \cdot 2\text{H}_2\text{O}$ [7]. Figure 4-5 reveals that both of the citrate ligands in the cobalt(II) and nickel(II) monomers point to the same side in a ‘cis’ arrangement compared to the ‘trans’ copper(II) monomer where the two citrates point in opposite directions. This variation in the citrate ligands positions can be explained by considering the hydrogen bonding interactions of the carboxylate groups.

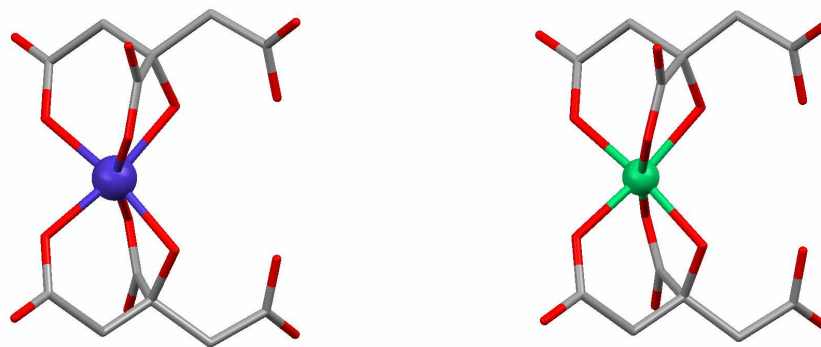


Figure 4-5 – The structures of the cobalt(II) (left) and nickel(II) (right) citrate monomers with guanidinium counterions, (Co blue, Ni green, O red, C grey, H omitted). CSD structures Co QEQVAJ and Ni QEQTUB [7].

Figure 4-6 shows that in the nickel(II) monomer the oxygen atoms of the three carboxylate groups hydrogen bond to the hydrogen atoms of three guanidinium ions. Since each carboxylate makes two bonds to a guanidinium, clearly all three must be deprotonated and therefore the citrate has a central alcohol group. The cobalt(II) monomer has the same structure and packing as the nickel(II) analogue. In the case of the copper(II) monomer only two of the carboxylate groups have a hydrogen bonded guanidinium ion, with the trailing β -carboxylic acid hydrogen bonding with an equivalent group on a neighbouring monomer (as seen in Figure 4-4). Therefore the carboxylic acid is protonated in addition to the central alcohol group of citrate.

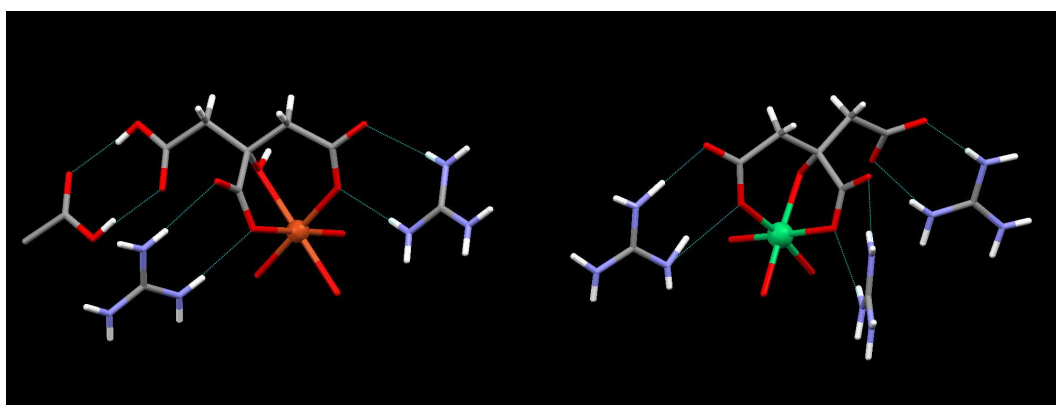


Figure 4-6 – The citrate carboxylate hydrogen bonding seen in the copper(II) (left) and nickel(II) (right) monomers, with only one ligand shown for clarity (Cu orange, Ni green, O red, C grey, H white). CSD structure Ni QEQTUB [6].

As expected, the guanidinium counterions play an important role in the hydrogen bonding network of the each of the monomer structures. Each cation has two hydrogen bonds to each carboxylate (one α -, one β -) of neighbouring monomer units, as shown for copper(II) structure $[\text{C}(\text{NH}_2)_3]_2\{\text{Cu}(\text{H}_2\text{cit})_2\}$ in Figure 4-7 and the nickel(II) structure $[\text{C}(\text{NH}_2)_3]_4\{\text{Ni}(\text{Hcit})_2\} \cdot 2\text{H}_2\text{O}$ in Figure 4-8.

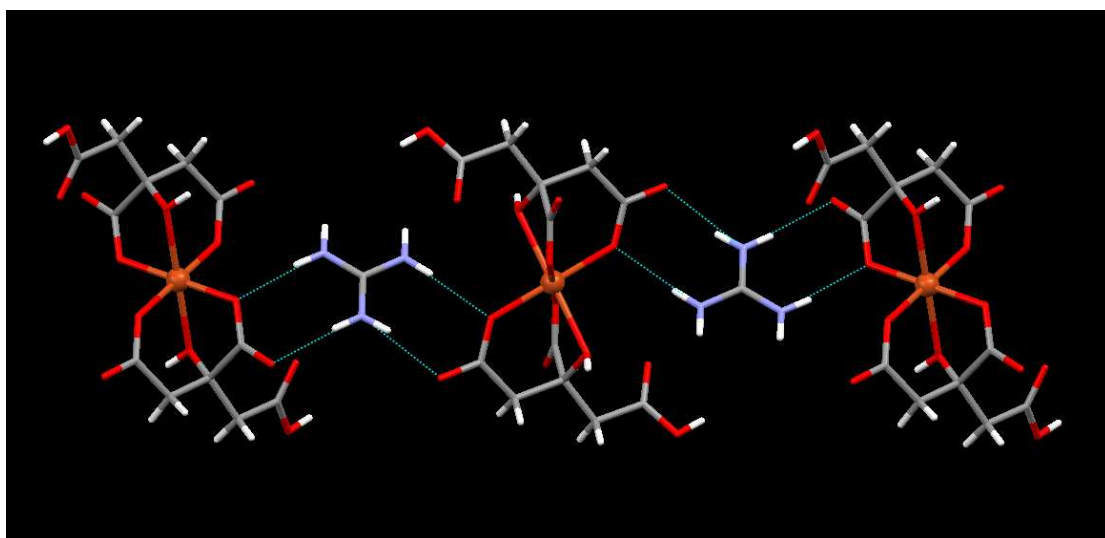


Figure 4-7 – Hydrogen bonding between the copper(II) monomer citrate carboxylates and the guanidinium counterions, (Cu orange, O red, C grey, N pale blue, H white).

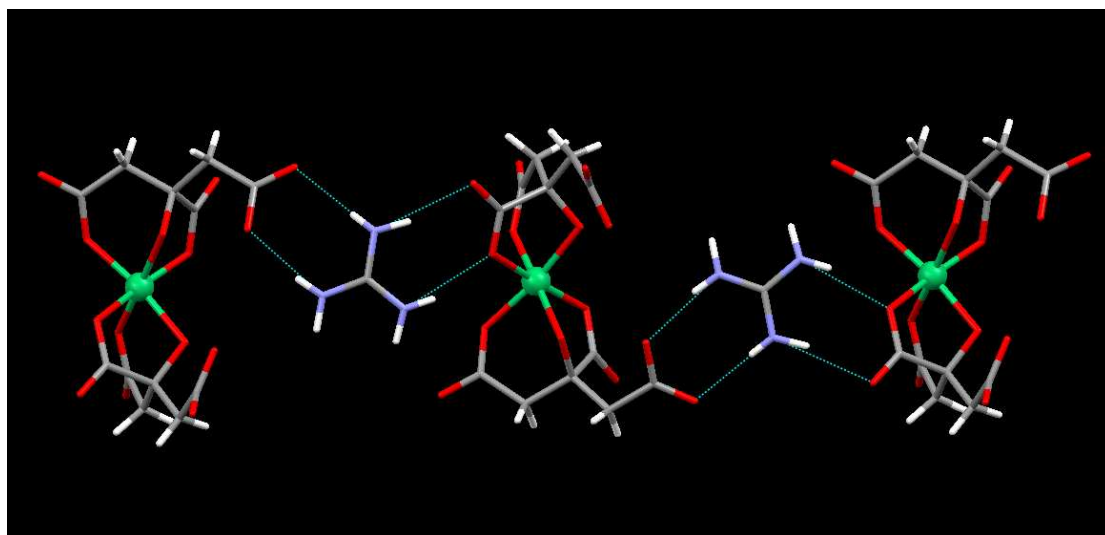


Figure 4-8 – Hydrogen bonding between the nickel(II) monomer citrate carboxylates and the guanidinium counterions, (Ni green, O red, C grey, N pale blue, H white).

CSD structure QEQTUB.

4.2.2 – The Copper(II) Erbium(III) Network

$\{[\text{C}(\text{NH}_2)_3]_{5.33}\text{Na}_2\text{Cu}_{1.33}\text{Er}_2(\text{CO}_3)_8(\text{H}_2\text{O})_2\}.6\text{H}_2\text{O}$

4.2.2.1 – Synthesis of $\{[\text{C}(\text{NH}_2)_3]_{5.33}\text{Na}_2\text{Cu}_{1.33}\text{Er}_2(\text{CO}_3)_8(\text{H}_2\text{O})_2\}.6\text{H}_2\text{O}$

Citric acid monohydrate (1.09 g, 5.2 mmol), $\text{Cu}(\text{NO}_3)_2 \cdot 3\text{H}_2\text{O}$ (1.26 g, 5.2 mmol), guanidinium nitrate (1.27g, 10.4 mmol) and $\text{Er}(\text{NO}_3)_3$ (1.26 ml, 2.055 M, 2.6 mmol) were combined in water (20 ml). NaOH (~1.41 g) was gradually added with rapid magnetic stirring. A precipitate bloom appeared at pH 2.15 which slowly redissolved at ~ pH 7.2 followed by a rapid jump to a final pH 12.90. The solution was filtered and left to slowly evaporate. Pale blue crystals formed in low yield, selected IR data (cm^{-1}): 3324 (m), 3116 (m), 1683 (s), 1594 (w), 1478 (s), 1408 (s), 1339 (s), 1157 (w), 1045 (w), 849 (m), 726 (s). Analysis, calculated (found) for $\text{C}_{13.33}\text{H}_{47.98}\text{Cu}_{1.33}\text{Er}_2\text{N}_{15.99}\text{O}_{32}\text{Na}_2$: C, 11.36 (10.96); H, 3.43 (2.64); N, 15.89 (15.33). Only small quantities of product crystals were available for analysis, and the formula given was the best agreement between microanalysis and crystallography studies for this complicated non-stoichiometric network compound.

4.2.2.2 – Structure of $\{[\text{C}(\text{NH}_2)_3]_{5.33}\text{Na}_2\text{Cu}_{1.33}\text{Er}_2(\text{CO}_3)_8(\text{H}_2\text{O})_2\}.6\text{H}_2\text{O}$

The three dimensional copper(II) erbium(III) network crystallises in the $Pm\bar{3}n$ space group. It consists of eight coordinate erbium(III) centres that are linked by carbonate ions to four coordinate, square planar copper(II) centres in plate-like structural subunits as shown in Figure 4-9. Charge balance for the network is provided by guanidinium and sodium counterions. The sodium counterions are coordinated by the carbonate ions and are disordered over octahedral sites in the centre of the plates and also over sites on either side of the copper(II) centre (which are occupied in the absence of a copper(II) centre at such a point in the network). The central octahedral sodium centres have an out-of-plane displacement relative to the network carbonate ions, which has previously been observed for other alkali metal ions in copper carbonate networks [8]. Each guanidinium counterion has six hydrogen bonds between the hydrogen atoms of the NH_2 groups and the oxygen atoms of three neighbouring carbonate ions. Such extensive hydrogen bonding explains why the product crystals are insoluble once formed.

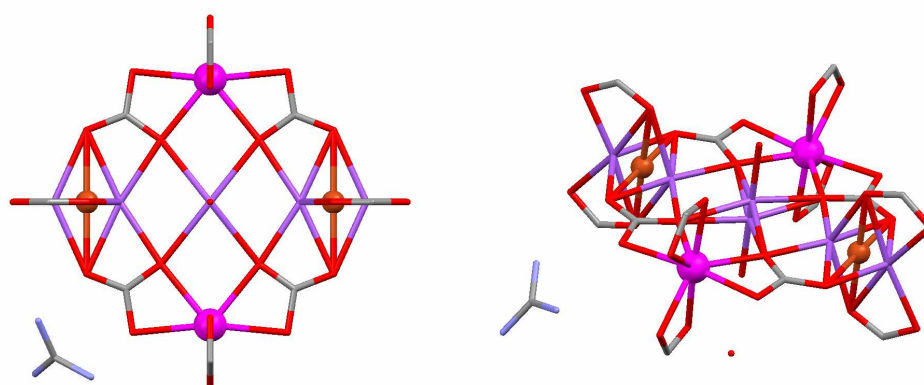


Figure 4-9 – Two views of the plate like structural subunit seen in $\{[C(NH_2)_3]_{5.33}Na_2Cu_{1.33}Er_2(CO_3)_8\} \cdot 6H_2O$, (Cu orange, Er pink, O red, C grey, N pale blue, Na violet, H omitted).

The plate-like structural subunits are linked via the metal centres to neighbouring perpendicular plates to form cages as shown in Figure 4-10. Six of the plate subunits form a cube which has truncated corners (of hexagonal shape) that are occupied by the hydrogen bonded guanidinium ions. This gives an overall structure (Figure 4-11) that has the sodalite topology [8]. The inside of each cage is lined by eight guanidinium ions that define the triangular faces of a central octahedron that is filled by six lattice water as shown in Figure 4-12.

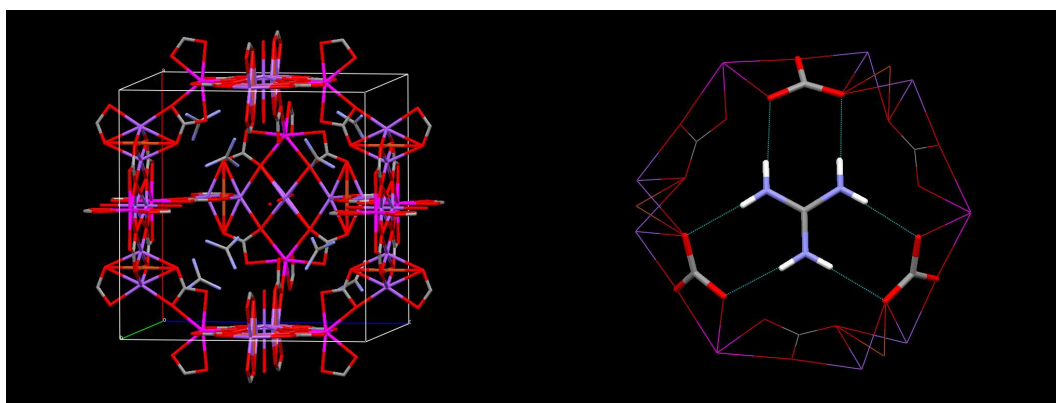


Figure 4-10 – The perpendicular arrangement of the plate like subunits to form a sodalite type cage (left, with nearest cage face and hydrogen omitted for clarity) and the guanidinium counterion hydrogen bonding on the hexagonal faces (right), (Cu orange, Er pink, O red, C grey, N pale blue, Na violet, H white).

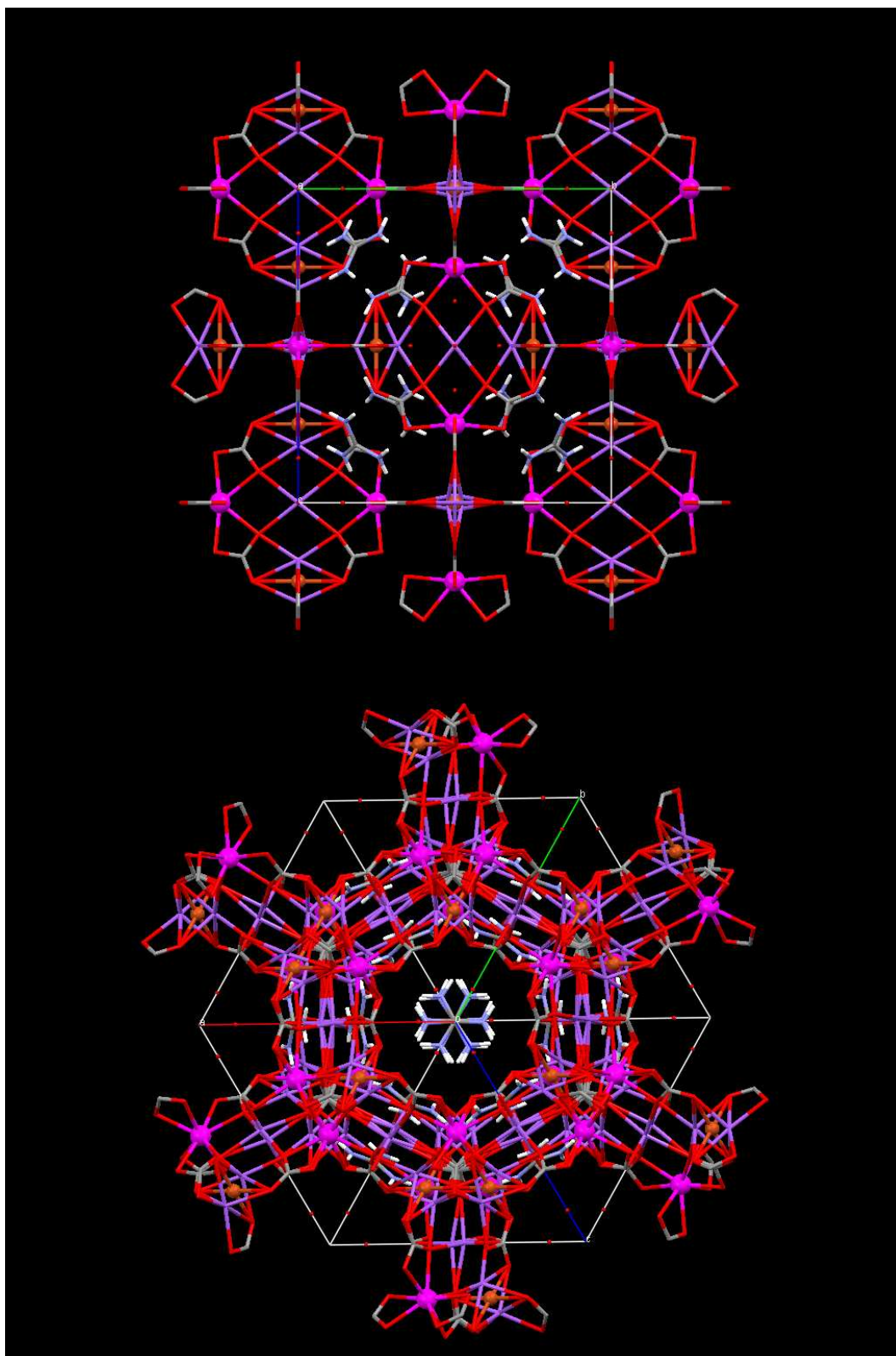


Figure 4-11 – The Cu(II) Er(III) network structure, viewed along the crystallographic *a* axis (upper) and along the channels containing guanidinium counterions and lattice water (lower), (Cu orange, Er pink, O red, C grey, N pale blue, Na violet, H white).

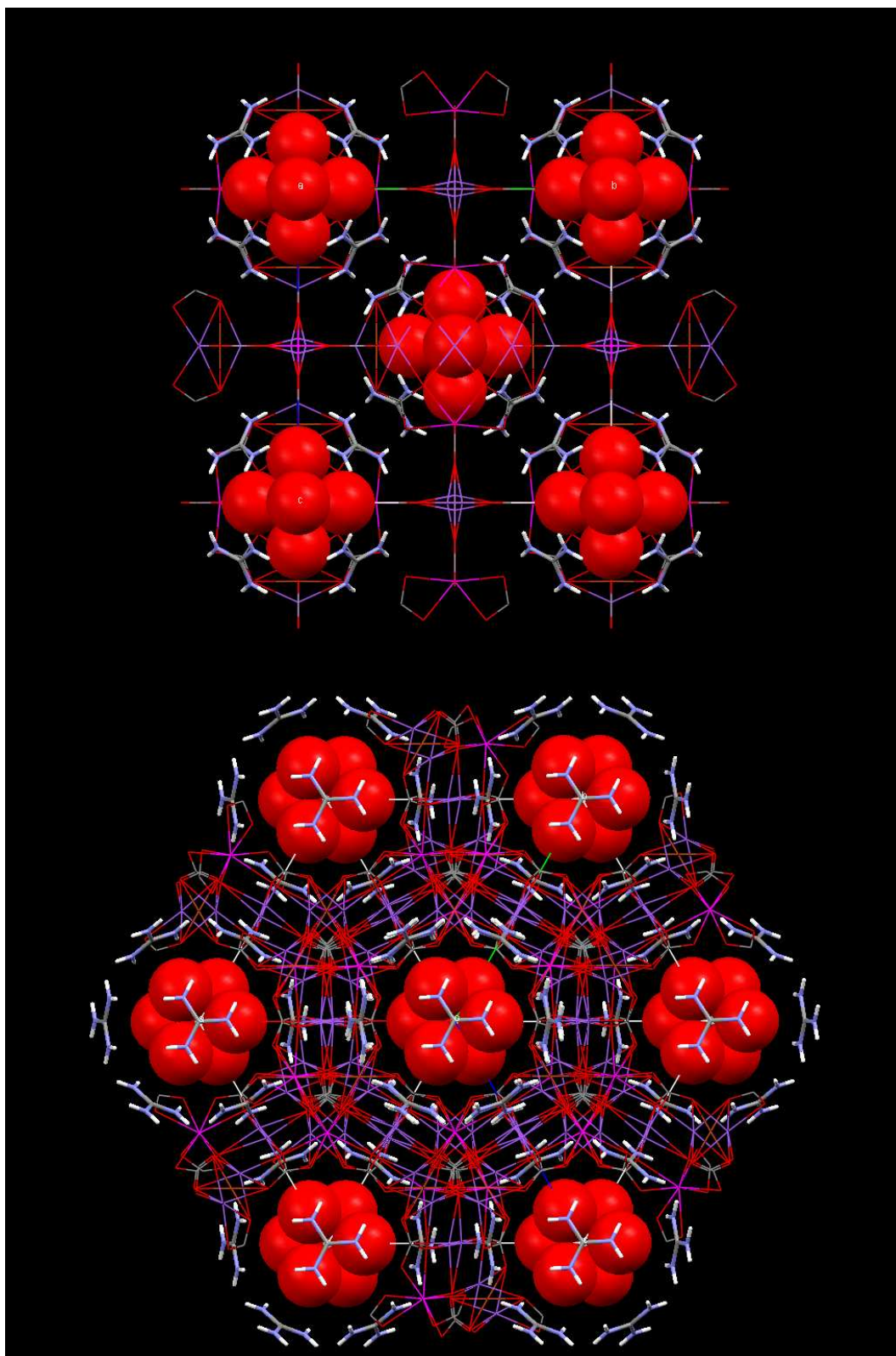


Figure 4-12 – The Cu(II) Er(III) network structure, highlighting the lattice water in the cage centres (red oxygen spacefill) and the surrounding guanidinium counterions, viewed along the crystallographic *a* axis (upper) and along the channels (lower), (Cu orange, Er pink, O red, C grey, N pale blue, Na violet, H white).

It is interesting to note that a similar carbonate based copper(II) gadolinium(III) network $\{\text{Cu}_6(\text{CO}_3)_{12}[\text{C}(\text{NH}_2)_3]_8\} \cdot 2\text{Gd} \cdot 2\text{K} \cdot 4\text{OH} \cdot \text{H}_2\text{O}$ has previously been reported in the literature [8], which crystallises in the $Im\bar{3}m$ space group. The overall structural features of the two networks are similar in appearance as shown in Figure 4-13. However, the literature structure differs in that the network consists only of (six coordinate) octahedral copper(II) centres linked by carbonate ions, while the gadolinium(III) ions are located within the highly disordered contents of the cages. In some respects this is quite surprising, since the copper(II) centres occupy sites that could accommodate larger eight coordinate lanthanide(III) centres (as found in our erbium(III) network). It is also surprising that the large gadolinium(III) ions can fit inside the cages that also contain lattice water (as discussed earlier) and potassium counterions, in an environment that provides comparatively few coordination sites. No detailed discussion of the network structure was presented in the literature [8].

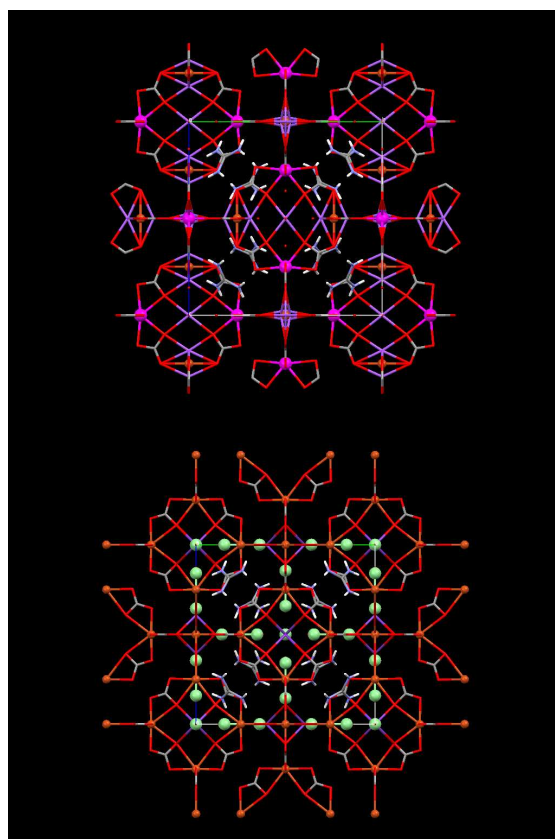


Figure 4-13 – A comparison of the unit cells viewed along the a axis in $\{[\text{C}(\text{NH}_2)_3]_{5.33}\text{Na}_2\text{Cu}_{1.33}\text{Er}_2(\text{CO}_3)_8(\text{H}_2\text{O})_2\} \cdot 6\text{H}_2\text{O}$ (upper) and CSD structure WABWEC $\{\text{Cu}_6(\text{CO}_3)_{12}[\text{C}(\text{NH}_2)_3]_8\} \cdot 2\text{Gd} \cdot 2\text{K} \cdot 4\text{OH} \cdot \text{H}_2\text{O}$ (lower) [8], (Cu orange, Er pink, Gd pale green, O red, C grey, N pale blue, Na violet, K purple, H white).

4.2.2.3 – Magnetic Properties of

$\{[\text{C}(\text{NH}_2)_3]_{5.33}\text{Na}_2\text{Cu}_{1.33}\text{Er}_2(\text{CO}_3)_8(\text{H}_2\text{O})_2\} \cdot 6\text{H}_2\text{O}$

The temperature dependence of χT for the copper(II) erbium(III) network is shown in Figure 4-14. On cooling from 300 K the curve shows a gradual decline with a more rapid decrease below 50 K. This decrease in χT is indicative of antiferromagnetic exchange interactions between the metal centres of the network. The χT curve shape is similar to that reported for the 2D erbium(III) network $\{\text{Er}(\text{Hcit})\text{H}_2\text{O}\}_n$ which exhibits antiferromagnetic coupling, and both network compounds display linear relationships in plots of χ^{-1} vs T [9]. The field cooled and zero field cooled curves for the copper(II) erbium(III) network sample were coincident. No frequency dependent signals were observed in the out-of-phase component of the ac susceptibility, and no hysteresis loops were observed in magnetisation measurements at 2 K.

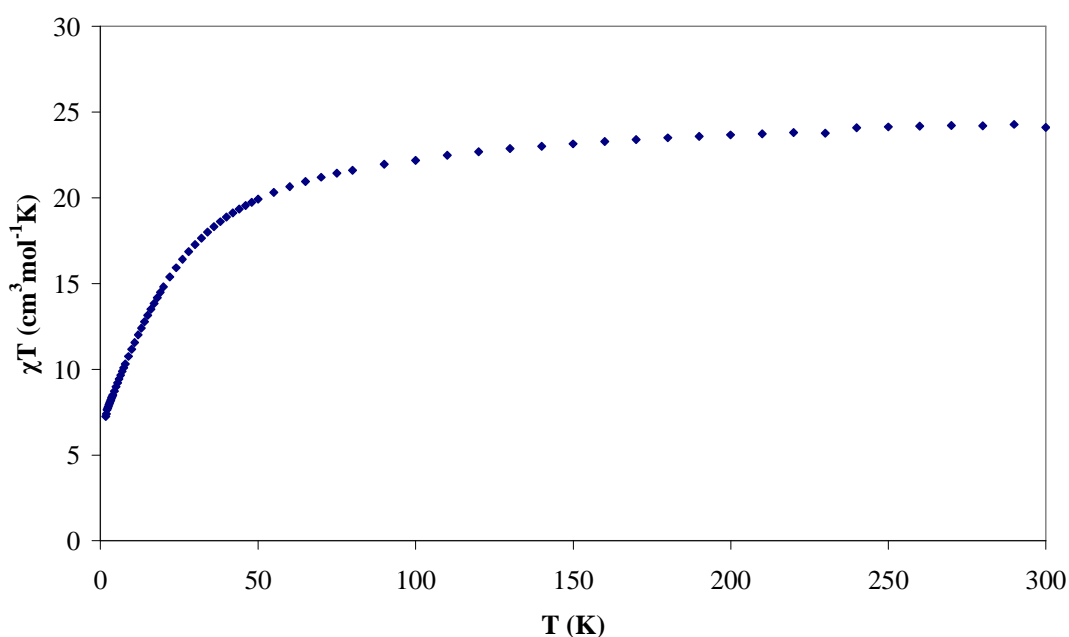


Figure 4-14 – Temperature dependence of χT for $\{[\text{C}(\text{NH}_2)_3]_{5.33}\text{Na}_2\text{Cu}_{1.33}\text{Er}_2(\text{CO}_3)_8(\text{H}_2\text{O})_2\} \cdot 6\text{H}_2\text{O}$, measured in a 1000 Oe field.

- [1] Murrie, M.; Price, D. J. *Annu. Rep. Prog. Chem., Sect A*, 2007, 103, 20.
- [2] Aromi, G.; Brechin, E. K., *Synthesis of 3d Metallic Single-Molecule Magnets, Structure and Bonding*, Springer, Berlin, 2006, 122, 1.
- [3] Aronica, C.; Chastanet, G.; Pilet, G.; Le Guennic, B.; Robert, V.; Wernsdorfer, W.; Luneau, D. *Inorg. Chem.* 2007, 46, 6108.
- [4] Murrie, M.; Teat, S. J.; Stöckli-Evans, H.; Gudel, H. U. *Angew. Chem. Int. Ed.* 2003, 42, 4653.
- [5] Peacock, R. D., *The Intensities of Lanthanide f-f Transitions, Structure and Bonding 22*, Springer, Berlin, 1975, 104.
- [6] Bott, R. C.; Sagatys, D. S.; Lynch, D. E.; Smith, G.; Kennard, C. H. L.; Mak, T. C. W. *Aust. J. Chem.* 1991, 44, 1495. (CSD structure JOCNEU)
- [7] Shvelashvili, A. E.; Miminoshvili, E. B.; Belsky, V. K.; Kuteliya, E. R.; Sakvarelidze, T. N.; Ediberidze, D. A.; Tavberidze, M. G. *Bull. Acad. Sci. Georgia.* 2000, 94. (CSD structures QEQVAJ, QEQTUB)
- [8] Abrahams, B. F.; Haywood, M. G.; Robson R.; Slizys, D. A. *Angew. Chem. Int. Ed.* 2003, 42, 1112. (CSD structures WABVOL, WABWEC)
- [9] Zhou, R.; Song, J.; Yang, Q.; Xu, X.; Xu, J.; Wang, T. *Journal of Molecular Structure* 2008, 877, 115.

5.0 – The Nickel Citrate System

The nickel citrate system has previously yielded a variety of interesting products, including Ni₄, Ni₇, Ni₈, and Ni₂₁ clusters. The Ni₄ cluster [C(NH₂)₃]₈{Ni₄(cit)₄}.6H₂O [1] is a cubane that is an analogue of the Co₄ cluster (Section 2.1), and it will be discussed later in Section 5.3. The Ni₈ clusters include an example containing two distorted nickel tetrahedra ('open' cubane type structures) in the cluster [NMe₄]₁₀{Ni₈(cit)₆(OH)₂(H₂O)₂} [2] that can also be obtained with an alternative crystal packing due to variation in the number of lattice water molecule involved [3]. A second 'dehydrated' Ni₈ cluster [NMe₄]₁₀{Ni₈(cit)₆(OH)₂} can be obtained from the reaction by crystallisation at 50 °C rather than ambient temperature. The application of heat causes reorganisation of the citrate ligands and the formation of two nickel cubanes (Figure 5-1) [2].

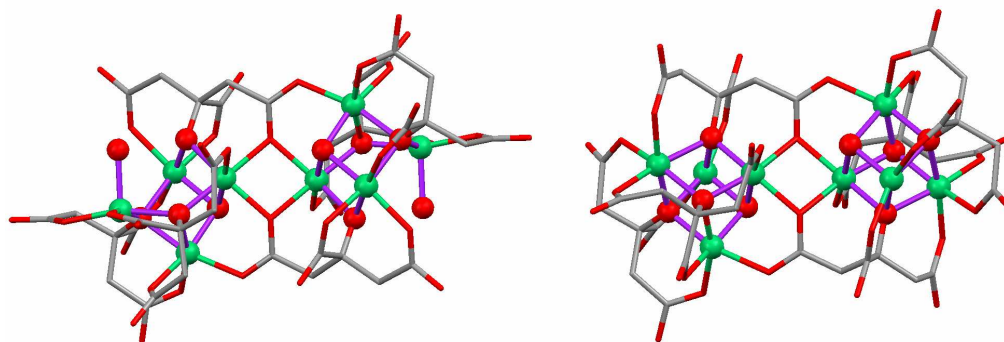


Figure 5-1 – Comparison of the anion structures in [NMe₄]₁₀{Ni₈(cit)₆(OH)₂(H₂O)₂} with 'open' cubanes (left) and [NMe₄]₁₀{Ni₈(cit)₆(OH)₂} with complete cubanes (right), (Ni green, O red, C grey, H omitted). CSD structures HUPQOY and HUPQUE [2].

The Ni₇ cluster [NMe₄]₅Na₅{Ni₇(cit)₆(H₂O)₂} and the Ni₂₁ cluster [NMe₄]₈Na₈{Ni₂₁(cit)₁₂(OH)₁₀(H₂O)₁₀} can both be obtained from one reaction solution via careful control of the amount of co-solvent used for the crystallisation process (Figure 5-2) [4]. Further work [5] revealed that reducing the solution volume by heating rather than slow evaporation favours the formation of the Ni₂₁ cluster over the smaller Ni₇. Variation in the metal to ligand ratio also allowed isolation of the Ni₂₁ cluster with different combinations of counterions in the form of [NMe₄]₁₆{Ni₂₁(cit)₁₂(OH)₁₀(H₂O)₁₀} and [NMe₄]₁₄Na₂{Ni₂₁(cit)₁₂(OH)₁₀(H₂O)₁₀}, the later having also been shown to function as a single molecule magnet [5].

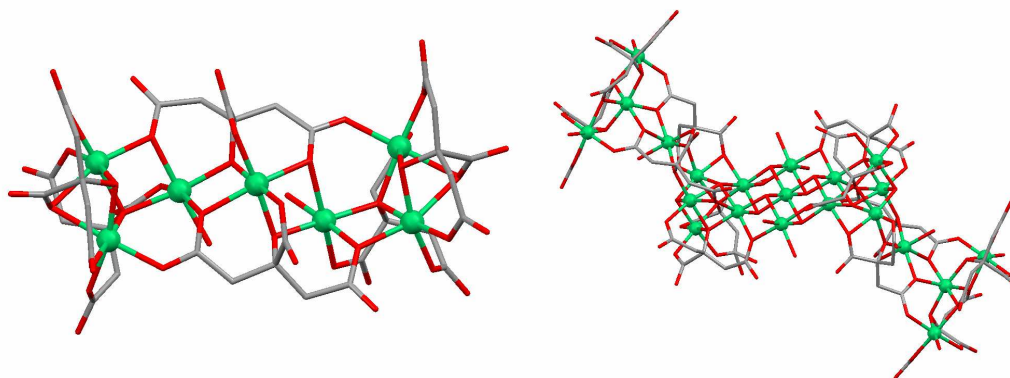


Figure 5-2 – The anion structures in $[\text{NMe}_4]_5\text{Na}_5\{\text{Ni}_7(\text{cit})_6(\text{H}_2\text{O})_2\}$ (left) and $[\text{NMe}_4]_8\text{Na}_8\{\text{Ni}_{21}(\text{cit})_{12}(\text{OH})_{10}(\text{H}_2\text{O})_{10}\}$ (right), (Ni green, O red, C grey, H omitted), CSD structures XEZFOX and XEFIR [4].

The citrate ligand displays a wide variety of coordination modes in this family of nickel clusters, leading to a more diverse set of structures compared with the cobalt citrate system. As an example, Figure 5-3 illustrates the variety of binding modes present in the Ni_{21} cluster.

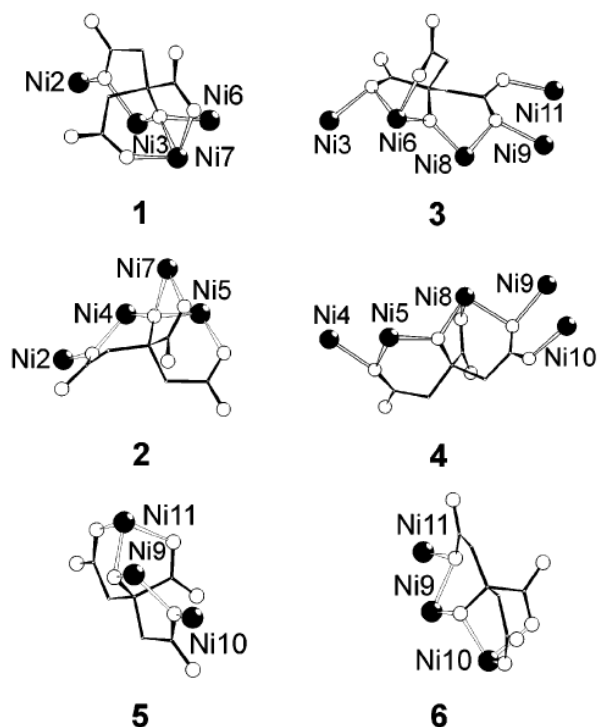


Figure 5-3 – The five different binding modes of the citrate ligand found in the Ni_{21} clusters (modes 5 and 6 are equivalent), (Ni black, O white, C line, H omitted) [5].

5.1 – Discussion of Reaction Methodology

The most striking feature of the nickel citrate system is the assortment of different products and structures available from reaction conditions that are very similar in terms of metal to ligand ratio and final solution pH (~9.2). A delicate balance must exist in the system, with subtle alterations such as applying heat or small changes in the amount of cosolvent being able to alter the product obtained. Even so, it is common to find more than one type of product crystals from these reactions, particularly in the case of the Ni₂₁ synthesis [4]. One hypothesis is that several structural elements exist in equilibrium in solution, which can then assemble into the different products depending on their solubility under the crystallisation conditions. This theory is supported by the structure of the Ni₂₁ cluster, which has a central flat region comprising seven nickel(II) ions and hydroxide bridges that is a nucleus of the crystallisation of Ni(OH)₂ [5], which has two attached (seven nickel) citrate fragments. Presumably the anion of the Ni₇ cluster [NMe₄]₅Na₅{Ni₇(cit)₆(H₂O)₂} may also be present in solution, as it can be obtained by adding less co-solvent [4].

In order to try and isolate the species that may be present, samples of the Ni₈ and Ni₂₁ reaction solutions were made as per the literature [2,5] and guanidinium salts added in an attempt to rapidly crystallise the citrate products as the result of hydrogen bonding with the counterion. Surprisingly, it was discovered that the species remained soluble even after addition of the guanidinium salt, and ambient temperature slow evaporation (Ni₈ synthesis) or mixing with EtOH cosolvent (Ni₂₁ synthesis) was required to effect crystallisation. The majority of the product crystals obtained from these investigations were found to be the Ni₄ cluster [C(NH₂)₃]₈{Ni₄(cit)₄}.6H₂O (Section 5.3). However in the Ni₂₁ system multiple products were obtained.

5.2 – Investigation of the Ni₂₁ Synthesis

5.2.1 – Addition of Guanidinium Ions to the Ni₂₁ Synthesis

Addition of an aqueous solution (15 mL) of NaOH (3.520 g, 88.0 mmol) to an aqueous solution (25 mL) of NiSO₄.6H₂O (10.907 g, 41.5 mmol) gave a pale green precipitate, which was collected by filtration and washed with distilled water (3×100 mL). Dissolution of this solid in an aqueous solution (20 mL) of citric acid

monohydrate (7.985 g, 38.0 mmol) gave a solution of pH 2.94. The pH was raised to 9.20 by the addition of $\text{NMe}_4\text{OH}\cdot 5\text{H}_2\text{O}$ (12.50 g, 69.0 mmol) and the aqueous solution concentrated to a volume of 35 mL on a rotary evaporator without heating. Aliquots of the concentrated solution (1 ml) were mixed with a solution of guanidinium nitrate (0.043 g in 1 ml water) then mixed with EtOH (3 ml) and the solution kept in sealed sample vials.

Three different types of crystal formed in the vials which were identified by single crystal X-ray diffraction. The light green block crystals were found to be the Ni_4 cubane cluster, while the hedgehog formations of pale green plates were identified as the Ni_8 cluster $[\text{NMe}_4]_{10}\{\text{Ni}_8(\text{cit})_6(\text{OH})_2(\text{H}_2\text{O})_2\}$ [2]. The third type of crystal was formed in smaller numbers and appeared as isolated dark green plates. These crystals were very thin and fragile, and when examined using a polarising microscope were found to be highly crazed. As a result of this, the data collected from the single crystal X-ray diffraction study was poor. A preliminary structure solution of the novel $\{\text{Ni}_8(\text{cit})_6(\text{OH})_6\}^{14-}$ cluster was obtained and is shown in Figure 5-4.

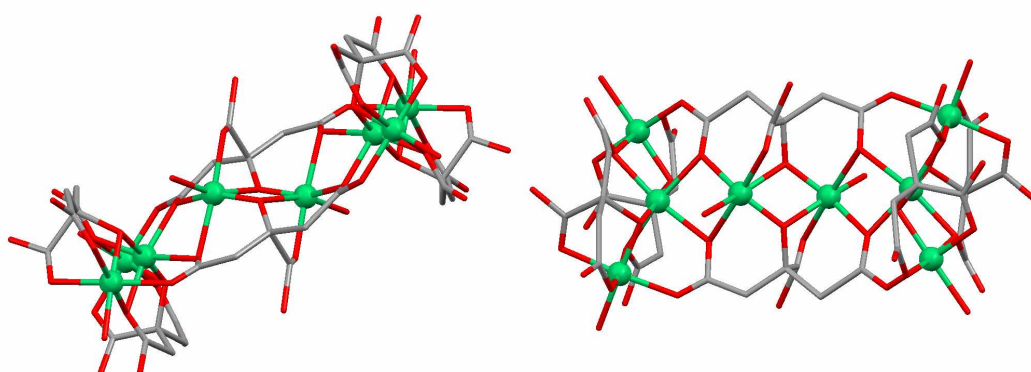


Figure 5-4 – Preliminary structure of the novel $\{\text{Ni}_8(\text{cit})_6(\text{OH})_6\}^{14-}$ cluster anion, (Ni green, O red, C grey, H omitted).

The diffraction data was of insufficient quality to locate the counterions, though initial results suggest the presence of guanidinium and sodium ions. Although a detailed analysis of the structure is not practical, it is interesting to compare the general connectivity with the other nickel citrate clusters. Firstly, by comparison of Figure 5-4 with Figure 5-1, it can be seen that this novel cluster is unlike the previously reported Ni_8 clusters in that it does not feature any nickel cubane or ‘open cubane’ elements. The overall appearance of the $\{\text{Ni}_8(\text{cit})_6(\text{OH})_6\}^{14-}$ cluster with the central

region and two ‘wings’ is reminiscent of the Ni₂₁ cluster (Figure 5-2). Indeed, closer examination of the terminal structure of the ‘wings’ reveals that these are alike in both clusters. As can be seen from Figure 5-5, the coordination of the three terminal nickel centres is very similar in both clusters, but the coordination by the second pair of citrate ligands in the fragment is different. In the Ni₂₁ cluster the β-carboxylate of the highlighted citrate in Figure 5-5 twists away, and so the ligand pair shares coordination to only two nickel centres. In the {Ni₈(cit)₆(OH)₆}¹⁴⁻ structure the ligand pair shares the coordination of a central line of four nickel centres. Each of these two citrate ligands binds to six nickel(II) ions (see Figure 5-6), which is a novel binding mode not previously observed (CSD version 5.29). Overall, these results once again support the hypothesis that that several structural elements exist in equilibrium in solution which can assemble in different ways, such as the common terminal groups seen in both of these two clusters.

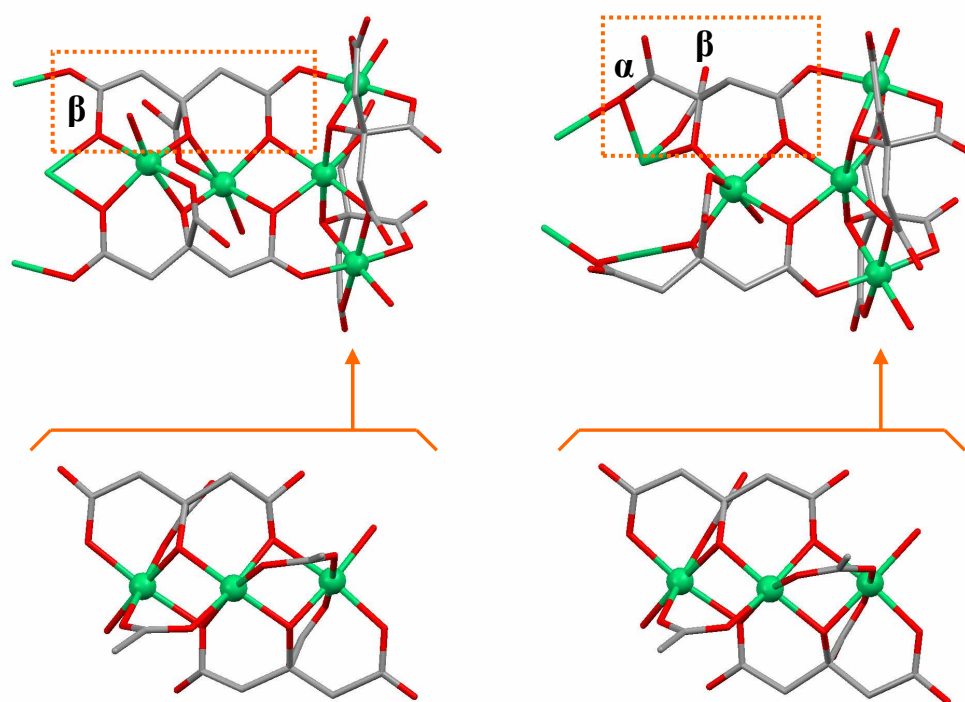


Figure 5-5 – A comparison of the four citrate fragments at the end of the ‘wings’ of the {Ni₈(cit)₆(OH)₆}¹⁴⁻ anion (left) and the {Ni₂₁(cit)₁₂(OH)₁₀(H₂O)₁₀}¹⁶⁻ anion (right). The similarity in the coordination of the three terminal nickel centres is highlighted in the truncated view from the nickel plane shown beneath, (Ni green, O red, C grey, H omitted), Ni₂₁ CSD structure XEFIR [4].

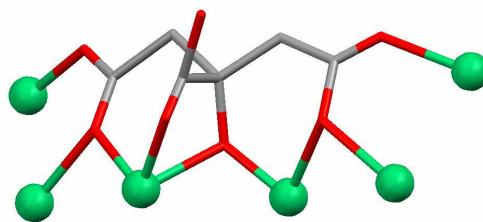


Figure 5-6 – The novel nickel(II) citrate binding mode observed in the $\{\text{Ni}_8(\text{cit})_6(\text{OH})_6\}^{14-}$ anion (Ni green, O red, C grey, H omitted).

5.2.2 – Nickel(II) Monomer $[\text{NMe}_4]_4\{\text{Ni}(\text{Hcit})_2\} \cdot 11\text{H}_2\text{O}$

5.2.2.1 – Synthesis of $[\text{NMe}_4]_4\{\text{Ni}(\text{Hcit})_2\} \cdot 11\text{H}_2\text{O}$

Citric acid monohydrate (7.99 g, 38.0 mmol) and $\text{Ni}(\text{OH})_2$ (3.85 g, 41.5 mmol) were combined in water (20 ml). The nickel hydroxide displayed little sign of dissolving or reacting and so the suspension was stirred rapidly on a hotplate and heated to $\sim 100^\circ\text{C}$. The solution was cooled and $\text{NMe}_4\text{OH} \cdot 5\text{H}_2\text{O}$ (~ 8.23 g) was added but no changes were observed. The beaker was covered, stirred overnight and allowed to stand for a further two days. The unreacted nickel residue was removed by filtration and the green solution was left to stand uncovered. Green plate crystals formed in large yield by slow evaporation, selected IR data: 3265 (m), 1567 (s), 1487 (s), 1411 (s), 1379 (s), 1281 (m), 1186 (w), 1151 (w), 1068 (w), 950 (s), 910 (m), 884 (w), 844 (w). A large sample of the crystals suitable for microanalysis was only available after the solution had evaporated to minimal volume, and the results suggest that residual nickel hydroxide reagent from the synthesis was present in the sample. Analysis, calculated (found) for $[\text{NMe}_4]_4\{\text{Ni}(\text{Hcit})_2\} \cdot 11\text{H}_2\text{O} \cdot \frac{1}{4}(\text{Ni}(\text{OH})_2)$, $\text{C}_{28}\text{H}_{80.5}\text{Ni}_{1.25}\text{N}_4\text{O}_{25.5}$: C, 35.22 (35.01); H, 8.50 (8.17); N, 5.87 (5.97).

The nickel(II) monomer was obtained from a reaction related to the Ni_{21} cluster synthesis, which in this case used commercially available $\text{Ni}(\text{OH})_2$ rather than freshly prepared ‘wet’ precipitate. The commercially available dry powder nickel hydroxide was insoluble (as expected) but was also extremely slow to react with the citric acid solution. Addition of tetramethylammonium hydroxide did not appear to have a great effect, most probably as the vast majority of the nickel remained as the insoluble hydroxide and so was not available for coordination to the deprotonated ligand. By comparison, in the literature Ni_{21} synthesis [4,5] the freshly prepared nickel hydroxide

precipitate is washed with water and then added to the citric acid solution while still damp and is found to dissolve completely after stirring for a few hours. The damp precipitate must also provide the source of the Na^+ counterions, since the only reagent to include sodium ions is the NaOH added to the nickel sulphate solution to form the nickel(II) hydroxide.

5.2.2.2 – Structure of $[\text{NMe}_4]_4[\text{Ni}(\text{Hcit})_2] \cdot 11\text{H}_2\text{O}$

The nickel(II) monomer $[\text{NMe}_4]_4[\text{Ni}(\text{Hcit})_2] \cdot 11\text{H}_2\text{O}$ crystallises in the $P\bar{1}$ space group. The monomer structure consists of a nickel(II) centre with two bound citrate ligands (Figure 5-3). The citrate ligands are triply deprotonated and coordinate to the metal with the central (protonated) alcohol group, one α -carboxylate and one β -carboxylate. Charge balance is provided by four tetramethylammonium ions per monomer, and a large amount of lattice water is also present, which is a common feature of the tetramethylammonium nickel citrate products [2-5]. The octahedral nickel(II) centre is distorted due to the shorter length of the α -carboxylate arm, with the α -carboxylate-Ni-OH angles reduced to 80° . Meanwhile the β -carboxylate-Ni-OH angles are 88° , and therefore close to the ideal 90° due to coordination by the longer and more flexible arm of citrate. This is a common feature of this type of nickel citrate binding, with similar distortions also observed in the nickel citrate monomers $[\text{NH}_4]_4[\text{Ni}(\text{Hcit})_2] \cdot 2\text{H}_2\text{O}$ with ammonium counterions (Figure 5-3) [6] or $[\text{C}(\text{NH}_2)_3]_4[\text{Ni}(\text{Hcit})_2] \cdot 2\text{H}_2\text{O}$ with guanidinium counterions (Figure 4-5) [7].

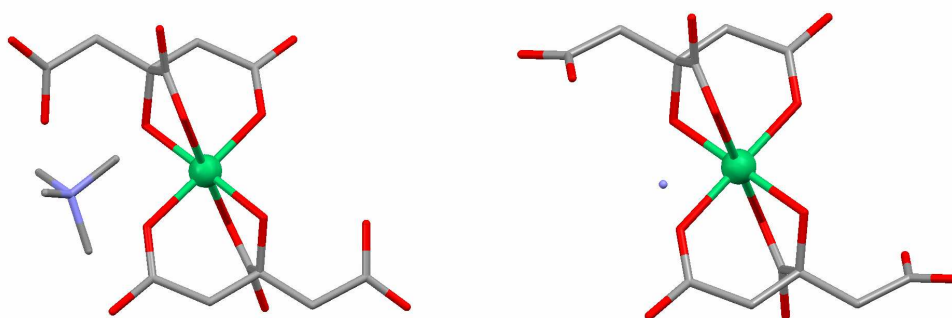


Figure 5-3 – Comparison of the nickel(II) citrate monomer structures with tetramethylammonium (left) and ammonium (right) counterions, (Ni green, O red, C grey, N pale blue, H omitted). Ammonium example is CSD structure NASDAM [6].

5.3 – The Ni₄ Cluster [C(NH₂)₃]₈{Ni₄(cit)₄}.6H₂O

5.3.1 – Synthesis of [C(NH₂)₃]₈{Ni₄(cit)₄}.6H₂O

To a solution of citric acid monohydrate (1.09 g, 5.2 mmol) in water (50 mL) was added a solution of Ni(NO₃)₂.6H₂O (1.51 g, 5.2 mmol) in water (50 mL) followed by a solution of guanidinium carbonate (3.75 g, 20.8 mmol) in water (50 mL). The solution was then left to stand overnight, producing a very large yield of green crystals, which were air-dried. Analysis, calculated (found) for C₃₂H₇₆Ni₄N₂₄O₃₄: C, 24.39 (24.49); H, 4.86 (4.65); N, 21.33 (21.01). Selected IR data (cm⁻¹): 3331 (m), 3130 (m), 1660 (m), 1602 (m), 1580 (m), 1535 (s), 1427 (m), 1378 (s), 1235 (m), 1094 (w), 959 (m), 929 (m), 849 (m).

5.3.2 – Structure of [C(NH₂)₃]₈{Ni₄(cit)₄}.6H₂O

The Ni₄ cubane is the nickel(II) analogue of the Co₄ cluster discussed earlier in Section 2.1.2. Both the Ni₄ and Co₄ clusters have the same structure, where the four metal ions are coordinated by four tetradeprotonated citrate ligands with the alkoxide groups providing the corner bridging oxygen of the cubane. The cubane geometries are similar, with Ni-Ô-Ni bridging angles in the range 96.98-99.81° with Ni-O bond lengths of 2.047-2.112 Å, compared to Co-Ô-Co angles of 97.18-99.24° with Co-O bond lengths of 2.090-2.136 Å. The microanalysis suggests that the product forms as a hexahydrate, and so two water molecules may be present in the cavities between the cubanes (as discussed in Section 2.1.5) in addition to the four water molecules per cluster that are involved in the hydrogen bonding network.

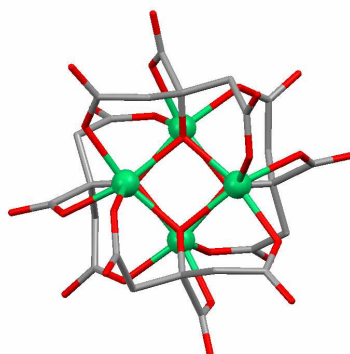


Figure 5-4 – The cubane structure of the {Ni₄(cit)₄}⁸⁻ anion, (Ni green, O red, C grey, H omitted), CSD structure CEHVUH [1].

5.3.3 – Magnetic Properties of $[\text{C}(\text{NH}_2)_3]_8\{\text{Ni}_4(\text{cit})_4\} \cdot 6\text{H}_2\text{O}$

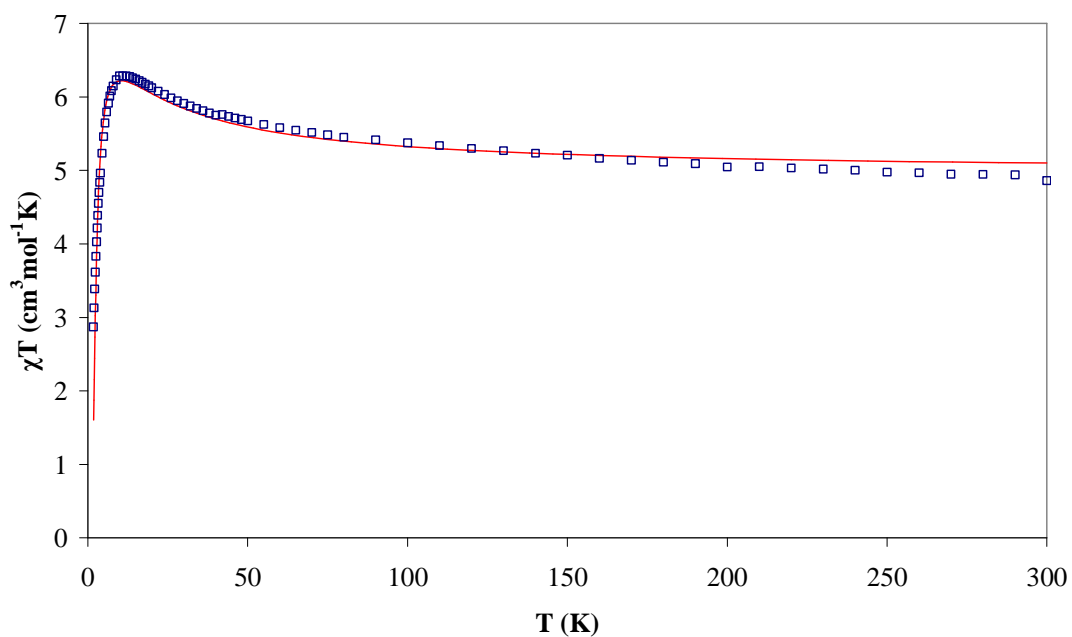


Figure 5-5 – Temperature dependence of χT for $[\text{C}(\text{NH}_2)_3]_8\{\text{Ni}_4(\text{cit})_4\} \cdot 6\text{H}_2\text{O}$, measured in a 1000 Oe field, with the fit shown as a red line ($J_1 = +5$ K, $J_2 = -4$ K, $g = 2.23$)

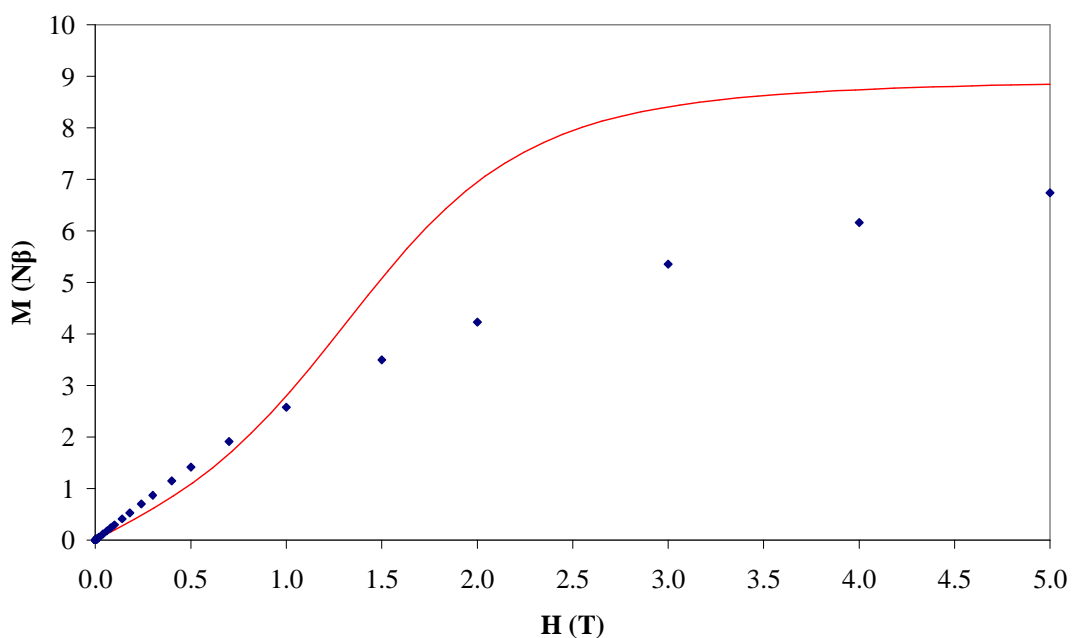


Figure 5-6 – Field dependence of the magnetisation at 2 K for $[\text{C}(\text{NH}_2)_3]_8\{\text{Ni}_4(\text{cit})_4\} \cdot 6\text{H}_2\text{O}$, with the simulation shown as a red line ($J_1 = +5$ K, $J_2 = -4$ K, $g = 2.23$)

The temperature dependence of the χT curve for $[\text{C}(\text{NH}_2)_3]_8\{\text{Ni}_4(\text{cit})_4\} \cdot 6\text{H}_2\text{O}$ measured in a 1000 Oe field is shown in Figure 5-5. This is seen to increase gradually on cooling from 300 K, with a more rapid increase below ~ 50 K to a peak value of $6.29 \text{ cm}^3 \text{ mol}^{-1} \text{ K}$ at 10 K after which the curve decreases rapidly. The curve of Figure 5-6 reveals that at 2 K the magnetisation is not saturated at 5 T, with a value of $M/N\beta = 6.74$. No signals were observed in the out-of-phase component of the ac susceptibility measurements, and so unlike the cobalt(II) analogue discussed earlier, the Ni_4 cubane does not display single molecule magnet properties. The Co_4 cubane did not have a large peak in the χT curve as seen for Ni_4 , however it did display a plateau in the magnetisation curve indicative of low lying excited states and this feature is not observed in the Ni_4 measurements (Compare Figure 2-6 with Figures 5-5 and 5-6).

It was found that the best fit of the χT curve over the temperature range 300-2 K could be obtained using the numbering scheme shown in Figure 5-7 with a two J model ($\hat{H} = -2J_1(S_1S_2 + S_2S_3 + S_3S_4 + S_1S_4) - 2J_2(S_1S_3 + S_2S_4)$) for the coupling between the four Ni(II) centres. J_1 occurs across the four cubane faces with bridging angles of 96.98 and 98.68° , while J_2 occurs across the two faces with equal angles of 99.81°

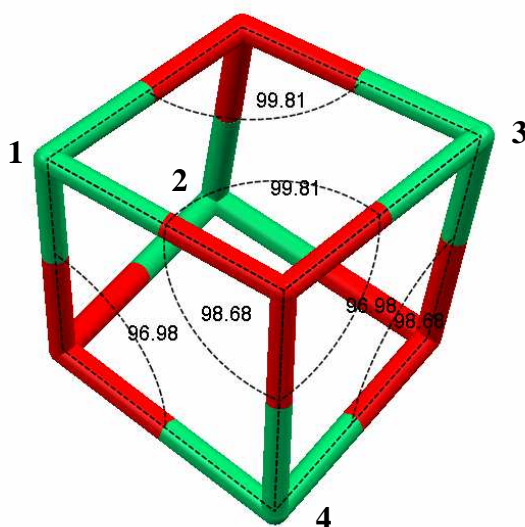


Figure 5-7 – The numbering scheme for the Ni_4 cluster, highlighting the bridging angles of the cubane, (Ni green, O red).

As can be seen in Figure 5-5, a fit using values of $J_1 = +5$ K, $J_2 = -4$ K, $g = 2.23$ reproduces the χT curve shape over the full temperature range measured. This suggests that both ferromagnetic (J_1) and antiferromagnetic (J_2) interactions occur within the cubane. These can be correlated to the bridging angles, with the smaller pair (96.98 & 98.68°) favouring ferromagnetic exchange and larger pair ($2 \times 99.81^\circ$) favouring antiferromagnetic exchange. The two exchange parameters are also seen to be of similar magnitude. The fitting parameters do not reproduce the measured magnetisation curve, although this could be due to neglect of the zero-field splitting of the excited spin levels that are close to the $S = 0$ ground state [1], which are likely to be populated at 2 K.

Clearly the main difference in the magnetic properties of the cobalt(II) and nickel(II) cubane clusters is that Co_4 has a non-zero spin ground state, whereas Ni_4 is $S = 0$. Differences in the specific cubane bridging geometries, zero-field splitting effects, and the much greater orbital contribution to the magnetic moment for cobalt(II), when taken in combination, are likely to be responsible for the unique SMM behaviour of the Co_4 cluster in the family of transition metal guanidinium citrate cubanes.

- [1] Hudson, T. A.; Berry, K. J.; Moubaraki, B.; Murray, K. S.; Robson, R. *Inorg. Chem.* 2006, 45, 3549.
- [2] Murrie, M.; Biner, D.; Stoeckli-Evans, H.; Güdel, H. U. *Chem. Commun.* 2003, 230.
- [3] Strouse, J.; Layten, S. W.; Strouse, C. E. *J. Am. Chem. Soc.* 1977, 99, 562.
- [4] Murrie, M.; Stoeckli-Evans, H.; Güdel, H. U. *Angew. Chem. Int. Ed.* 2001, 40, 1957.
- [5] Ochsenbein, S. T.; Murrie, M.; Rusanov, E.; Stoeckli-Evans, H.; Sekine, C.; Güdel, H. U. *Inorg. Chem.* 2002, 41, 5133.
- [6] Zhou, Z.; Lin, Y.; Zhang, H.; Lin, G.; Tsai, K. *J. Coord. Chem.* 1997, 42, 131.
- [7] Shvelashvili, A. E.; Miminoshvili, E. B.; Belsky, V. K.; Kuteliya, E. R.; Sakvarelidze, T. N.; Ediberidze, D. A.; Tavberidze, M. G. *Bull. Acad. Sci. Georgia.* 2000, 94. (CSD structure QEQTUB)

CAMMAG – Rawson, J. M. *Cammag version 4.1*, University of Cambridge, 2005.

MAGPACK – Borrás-Almenar, J. J.; Clemente-Juan, J. M.; Coronado, E.; Tsukerblat, B. S. *Journal of Computational Chemistry* 2001, 22, 985.

Conclusions

In conclusion, citric acid $[C(OH)(CO_2H)(CH_2CO_2H)_2 = H_4cit]$ has been shown to display a rich variety of coordination chemistry in reaction systems involving cobalt(II), copper(II) and nickel(II). This allows the formation of a wide range of compounds that are of interest for structural and magnetic studies.

It has been discovered that the $\{Co_4(cit)_4\}^{8-}$ cubane subunit is a common structural motif within the family of products obtained from the cobalt(II) citrate system. This discrete unit has been shown to display single molecule magnet behaviour in the Co_4 cluster $[C(NH_2)_3]_8\{Co_4(cit)_4\}.4H_2O$. It is therefore an ideal candidate for use in the development of larger clusters due to the numerous vacant oxygen coordination sites that are available around the outside of the cubane subunit.

The addition of two peripheral cobalt(II) centres to the cubane structure gives the Co_6 cluster $[NMe_4]_3Na\{Co_4(cit)_4[Co(H_2O)_5]_2\}.11H_2O$, which has been shown to be a single molecule magnet that is complicated by intermolecular interactions. The Co_6 cluster displays hydration dependent magnetic behaviour which can be altered using vacuum dehydration. The associated crystal colour change has been investigated using electronic spectroscopy in order to gain insight into the processes occurring. A new and improved synthesis of the Co_6 cluster has provided high quality erinaceous crystals, whilst also allowing access to novel alkali metal ion analogues for comparable structural and magnetic studies. The crystal structure of the Co_6 cluster $[NMe_4]_4\{Co_4(cit)_4[Co(H_2O)_5]_2\}.18H_2O$ with four tetramethylammonium counterions has been determined for the first time, which features a novel cluster packing arrangement and yet also retains similar hydration dependent magnetic behaviour.

The cobalt(II) citrate cubanes have been linked into a 3D coordination network $\{Na_4Co_4(cit)_4[Co(H_2O)_3]_2(H_2O)_{15}\}.3H_2O$ using octahedral cobalt(II) linkers, which is a rare example of an extended network structure consisting of single molecule magnet subunits. The 3D network displays ferromagnetic interactions at low temperature, frequency dependent ac signals, and magnetisation versus field hysteresis loops that suggest an easy-plane magnetic anisotropy.

The cobalt(II) citrate system provides a rare opportunity to observe the changes in the magnetic properties of a structurally related series of compounds of increasing size, which illustrates the transition from the quantum world of discrete SMM clusters to the ‘classical’ world of long range ordering in the extended network. Comparison of the structural and magnetic data for the family of related products has also allowed the formulation of hypothetical magnetostructural correlations to rationalise the observed magnetic behaviour.

The copper(II) guanidinium system has produced two related dimers featuring unusual ‘long contacts’ between the citrate α -carboxylate and the copper(II) centres. High pressure structural studies have revealed that the long contact distance in $[\text{C}(\text{NH}_2)_3]_4\{\text{Cu}_2(\text{cit})_2\} \cdot \text{H}_2\text{O}$ decreases considerably on application of pressure, with a colour change that suggests a change in the copper(II) coordination number. Similar studies of $[\text{C}(\text{NH}_2)_3]\{\text{Cu}_2\text{cit}[\text{C}(\text{NH}_2)_2\text{NH}]_2(\text{OH})\}$ reveal an unusual two stage polymerisation at high pressure with associated phase changes. Analysis of the dimers suggests that the long contact plays an important role in generating the structural features that are thought to be responsible for the observed coupling behaviour of the copper(II) spins. This is supported by structural studies of products formed using related ligands that have the citrate backbone, but do not include an α -carboxylate group. These include the dimer $\{\text{Cu}_2(\text{H}_2\text{L1})_2\}(\text{NO}_3)_2$ [$\text{H}_3\text{L1}$ = 3-methyl-1,3,5-pentanetriol] and tetramer $\{\text{Cu}_4(\text{L2})_2[\text{C}(\text{NH}_2)_2\text{NH}]_4(\text{OMe})_2\} \cdot 2\text{MeOH} \cdot 3\text{H}_2\text{O}$ [$\text{H}_3\text{L2}$ = 3-hydroxy-3-methyl-glutaric acid].

The hydrogen bonding of the guanidinium ion is an important part of the crystal structure for many of the compounds, including a novel copper(II) citrate trimer where the $\{\text{Cu}_3(\text{cit})_3\text{Na}(\text{OH})\}^{6-}$ cluster anions form a hexagonal hydrogen bonding network with three $[\text{C}(\text{NH}_2)_3]^+$ ions per cluster. This results in large channels that run through the structure that are filled with the other highly disordered counterions. The coordinative flexibility of copper(II) is also an important factor in formation of the different compounds due to the possibility of square planar (four coordinate), square-based pyramidal (five coordinate) and octahedral (six coordinate) geometries. This is reflected in the range of cluster sizes that includes monomer, dimer, trimer and tetramer products.

Initial work has been reported on the development of the cobalt(II) and copper(II) citrate systems to include lanthanide(III) ions. Investigation of the cobalt(II) syntheses to reduce problems with precipitation has produced reaction solutions containing both cobalt(II) and erbium(III), with the results of electronic spectroscopy suggesting the successful binding of both metal ions. Although no product crystals were obtained in the Co(II)/Er(III) syntheses, reactions involving Cu(II)/Er(III) produced crystals of a novel 3d-4f network compound.

A central theme in the investigation of these reaction systems is the role of the counterion in product selection. By simply altering the counterion in our cobalt(II) reaction system we can vary the type of product obtained from a Co₄ SMM, via a Co₆ SMM, to a 3D network. The first product changeover is obtained by altering the type of counterions, while the second is achieved by adjusting the counterion concentrations. Studies of the cobalt(II) system at lower pH have shown that tuning the size of the counterion can be used to tune the structural motif of the products, illustrated by a range of compounds from double salts to a 1D coordination polymer (Galloway *et al.*, Ref. [3], Ch. 2). The addition of rubidium sulphate for the crystallisation of the alkali metal analogue of the Co₆ cluster did not give a product containing Rb⁺ counterions. Instead, a pure tetramethylammonium analogue was produced, which highlights the ability of the counterion to select products via subtle solubility effects under the crystallisation conditions employed.

The hydrogen bonding ability of the guanidinium ion plays a key role in the formation of the product crystals in the copper(II) systems, particularly when it becomes incorporated into the cluster structure as the neutral guanidine ligand. An extensive hydrogen bonding network is beneficial for rapid crystallisation, although it can also lead to the preferential selection of a dominant product. In the nickel(II) citrate system, a diverse family of structures can be obtained from very similar reaction conditions. The addition of guanidinium ions produced a dominant Ni₄ cluster [C(NH₂)₃]₈{Ni₄(cit)₄}.6H₂O, however several additional product crystals were formed simultaneously, which allowed the discovery of a novel nickel(II) citrate binding mode in the anion {Ni₈(cit)₆(OH)₆}¹⁴⁻. Overall, this work highlights the important role of the counterion in self-assembly reaction conditions.

Appendix – Crystallography

The crystal structures of the novel products reported are provided on the enclosed Supporting Information CD. Also included are selected reference structures, and the Mercury program installer for viewing the cif files. Note that the structure file names refer to the section number of the compound. See also Section 1.5.3.

Chapter 2 (Notes - 2.1.2 & 2.2.2 literature structures, 2.3.1.2 & 2.4.2 Rigaku data collection, 2.3.4.2 Synchrotron data collection)

Compound	2.1.2 - Co₄	2.2.2 - Na{Co₆}	2.3.1.2 - Li{Co₆}
Formula	C ₃₂ H ₈₀ Co ₄ N ₂₄ O ₃₆	C ₃₆ H ₉₄ Co ₆ N ₃ NaO ₄₉	C ₄₂ H ₅₀ Co ₆ LiN ₃ O ₃₈
Space Group	<i>P4₂/n</i>	<i>Pna2₁</i>	<i>Pna2₁</i>
a (Å)	16.1224(8)	23.093(3)	23.240(5)
b (Å)	16.1224(8)	14.3843(18)	14.527(3)
c (Å)	11.5088(11)	21.691(3)	22.523(5)
α (°)	90	90	90
β (°)	90	90	90
γ (°)	90	90	90
Volume (Å³)	2991.5	7205.24	7603.93
R (%)	5.79	5.65	12.31
Goodness of fit	1.058	1.029	1.119
Residual (eÅ⁻³)	1.548 (-0.396)	0.662 (-0.681)	1.831 (-1.233)
Unique Reflections	3430	11940	16947
Parameters	224	632	758
Restraints	0	1	1
Compound	2.3.3.2 - Cs{Co₆}	2.3.4.2 - NMe₄{Co₆}	2.4.2 - 3D Network
Formula	C ₄₂ H ₅₀ Co ₆ CsN ₃ O ₃₈	C ₄₀ H ₁₂₀ Co ₆ N ₄ O ₅₆	C ₂₄ H ₆₄ Co ₆ Na ₄ O ₅₂
Space Group	<i>Pna2₁</i>	<i>Pbca</i>	<i>P$\bar{1}$</i>
a (Å)	23.0490(13)	23.0160(17)	12.260(5)
b (Å)	14.6342(8)	24.4060(18)	12.366(6)
c (Å)	20.9420(13)	57.227(4)	19.101(9)
α (°)	90	90	78.180(16)
β (°)	90	90	84.625(16)
γ (°)	90	90	89.511(17)
Volume (Å³)	7063.81	32146	2821.81
R (%)	5.95	11.28	11.85
Goodness of fit	1.037	1.117	1.181
Residual (eÅ⁻³)	1.221 (-0.955)	1.426 (-0.801)	2.168 (-1.083)
Unique Reflections	12476	31747	12280
Parameters	846	1742	761
Restraints	1	0	0

Chapter 3 (Notes – 3.1.2 Edinburgh data collection at ambient temperature, 3.2.2 Edinburgh data collection at 150 K, 3.4.1.2 literature structure)

Compound	3.1.2 - Cu citrate dimer	3.2.2 - Hydroxy bridged	
Formula	$C_{16}H_{36}Cu_2N_{12}O_{16}$	$C_9H_{21}Cu_2N_9O_8$	
Space Group	<i>Pbca</i>	<i>Pnma</i>	
a (Å)	11.716(7)	15.679(4)	
b (Å)	14.713(9)	12.699(3)	
c (Å)	17.934(11)	8.932(2)	
α (°)	90	90	
β (°)	90	90	
γ (°)	90	90	
Volume (Å³)	3091.42	1778.43	
R (%)	3.32	5.82	
Goodness of fit	1.0554	0.9563	
Residual (eÅ⁻³)	0.76 (-0.55)	0.79 (-0.78)	
Unique Reflections	3153	2577	
Parameters	208	139	
Restraints	0	0	
Compound	3.3.2 - Na copper trimer	3.3.2 - K copper trimer	
Formula	$C_{14}H_{20}Cu_2N_6Na_{0.67}O_{14.67}$	$C_{14}H_{20}Cu_2K_{0.67}N_6O_{14.67}$	
Space Group	$P\bar{3}$	$P\bar{3}$	
a (Å)	18.9523(3)	19.1180(4)	
b (Å)	18.9523(3)	19.1180(4)	
c (Å)	9.4868(3)	9.4773(4)	
α (°)	90	90	
β (°)	90	90	
γ (°)	120	120	
Volume (Å³)	2951.03	2999.85	
R (%)	12.65	16.25	
Goodness of fit	1.9066	2.5297	
Residual (eÅ⁻³)	3.80 (-2.21)	3.71 (-2.90)	
Unique Reflections	5741	4078	
Parameters	169	77	
Restraints	0	0	
Compound	3.4.1.2 - CO₃ Net	3.4.2.2 - Triol dimer	3.4.3.2 - Tetramer
Formula	$C_8H_{24}Cu_2N_{12}O_{12}$	$C_{12}H_{26}Cu_2N_2O_{12}$	$C_{21}H_{54}Cu_4N_{12}O_{16}$
Space Group	$P\bar{4}n2$	C_2/m	C_2/c
a (Å)	9.0368(6)	8.4080(10)	22.255(5)
b (Å)	9.0368(6)	11.9850(14)	10.971(3)
c (Å)	12.5364(16)	9.6530(13)	18.817(7)
α (°)	90	90	90
β (°)	90	108.331(2)	123.247(9)
γ (°)	90	90	90
Volume (Å³)	1023.77	923.371	3842.32
R (%)	2.06	4.04	5.94
Goodness of fit	1.069	1.139	1.040
Residual (eÅ⁻³)	0.216 (-0.404)	1.203 (-1.028)	1.026 (-0.732)
Unique Reflections	1187	1670	3864
Parameters	102	81	253
Restraints	6	0	0

Chapter 4

Compound	4.2.1.2 - Copper monomer	4.2.2.2 - Cu Er Network
Formula	$C_{28}H_{48}Cu_2N_{12}O_{28}$	$C_{13.33}H_{48}Cu_{1.33}Er_2N_{16}Na_2O_{32}$
Space Group	$P2_1/n$	$Pm3n$
a (Å)	10.3389(11)	14.7660(2)
b (Å)	10.2557(12)	14.7660(2)
c (Å)	11.3067(13)	14.7660(2)
α (°)	90	90
β (°)	117.21	90
γ (°)	90	90
Volume (Å³)	1066.21	3219.5
R (%)	5.74	3.25
Goodness of fit	0.8889	1.294
Residual (eÅ⁻³)	1.31 (-1.18)	0.739 (-0.829)
Unique Reflections	2365	628
Parameters	160	56
Restraints	0	0

Chapter 5 (Notes – 5.3.2 literature structure)

Compound	5.2.1 - Novel Ni8	5.2.2.2 - Ni monomer	5.3.2 - Ni4
Formula	$C_{20}N_6Ni_4O_{41}$	$C_{28}H_{56}N_4NiO_{24}$	$C_{32}H_{80}N_{24}Ni_4O_{36}$
Space Group	$P\bar{1}$	$P\bar{1}$	$P4_2/n$
a (Å)	11.204(5)	8.5923(3)	16.0562(8)
b (Å)	13.606(6)	11.1026(5)	16.0562(8)
c (Å)	19.912(9)	25.5595(10)	11.6135(12)
α (°)	90.083(15)	85.701(2)	90
β (°)	90.086(16)	88.675(2)	90
γ (°)	113.751(14)	79.842(2)	90
Volume (Å³)	2778.32	2393.2	2993.98
R (%)	30.53	16.36	4.87
Goodness of fit	3.8455	1.5058	1.062
Residual (eÅ⁻³)	7.06 (-3.07)	7.46 (-2.36)	1.199 (-0.308)
Unique Reflections	2728	18143	3437
Parameters	285	474	224
Restraints	0	0	0

Acknowledgements

<i>Scholarship Funding</i>	The Carnegie Trust for the Universities of Scotland The Society of Chemical Industry
<i>Research Supervisor</i>	Mark Murrie
<i>Crystallography</i>	Marc Schmidtman Andrew Parkin Louis Farrugia
<i>(at high pressure)</i>	Stephen Moggach (University of Edinburgh) Pascal Parois
<i>MicroSQUID measurements</i>	Wolfgang Wernsdorfer (Institut Néel)
<i>SQUID measurements</i>	Javier Sanchez-Benitez (University of Edinburgh) Floriana Tuna (University of Manchester)
<i>Spectroscopy</i>	Robert D. Peacock
<i>(at high pressure)</i>	Rafael Valiente (Universidad de Cantabria)
<i>Microanalysis</i>	Kim Wilson

Thank you for reading my *Hitch Hiker's Guide to Citrate Coordination Chemistry* – a trilogy in five parts, now including COSHH analysis: Mostly Harmless. Of course this assumes that you have read the text, so if you have come here directly, or via the abstract and/or conclusions, I can assure you that the bulk of the text is actually quite interesting and has lots of pretty pictures that are suitable even for the non-expert. The *Guide* is probably the most remarkable creation ever to come out of KWG Chemistry publishing – more extensive than *Spin Clusters and Single Molecule Magnets*, more detailed than *The Catalytic Hydrogenation of trans-3-(2-furanyl)-3-propenal* and less bleak than *Nuclear Reactor Disasters*. In many of the more relaxed parts of the Galloway family, the *Hitch Hiker's Guide to Citrate Coordination Chemistry* has already supplanted the great *Diffusion of Electrons in the Solar Corona* (Ross K. Galloway, 2006) as the standard repository of scientific knowledge and wisdom, for it scores over the older astrophysics work in two important respects. Firstly, it has fewer equations; and secondly it has large, friendly, full-colour diagrams printed on the majority of its pages.

Modern scientific research is very much a group activity and I am grateful for the productive collaborations I had with the researchers listed at the start of this section. Special mention must go to Marc Schmidtman for sorting out my crystal structures and to Stephen Moggach for enabling the study of my products at high pressure. I would also like to thank all of the members of the Murrie Group for making Glasgow such an enjoyable place to work, particularly my fellow PhD students (you know who you are!). My two project students, Alex and Niall, were a pleasure to work with and provided many interesting results that form part of this thesis.

Special thanks go to my two supervisors, Mark Murrie and Bob Peacock for their long-standing interest in my academic development, which stretches all the way back to my undergraduate days. The submission of this thesis and my career progression owes much to the continued support and encouragement of these two fine gentlemen. I must also acknowledge their rapid and insightful feedback on the large number of reports and paperwork that seems to accompany any research task, and for looking over the draft thesis chapters in recent months. I hope it was an interesting read!

Most importantly, I would like to thank my family for their unwavering support throughout my studies. My Grandparents, Mum, Dad and Ross have been a massive help over the years, and their enthusiasm and interest kept me going when times were tough. I could not have done it without you.

As a final note, it is worthwhile to observe that a thesis only contains the highlights of any given research project, and much work occurs behind the scenes which goes unreported. I think this was best described by Douglas Adams:

“I worked on a lot of things that were almost incredibly successful
but in fact just failed to see the light of day.”